UNIVERSIDAD POLITÉCNICA DE MADRID
Escuela Técnica Superior de Ingeniería Aeronáutica y del Espacio

Nonlinear Vibrations in Turbomachinery: an Asymptotic Approach

D O C T O R A L T H E S I S

Submitted for the degree of Doctor by:

Javier Luis González Monge
MSc in Space Systems

Madrid, 2025


UNIVERSIDAD POLITÉCNICA DE MADRID
Escuela Técnica Superior de Ingeniería Aeronáutica y del Espacio

Doctoral Degree in Aerospace Engineering

Nonlinear Vibrations in Turbomachinery: an Asymptotic Approach

D O C T O R A L T H E S I S

Submitted for the degree of Doctor by:

Javier Luis González Monge
MSc in Space Systems

Under the supervision of:
Dr. Carlos Martel Escobar

Madrid, 2025

Title: Nonlinear Vibrations in Turbomachinery: an Asymptotic Approach

Author: Javier Luis González Monge

Doctoral Programme: Aerospace Engineering

Thesis Supervision:

Dr. Carlos Martel Escobar, Professor of Aerospace Engineering, Universidad Politécnica de Madrid (Supervisor)

External Reviewers:

Thesis Defense Committee:

Thesis Defense Date:

This Thesis has been supported by Programa Propio de I+D+i 2020 de la Universidad Politécnica de Madrid.

Acknowledgements

En primer lugar, me gustaría agradecer a mi director de tesis, Carlos Martel, por tu orientación y apoyo a lo largo de estos años. Siempre has compartido tu conocimiento y experiencia conmigo, dándome tu punto de vista sobre cualquier tema académico sobre el que hemos hablado.

A mi compañero Salva, con el que he compartido muchos momentos a lo largo del desarrollo de la tesis. A Ruth y Eduardo, con los que he disfrutado hablando sobre nuestros temas de investigación y también de nuestras charlas sobre temas extra-académicos.

A Sergio, Blanca y Ángel, con los que he pasado muy buenos momentos desde que nos conocimos en el máster, y he seguido creciendo con ellos durante la etapa de doctorado.

A Roque, por darme la confianza y permitirme trabajar en temas interesantes durante el doctorado.

A mi hermano Juan, con el que he vivido tantas cosas a lo largo de los años. Estoy muy orgulloso de ti, pronto serás físico, y espero que sigamos compartiendo nuestras inquietudes toda la vida.

A mis abuelos, que aunque ya no están con nosotros, ayudaron a que tuviera una infancia y adolescencia muy feliz.

Finalmente, a mis padres, que siempre me han brindado su amor incondicional y apoyo para hacer aquellas cosas que me gustan. Gracias por todo.

Abstract

The study of vibrations in turbomachinery is complex but important to optimize design and estimate component life. In recent years, blades have become more slender to increase efficiency, making them more prone to flutter—an aeroelastic instability where blade motion induces aerodynamic forces that can inject energy into the structure. This causes exponential growth in the response, unless counteracted by other effects such as nonlinear friction, which can balance this instability producing limit cycle oscillations. These systems are also subjected to forced response, arising from aerodynamic forces generated by stator vane wakes upstream of the rotor. Depending on the excitation frequency, the response can be amplified. Nonlinear friction couples forced response and flutter, leading to complicated vibration states.

Several methodologies have been used to analyze the behavior of these systems. Time-domain simulations typically require long integration times to capture nonlinear effects, whereas harmonic balance methods offer an alternative by assuming periodic response and transforming the differential equations into a nonlinear algebraic system. Asymptotic methods have been introduced recently in this field, which exploit the large timescale separation between the oscillations with the natural frequency of the system and the slow envelope due to friction and the aerodynamic instability. As a result, a reduced model accurate in the specific physical regime of interest is obtained, without assuming a particular response type.

This dissertation focuses on the analysis of the nonlinear vibrations of a tuned bladed-disk from a low-pressure turbine using asymptotic techniques. Considering a simplified mass-spring model, the interaction of flutter and friction is studied. Asymptotic equations are derived on the slow timescale where these effects are relevant, and a stability analysis through numerical continuation of the solutions is performed for different levels of the aerodynamic instability. Results show that, for an unstable rotor, single traveling wave (TW) solutions emerge in which friction compensates instability, forming bounded limit cycles. Multi-TW states can arise near stability changes of single-TW solutions.

The analysis is extended to the interaction of flutter and forced response. Results show a nonlinear switching between forced response—where the blades oscillate with the forcing frequency—and flutter. Near the resonance peak, the system follows the excited TW locked to the forcing frequency. Moving away from resonance, the forced response solution loses stability and new branches of solutions emerge. The oscillations associated to these states contain the flutter and forcing frequencies, eventually leading to pure flutter saturated states far enough from the resonance. A new class of solutions is found at the resonance, where

the response is synchronous with the forcing but involves two TWs: the excited one, which has to be stable, and an unstable mode. This corresponds to a configuration with blades vibrating at different amplitude levels, despite the rotor being tuned. All these states are also recovered analyzing a realistic bladed-disk.

The next part of the thesis extends the asymptotic formulation to high-fidelity FEM. The derived model applies to systems where the motion of the contact interfaces is small relative to the overall structure. The full FEM equations are reduced to a single complex differential equation describing the dynamics near resonance. Nonlinear friction is encoded in a single function describing contact conditions such as stick, slip, or gap.

Finally, the methodology is expanded to study interaction between two modes with different mode shapes and friction cycles. It is found that their linear superposition significantly overestimates the response, since activating both modes increases the global nonlinear dissipation.

Keywords: Turbomachinery, Flutter, Forced Response, Asymptotic Methods, Nonlinear Friction.

Resumen

El estudio de las vibraciones en turbomaquinaria es importante para optimizar el diseño y estimar la vida de los componentes. En los últimos años, el diseño de los álabes tiende a geometrías más esbeltas para aumentar su eficiencia, haciéndolos más propensos al flameo, una inestabilidad aeroelástica en la que el movimiento del álabe induce fuerzas aerodinámicas que pueden inyectar energía en la estructura. Esto conllevaría un aumento exponencial de la amplitud de oscilación a menos que sea contrarrestado por otros efectos como la fricción no lineal. Además, estas estructuras pueden experimentar respuesta forzada como consecuencia de las fuerzas aerodinámicas generadas por los estelas de los álabes del estator situados aguas arriba del rotor.

Diversas estrategias se han utilizado para analizar el comportamiento de estas estructuras. Las simulaciones en el dominio temporal requieren integración a lo largo de muchos ciclos para capturar los efectos no lineales. Los métodos de harmonic balance son una alternativa en la que se asume una respuesta periódica y se transforman las ecuaciones en un sistema algebraico no lineal. Los métodos asintóticos, introducidos recientemente en este contexto, explotan la separación de escalas temporales entre las oscilaciones con la frecuencia modal y la evolución lenta debida a la fricción, resultando en un modelo reducido preciso en la situación física de interés.

Esta tesis analiza las vibraciones no lineales de un sistema álabe-disco con álabes idénticos utilizando técnicas asintóticas. Considerando un modelo simplificado de masas y muelles, se estudia la interacción entre flameo y fricción. Se obtienen las ecuaciones asintóticas y se realiza un análisis de estabilidad a través de continuación numérica de sus soluciones para diferentes niveles de la inestabilidad aerodinámica. Los resultados muestran que, para un rotor inestable, aparecen soluciones formadas por una traveling wave (TW) donde la fricción compensa la inestabilidad (ciclos límite). También pueden aparecer soluciones multi-TW cerca de cambios de estabilidad de los estados de una TW.

El análisis se extiende a la interacción entre flameo y respuesta forzada provocada por la fricción no lineal. Los resultados muestran una alternancia no lineal entre la respuesta forzada—donde los álabes oscilan con la frecuencia de excitación—y el flameo. Cerca del pico de resonancia, el sistema responde con la TW excitada a la frecuencia del forzamiento. Lejos de la resonancia, este estado pierde estabilidad y las soluciones de flameo emergen. Aparecen estados de dos frecuencias donde interactúan las frecuencias de flameo y forzamiento, que eventualmente conducen a soluciones saturadas de flameo suficientemente lejos de la resonancia. Además, aparece una nueva clase de soluciones en la resonancia donde la

respuesta es sincrónica con el forzamiento, pero involucra dos TW: la excitada, que debe ser estable, y una inestable. Esto corresponde a una configuración donde los álabes vibran con amplitudes diferentes, a pesar de que todos los sectores son idénticos. Todos estos estados también se obtienen en un modelo realista.

La siguiente parte de la tesis extiende la formulación asintótica a modelos de elementos finitos. La derivación del modelo asintótico se aplica a sistemas donde el movimiento de los contactos es pequeño en comparación con la estructura. Las ecuaciones completas de la estructura se reducen a una sola ecuación diferencial compleja que describe la dinámica cerca de la resonancia. La fricción no lineal se encapsula en una única función que describe las condiciones de contacto, como deslizamiento o separación.

Finalmente, se amplía la metodología para estudiar la interacción entre dos modos con diferentes formas modales y ciclos de fricción. Los resultados muestran que su superposición lineal sobreestima significativamente la respuesta, ya que la activación simultánea de ambos modos incrementa la disipación no lineal global.

Palabras Clave: Turbomaquinaria, Flameo, Respuesta Forzada, Métodos Asintóticos, Fricción no lineal.

Table of Contents

List of Figures

List of Tables

Abbreviations and acronyms

AFT Alternated Fourier Time

CB Craig Bampton

CFD Computational Fluid Dynamics

DFT Discrete Fourier Transform

DOF Degree of Freedom

EO Engine Order

FEM Finite Element Method

FFT Fast Fourier Transform

HB Hopf Bifurcation

HBM Harmonic Balance Method

IBPA Inter-Blade Phase Angle

LCO Limit Cycle Oscillation

LPT Low Pressure Turbine

ROM Reduced Order Model

TB Torus Bifurcation

TW Traveling Wave

UPM Universidad Politécnica de Madrid

c.c. Complex conjugate

Chapter 1

Introduction

Aeroelasticity studies the interaction between the motion of a structure and the surrounding fluid. An overview of the different aspects involved in aeroelasticity is usually presented in the form of Collar's triangle [1], as depicted in Fig. 1.1.

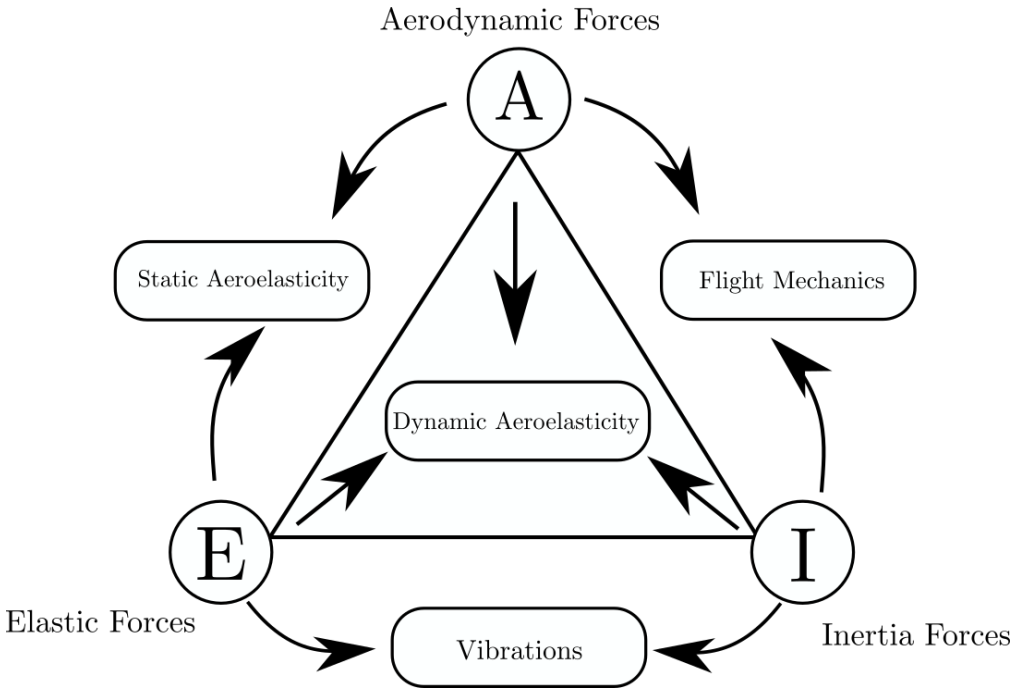

Figure 1.1: Collar's triangle.

The development of this branch started in last century, with the goal of understanding the oscillations of aircraft wings [2]. In the context of turbomachinery, aeroelasticity analyses have received much attention in the past 70 years, and the state of knowledge increased significantly in the last decades [3].

Gas turbine engines are widely used in the industry for propulsion and power generation. These are extremely complex devices from the structural as well as the aerodynamic point of view, and, during operation conditions, they are typically subjected to highly unsteady aerodynamic loads.

The recent review [4] highlights several dynamic challenges in modern aero-engines. Notably, tip clearance instabilities in compressors, exacerbated by engine deterioration, can trigger rotating stall and surge, particularly during transient operations like take-off acceleration. The paper also highlights combustion-related instabilities, where unsteady heat release couples with acoustic modes, amplifying pressure waves that challenge structural integrity. These dynamic issues, distinct from static problems of earlier decades, require advanced modeling of fluid-structure interactions and damping characterization to mitigate certification delays and operational hazards.

Therefore, the study of the dynamic response of turbomachinery systems continues to be a very active research field, with scientific and industrial interest. In particular, the study of turbine blade vibrations is an important area of investigation [3], [5]. Over the last years, the demand for more efficient systems with less fuel consumption, have led to mechanical designs which are closer to their structural limits, increasing the risk of high cycle fatigue (HCF) damage and failure of the structure [6]–[9].

The aerodynamic loads create two main types of problems: forced response and self-excited oscillations. Forced response problem in turbomachinery occurs due to the wakes generated from the stator that are seen as a periodic forcing from the downstream rotor in a turbine. The self-excited oscillations are more complicated, since these aerodynamic forces are induced by the motion of the structure, which distorts the surrounding flow field. Depending on the relative phase of the oscillations of the structure and the aerodynamic force, energy could be pumped into the system, leading to an exponential growth of the vibration. This phenomenon is known as flutter, which has been studied extensively in the context of low pressure turbines [5].

One of the main sources of damping to dissipate energy from the blade oscillations is dry friction, present at the contact interfaces between the blades and the disk. This effect can balance the flutter instability, reaching bounded oscillations with a limited maximum amplitude. A detailed analysis of this saturation is critical to determine if the vibration levels of the system are safe from the point of view of fatigue.

Friction effects are, therefore, crucial for the determination of the final blade vibration amplitude, but due to their highly nonlinear character, their description can be quite complex. For

this reason, the use of reduced models is of great interest to increase the understanding of the different phenomena that can appear and to be able to quickly estimate the final vibration levels of the blades in the system.

In this chapter, we describe the main equations that are used to analyze the vibration of bladed-disk structures, paying particular attention to Low Pressure Turbine (LPT) configurations. In addition, a review of the current state of knowledge in the aeroelastic analysis of these structures is presented.

1.1 Problem Description

Bladed-disk structures, such as the one depicted in Fig. 1.2, are nearly conservative systems which can be described by the system of equations

$$\mathbf{M}_s\ddot{\mathbf{x}} + \mathbf{K}_s\mathbf{x} + \mathbf{G}(\mathbf{x}, \dot{\mathbf{x}}) + \mathbf{f}_a = \mathbf{f}(t), \tag{1.1}$$

where $\mathbf{x}$ is the vector containing all the DOFs of the structure, $\mathbf{M}_s$ is the mass matrix of the structure, $\mathbf{K}_s$ is the stiffness matrix, $\mathbf{G}(\mathbf{x}, \dot{\mathbf{x}})$ is the vector of nonlinear forces, $\mathbf{f}_a$ contains the aerodynamic forces induced by the motion of the structure, and $\mathbf{f}(t)$ is the external forcing.

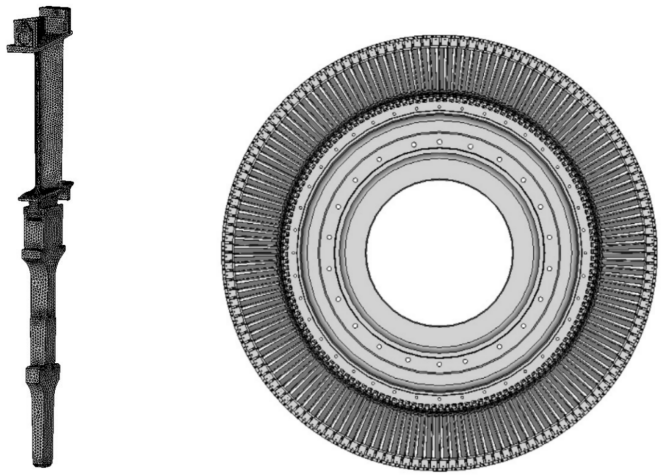

Figure 1.2: Bladed-disk (sector and full annulus).

A direct analysis of this problem is extremely prohibitive because the elastic problem is coupled with the aerodynamic one. The discretization of a FEM model of a bladed-disk can have several millions of DOFs. In addition, since the aerodynamic flow is affected by the motion of the structure, an accompanying CFD analysis would be required at each time step to evaluate the aerodynamic forces.

The problem is even more complicated due to the presence of nonlinear forces, usually related to friction at the contact interfaces between the different parts of the structure. They have a very local effect, and, in general, require long computational times since they are typically small effects that act on a much slower timescale.

Therefore, before trying to solve the problem directly, several assumptions can be made to simplify it but still capture the response with a high degree of accuracy.

1.1.1 Free Vibration

The free vibration problem of the structure is given by

$$\mathbf{M}_s\ddot{\mathbf{x}} + \mathbf{K}_s\mathbf{x} = 0, \tag{1.2}$$

where the contacts are fixed, and the structural matrices that now do not contain the contact DOFs are slightly smaller than the ones from Eq. (1.1). A bladed-disk is normally comprised of the same sector repeated several times in the circumferential direction (Fig. 1.2). If we assume all sectors identical (tuned configuration), the mass and stiffness matrices can be written as

$$\mathbf{M}_s = \begin{pmatrix} \mathbf{M} & \mathbf{M}_c & \mathbf{0} & \cdots & \mathbf{M}_c^\top \\ \mathbf{M}_c^\top & \mathbf{M} & \mathbf{M}_c & \cdots & \mathbf{0} \\ \vdots & \vdots & \vdots & \ddots & \vdots \\ \mathbf{0} & \cdots & \mathbf{M}_c^\top & \mathbf{M} & \mathbf{M}_c \\ \mathbf{M}_c & \cdots & \mathbf{0} & \mathbf{M}_c^\top & \mathbf{M} \end{pmatrix}, \quad \mathbf{K}_s = \begin{pmatrix} \mathbf{K} & \mathbf{K}_c & \mathbf{0} & \cdots & \mathbf{K}_c^\top \\ \mathbf{K}_c^\top & \mathbf{K} & \mathbf{K}_c & \cdots & \mathbf{0} \\ \vdots & \vdots & \vdots & \ddots & \vdots \\ \mathbf{0} & \cdots & \mathbf{K}_c^\top & \mathbf{K} & \mathbf{K}_c \\ \mathbf{K}_c & \cdots & \mathbf{0} & \mathbf{K}_c^\top & \mathbf{K} \end{pmatrix}, \tag{1.3}$$

where $\mathbf{M}$ is the mass matrix of the interior DOFs of a single sector and $\mathbf{M}_c$ is the mass matrix related to the DOFs at the interface between the adjacent sectors. We assume that there is a total of N sectors. These matrices have a circulant structure [10], since each row is the same as the previous one but with a shift in the position. This cyclic symmetry property will be exploited to reduce the computational cost of the analysis.

The natural modes of vibration are solutions where the entire system is vibrating at the same frequency. Therefore, to find these states, the displacement vector can be written as

$$\mathbf{x} = \mathbf{X}e^{i\omega t} + \text{c.c.}, \tag{1.4}$$

where c.c. stands for the complex conjugate,

$$\mathbf{X} = \begin{pmatrix} \mathbf{X}_1 \\ \mathbf{X}_2 \\ \vdots \\ \mathbf{X}_N \end{pmatrix}, \tag{1.5}$$

and $\mathbf{X}_j$ is the displacement vector of the j-th sector. Substituting this expression into Eq. (1.2), we obtain the eigenvalue problem

$$\left[\begin{pmatrix} \mathbf{K} & \mathbf{K}_c & \mathbf{0} & \cdots & \mathbf{K}_c^\top \\ \mathbf{K}_c^\top & \mathbf{K} & \mathbf{K}_c & \cdots & \mathbf{0} \\ \vdots & \vdots & \vdots & \ddots & \vdots \\ \mathbf{0} & \cdots & \mathbf{K}_c^\top & \mathbf{K} & \mathbf{K}_c \\ \mathbf{K}_c & \cdots & \mathbf{0} & \mathbf{K}_c^\top & \mathbf{K} \end{pmatrix} - \omega^2 \begin{pmatrix} \mathbf{M} & \mathbf{M}_c & \mathbf{0} & \cdots & \mathbf{M}_c^\top \\ \mathbf{M}_c^\top & \mathbf{M} & \mathbf{M}_c & \cdots & \mathbf{0} \\ \vdots & \vdots & \vdots & \ddots & \vdots \\ \mathbf{0} & \cdots & \mathbf{M}_c^\top & \mathbf{M} & \mathbf{M}_c \\ \mathbf{M}_c & \cdots & \mathbf{0} & \mathbf{M}_c^\top & \mathbf{M} \end{pmatrix} \right] \begin{pmatrix} \mathbf{X}_1 \\ \mathbf{X}_2 \\ \vdots \\ \mathbf{X}_{N-1} \\ \mathbf{X}_N \end{pmatrix} = \begin{pmatrix} \mathbf{0} \\ \mathbf{0} \\ \vdots \\ \mathbf{0} \\ \mathbf{0} \end{pmatrix}. \tag{1.6}$$

This problem can be reduced to a single sector if we use the invariance of the structure under rotations by the inter-blade phase angle (IBPA) $2\pi/N$. In other words, the problem is invariant under the change

$$\mathbf{X}_1 \to \mathbf{X}_2, \cdots, \mathbf{X}_N \to \mathbf{X}_1, \tag{1.7}$$

which is sketched in Fig. 1.3.

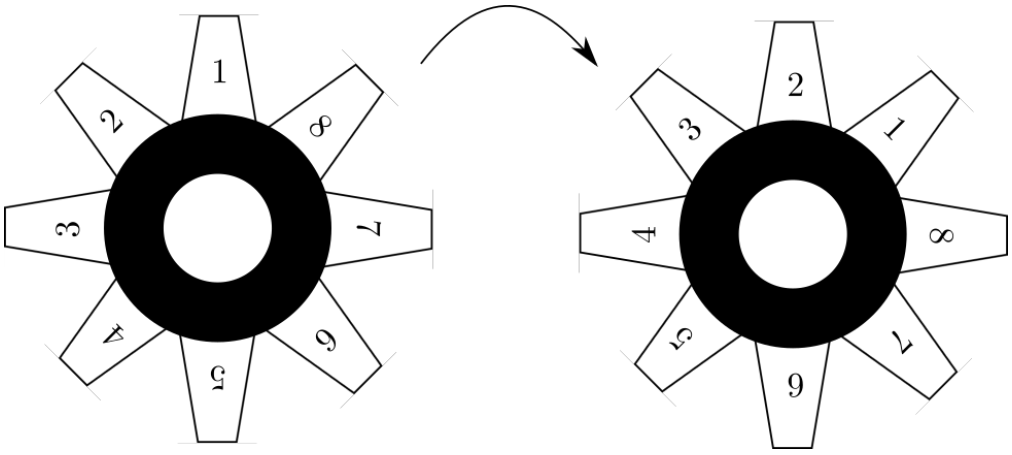

Figure 1.3: Rotational symmetry of a tuned bladed-disk.

This transformation can be expressed through a symmetry matrix

$$\mathbf{S} = \begin{pmatrix} \mathbf{0} & \mathbf{I} & \mathbf{0} & \cdots & \mathbf{0} \\ \mathbf{0} & \mathbf{0} & \mathbf{I} & \cdots & \mathbf{0} \\ \vdots & \vdots & \vdots & \ddots & \vdots \\ \mathbf{0} & \mathbf{0} & \mathbf{0} & \cdots & \mathbf{I} \\ \mathbf{I} & \mathbf{0} & \mathbf{0} & \cdots & \mathbf{0} \end{pmatrix}, \tag{1.8}$$

where $\mathbf{I}$ is an identity matrix with the same size as number of DOFs of each sector, m. It is well-known [11] that this symmetry matrix commute with the mass and stiffness matrices in (1.6).

The eigenvectors of the symmetry matrix $\mathbf{S}$ can be used to reduce the computation of the eigenvalue problem of the bladed-disk. More precisely, for this rotational symmetry, the eigenvectors of $\mathbf{S}$ can be expressed as

$$\mathbf{X} = \begin{pmatrix} \mathbf{Z}_k e^{i\frac{2\pi k}{N}1} \\ \mathbf{Z}_k e^{i\frac{2\pi k}{N}2} \\ \vdots \\ \mathbf{Z}_k e^{i\frac{2\pi k}{N}N} \end{pmatrix}, \tag{1.9}$$

for $k = 1, \ldots, N$. This expression implies that the in-sector motion is the same for all sectors, but with a phase shift of between them. This way of writing the displacements is nothing more than the discrete Fourier transform in the circumferential direction. Substituting Eq. (1.9) into Eq. (1.6), we reduce the eigenvalue problem to a single sector

$$\left[(\mathbf{K}_c - \omega_k^2 \mathbf{M}_c)^\top e^{-i\frac{2\pi k}{N}} + (\mathbf{K} - \omega_k^2 \mathbf{M}) + (\mathbf{K}_c - \omega_k^2 \mathbf{M}_c) e^{i\frac{2\pi k}{N}}\right] \mathbf{Z}_k = 0, \tag{1.10}$$

for $k = 1, \ldots, N$. This is drastic reduction, especially for systems with a high count of sectors, going from $N \cdot m$ to m DOFs. For each k, one can obtain a set of m natural modes of vibration, and ω_k are the associated frequencies.

These natural modes are usually organized in modal families, and are represented in a diagram like the one shown in Fig. 1.4. Each family is represented with a single color, and in a bladed-disk they typically correspond to a different mode shape, such as bending, torsion, etc. The index k, which is the sector-to-sector wavenumber of the mode, is usually called number of Nodal Diameters (ND) in this context, since it is related to the number of node lines that appear around the rotor.

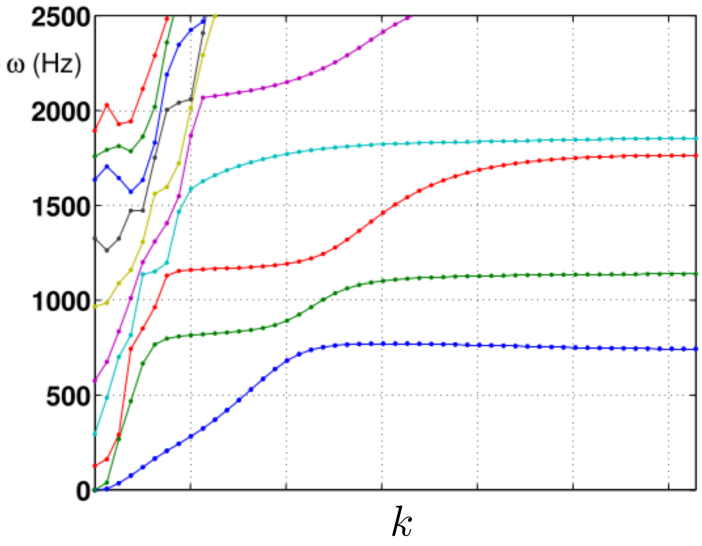

Figure 1.4: Natural frequencies of a bladed-disk.

The flat part of the family is usually related to blade alone modes, with a very small coupling effect of the disk. Nevertheless, for lower NDs, the influence of the disk can be appreciated, where there can be a significant change in the frequency of vibration and the mode shape.

These natural modes of vibration are a very convenient way to express the physical displacements of a structure as a linear combination of them. In the present formulation, the modes are traveling waves (TW), corresponding to a motion that is propagating continuously throughout the disk. A representation of the decomposition of displacements in terms of these modes is shown in Fig. 1.5.

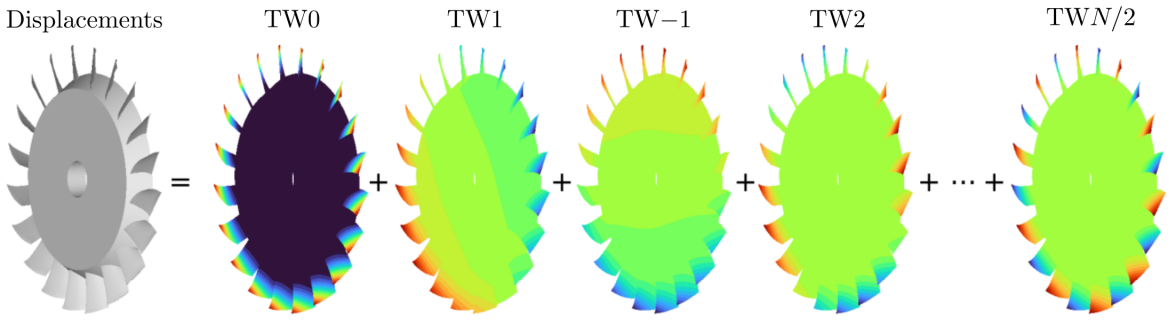

Figure 1.5: Decomposition of blade displacements as a linear combination of TW modes [12].

Another set of modes, which are a linear combination of the traveling waves, are the standing waves. They can also be used to decompose the motion of the structure, but they are not convenient since the matrices of the aerodynamic forces will also have the circulant property,

as will be shown later.

Mathematically, we could organize the modes associated to wavenumber k,

$$\omega_{k1}, \ldots, \omega_{km}, \qquad \mathbf{Z}_{k1}, \ldots, \mathbf{Z}_{km}, \tag{1.11}$$

as columns of a matrix

$$\Phi_k = \begin{pmatrix} \mathbf{Z}_{k1} & \mathbf{Z}_{k2} & \cdots & \mathbf{Z}_{km} \end{pmatrix}. \tag{1.12}$$

Considering the sector to sector symmetry from Eq. (1.9), we can define a transformation matrix

$$\mathbf{X} = \Phi \mathbf{A}, \tag{1.13}$$

where $\mathbf{A}$ contains the TW amplitudes, and Φ is given by

$$\Phi = \frac{1}{\sqrt{N}} \begin{pmatrix} \Phi_1 e^{i\frac{2\pi 1}{N}1} & \ldots & \Phi_N e^{i\frac{2\pi N}{N}1} \\ \vdots & \ddots & \vdots \\ \Phi_1 e^{i\frac{2\pi 1}{N}N} & \ldots & \Phi_N e^{i\frac{2\pi N}{N}N} \end{pmatrix}, \tag{1.14}$$

where the factor of $1/\sqrt{N}$ is included to have a unitary transformation matrix. This change of basis makes the eigenvalue problem (1.6) diagonal, since substituting Eq. (1.13) into Eq. (1.6) and premultiplying by Φ^H, gives

$$\begin{pmatrix} \mathbf{\Omega}_1^2 - \omega^2 \mathbf{I} & \cdots & \mathbf{0} \\ \vdots & \ddots & \vdots \\ \mathbf{0} & \cdots & \mathbf{\Omega}_N^2 - \omega^2 \mathbf{I} \end{pmatrix} \begin{pmatrix} \mathbf{A}_1 \\ \vdots \\ \mathbf{A}_N \end{pmatrix} = \begin{pmatrix} \mathbf{0} \\ \vdots \\ \mathbf{0} \end{pmatrix}, \tag{1.15}$$

where

$$\mathbf{\Omega}_k^2 = \begin{pmatrix} \omega_{k1}^2 & 0 & \cdots & 0 \\ 0 & \omega_{k2}^2 & \cdots & 0 \\ \vdots & \vdots & \ddots & \vdots \\ 0 & 0 & \cdots & \omega_{km}^2 \end{pmatrix}. \tag{1.16}$$

This TW formulation is very convenient, especially when the problem is linear since it uncouples the equations.

1.1.2 Aerodynamic Forces

We first discuss the aerodynamic term $\mathbf{F}(t)$ from Eq. (1.1), which corresponds to the forced response problem [13]. In a rotor, this forcing is periodic with the shape of a traveling wave,

which can be expressed as

$$\mathbf{f}(t) = \mathbf{F}e^{i\omega t} + \text{c.c.}, \tag{1.17}$$

where

$$\mathbf{F} = \begin{pmatrix} \mathbf{F}_0 e^{i\frac{2\pi \text{EO}}{N}1} \\ \vdots \\ \mathbf{F}_0 e^{i\frac{2\pi \text{EO}}{N}N} \end{pmatrix}. \tag{1.18}$$

The wavenumber of the forced TW is denoted by the Engine Order (EO). To compute the amplitude of the response under this external forcing, provided that there are not any other effects, one can solve the equation

$$(\mathbf{K}_s - \omega^2 \mathbf{M}_s)\mathbf{X} = \mathbf{F}. \tag{1.19}$$

Nevertheless, if we use the TW transformation from Eq. (1.13), this can be expressed more simply as

$$\begin{pmatrix} \mathbf{\Omega}_1^2 - \omega^2\mathbf{I} & \cdots & \mathbf{0} \\ \vdots & \ddots & \vdots \\ \mathbf{0} & \mathbf{\Omega}_{\text{EO}}^2 - \omega^2\mathbf{I} & \mathbf{0} \\ \vdots & \ddots & \vdots \\ \mathbf{0} & \cdots & \mathbf{\Omega}_N^2 - \omega^2\mathbf{I} \end{pmatrix} \begin{pmatrix} \mathbf{A}_1 \\ \vdots \\ \mathbf{A}_{\text{EO}} \\ \vdots \\ \mathbf{A}_N \end{pmatrix} = \begin{pmatrix} \mathbf{0} \\ \vdots \\ \Phi_{\text{EO}}^H \mathbf{F} \\ \vdots \\ \mathbf{0} \end{pmatrix}, \tag{1.20}$$

where it can be seen that the forcing only affects the TW amplitudes $\mathbf{A}_{\text{EO}}$.

The amplification of the response can be increased when the forcing frequency is close to one of the natural frequencies. This is typically represented using the Campbell diagram (Fig. 1.6), in which the speed lines for different NDs are superimposed against the natural frequency lines. The crossing of these lines highlight a point susceptible of having a large response, marked as FR in the plot.

The other main aerodynamic effect that can appear is flutter [5], [14], related to the term $\mathbf{f}_a$ in Eq. (1.1). In turbine bladed-disks, the aerodynamic forces are usually modelled as linear, because the motion of the blades is assumed to be small. Since these forces depend on the displacements, taking them into account results in modifying the structural eigenvalue problem with the addition of the aerodynamic matrix

$$(\mathbf{K}_s - \omega^2 \mathbf{M}_s)\mathbf{X} = \mathbf{M}_{\text{aero}}(\omega)\mathbf{X}, \tag{1.21}$$

which depends on the frequency ω of the oscillation. Nevertheless, even with the linearization assumption, the cost of this eigenvalue problem is not realizable, since it would require fully

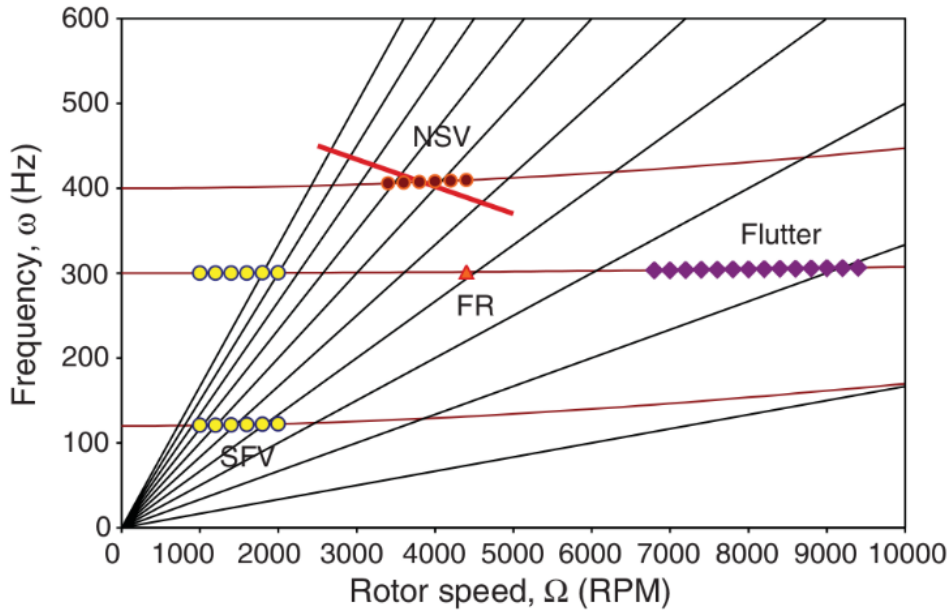

Figure 1.6: Campbell Diagram [5].

coupled aerodynamic calculations using the linearized Navier-Stokes equations for all ω and all possible independent displacements.

Therefore, some additional simplifications are included in the analysis. First, we remark that the structure of the aerodynamic matrix is cyclic, with the following form

$$\mathbf{M}_{\text{aero}} = \begin{pmatrix} \mathbf{L}_0 & \mathbf{L}_1 & \cdots & \mathbf{L}_{N-1} \\ \mathbf{L}_{N-1} & \mathbf{L}_0 & \cdots & \mathbf{L}_{N-2} \\ \vdots & \vdots & \ddots & \vdots \\ \mathbf{L}_1 & \mathbf{L}_2 & \cdots & \mathbf{L}_0 \end{pmatrix}, \tag{1.22}$$

where $\mathbf{L}_{j-i}$ contains the aerodynamic forces acting on sector i due to the vibration of sector j. The elements of this matrix are the so-called influence coefficients. Typically, their computation just requires taking into account the effect of the immediately adjacent sectors, since the effect on further sectors becomes smaller [15].

As mentioned, this matrix is circulant, in the same way as the mass and stiffness matrices of the structural part of the bladed-disk. Therefore, the aeroelastic modes are also traveling

waves. Using this fact, we can express the eigenvalue problem in TW basis as

$$\begin{pmatrix} \mathbf{\Omega}_1^2 - \omega^2\mathbf{I} & \cdots & \mathbf{0} \\ \vdots & \ddots & \vdots \\ \mathbf{0} & \cdots & \mathbf{\Omega}_N^2 - \omega^2\mathbf{I} \end{pmatrix} \begin{pmatrix} \mathbf{A}_1 \\ \vdots \\ \mathbf{A}_N \end{pmatrix} = \Phi^H \mathbf{M}_{\text{aero}}(\omega)\Phi \begin{pmatrix} \mathbf{A}_1 \\ \vdots \\ \mathbf{A}_N \end{pmatrix} = \begin{pmatrix} \mathbf{M}_1(\omega) & \cdots & \mathbf{0} \\ \vdots & \ddots & \vdots \\ \mathbf{0} & \cdots & \mathbf{M}_N(\omega) \end{pmatrix} \begin{pmatrix} \mathbf{A}_1 \\ \vdots \\ \mathbf{A}_N \end{pmatrix}, \tag{1.23}$$

where the aerodynamic part is now block-diagonal, although the matrices $\mathbf{M}_k$ are not diagonal. These matrices still require very computationally expensive calculations, since one needs m solutions of the linearized Navier-Stokes equations, where m is the number of DOFs inside a sector, for each $\mathbf{M}_k$ and frequency. Therefore, an additional assumption is made, which is that the aerodynamic effects only produce a small correction to the natural frequencies of the structure.

These corrections are typically computed with the energy method [5]. The assumptions that are made is that only the diagonal terms of the $\mathbf{M}_k(\omega_0)$ matrices are relevant, and they are evaluated at the mode frequency ω_0. This translates into a correction of the natural frequencies with two coefficients $\omega_{kj} \to \omega_{kj}(1 + (\eta + i\xi))$. The real part of this correction, η, is the small frequency shift induced by the aerodynamic forces and the imaginary part, ξ, is the aerodynamic damping. If this coefficient is negative, the aerodynamic forces are pumping energy into the system, corresponding to a flutter situation.

The energy method is much less expensive, since it just requires one linear CFD simulation per mode.

1.1.3 Nonlinear Friction

Dry friction is usually present at the contact interfaces, for instance at the fir-tree connecting the blades with the disk (see Fig. 1.7). If these effects are taken into account, such as in Eq. (1.1), the simple treatment described in the previous subsection is no longer applicable. Due to the nonlinearity, the TW amplitudes are coupled.

An extensive review of the friction effects and several strategies to compute the dynamics of the bladed-disk with friction can be found in [16]. The study of these effects has attracted a lot of attention [17], since an accurate modeling of the friction is essential to estimate the response of the system. Even if a system exhibits flutter (linear regime), bounded oscillations can be reached due to the nonlinear friction, which can balance the instability (nonlinear regime).

A model of the nonlinearities typically includes stick-slip transitions and a gap regime [18].

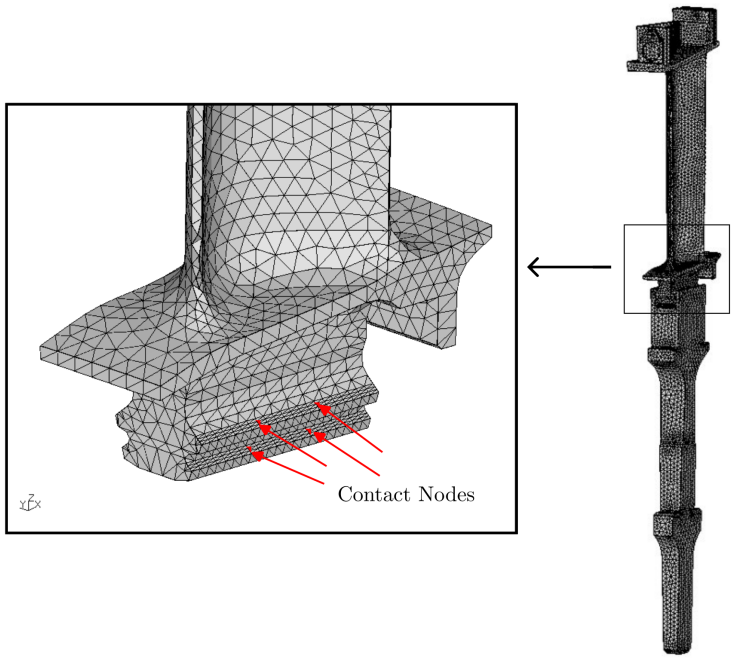

Figure 1.7: Contact interfaces in the fir-tree union.

The contacts have a normal variable load, and depending on the force in the tangential direction the contact can slide, if the maximum Coulomb limit is exceeded, or stick, if the force is below this limit. Another alternative to model friction is the so-called microslip limit [19], where the displacements of the contact only have a local deformation, without observable macroscopic oscillations.

There have been several efforts to model these effects and include them in the formulation of the equations of motion [20]–[25]. These contact laws are highly nonlinear, and the dissipation depends on the past history of the system.

Numerically, several models were considered in [26], [27], comparing different strategies such as including the contact forces as two 1D elements or a single 2D friction element. The transition between gap/contact is usually smoothed numerically with a very stiff spring in the normal direction to the contact surface. This usually ensures that the transition from gap to contact is better behaved numerically even though a small penetration between the structures is allowed.

There is an additional difficulty with these laws, which is the multiplicity of solutions in the static equilibrium, especially in structures with complex geometries. Very recently, a study [28] assessed this effect for a simplified model of an underplatform damper. By converging first a static analysis and then doing a frequency sweep, or by directly performing a frequency

sweep, it was found that the maximum value of the response could have significant differences.

1.2 Solution Methods

In order to solve the equations of motion (1.1) of a bladed-disk under these nonlinearities, one may try different strategies. Direct simulation of the system is not feasible, due to the large number of DOFs that need to be retained due to the coupling induced by the friction. In addition, nonlinear friction is a small force that is only applied to a small subset of contact nodes, making the equations stiff and require integration over many elastic cycles.

For this reason, several strategies have been developed throughout the years. In the next section, we go through some of these techniques, which are the time integration of reduced order models (ROMs), the method of harmonic balance (HBM), or the more recent use of asymptotic techniques.

1.2.1 Reduced Order Models

Time domain methods integrate the equations of motion (1.1) directly, but some reduction has to be applied first to make the system more manageable. An extensive review of ROMs can be found in [29].

One of the most classic methods, which has been extensively used, is the Craig-Bampton (CB) reduction [30]. In its early conception, this method was used to describe several substructures using a reduced set of modes for each, which were then used to assemble the complete system. The use of substructuring made sense when the computational resources in terms of memory were very limited. More recently, the CB method is used directly without substructuring, since it still provides a basis of modes that can be used to reduce the system. For example, one could use the TW modes to express the DOFs of the structure (except the contacts) as a linear combination of just a reduced set of them. Then, by also including the motion of the contacts, one has to solve numerically a system with a much smaller DOF count. Different variations of the CB method have also been proposed in [31], [32]

In the context of turbomachinery, several ROMs have been used. For mistuned bladed-disks, a reduction using a subset of nominal modes was introduced in [33], [34], which then lead to the subsequent fundamental mistuning model [35]. This model reduced the problem of mistuning analysis to a single modal family of interest, where the structural mass matrices were projected onto a very reduced lower-dimensional subspace. For other configurations with mistuning, such as shrouded bladed-disks, dove-tail connections, or underplatform dampers,

several investigations were also carried out to produce different ROMs [36]–[43].

Nonlinear effects have been also introduced successfully in ROMs, yielding an accurate prediction of the response of the complete system [44]–[48]. Time domain approaches for the integration are usually accompanied by HBM methods, which are detailed below.

The inclusion of transient effects is also of interest in operation conditions, where the rotor has to accelerate until it reaches the design speed. The works [49], [50] analyzed the transient effect in a frequency sweep over the resonance, highlighting the importance of different parameters, such as the acceleration rate, in the response of the system.

In addition to reduction methods of detailed structures, lumped mass-spring models are of great interest to understand complex physical phenomena. These models constitute a simplified description of a realistic structure designed to retain the same dynamics in a specific regime of interest. For example, the interaction of flutter with nonlinear friction was initially studied using a mass-spring model of a bladed-disk in [51]–[53]. In these works, each blade was modeled by a single mass, resembling the case where only one modal family is present in the solution of the system. Through direct time integration, the flutter saturated states by friction were obtained. The calculations would have been extremely expensive if the full structure was considered. These mass-spring models were also used to study more complicated states that could appear in the nonlinear dynamics of the bladed-disk in [54], [55], where the interaction of multiple TWs due to flutter was considered.

1.2.2 Harmonic Balance

Harmonic balance techniques are used to compute periodic solutions, with a given frequency ω, of a nonlinear problem by expressing the solution as a truncated Fourier series

$$\mathbf{x} = \sum_{k=-H}^{H} \mathbf{x}^k e^{ik\omega t}, \tag{1.24}$$

where H is the number of harmonics used in the approximation. This expansion is substituted into the equations of motion, and the projection of the residual along the truncated set of Fourier basis functions, $\{e^{ik\omega t}\}_{k=0}^{H}$, is required to vanish, producing the following set of algebraic equations

$$(-k^2\omega^2\mathbf{M}_s + \mathbf{K}_s)\mathbf{x}^k + \mathbf{G}^k(\mathbf{x}) - \mathbf{F}^k = 0, \quad k = 0, \ldots, H. \tag{1.25}$$

This is a standard Galerkin method using the Fourier basis, which is why harmonic balance

is sometimes also referred to as Fourier-Galerkin method.

The problem (1.25) is nonlinear, since the H harmonics involved are coupled through the nonlinear friction forces, and the solution is expected to converge as the number of harmonics is increased. This approach has the advantage that the problem is no longer a differential equation, eliminating the requirement of time integration over many elastic cycles. The drawback is that only periodic solutions are captured with this method, potentially missing more complicated dynamics.

The nonlinear system is usually solved using Newton's method and a continuation scheme, with the excitation frequency as a parameter, to compute the resonance curve of the system over a frequency sweep in a much more efficient way than with time domain methods. This process is carried out in real variables due to the non-analyticity of the projected residual in complex variables [56].

In turbomachinery, these methods have been extensively used, with variants designed to exploit the cyclic symmetry of a structure [57]. Harmonic Balance has been used to compute the response under different type of nonlinearities, and a complete description of the method and its numerical implementation can be found in the book [58].

Since nonlinear forces are not easily expressed in the frequency domain, their evaluation is typically carried out with an alternated Fourier-time scheme [59], in which the nonlinearities are evaluated in physical time and then passed to the Fourier domain. Using this approach, there have been many works over the past years that studied the nonlinear response of turbomachinery systems [60]–[70]. In some cases, the computation of the jacobian can be reduced by exploiting its Toeplitz structure [71], [72].

Modifications of HBM approach, extending the concept of nonlinear normal modes introduced by Rosenberg [73], have been considered in [74], [75]. The nonlinear normal modes are defined in the context of conservative systems, and their extension to dissipative ones is carried out by including a prescribed pumping term, which allows the use of the HBM methodology to compute them. This framework has been used recently in the study of the nonlinear friction saturated flutter cycles and forced response problems [76]–[78], using different coupling level approaches between the structure and the fluid flow.

To overcome the limitations of HBM to periodic solutions, several efforts have been made during the past years to improve the method to be able to compute quasi-periodic states [79]–[84]. In these works, for polynomial nonlinearities, the HBM methodology was extended to include an arbitrary selection of frequencies (not just multiples of the forcing one). In particular, the case of two different forcing frequencies was tackled, which usually requires an

a priori knowledge of their values in the system. Alternatively, the frequency of oscillation could be taken as an unknown, and by means of the linear stability analysis an initial approximation of the emergent frequency could be obtained and then tracked using continuation techniques. The extension of HBM for quasi-periodic solutions with dry friction forces was carried out very recently in [85], for the case of two forcing terms with different frequencies of excitation.

1.2.3 Asymptotic Techniques

Asymptotic methods are used to obtain a very reduced description of the complete governing equations, which is valid in some regime of interest and can be quantitatively accurate. These are approximate methods, but in contrast to HBM, no particular assumption of the form of the solution is made, so the space of states is not restricted to periodic solutions.

Perturbation techniques were first developed by Poincaré [86], [87] in the study of the three body problem, and they have been crucial in the developments of multiple scientific fields over the last century, like fluid mechanics or quantum mechanics.

In the context of turbomachinery, they were first formally introduced in [88], to study the amplification due to mistuning in the forced response of a bladed-disk. Even though this dissertation will not include mistuning effects, a brief overview of the contributions of asymptotic techniques in this context is given.

This method, called Asymptotic Mistuning Model (AMM), provided a more detailed physical understanding of the phenomena, and an even larger reduction with respect to the previous fundamental mistuning model (FMM) [35], [89], [90]. Depending on the frequency difference between the modes relative to the mistuning size, the AMM produces a formulation in which only a set of active modes is considered [91]. These methods also provided a tighter upper bound on the maximum amplification that could be induced by random mistuning, improving the previous one given by Whitehead [92].

Asymptotic models were also used to design intentional mistuning patters to reduce the forced response of bladed-disks [93]–[96], and they were also used to study the transient response of a mistuned rotor [97].

For the case of nonlinear friction forces, which is the main focus of this dissertation, asymptotic techniques were applied first to mass-spring models in [98], [99]. The key idea of this technique is to separate the dynamics of the system into two timescales: a fast one, related to the elastic oscillations of the structure with the natural frequency, and a slow one, related to the small effect of nonlinear friction and the aerodynamic instability. This methodology

produces a description of the system directly on the slow timescale where flutter and friction interact. Direct time integrations of this system showed that the accuracy of the asymptotic model is quite good in the physical regime of interest. Additionally, an asymptotic model for the problem of forced response with nonlinear friction and mistuning was proposed in [100], [101].

Over the next chapters, this dissertation will study in more detail the derivation of the asymptotic equations, since they allow for easier analytical manipulations, and to track the bifurcation diagrams of solutions using numerical continuation techniques. But, more important than the simplicity of the resulting system, is the fact that these asymptotic models provide a clear indication of the key factors that are relevant for the dynamics of the system.

1.3 Objectives

The objectives of this thesis are:

- Understand, using an asymptotic model, the different flutter saturated states that can appear in a tuned bladed-disk under the effect of nonlinear friction.
- Study the interaction of flutter and forced response and their coupling due to the nonlinear friction at the blade root.
- Extend the asymptotic methodology to high-fidelity finite element models with nonlinear friction elements.
- Develop an asymptotic model in a more complicated configuration, such as the interaction of modes from different families through the nonlinear effect of the friction forces.

1.4 Scientific Production

During the development of this thesis, the following journal articles related to the research topic have been produced:

- J. González-Monge, S. Rodríguez-Blanco, and C. Martel, "Friction-induced traveling wave coupling in tuned bladed-disks", *Nonlinear Dynamics*, vol. 106, no. 4, pp. 2963–2973, 2021. DOI: https://doi.org/10.1007/s11071-021-06930-1.
- J. González-Monge, S. Rodríguez-Blanco, and C. Martel, "Nonlinear switching between flutter and forced response in bladed disks", *Nonlinear Dynamics*, vol. 111,no. 6, pp.

5237–5247, 2023. DOI: https://doi.org/10.1007/s11071-022-08140-9.

- S. Rodríguez-Blanco, J. González-Monge, and C. Martel, "Numerical investigation of friction induced interaction of flutter modes in a realistic low pressure turbine rotor", *Journal of Engineering for Gas Turbines and Power*, vol. 145, no. 11, 2023. DOI: https://doi.org/10.1115/1.4063374.
- S. Rodríguez-Blanco, J. González-Monge, and C. Martel, "Interaction of flutter and forced response in a low pressure turbine rotor with friction damping and mistuning effects", *Journal of Sound and Vibration*, vol. 572, p. 118 181, 2024. DOI: https://doi.org/10.1016/j.jsv.2023.118181
- J. González-Monge, A. Bouras, and L. Carassale, "Modal properties of mechanical systems under geometric variations by perturbation theory", *Journal of Sound and Vibration*, p. 118 942, 2025. DOI: https://doi.org/10.1016/j.jsv.2025.118942
- A. Bouras, J. González-Monge, and L. Carassale, "Reduced-order modeling of rotor disks with geometric mistuning by uncertainty propagation.", *Accepted for Publication in ASME Journal*, 2025.
- C. Martel, S. Rodríguez-Blanco, and J. González-Monge, "Forced response of an unstable LPT: New states with different vibration amplitude.", *Accepted for Publication in ASME Journal*, 2025.
- S. Rodríguez-Blanco, J. González-Monge, and C. Martel, "Asymptotic Description of Mechanical Systems with Non-Smooth Nonlinear Friction Effects" *Manuscript in preparation*
- J. González-Monge, S. Rodríguez-Blanco, and C. Martel, "Modal Interaction in the Presence of Nonlinear Friction: An Asymptotic Approach" *Manuscript in preparation*

In international conferences, the following contributions have been presented:

- J. González-Monge, S. Rodriguez, and C. Martel, "Numerical continuation of the interaction of flutter and forced response", in AIAA Propulsion and Energy 2021 Forum, 2021, p. 3457. DOI: https://doi.org/10.2514/6.2021-3457.
- J. González-Monge, S. Rodriguez, and C. Martel, "Multi Traveling Wave Flutter Onset in Tuned Bladed-Disks", in *Global Power & Propulsion Society*, 2021. DOI: https://doi.org/10.33737/gpps21-tc-28.
- S. Rodríguez-Blanco, J. González-Monge, and C. Martel, "Asymptotic evaluation of nonlinear friction effects in realistic LPT rotors", in *Turbo Expo: Power for Land, Sea,*

and Air, American Society of Mechanical Engineers, vol. 87066, 2023, V11BT27A017. DOI: https://doi.org/10.1115/GT2023-102829.

- S. Rodríguez-Blanco, J. González-Monge, and C. Martel, "Accurate asymptotic description of nonlinear friction states for a detailed FEM model" (Abstract). *NODYCON* 2023. URL: https://nodycon.org/2023/papers/245/abstract_submissions/357/view_abstract
- S. Rodríguez-Blanco, J. González-Monge, and C. Martel, "Numerical investigation of friction induced interaction of flutter modes in a realistic low pressure turbine rotor", *Turbo Expo: Power for Land, Sea, and Air, vol. Volume 11A: Structures and Dynamics — Aerodynamics Excitation and Damping; Bearing and Seal Dynamics*, Jun. 2023. DOI: https://doi.org/10.1115/GT2023-103099.
- A. Bouras, J. González-Monge, and L. Carassale, "Reduced-order modeling of rotor disks with geometric mistuning by uncertainty propagation.", *ASME Turbo Expo 2025*, 2025.
- C. Martel, S. Rodríguez-Blanco, and J. González-Monge, "Forced response of an unstable LPT: New states with different vibration amplitude.", *ASME Turbo Expo 2025*, 2025.
- C. Martel, J. González-Monge, and S. Rodríguez-Blanco, "Computation of bladed disk response with nonlinear friction effects.", *Accepted Abstract for GPPS 2025*, 2025.
- C. Fan, J. González-Monge, S. Rodríguez-Blanco, and C. Martel, "Structural Analysis of Interlocked Low-Pressure Turbine Blades: Influence of Contact Conditions and Pretwist Angles.", *Accepted Abstract for GPPS 2025*, 2025.

1.5 Outline of the Thesis

This dissertation is divided in the following chapters:

- The study of the flutter saturated states in a tuned bladed-disk is presented in Chapter 2. The derivation of a multiple scales asymptotic model from a simplified bladed-disk is presented, and the stability analysis of the single-TW saturated solutions by nonlinear friction is carried out. The bifurcation diagrams are computed using numerical continuation methods, in which stable multi-TW states are found and described.
- The interaction of flutter and forced response through nonlinear friction is analyzed in Chapter 3. The asymptotic equations are extended to include an external forcing with

the form of a traveling wave, and the different solutions of the system are computed using continuation methods. Bifurcation diagrams are generated to characterize and describe with detail the different final states of the system. The results obtained in this and the previous chapter are analyzed using a high-fidelity FEM, where the solutions predicted by the asymptotic model are also found in the more realistic setup.

- The asymptotic methodology is extended to high-fidelity finite element models in Chapter 4. This analysis enables a more convenient description to work directly with realistic structures. A detailed derivation of the equations is given, and the results are validated with a simplified structure and a realistic model of a bladed-disk.
- In Chapter 5, a novel asymptotic model is presented to study the interaction of modes from different families under nonlinear friction effects. A systematic derivation of the asymptotic equations is given, and the results are validated using a lumped model.
- A brief and global description of the main results obtained in this dissertation are discussed in Chapter 6.
- Finally, in Chapter 7, the main conclusions of this dissertation are summarized, and several future lines of research are outlined.

Chapter 2

Friction Saturated Flutter Solutions

Modern designs of LPT blades tend to a more slender geometry, which is prone to exhibit flutter. This aeroelastic instability is produced when the gas flowing around the blades pumps energy into the system, producing an amplification of the blade vibration. This growth is exponential, unless there are other effects which can balance the energy input. Dry friction is present at the contact surfaces between the blade and the disk, which can be in the form of a fir-tree, for instance. This effect is nonlinear, and although small, it is crucial to counteract flutter, producing limit cycle oscillations.

The effect of nonlinear friction on the dynamics of an unstable bladed-disk was analyzed in [53], using direct time integration of a mass-spring system. It was shown that the final state for a nearly flat modal family consisted of the most unstable TW, after a slow nonlinear selection process between all the different TWs present in the system. An asymptotic analysis, in the form of a multiple scales method, was introduced in [98], [99], producing a set of differential equations whose solution is directly the envelope of the amplitude of vibration, which is the quantity of interest for calculating the maximum response of the structure and predicting blade fatigue damage.

The goal of this chapter is to provide a more detailed description of the nonlinear dynamics of the bladed-disk, starting from the asymptotic model developed in [98]. First, this chapter will include the derivation of the asymptotic model from a lumped system resembling the first modal family (blade dominated) of a low pressure turbine bladed-disk. Then, a stability analysis using the asymptotic equations will be carried out, computing analytically the stability of the trivial solutions and the single-TW saturated solutions. Numerical continuation is used to track new possible states of the system from the bifurcation points, such as multi-TW solutions.

2.1 Mass-spring Model

The bladed-disk is modeled as a mass-spring system (Fig. 2.1), where the blades are represented by a single degree of freedom, x_j, which can be thought of as the modal displacement of the first family of a tuned system (usually flap). There is an additional DOF, y_j, to capture the nonlinear friction effects present at the fir-tree.

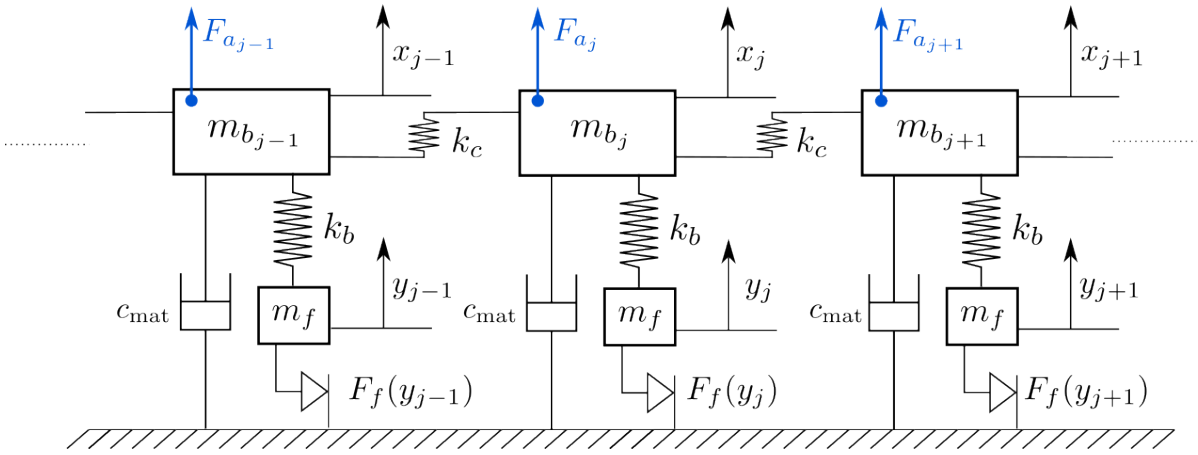

Figure 2.1: Mass-spring model representing a single family of a bladed-disk with nonlinear friction.

The equations of motion of this system are

$$\begin{aligned} m_b\ddot{x}_j + c_{\text{mat}}\dot{x}_j + k_b(x_j - y_j) - k_c(x_{j+1} - 2x_j + x_{j-1}) + F_{a_j}(\mathbf{x}, \dot{\mathbf{x}}) = 0, \\ m_f\ddot{y}_j + +k_b(y_j - x_j) + F_f(y_j) = 0, \end{aligned} \tag{2.1}$$

with $j = 1, \ldots, N$, where N is the number of sectors of the structure. The blade mass is m_b (assumed to be equal for all sectors, since the analysis is carried out for a tuned system), and m_f is the mass of the nonlinear DOF. The elastic coupling between both DOFs is k_b, modeling the stiffness of the blade. Material damping (assumed to be smaller than nonlinear dissipation) is represented by c_{mat}, and k_c is the coupling between the blades, which in a real assembly is due to the disk, if we do not consider a shrouded configuration.

The term $F_{a_j}(\mathbf{x}, \dot{\mathbf{x}})$ corresponds to the aerodynamic forces induced by the motion of the blades. The aerodynamic forces in LPTs are, to a very good approximation, linear [51], and the motion of one sector influences the neighboring ones, although this effect is usually more significant on the directly adjacent ones [15]. In this chapter, we do not consider any external loads, since the problem of additionally including forced response is carried out in Chapter 3. Finally, $F_f(y_j)$ is the nonlinear friction force, which only depends on the displacements of each sector.

The equations may be written in matrix form as

$$\begin{aligned} \mathbf{M}_b\ddot{\mathbf{x}} + \mathbf{C}\dot{\mathbf{x}} + \mathbf{K}_b(\mathbf{x}-\mathbf{y}) + \mathbf{K}_c\mathbf{x} + \mathbf{F}_a(\mathbf{x},\dot{\mathbf{x}}) = 0, \\ \mathbf{M}_f\ddot{\mathbf{y}} + \mathbf{K}_b(\mathbf{y}-\mathbf{x}) + \mathbf{F}_f(\mathbf{y}) = 0. \end{aligned} \tag{2.2}$$

In order to analyze the problem and identify the governing parameters, it is necessary to write it in dimensionless form. Therefore, we introduce a characteristic length for the blade and fir-tree motion, x_c and y_c, respectively, and a characteristic time $t_c = 1/\omega_b$, where $\omega_b = \sqrt{k_b/m_b}$ is the natural frequency of the blade alone case with no friction. Additionally, a characteristic elastic force $F_c = m_b\omega_b^2 x_c$ is considered. The dimensionless variables are then defined as

$$\begin{aligned} \theta = y_c/x_c,\ \gamma = m_f/m_b,\ T = t/t_c,\ \tilde{x}_j = x_j/x_c,\ \tilde{y}_j = y_j/y_c, \\ \xi_{\text{mat}} = c_{\text{mat}}/2\sqrt{k_b m_b}, \tilde{k}_c = k_c/k_b,\ \tilde{F}_{a_j} = F_{a_j}/F_c,\ \tilde{F}_f = F_f/F_c, \end{aligned}$$

where θ is a very relevant parameter in the system since it represents the size of the fir-tree motion with respect to the modal displacement. This ratio is typically very small in a realistic bladed-disk, as sketched in Fig. 2.2. The other dimensionless parameter that appears in the system is γ, which represents the ratio between the inertia of the blade and the friction DOF, also typically very small $\gamma \ll 1$.

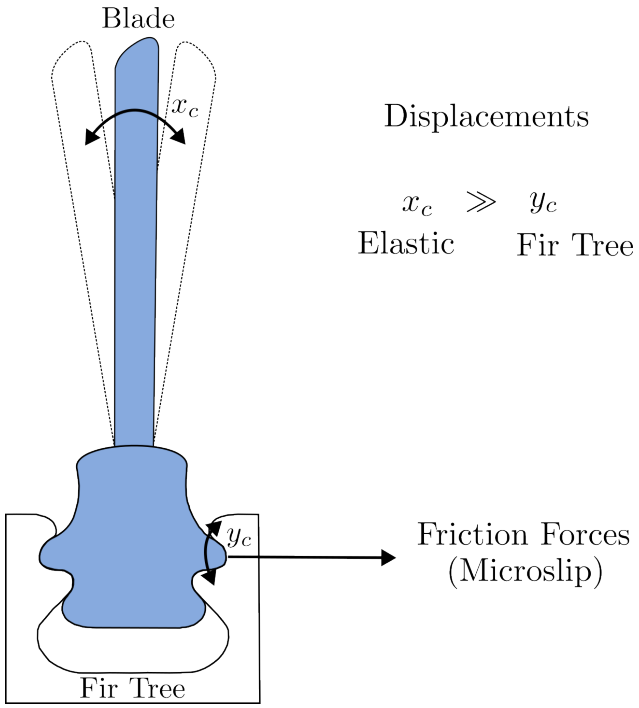

Figure 2.2: Length scale of the blade vibration compared to the fir-tree displacement.

It has been established that a good model for the friction forces in the fir-tree of LPTs is the

microslip regime [51], which will be introduced in the next section.

Using dimensionless variables, Eq. (2.2) becomes

$$\begin{aligned} \ddot{\tilde{\mathbf{x}}} + 2\xi_{\text{mat}}\dot{\tilde{\mathbf{x}}} + (\tilde{\mathbf{x}} - \theta\tilde{\mathbf{y}}) + \tilde{\mathbf{K}}_c\tilde{\mathbf{x}} + \tilde{\mathbf{F}}_a(\tilde{\mathbf{x}}, \dot{\tilde{\mathbf{x}}}) = 0, \\ \gamma\theta\ddot{\tilde{\mathbf{y}}} + (\theta\tilde{\mathbf{y}} - \tilde{\mathbf{x}}) + \tilde{\mathbf{F}}_f(\tilde{\mathbf{y}}) = 0. \end{aligned} \tag{2.3}$$

2.2 Asymptotic Model

An asymptotic description for Eq. (2.3) is obtained in this section considering the following assumptions

- The mass ratio is small, $\gamma \ll 1$.
- The friction displacement is much smaller than the modal displacement, $\theta \ll 1$.
- Nonlinear friction is computed using the Olofsson microslip model [19].
- The aerodynamic forces are much smaller than the elastic forces, $F_a \ll F_c$, and are considered to be linear.
- A nearly flat modal family is considered, so all TW modes are taken into account.

Before proceeding with the derivation of the asymptotic equations, we will introduce in more detail the shape of the modal family of interest, the friction model, and the aerodynamic forces. For concreteness, we will consider a bladed-disk of $N = 24$ blades.

2.2.1 Frequency Distribution of the First Family

The modal family of interest is nearly flat, as presented in Fig. 2.3. The frequency with respect to the ND is presented normalized to the blade alone frequency ω_b. The resonant frequency for each mode can be expressed as

$$\omega_j = \omega_b \left(1 + \Delta\omega_j\right), \tag{2.4}$$

with $j = 1, \ldots, N$, where $\Delta\omega_j$ is the normalized frequency shift with respect to the blade alone, which is given by the following expression

$$\Delta\omega_j = \tanh(c_1 j + c_2) - 1, \tag{2.5}$$

where $c_1 = 0.45$ and $c_2 = 1.85$, and j is the corresponding ND.

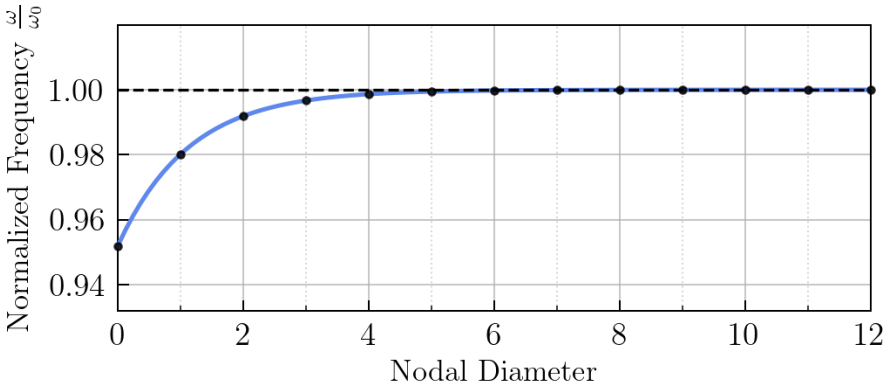

Figure 2.3: Frequency distribution of the modal family.

This frequency distribution is typically encountered for systems where the disk is very stiff, and thus the coupling between the different blades is small. This particular distribution was chosen to resemble the one shown in [96], for the LPT rotor developed in the context of the European project FUTURE [102].

2.2.2 Microslip Friction Model

The microslip friction law selected for the model is described by Olofsson in [19]. This law exhibits a hysteresis cycle, where there is a preload phase (only occurring at the beginning), followed by unloading and loading phases, which alternate in time.

In dimensionless form, the expression of the force during the preload is

$$\tilde{F}_f(\tilde{y}) = 1 - (1 - \tilde{y})^{5/2}, \tag{2.6}$$

where the value of the displacement has to start from zero, $\tilde{y}(0) = 0$, and ends at $\tilde{y}^L$, corresponding to $\tilde{F}_f(\tilde{y}^L) \equiv \tilde{F}^L$. After the preload phase, there is an unloading process, given by

$$\tilde{F}_f(\tilde{y}) = \tilde{F}^L - 2\left(1 - \left(1 - \frac{\tilde{y}^L - \tilde{y}}{2}\right)^{5/2}\right). \tag{2.7}$$

The unloading process continues until reaching a displacement denoted by $\tilde{y} = -\tilde{y}^U$, which has the forcing $\tilde{F} = -\tilde{F}^U$ associated. Then, a loading phase starts, described by

$$\tilde{F}_f(\tilde{y}) = -\tilde{F}^U + 2\left(1 - \left(1 - \frac{\tilde{y}^U + \tilde{y}}{2}\right)^{5/2}\right). \tag{2.8}$$

After this, the unloading phase starts again, and the process repeats. Note that, due to the symmetry of the cycle, $\tilde{y}^L = \tilde{y}^U$ and $\tilde{F}^L = \tilde{F}^U$. Fig. 2.4 shows the hysteresis cycle described by the previous expressions, where the unloading and loading phases are plotted, and the preload has been omitted. An important remark is that, in dimensionless variables, the microslip regime is restricted to $|\tilde{y}| \leq 1$. If the displacement is larger, a macroslip model has to be used, although in the analysis of the mass-spring model in this chapter we restrict ourselves to the microslip regime.

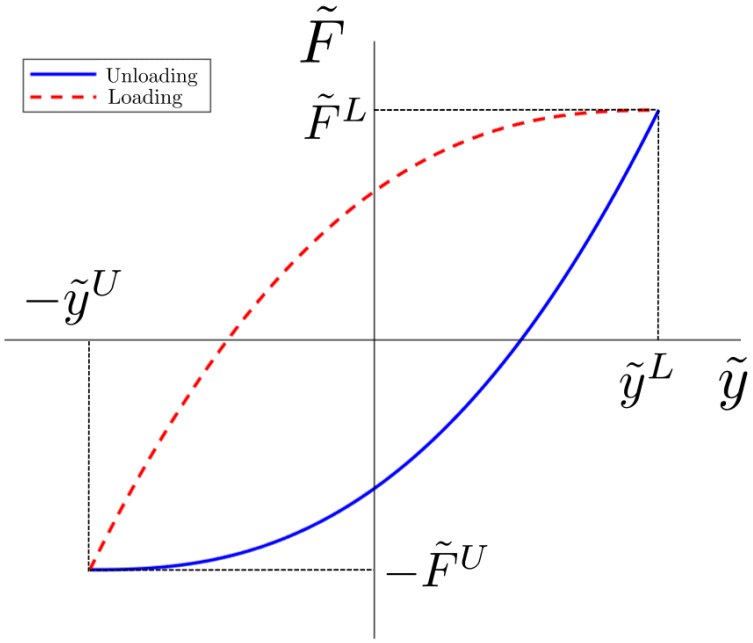

Figure 2.4: Microslip friction force against contact displacement.

2.2.3 Aerodynamic Forces

The aerodynamic forces have the form of a traveling wave and are typically computed using the influence coefficients. The information of these forces, with the linear assumption due to the small displacements of the blades, is contained in two aerodynamic coefficients: the aerodynamic damping ξ_a and frequency correction η_a. As a function of the ND, these coefficients typically have a sinusoidal shape [96] for a LPT, and in this work we choose a distribution similar to the one from the LPT rotor used in the context of the European project FUTURE [102], plotted in Fig. 2.5.

The distributions mimic the typical data in a realistic configuration, and follow the expres-

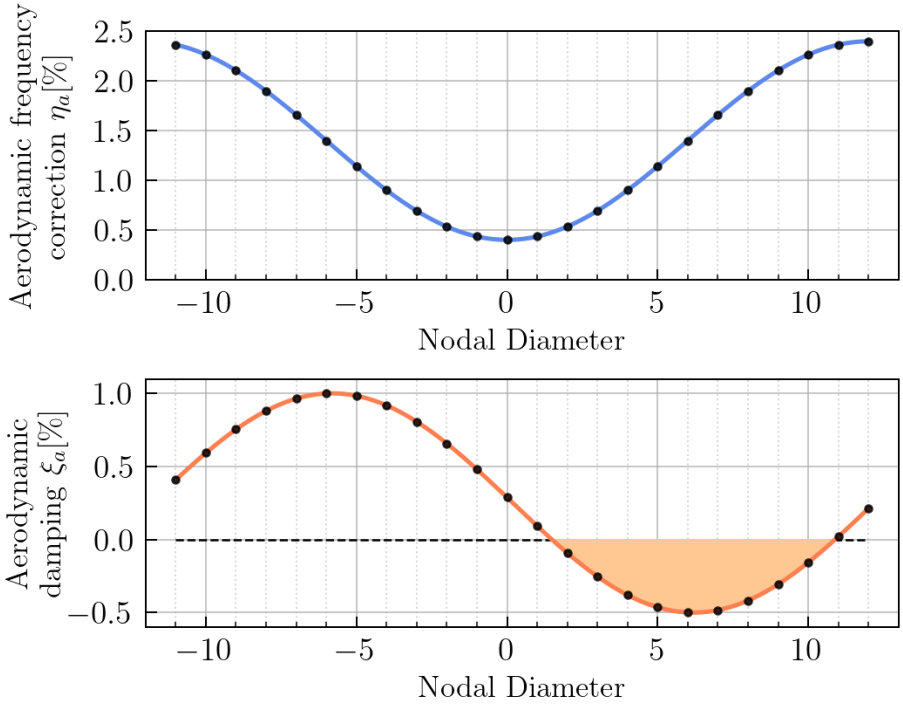

Figure 2.5: Aerodynamic damping and frequency correction coefficients

sions

$$\xi_a^j = \xi_{a_0} - \xi_{a_1} \sin\left(\frac{2\pi j}{N} + \xi_{a_2}\right) \quad (\%), \tag{2.9}$$

and

$$\eta_a^j = \eta_{a_0} - \eta_{a_1} \cos\left(\frac{2\pi j}{N}\right) \quad (\%), \tag{2.10}$$

where j is the index of the TW wavenumber, and the values of the constants are $\xi_{a_0} = 0.25$, $\xi_{a_1} = 0.75$, $\xi_{a_2} = -0.05$, $\eta_{a_0} = 1.4$, and $\eta_{a_1} = 1.0$.

The analyzed system has some unstable TW modes, which correspond to the shaded area of the aerodynamic damping ($\xi_a^j < 0$) in Fig. 2.5. These modes exhibit flutter and their growth saturation due to nonlinear friction will be investigated.

2.2.4 Multiple Scales Method

The typical response of the system from Eq. (2.3), using the aerodynamic coefficients and friction model described above, is sketched in Fig. 2.6. This plot shows the evolution in time of the displacement of one of the blades. At the beginning, when the amplitude of vibration is small, an exponential growth is observed due to the presence of flutter. Then, as the vibration level increases, the nonlinear friction effects start to become more relevant, saturating the instability and producing bounded oscillations in the form of a limit cycle.

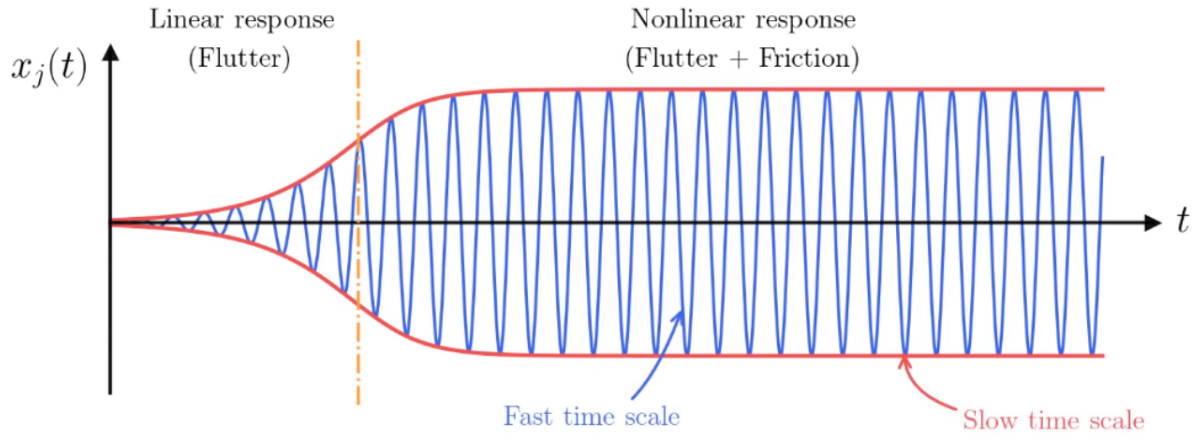

Figure 2.6: Typical evolution of the displacement of one blade under the effects of flutter and nonlinear friction. The fast timescale is highlighted in blue and the slow timescale in red.

The determination of the maximum amplitude oscillation is of very important in order to estimate quantities such as the high cycle fatigue life of the blades [6]–[8]. This amplitude is given by the slow evolution of the envelope of vibration, which changes in the slower timescale in which flutter and nonlinear friction interact. The fast timescale associated with the elastic vibrations does not provide relevant information and can be filtered out.

The idea of the asymptotic model is to exploit this separation of timescales, producing a reduced description that is consistent and quantitatively accurate. Additionally, the model will retain only the main aspects that play a role in the system dynamics, providing the relevant parameters and a more direct understanding of the phenomenon.

There are many excellent books about perturbation methods [103]–[105], which contain a description of the multiple scales method. Nevertheless, to provide a self-contained description in this dissertation, a simple example of the application of this technique to the Duffing oscillator is included in Appendix A.

The derivation of the asymptotic method will follow closely the one presented in previous works [98], [99]. The key idea is to introduce a slow timescale in which nonlinear friction and flutter interact. From the dimensionless problem, we saw that the parameter θ is the one that controls the magnitude of the nonlinearity. As explained before, in a realistic situation, the nonlinearity is weak, and hence we are in the limit $\theta \ll 1$.

Therefore, apart from the fast timescale associated with the elastic oscillations, T, we introduce the slow timescale defined as $\tau = \theta T$. Then, we express the DOFs of the system as functions of the two time variables, in a perturbation expansion of the form

$$\begin{aligned} \tilde{\mathbf{x}} &= \tilde{\mathbf{x}}^{(0)}(T,\tau) + \theta\tilde{\mathbf{x}}^{(1)}(T,\tau) + \mathcal{O}\big(\theta^2\big), \\ \tilde{\mathbf{y}} &= \tilde{\mathbf{y}}^{(0)}(T,\tau) + \theta\tilde{\mathbf{y}}^{(1)}(T,\tau) + \mathcal{O}\big(\theta^2\big). \end{aligned} \tag{2.11}$$

Additionally, we need to express the time derivatives from the equations of motion (2.3) in terms of the two timescales. Applying the chain rule, we get

$$\begin{aligned} \frac{\mathrm{d}}{\mathrm{d}T} &= \frac{\partial}{\partial T} + \theta\frac{\partial}{\partial \tau}, \\ \frac{\mathrm{d}^2}{\mathrm{d}T^2} &= \frac{\partial^2}{\partial T^2} + 2\theta\frac{\partial^2}{\partial T\partial \tau} + \theta^2\frac{\partial^2}{\partial \tau^2}. \end{aligned} \tag{2.12}$$

Plugging these derivatives (2.11) and (2.12) into Eq. (2.3), and separating the terms at different orders in θ, we obtain the following equations

$$\begin{aligned} (\tilde{\mathbf{x}}^{(0)}_{TT} + \tilde{\mathbf{x}}^{(0)}) + \theta(\tilde{\mathbf{x}}^{(1)}_{TT} + \tilde{\mathbf{x}}^{(1)} + 2\tilde{\mathbf{x}}^{(0)}_{T\tau} - \tilde{\mathbf{y}}^{(0)} + 2\frac{\xi_{\mathrm{mat}}}{\theta}\tilde{\mathbf{x}}^{(0)}_{T} + \frac{1}{\theta}\tilde{\mathbf{K}}_c\tilde{\mathbf{x}}^{(0)} + \frac{1}{\theta}\tilde{\mathbf{F}}_a) + \mathcal{O}\big(\theta^2\big) = 0, \\ (\tilde{\mathbf{F}}_f(\tilde{\mathbf{y}}^{(0)}) - \tilde{\mathbf{x}}^{(0)}) + \mathcal{O}(\theta) = 0, \end{aligned} \tag{2.13}$$

where the aerodynamic forces and linear damping are considered to be of $\mathcal{O}(\theta)$, and hence will be taken into account in the first order of the perturbation expansion. The subscripts with T, τ are used to indicate partial derivatives with respect to those variables. From the second equation, related to the friction DOF, we only explicitly write the leading order terms, since it will be enough for the derivation of the amplitude equation. Now, we solve Eqs. (2.13) by equating the terms to zero order by order, computing successive approximations to the solution of the exact nonlinear problem.

Zeroth order $\mathcal{O}(\theta^0)$: The system of equations is

$$\tilde{\mathbf{x}}^{(0)}_{TT} + \tilde{\mathbf{x}}^{(0)} = 0, \tag{2.14}$$

$$\tilde{\mathbf{x}}^{(0)} = \tilde{F}_f(\tilde{\mathbf{y}}^{(0)}). \tag{2.15}$$

The first of this set of equations, Eq. (2.14), is a harmonic oscillator, which can be solved directly as

$$\tilde{\mathbf{x}}^{(0)} = \mathbf{X}(\tau)e^{iT} + \text{ c.c.}, \tag{2.16}$$

where $\mathbf{X}(\tau)$ is the slowly varying amplitude of the vibration, and c.c. stands for the complex conjugate. The envelope of the vibration will be resolved at the next order. With the knowledge of $\tilde{\mathbf{x}}^{(0)}$, Eq. (2.15) gives a nonlinear algebraic equation to obtain $\tilde{\mathbf{y}}^{(0)}$, which could be rewritten as

$$2|X_j(\tau)|\cos(T) = \tilde{F}_f(\tilde{y}_j^{(0)}), \quad j = 1, \ldots, N, \tag{2.17}$$

since it is uncoupled for each sector. Technically, there should be an initial phase on the cosine on the left-hand side of the equations, but a redefinition of the initial time can be used to absorb it, so it is omitted in this step without loss of generality.

Since the friction function is nonlinear, the solution of the previous equation will produce displacements $\tilde{\mathbf{y}}^{(0)}$ containing a possibly infinite number of Fourier harmonics, that can be expressed as

$$\tilde{y}_j^{(0)} = \sum_{k=1}^{\infty} P_k(|X_j|)e^{ikT} + \text{ c.c.}. \tag{2.18}$$

There is no zeroth harmonic since the hysteresis cycle is symmetric, and therefore the average of the function $\tilde{y}_j^{(0)}$ over a period is zero. Additionally, we could now include the change in phase omitted before by a change in the time variable. Therefore, we can write

$$\tilde{y}_j^{(0)} = \sum_{k=1}^{\infty} P_k(|X_j|)e^{ikT}e^{ik\phi_j} + \text{ c.c.}, \tag{2.19}$$

where ϕ_j is the phase of the complex number $X_j = |X_j|e^{i\phi_j}$. The solution is expressed in this form since it will be convenient when solving the next order of the perturbation expansion. The Fourier coefficients P_k can be computed by performing a discrete Fourier transform of the friction DOF $\tilde{y}_j^{(0)}$ time evolution after solving Eq. (2.15) over a complete period in T. Actually, from the friction laws given before in the explanation of the Olofsson model in Eqs. (2.7) and (2.8), the displacements can be computed explicitly. Inverting these expressions, one obtains for the unloading cycle

$$\tilde{y}_j^{(0)} = \tilde{y}^L - 2\left(1 - \left(1 + \frac{\tilde{F}_f - \tilde{F}^L}{2}\right)^{2/5}\right), \tag{2.20}$$

where $\tilde{F}_f = 2|X_j|\cos(T)$ and $\tilde{F}^L = 2|X_j|$, so that $\tilde{y}^L = 1-(1-2|X_j|)^{2/5}$, and for the loading part

$$\tilde{y}_j^{(0)} = -\tilde{y}^U + 2\left(1-\left(1-\frac{\tilde{F}_f+\tilde{F}^U}{2}\right)^{2/5}\right), \tag{2.21}$$

Additionally, when performing the detailed analysis of the asymptotic equations, it would be necessary to compute the derivative of the nonlinear friction forces with respect to $|X_j|$, in order to determine the stability of the solution. For this reason, the derivation is included here, where the notation $\tilde{y}_j^{(0)\prime}$ is used to denote derivative with respect to $|X_j|$. The derivative of the unloading part is

$$\tilde{y}_j^{(0)\prime} = \tilde{y}^{L\prime} + \frac{4}{5}\left(1+\frac{\tilde{F}_f-\tilde{F}^L}{2}\right)^{-3/5}\left(\frac{\tilde{F}_f'-\tilde{F}^{L\prime}}{2}\right), \tag{2.22}$$

where $\tilde{F}^{L\prime} = 2$ and $\tilde{F}_f' = 2\cos(T)$. For the loading part

$$\tilde{y}_j^{(0)\prime} = -\tilde{y}^{U\prime} + \frac{4}{5}\left(1-\frac{\tilde{F}_f+\tilde{F}^U}{2}\right)^{-3/5}\left(\frac{\tilde{F}_f'+\tilde{F}^{U\prime}}{2}\right). \tag{2.23}$$

Then, computing the Fourier harmonics over an entire cycle gives

$$\tilde{y}_j^{(0)\prime} = \sum_{k=1}^{\infty} P_k'(|X_j|)e^{ikT}e^{ik\phi_j} + \text{ c.c.}, \tag{2.24}$$

which allows computing the derivative of the Fourier coefficients $P_k'(|X_j|)$ by performing an FFT.

First order $\mathcal{O}(\theta)$: In the next order, we only need to consider the equation related to the modal displacement of the blade, which is

$$\tilde{\mathbf{x}}_{TT}^{(1)} + \tilde{\mathbf{x}}^{(1)} = -2\tilde{\mathbf{x}}_{T\tau}^{(0)} + \tilde{\mathbf{y}}^{(0)} - 2\frac{\xi_{\text{mat}}}{\theta}\tilde{\mathbf{x}}_T^{(0)} - \frac{1}{\theta}\tilde{\mathbf{K}}_c\tilde{\mathbf{x}}^{(0)} - \frac{1}{\theta}\tilde{\mathbf{F}}_a. \tag{2.25}$$

On the left-hand side of Eq. (2.25), the same linear operator as in the previous order appears, although now acting on the first order correction. The terms on the right-hand side can be

directly computed using Eqs. (2.16) and (2.18), resulting in

$$\tilde{\mathbf{x}}^{(1)}_{TT} + \tilde{\mathbf{x}}^{(1)} = -2i\mathbf{X}_\tau e^{iT} + \sum_{k=1}^{\infty} P_k(|\mathbf{X}|)e^{ikT}e^{ik\boldsymbol{\Phi}} - 2i\frac{\xi_{\text{mat}}}{\theta}\mathbf{X}e^{iT} - \frac{1}{\theta}\tilde{\mathbf{K}}_c\mathbf{X}e^{iT} - \frac{1}{\theta}\tilde{\mathbf{F}}_a(\mathbf{X})e^{iT} + \text{ c.c.}, \tag{2.26}$$

where the term $P_k(|\mathbf{X}|)$ has to be understood as the vector with elements $P_k(|X_1|), \ldots, P_k(|X_N|)$ and the vector $e^{i\boldsymbol{\Phi}} = (e^{i\phi_1}, \ldots, e^{i\phi_N})$ is the exponential applied elementwise to each individual phase. Since any term proportional to e^{iT} is a solution of the homogeneous problem for $\tilde{\mathbf{x}}^{(1)}$, they need to be canceled out from the right-hand side to produce a bounded solution. This elimination of the resonant terms is usually called solvability condition in the context of perturbation theory, and provides a system of complex differential equations to determine the slowly varying amplitude $\mathbf{X}(\tau)$. Equating these terms to zero gives

$$2i\frac{\mathrm{d}\mathbf{X}}{\mathrm{d}\tau} = P_1(|\mathbf{X}|)e^{i\boldsymbol{\Phi}} - 2i\frac{\xi_{\text{mat}}}{\theta}\mathbf{X} - \frac{1}{\theta}\tilde{\mathbf{K}}_c\mathbf{X} - \frac{1}{\theta}\tilde{\mathbf{F}}_a(\mathbf{X}), \tag{2.27}$$

which is the sought-after asymptotic model. The nonlinearity due to friction is contained inside the first Fourier coefficient $P_1(|\mathbf{X}|)$ of the friction DOF in Eq. (2.18). This harmonic gives all the information of the friction cycle in Fig. 2.4, and could be expressed in the more convenient form

$$Q(|X_j|) = \frac{P_1(|X_j|)}{|X_j|}, \tag{2.28}$$

since then $P_1(|X_j|)e^{i\phi_j} = Q(|X_j|)|X_j|e^{i\phi_j} = Q(|X_j|)X_j$. The function $Q(|X_j|)$ will be denoted as the complex friction coefficient. The imaginary part of this function is always negative, representing the nonlinear dissipation. The real part is related to a nonlinear shift of the resonance frequency.

For the Olofsson friction law, the function Q is computed and shown in Fig. 2.7. The top part of the plot shows the nonlinear frequency shift, which is nonzero for $|X| = 0$, and then increases nonlinearly with the amplitude. In contrast, at the bottom of the plot, the nonlinear damping is plotted, starting at zero damping, since there is no dissipation from dry friction in the absence of motion. For increasingly larger amplitudes of vibration, the damping grows as one moves closer to the microslip limit, which is $|X| = 0.5$ in this model.

The derivative of this complex friction function will be needed later on for the stability analysis, and is given by

$$Q'(|X_j|) = \frac{P_1'(|X_j|)|X_j| - P_1(|X_j|)}{|X_j|^2}, \tag{2.29}$$

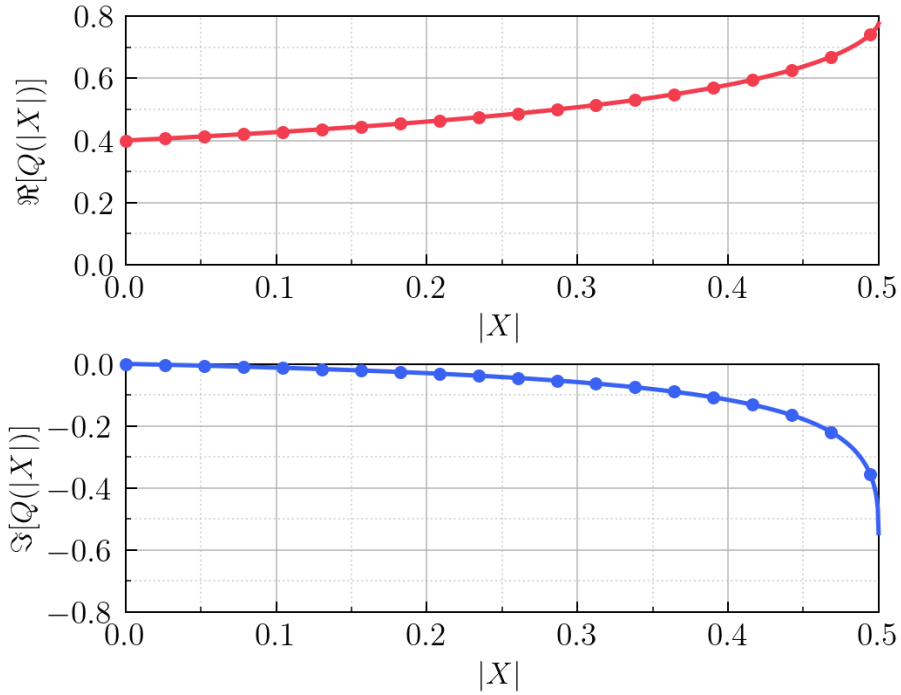

Figure 2.7: Real (top) and imaginary (bottom) parts of the friction coefficient $Q(|X|)$ as a function of the modulus of the amplitude of vibration.

where the expression for $P_1'(|X_j|)$ was given in Eq. (2.24).

Inserting the complex friction coefficient in the system of equations (2.27), yields

$$2i\frac{\mathrm{d}\mathbf{X}}{\mathrm{d}\tau} = Q(|\mathbf{X}|)\mathbf{X} - 2i\frac{\xi_{\mathrm{mat}}}{\theta}\mathbf{X} - \frac{1}{\theta}\tilde{\mathbf{K}}_c\mathbf{X} - \frac{1}{\theta}\tilde{\mathbf{F}}_a(\mathbf{X}). \tag{2.30}$$

The coupling stiffness and the aerodynamic forces, which are linear, are more conveniently expressed in the TW basis, since their values were already given in Figs. 2.3 and 2.5. We can perform a change of basis from displacements to TW using $\mathbf{X} = \mathbf{E}\mathbf{A}$, where $\mathbf{A}$ are the amplitudes of the TW modes and the transformation matrix is defined as

$$\mathbf{E} = \frac{1}{\sqrt{N}}\begin{pmatrix} e^{i\left(\frac{2\pi 1}{N}\right)1} & \dots & e^{i\left(\frac{2\pi N}{N}\right)1} \\ \vdots & \ddots & \vdots \\ e^{i\left(\frac{2\pi 1}{N}\right)N} & \dots & e^{i\left(\frac{2\pi N}{N}\right)N} \end{pmatrix}, \tag{2.31}$$

which is a unitary DFT (Discrete Fourier Transform) matrix. The arguments of the exponential are the multiples of the interblade phase angle $2\pi/N$. Substituting the transformation in the equation, and premultiplying by $\mathbf{E}^H$ (which is the complex conjugate transpose of $\mathbf{E}$),

gives

$$2i\frac{\mathrm{d}}{\mathrm{d}\tau}\begin{pmatrix} A_1 \\ \vdots \\ A_N \end{pmatrix} = \mathbf{E}^H \begin{pmatrix} Q(|X_1|) & \dots & 0 \\ \vdots & \ddots & \vdots \\ 0 & \dots & Q(|X_N|) \end{pmatrix} \mathbf{E} \begin{pmatrix} A_1 \\ \vdots \\ A_N \end{pmatrix} - 2\begin{pmatrix} \frac{\Delta\omega_1+i\xi_{\mathrm{mat}}}{\theta} & \dots & 0 \\ \vdots & \ddots & \vdots \\ 0 & \dots & \frac{\Delta\omega_N+i\xi_{\mathrm{mat}}}{\theta} \end{pmatrix} \begin{pmatrix} A_1 \\ \vdots \\ A_N \end{pmatrix} - 2\begin{pmatrix} \frac{\eta_a^1+i\xi_a^1}{\theta} & \dots & 0 \\ \vdots & \ddots & \vdots \\ 0 & \dots & \frac{\eta_a^N+i\xi_a^N}{\theta} \end{pmatrix} \begin{pmatrix} A_1 \\ \vdots \\ A_N \end{pmatrix}, \tag{2.32}$$

where the structural damping and frequency corrections are included in the $\Delta\omega_j + i\xi_{\mathrm{mat}}$ and their aerodynamic counterparts in the $\eta_a^j + i\xi_a^j$ matrices. Note that, in the TW basis, these terms are diagonal, and the only term that is not diagonal is the one related with friction, present through the $Q(|X_j|)$ function. This is because nonlinear friction acts locally within each sector, and the TW formulation couples them.

For convenience, we group some of the terms in the right-hand side and write the final form of the system

$$\frac{\mathrm{d}}{\mathrm{d}\tau}\begin{pmatrix} A_1 \\ \vdots \\ A_N \end{pmatrix} = -\frac{i}{2}\mathbf{E}^H \begin{pmatrix} Q(|X_1|) & \dots & 0 \\ \vdots & \ddots & \vdots \\ 0 & \dots & Q(|X_N|) \end{pmatrix} \mathbf{E} \begin{pmatrix} A_1 \\ \vdots \\ A_N \end{pmatrix} + \begin{pmatrix} -\tilde{\xi}_1 + i\tilde{\omega}_1 & \dots & 0 \\ \vdots & \ddots & \vdots \\ 0 & \dots & -\tilde{\xi}_N + i\tilde{\omega}_N \end{pmatrix} \begin{pmatrix} A_1 \\ \vdots \\ A_N \end{pmatrix}, \tag{2.33}$$

where $\tilde{\xi}_j = (\xi_a^j + \xi_{\mathrm{mat}})/\theta$ and $\tilde{\omega}_j = (\eta_a^j + \Delta\omega_j)/\theta$.

It is also useful to express this asymptotic model in the displacement basis, since the nonlinear friction effects are diagonal there, although the linear damping and frequency corrections will now be coupled between the different sectors. The system of equations in the displacement basis takes the form

$$\frac{\mathrm{d}}{\mathrm{d}\tau}\begin{pmatrix} X_1 \\ \vdots \\ X_N \end{pmatrix} = -\frac{i}{2}\begin{pmatrix} Q(|X_1|) & \dots & 0 \\ \vdots & \ddots & \vdots \\ 0 & \dots & Q(|X_N|) \end{pmatrix} \begin{pmatrix} X_1 \\ \vdots \\ X_N \end{pmatrix} + \mathbf{E}\begin{pmatrix} -\tilde{\xi}_1 + i\tilde{\omega}_1 & \dots & 0 \\ \vdots & \ddots & \vdots \\ 0 & \dots & -\tilde{\xi}_N + i\tilde{\omega}_N \end{pmatrix} \mathbf{E}^H \begin{pmatrix} X_1 \\ \vdots \\ X_N \end{pmatrix}. \tag{2.34}$$

As an initial step in the analysis of the asymptotic model in Eq. (2.33), direct time integration of these equations can be performed. Starting from an initial condition of $A_j = 0.01$ for every TW mode, the time evolution of the amplitudes is shown in Fig. 2.8. Initially, for early times, the response is linear, so there is an exponential growth (unstable TWs) or decay (stable TWs)

represented by the straight lines (due to the logarithmic scale) with slope equal to $\tilde{\xi}_j$. In the figure, a dashed blue line is used to highlight the slope of the most unstable mode, which is TW6, as presented in Fig. 2.5. Then, between the times $\tau \sim 100 - 500$, there is a nonlinear interaction between the different TW modes, followed by the saturation of the most unstable TW6 and an exponential decay of the other unstable TWs. A dashed red line highlights the decay of the unstable modes 7 and 5, which have the highest instability after TW6. Therefore, the final solution of the system is a stable limit cycle with a single-TW mode. This final state is also plotted, for a fixed time, along the bladed-disk in the circumferential direction, in Fig. 2.9.

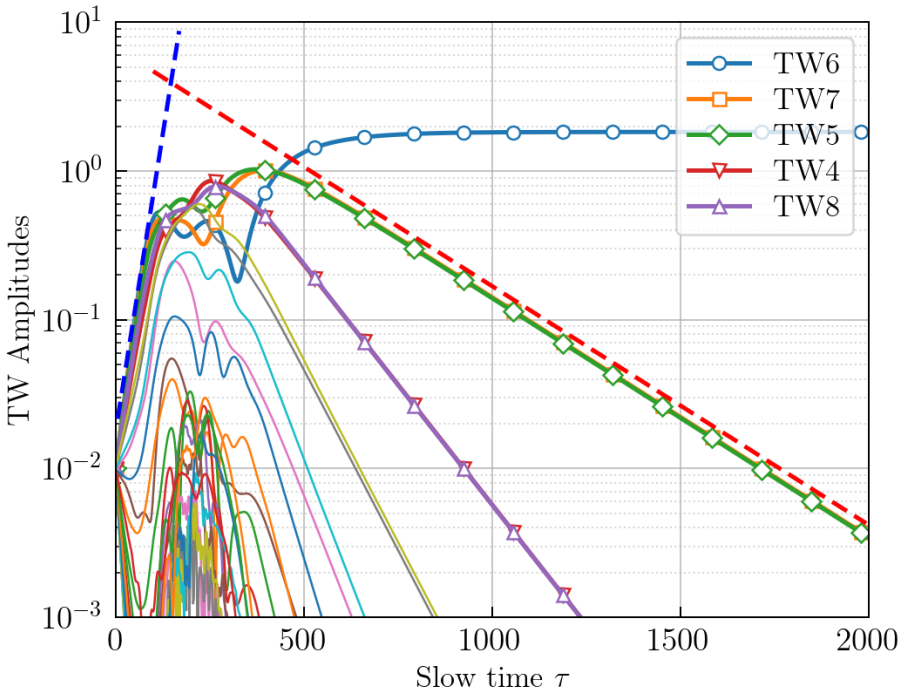

Figure 2.8: Time evolution of the TW amplitudes from the asymptotic model starting from an initial condition of $A_j = 0.01$ for every TW mode.

The solution obtained here is in total correspondence with previous works [52], [53], [99]. Time integration of the asymptotic model, although cheaper than the time integration of the initial equations of the mass-spring model since the fast timescale has been eliminated and the equations are less stiff, can still be computationally expensive. Additionally, with time integration there is no guaranteed convergence to the final stable state, since different dynamics could be developing on a much longer timescale which has not manifested yet.

For this reason, the next step is to make a formal stability analysis using the asymptotic equations, starting with the trivial solution and the single-TW saturated flutter solutions.

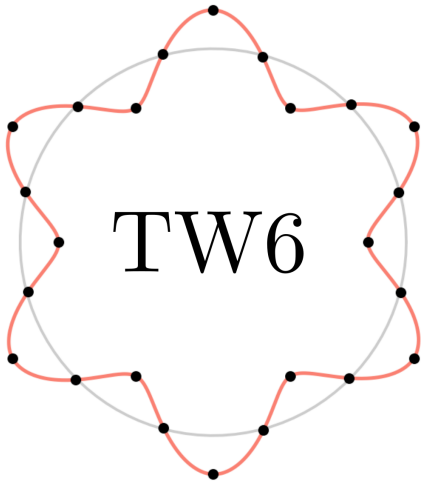

Figure 2.9: TW6 mode propagating around the bladed-disk.

This analysis will provide a more accurate description of the possible final states of the system, and will also enable the possibility of tracking solutions that have not been considered. For instance, in [55], a simplified model with negative mean aerodynamic damping is used where multi-TW solutions are found, via time integration of the system. Moreover, in [67], [68], these solutions are found in a more realistic model with nonlinear friction present at a small contact region in the shroud of a bladed-disk.

This analysis will be carried out by characterizing the different final states of the system for different aerodynamic intensity levels. The control parameter will be ξ_{a_1}, which was introduced in Eq. (2.9)

$$\xi_a^j = \xi_{a_0} - \xi_{a_1} \sin\left(\frac{2\pi j}{N} + \xi_{a_2}\right) \quad (\%),$$

and is repeated here for convenience. The aerodynamic damping curve is also repeated in Fig. 2.10. As one increases the value of ξ_{a_1}, more modes cross to the unstable region. For smaller values of this parameter, it is expected that the contribution of the aerodynamic forces stabilizes the system, and hence flutter solutions will not be present. For the simulation shown in Fig. 2.8, the value of ξ_{a_1} was set to 0.75.

Actually, before conducting the stability analysis, time integration of the asymptotic model for $\xi_{a_1} = 0.502$ produced a multi-TW solution, starting from a perturbation close to a TW4 mode. The evolution of the response is shown in Fig. 2.11, where now there is a participation

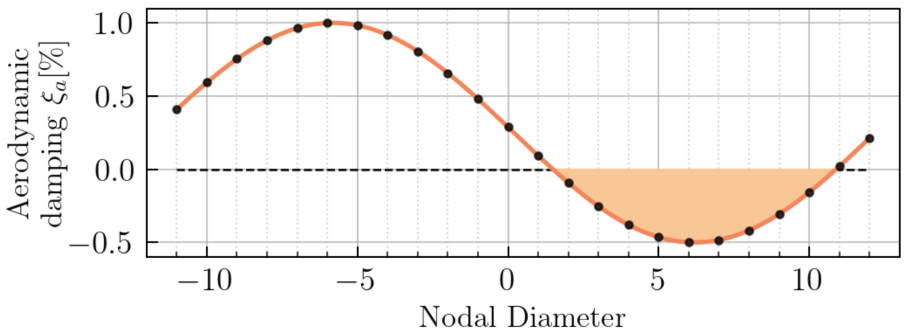

Figure 2.10: Aerodynamic damping curve.

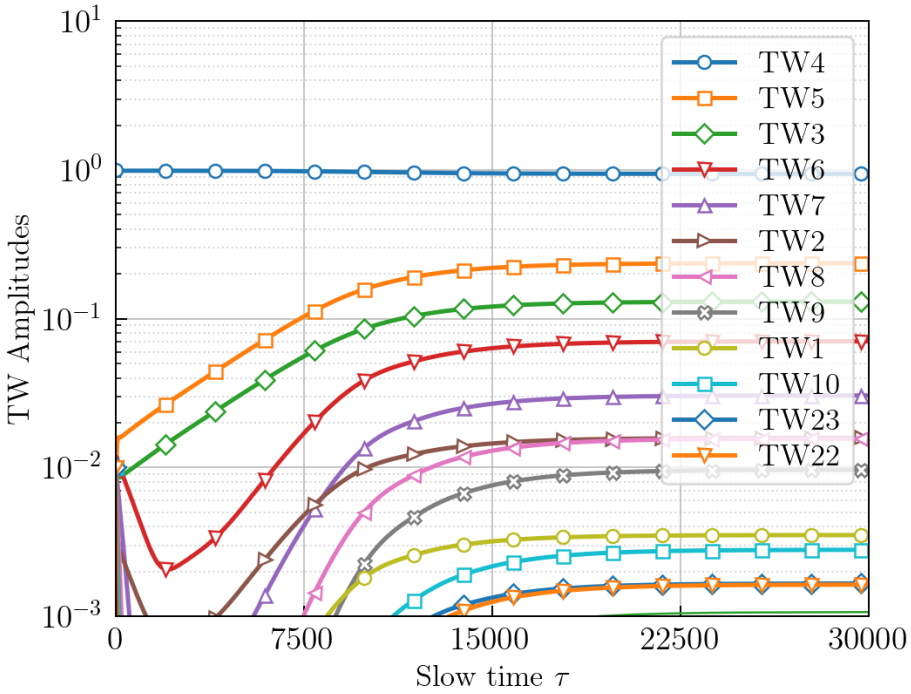

Figure 2.11: Time evolution of the TW amplitudes from the asymptotic model starting from an initial condition of $A_4 = 1$ and $A_j = 0.01$ for the rest of TW modes. The aerodynamic intensity is $\xi_{a_1} = 0.502$.

of every TW mode in the final state. An important remark is that the time that it requires for this multi-TW solution to settle is about 10 times more than that required to converge to a single-TW (Fig. 2.8). The presence of this much longer timescale indicates that a stability analysis is necessary to ensure the convergence to the different solutions.

2.3 Stability Analysis of the Trivial Solution

The asymptotic model

$$\frac{\mathrm{d}}{\mathrm{d}\tau}\begin{pmatrix} A_1 \\ \vdots \\ A_N \end{pmatrix} = -\frac{i}{2}\mathbf{E}^H \begin{pmatrix} Q(|X_1|) & \dots & 0 \\ \vdots & \ddots & \vdots \\ 0 & \dots & Q(|X_N|) \end{pmatrix} \mathbf{E} \begin{pmatrix} A_1 \\ \vdots \\ A_N \end{pmatrix} + \begin{pmatrix} -\tilde{\xi}_1 + i\tilde{\omega}_1 & \dots & 0 \\ \vdots & \ddots & \vdots \\ 0 & \dots & -\tilde{\xi}_N + i\tilde{\omega}_N \end{pmatrix} \begin{pmatrix} A_1 \\ \vdots \\ A_N \end{pmatrix}, \tag{2.33}$$

is a homogeneous system of differential equations, and hence admits the solution $A_j = 0$ for $j = 1, \dots, N$. We perturb the trivial solution by introducing small amplitudes a_j, such that

$$\begin{pmatrix} A_1 \\ \vdots \\ A_N \end{pmatrix} = \begin{pmatrix} 0 \\ \vdots \\ 0 \end{pmatrix} + \begin{pmatrix} a_1 \\ \vdots \\ a_N \end{pmatrix}, \text{ where } |a_j| \ll 1, \text{ for } j = 1, \dots, N. \tag{2.35}$$

Inserting the expressions in Eq. (2.35) into Eq. (2.33), and retaining only terms up to first order, one obtains

$$\frac{\mathrm{d}}{\mathrm{d}\tau}\begin{pmatrix} a_1 \\ \vdots \\ a_N \end{pmatrix} = \begin{pmatrix} -\tilde{\xi}_1 + i(\tilde{\omega}_1 - Q^R(0)/2) & \dots & 0 \\ \vdots & \ddots & \vdots \\ 0 & \dots & -\tilde{\xi}_N + i(\tilde{\omega}_N - Q^R(0)/2) \end{pmatrix} \begin{pmatrix} a_1 \\ \vdots \\ a_N \end{pmatrix}, \tag{2.36}$$

which is a linear diagonal system. The term $Q^R(0)$ is the real part of the complex friction coefficient evaluated at 0 amplitude, which has the effect of producing a frequency shift. The imaginary part of the friction coefficient (related to the dissipation) satisfied $Q^I(0) = 0$ (Fig. 2.7) and hence does not appear in the stability of the zero solution.

The stability of the system is determined by looking directly at the eigenvalues, which are the diagonal elements. Their expression is

$$\lambda_j = -\tilde{\xi}_j + i\left(\tilde{\omega}_j - \frac{Q^R(0)}{2}\right), \quad j = 1, \dots, N. \tag{2.37}$$

The trivial solution is then stable if the real part of all eigenvalues is negative, i.e., $\tilde{\xi}_j > 0$. If just one of the linear damping coefficients becomes negative, then, as expected, the trivial solution is unstable and the system will evolve to a different final state when a small perturbation is introduced. From the shape of the aerodynamic coefficient in Fig. 2.10, it is seen that, for sufficiently large aerodynamic intensity ξ_{a_1}, the first coefficient that will become

negative is $\tilde{\xi}_6$, since it corresponds to the most unstable mode. The effect of the material damping is much smaller, and it just produces a shift upwards to the damping curve.

Therefore, when $\tilde{\xi}_6 = 0$, a bifurcation occurs, and a new solution emerges from the trivial state. This corresponds to single-TW periodic states which are determined and analyzed next.

2.4 Stability Analysis of Single-Traveling Wave Solutions

2.4.1 Single-Traveling Wave Solutions

The solutions that emerge from the destabilization of the trivial solutions are single-TW solutions. These solutions can be found directly in the asymptotic Eq. (2.33) by setting $A_r = \sqrt{N} R_r e^{im_r\tau + i\alpha_r}$ and $A_j = 0$ for $j \neq r$. The modulus of the TW amplitude is $\sqrt{N}R_r$, the frequency correction of the single-TW solution is m_r, and α_r represents an arbitrary free phase. Note that, since there is only one TW component, $|X_j| = R_r$ for every j, so all the entries from the friction matrix in the asymptotic equation are equal to $Q(R_r)$. Introducing this *ansatz* into Eq. (2.33) gives

$$im_r = -\frac{i}{2}Q(R_r) + (-\tilde{\xi}_r + i\tilde{\omega}_r). \tag{2.38}$$

Taking the real part of Eq. (2.38) gives

$$Q^I(R_r) = 2\tilde{\xi}_r, \tag{2.39}$$

which is an implicit equation to determine the amplitude R_r. From the imaginary part we get

$$m_r = \tilde{\omega}_r - \frac{1}{2}Q^R(R_r), \tag{2.40}$$

where the frequency m_r can be obtained directly after computing R_r from Eq. (2.39).

The physical meaning of Eq. (2.39) is that the nonlinear dissipation has to compensate the flutter instability of the system. Note that, since the imaginary part of the friction coefficient is always negative ($Q^I(R_r) < 0$), there can only be a solution if $\tilde{\xi}_r < 0$, which corresponds to an unstable TW mode. Therefore, these single-TW solutions will only be present for those modes with negative aerodynamic damping (unstable TW). A similar relation for computing these limit cycle amplitudes in the study of blade-to-blade or blade-to-ground dampers was found in [106], [107], based on simplified bladed-disk models with 3 to 5 sectors.

2.4.2 Stability in the Traveling Wave Basis

The stability of single-TW solutions is again studied by adding a small perturbation and analyzing the resulting linearized system. Single-TW states are periodic solutions, but to study their stability it is convenient to first transform these solutions to stationary states with the following change of variable

$$A_j = B_j e^{im_r\tau}, \quad j = 1, \dots, N. \tag{2.41}$$

Introducing Eq. (2.41) into the system of equations, and using the value of m_r from the single-TW solution in Eq. (2.38), gives

$$\begin{aligned}\frac{\mathrm{d}}{\mathrm{d}\tau}\begin{pmatrix} B_1 \\ \vdots \\ B_r \\ \vdots \\ B_N \end{pmatrix} = -\frac{i}{2}\mathbf{E}^H \begin{pmatrix} Q(|X_1|)-Q(R_r) & & & & \\ & \ddots & & & \\ & & Q(|X_r|)-Q(R_r) & & \\ & & & \ddots & \\ & & & & Q(|X_N|)-Q(R_r) \end{pmatrix} \mathbf{E} \begin{pmatrix} B_1 \\ \vdots \\ B_r \\ \vdots \\ B_N \end{pmatrix} \\ + \begin{pmatrix} -(\tilde{\xi}_1-\tilde{\xi}_r)+i(\tilde{\omega}_1-\tilde{\omega}_r) & & & & \\ & \ddots & & & \\ & & 0 & & \\ & & & \ddots & \\ & & & & -(\tilde{\xi}_N-\tilde{\xi}_r)+i(\tilde{\omega}_N-\tilde{\omega}_r) \end{pmatrix} \begin{pmatrix} B_1 \\ \vdots \\ B_r \\ \vdots \\ B_N \end{pmatrix}.\end{aligned} \tag{2.42}$$

Note that the linear aerodynamic damping of the mode B_r is zero, since it corresponds to the saturated single-TW solution. In addition, the growth/decay rate of the other modes is determined by the difference of the linear damping of each mode with respect to the mode r. Since the unstable TW modes are close together (Fig. 2.10), their difference is expected to be even smaller than the actual values of the coefficients, resulting in long integration times until the final TW has settled.

Now, we linearize around the single-TW solution, which is a stationary state of this system, using

$$\begin{pmatrix} B_1 \\ \vdots \\ B_r \\ \vdots \\ B_N \end{pmatrix} = \left(\begin{pmatrix} 0 \\ \vdots \\ 1 \\ \vdots \\ 0 \end{pmatrix} + \begin{pmatrix} a_1 \\ \vdots \\ a_r \\ \vdots \\ a_N \end{pmatrix} \right) \sqrt{N} R_r e^{i\alpha_r}, \tag{2.43}$$

where $|a_j| \ll 1$ for $j = 1, \ldots, N$. Before inserting Eq. (2.43) into the asymptotic Eq. (2.42), the linearization of the difference of friction coefficients $Q(|X_j|) - Q(R_r)$ is carried out. Denoting $Z_j = X_j e^{im_r\tau}$, and since $|Z_j| = |X_j|$, we have that, up to linear order, the friction term reduces to

$$Q(|Z_j|) - Q(R_r) \approx Q'(R_r)(|Z_j| - R_r), \tag{2.44}$$

where the expression of the derivative of the friction coefficient $Q'(R_r)$ was given in Eq. (2.29). The linearization on the displacement basis can be written as

$$Z_j = R_r e^{i\alpha_r} e^{i\frac{2\pi r}{N}j} + z_j, \text{ where } |z_j| \ll R_r. \tag{2.45}$$

Since

$$|Z_j|^2 = Z_j \bar{Z}_j = R_r^2 + R_r z_j e^{-i\alpha_r} e^{-i\frac{2\pi r}{N}j} + R_r \bar{z}_j e^{i\alpha_r} e^{i\frac{2\pi r}{N}j} + \mathcal{O}\big(|z_j|^2\big), \tag{2.46}$$

then

$$|Z_j| = R_r \sqrt{1 + \frac{z_j}{R_r} e^{-i\alpha_r} e^{-i\frac{2\pi r}{N}j} + \frac{\bar{z}_j}{R_r} e^{i\alpha_r} e^{i\frac{2\pi r}{N}j} + \mathcal{O}(|z_j|^2)}, \tag{2.47}$$

which up to linear order yields

$$|Z_j| \approx R_r + \frac{1}{2} z_j e^{-i\alpha_r} e^{-i\frac{2\pi r}{N}j} + \frac{1}{2} \bar{z}_j e^{i\alpha_r} e^{i\frac{2\pi r}{N}j}. \tag{2.48}$$

Thus, the first order approximation of $Q(|Z_j|) - Q(R_r)$ is

$$Q(|Z_j|) - Q(R_r) \approx \frac{Q'(R_r)}{2} \left(z_j e^{-i\alpha_r} e^{-i\frac{2\pi r}{N}j} + \bar{z}_j e^{i\alpha_r} e^{i\frac{2\pi r}{N}j} \right), \tag{2.49}$$

which only has a linear term in the perturbation z_j. The complex conjugate $\bar{z}_j$ appears since the Q function is not analytic. Therefore, if we insert Eq. (2.43) into Eq. (2.42), and retain

only terms up to first order in the perturbation, we obtain

$$\frac{\mathrm{d}}{\mathrm{d}\tau}\begin{pmatrix} a_1 \\ \vdots \\ a_r \\ \vdots \\ a_N \end{pmatrix} = -\frac{i}{2}\mathbf{E}^H \begin{pmatrix} Q(|X_1|)-Q(R_r) & & & & \\ & \ddots & & & \\ & & Q(|X_r|)-Q(R_r) & & \\ & & & \ddots & \\ & & & & Q(|X_N|)-Q(R_r) \end{pmatrix} \mathbf{E}\begin{pmatrix} 0 \\ \vdots \\ 1 \\ \vdots \\ 0 \end{pmatrix} + \begin{pmatrix} -(\tilde{\xi}_1-\tilde{\xi}_r)+i(\tilde{\omega}_1-\tilde{\omega}_r) & & & & \\ & \ddots & & & \\ & & 0 & & \\ & & & \ddots & \\ & & & & -(\tilde{\xi}_N-\tilde{\xi}_r)+i(\tilde{\omega}_N-\tilde{\omega}_r) \end{pmatrix} \begin{pmatrix} a_1 \\ \vdots \\ a_r \\ \vdots \\ a_N \end{pmatrix}. \tag{2.50}$$

The term related to the nonlinear friction can be written in a much more simplified form by using the orthogonality relations of the DFT. Introducing the auxiliary vector $\mathbf{v}$ defined as

$$\mathbf{v} \equiv \mathbf{E}^H \begin{pmatrix} Q(|X_1|)-Q(R_r) & & & & \\ & \ddots & & & \\ & & Q(|X_r|)-Q(R_r) & & \\ & & & \ddots & \\ & & & & Q(|X_N|)-Q(R_r) \end{pmatrix} \mathbf{E}\begin{pmatrix} 0 \\ \vdots \\ 1 \\ \vdots \\ 0 \end{pmatrix}, \tag{2.51}$$

we can expand explicitly the j component, using Eq. (2.49) and

$$z_j = R_r e^{i\alpha_r} \sum_{k=1}^{N} a_k e^{i\frac{2\pi k}{N}j}, \tag{2.52}$$

to get

$$v_j = \frac{Q'(R_r)R_r}{2N}\left(\sum_{k=1}^{N} a_k \sum_{m=1}^{N} e^{i\frac{2\pi(k-j)}{N}m} + \sum_{k=1}^{N} \bar{a}_k \sum_{m=1}^{N} e^{-i\frac{2\pi(k-2r+j)}{N}m}\right). \tag{2.53}$$

From the orthogonality relation of the DFT, the summations of the complex exponential function take the values

$$\sum_{m=1}^{N} e^{i\frac{2\pi(k-j)}{N}m} = N\delta_{kj}, \quad \sum_{m=1}^{N} e^{-i\frac{2\pi(k-2r+j)}{N}m} = N\delta_{k,2r-j}, \tag{2.54}$$

where δ_{ij} is the Kronecker delta. A straightforward way of checking this result is using the

formula for the sum of a geometric series. Therefore, the jth component of the vector $\mathbf{v}$ is, finally,

$$v_j = \frac{Q'(R_r)R_r}{2}(a_j + \bar{a}_{2r-j}). \tag{2.55}$$

Notice that if $j = r$ the previous relation only involves the r component $(a_r + \bar{a}_r)$, but if $j = r + k$ is considered, then $(a_{r+k} + \bar{a}_{r-k})$ the amplitudes of different TWs are coupled. Substituting this result in Eq. (2.50) gives

$$\frac{\mathrm{d}}{\mathrm{d}\tau}\begin{pmatrix}\vdots\\ a_{r-1}\\ a_r\\ a_{r+1}\\ \vdots\end{pmatrix} = -\frac{i}{4}Q'(R_r)R_r\left(\begin{pmatrix}\vdots\\ a_{r-1}\\ a_r\\ a_{r+1}\\ \vdots\end{pmatrix} + \begin{pmatrix}\vdots\\ \bar{a}_{r+1}\\ \bar{a}_r\\ \bar{a}_{r-1}\\ \vdots\end{pmatrix}\right) + \begin{pmatrix}-(\tilde{\xi}_1 - \tilde{\xi}_r) + i(\tilde{\omega}_1 - \tilde{\omega}_r) & & & & \\ & \ddots & & & \\ & & 0 & & \\ & & & \ddots & \\ & & & & -(\tilde{\xi}_N - \tilde{\xi}_r) + i(\tilde{\omega}_N - \tilde{\omega}_r)\end{pmatrix}\begin{pmatrix}\vdots\\ a_{r-1}\\ a_r\\ a_{r+1}\\ \vdots\end{pmatrix}, \tag{2.56}$$

which is the final form of the linearized amplitude equations around a single-TW solution. There are some relevant characteristics of this system that are worth noting. First, the complex conjugate of the TW amplitudes appear through the linearization of the complex friction function Q, since this function is not analytic. The equation related to the TWr is decoupled from the rest of the TWs, and has no contribution from the linear aerodynamic and material coefficients. The TW $r + k$ is coupled through the nonlinear friction with TW $r - k$. Therefore, despite the fact that all sectors are identical (tuned system), the TW perturbations are coupled in pairs (because of the background TW).

The linear damping is now given by the differences $\tilde{\xi}_j - \tilde{\xi}_r$, which is related to the time decay of the TW amplitudes. For an unstable mode r, it is expected that this difference with respect to the other unstable modes is of a smaller order than the values of the aerodynamic damping, producing an even longer timescale, which explains why the time simulations take a long time to settle to the final state, as shown in the right of Fig. 2.8. The slope of the decay, related to the difference, is smaller than the growth given by the value $\tilde{\xi}_r$.

The stability of the single-TW solutions is given by the eigenvalues of Eq. (2.56) although, in order to compute them, we need to recast it to an augmented problem due to the presence

of the terms with the complex conjugate of the amplitude. Denoting system (2.56) as

$$\frac{\mathrm{d}\mathbf{a}}{\mathrm{d}\tau} = \mathbf{J}_{\mathrm{TW1}}\mathbf{a} + \mathbf{J}_{\mathrm{TW2}}\bar{\mathbf{a}}, \tag{2.57}$$

we obtain the expanded system

$$\frac{\mathrm{d}}{\mathrm{d}\tau}\begin{pmatrix}\mathbf{a}\\ \bar{\mathbf{a}}\end{pmatrix} = \begin{pmatrix}\mathbf{J}_{\mathrm{TW1}} & \mathbf{J}_{\mathrm{TW2}}\\ \bar{\mathbf{J}}_{\mathrm{TW2}} & \bar{\mathbf{J}}_{\mathrm{TW1}}\end{pmatrix}\begin{pmatrix}\mathbf{a}\\ \bar{\mathbf{a}}\end{pmatrix} = \mathbf{J}_{\mathrm{TW}}\begin{pmatrix}\mathbf{a}\\ \bar{\mathbf{a}}\end{pmatrix}. \tag{2.58}$$

The computation of the eigenvalues of the augmented problem, $\mathbf{J}_{\mathrm{TW}}$, for different aerodynamic intensities, will give the stability of the single-TW solutions. This jacobian has a zero eigenvalue related to an additional degree of freedom single-TW solutions have, which is the free phase α_r (see Eq. (2.43)) When analyzing the stability of the system, this zero can be ignored, and only check the signs of the real part of the rest of the eigenvalues.

2.4.3 Bifurcation Diagram of Single-Traveling Wave Solutions

The bifurcation diagram of the single-TW saturated states is computed using Eq. (2.39) and changing the aerodynamic intensity through ξ_{a_1}. Their stability is obtained from the eigenvalues of the jacobian of Eq. (2.58).

The stability plot for the most unstable TW mode, which is TW6 (see Fig. 2.10), is shown in Fig. 2.12. The solid (dashed) line is used to represent stable (unstable) solutions. The zero solution, at the bottom of the plot, is stable for values of the bifurcation parameter close to $\xi_{a_1} = 0.2$. Then, as soon as $\tilde{\xi}_6 = 0$, a bifurcation occurs, and there is a stability change of the trivial solution which becomes unstable for increasingly aerodynamic intensity, as discussed in Eq. (2.37).

From the bifurcation point, the single-TW6 solution emerges, which was the solution found in the time simulation shown in Fig. 2.8, where after nonlinear interaction between the different TW modes, the most unstable one was selected and settled as the saturated flutter solution by nonlinear friction. As illustrated in Fig. Fig. 2.12, from the bifurcation point, the solution is always stable. The basin of attraction of this state appears to be large, since after time integration for many random initial conditions, the system usually settles to it. This is also confirmed by previous works, where the only final solution found was always the most unstable TW [53], [99].

Next, we analyze the unstable TW4. The bifurcation diagram from Fig. 2.13 shows exactly the same stability for the trivial solution. Nevertheless, the single-TW solution for this mode

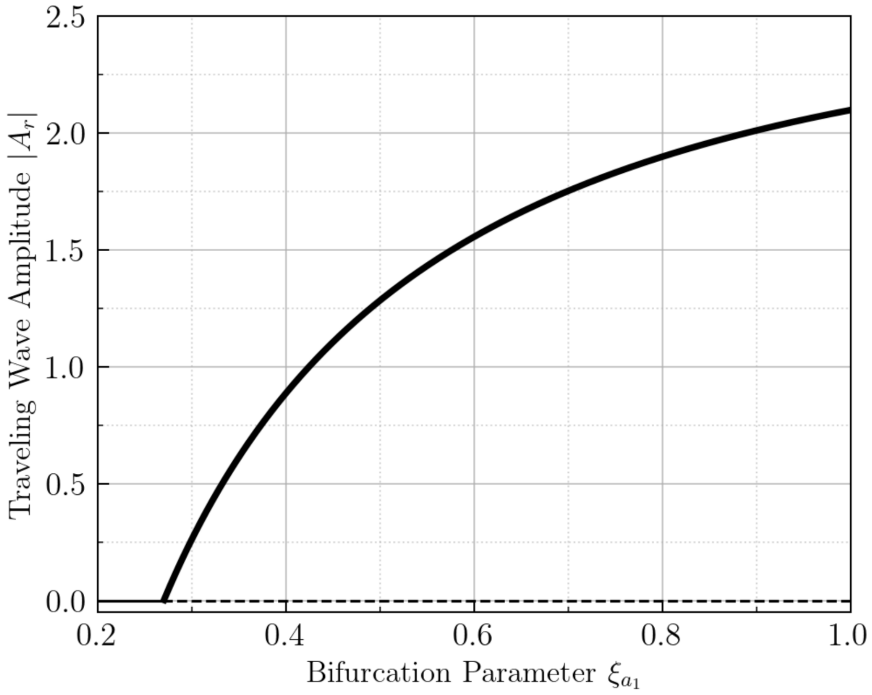

Figure 2.12: Bifurcation diagram of the single-TW6 solution with respect to the aerodynamic intensity parameter ξ_{a_1}. Solid (dashed) lines represent stable (unstable) solutions.

does not emerge at the stability change point. This state appears when $\tilde{\xi}_4 = 0$, and since this mode is less aerodynamically unstable than TW6, the branch emerges at a higher value of the aerodynamic intensity. This branch is unstable for smaller values of the aerodynamic intensity, and then it becomes stable. The analysis confirms that other TWs, apart from the most unstable one, can be the final state of the system.

Tracking the eigenvalues of the unstable branch shows that this solution undergoes several Hopf Bifurcations (HB), until becoming stable. In this dissertation, an extensive discussion of the different types of bifurcation is omitted, since there are many good introductions to the subject [108]–[110]. Therefore, we will only make use of some of the results of bifurcation theory, and motivate them when needed.

Recall that the single-TW solutions are time periodic, although for the stability analysis they transformed into stationary solutions via the change of variable from Eq. (2.41). Hopf Bifurcations occur when a pair of eigenvalues, one being the complex conjugate of the other, cross the imaginary axis with a non-zero speed with respect to the bifurcation parameter. This type of bifurcation is related to the appearance of new periodic states in the system, which in this case means solutions with two different frequencies, since the single-TW solutions

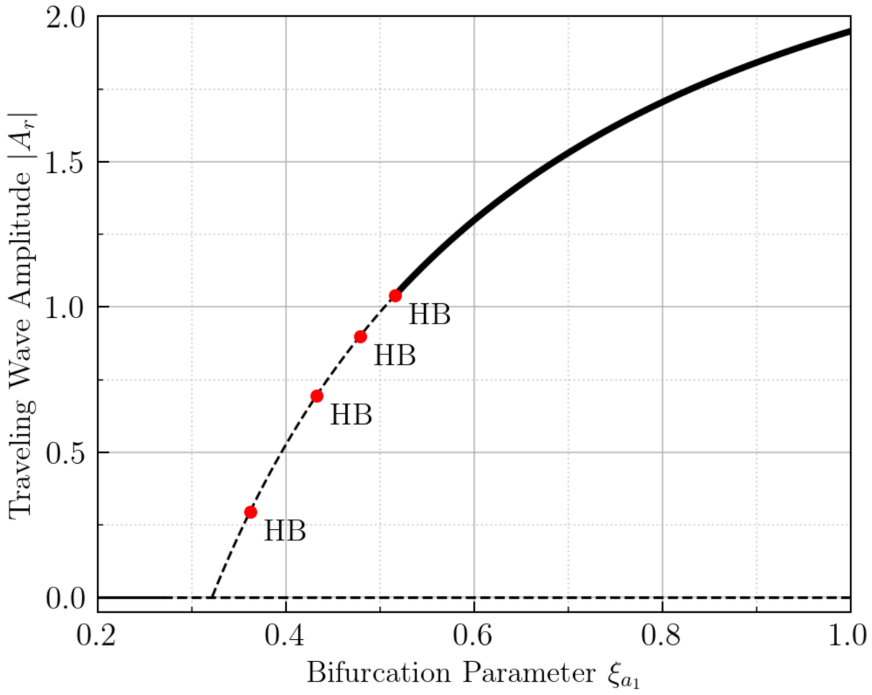

Figure 2.13: Bifurcation diagram of the single-TW4 solution with respect to the aerodynamic intensity parameter ξ_{a_1}. Solid (dashed) lines represent stable (unstable) solutions.

already contain a frequency of oscillation, which was calculated in Eq. (2.40). Actually, one of these solutions were found in the exploratory work presented in the time simulation from Fig. 2.11, where a multi-TW solution was found after a large integration time. This solution corresponded to a value of $\xi_{a_1} = 0.502$, which is very close to the bifurcation point of the stability change. In Section 2.5, the emergent solutions from the stability change at the HB points will be tracked by means of a numerical continuation algorithm.

Before performing this exploration, the stability chart of TW9, which is less unstable, is presented in Fig. 2.14. The trivial solution has exactly the same behavior, and the TW9 saturated solution emerges at $\tilde{\xi}_9 = 0$. In contrast to the previous cases, this branch of solutions is completely unstable, meaning that a slight perturbation from this state will make the system evolve to a different solution.

A convenient visualization for the bifurcation diagrams of all single-TW solutions is presented in Fig. 2.15. Here, all curves for the different unstable single-TW solutions with different ND are plotted together, to give a more visual description of their stability. As it can be seen, only the most unstable TW6 has a completely stable branch. The neighboring ones, from TW4 to TW8, also have a stable region, so they could be also found as possible final states

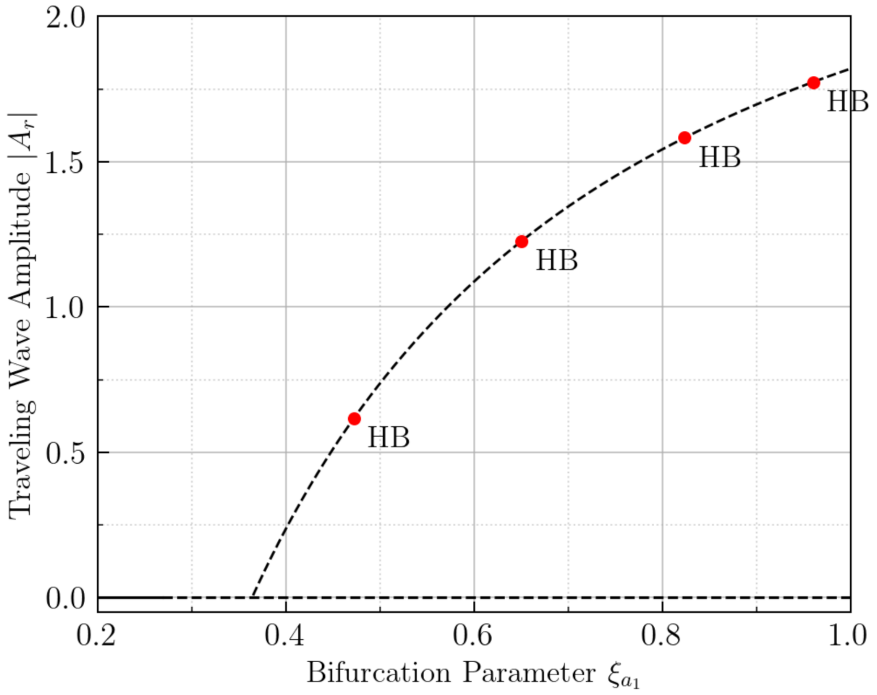

Figure 2.14: Bifurcation diagram of the single-TW9 solution with respect to the aerodynamic intensity parameter ξ_{a_1}. Solid (dashed) lines represent stable (unstable) solutions.

of the system. An important observation is that the more aerodynamically unstable a TW mode is, the sooner the single-TW saturated solution appears. The rest of the unstable TWs, although they are a solution of the system, they are unstable for the plotted range of values of the aerodynamic intensity. Additionally, in terms of amplitude, the more conservative analysis for the single-TW solutions is to consider the most unstable one, since it yields the largest vibration levels.

The results of the bifurcation diagram are now validated against direct time integration of the asymptotic equations for the five points highlighted in Fig. 2.15. The time integration is carried out starting from the solution branch and adding a perturbation $A_j = 0.01$ to every other TW mode as the initial condition.

Starting with the points from TW4, the time simulations presented in Fig. 2.16 are carried out for a point where the solution is unstable, and another point which corresponds to a stable state, which are points (a) and (b) in Fig. 2.15. The evolution from the unstable solution is shown Fig. 2.16a, where it is observed that the system starts close to TW4 and the other unstable modes start growing exponentially. Then, there is a nonlinear interaction where the TW5 is selected as the final single-TW state. The other unstable modes decay

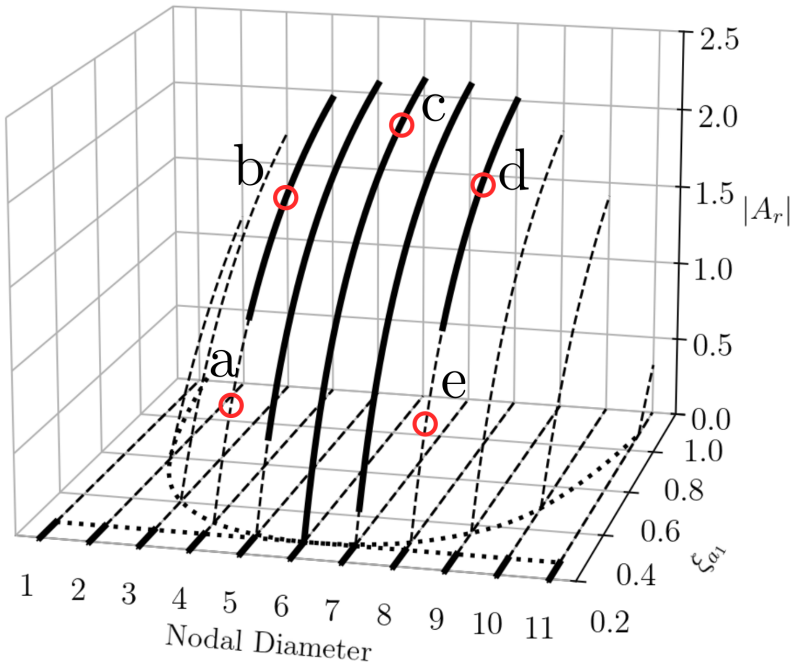

Figure 2.15: Bifurcation diagram of all the single-TW solutions with respect to the aerodynamic intensity parameter ξ_{a_1}. Solid (dashed) lines represent stable (unstable) solutions.

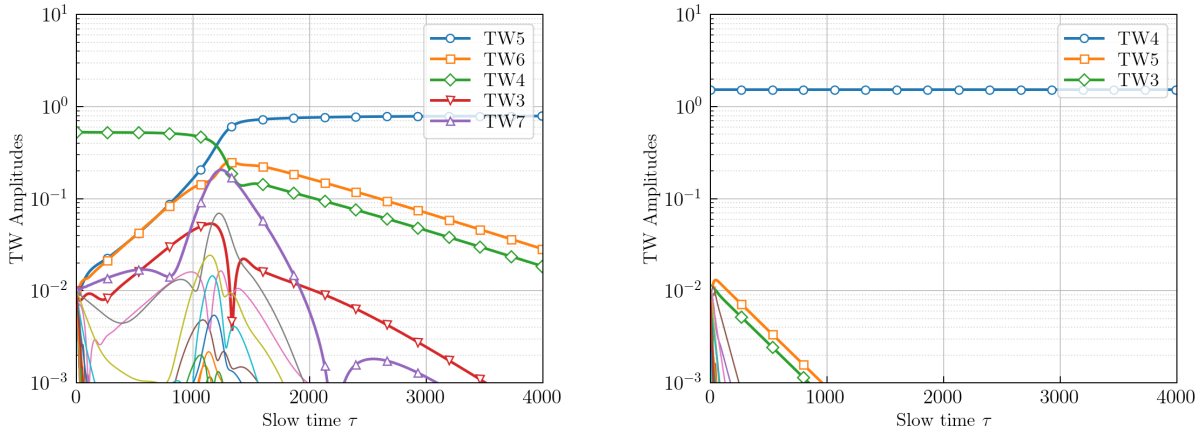

(a) Point a ($\xi_{a_1} = 0.4$).

(b) Point b ($\xi_{a_1} = 0.7$).

Figure 2.16: Time evolution of the TW amplitudes from the asymptotic model starting from an initial point of the bifurcation diagram in Fig. 2.15 corresponding to TW4 and a perturbation condition of $A_j = 0.01$ for the rest of TW modes.

in pairs with different slopes. This fact is consistent with the previous analysis because, if TW5 is the final single-TW state, the smaller decay rate corresponds to the $5+1$ and $5-1$ traveling waves, as predicted in system (2.56), since their damping is given by $\tilde{\xi}_{5\pm1} - \tilde{\xi}_5$.

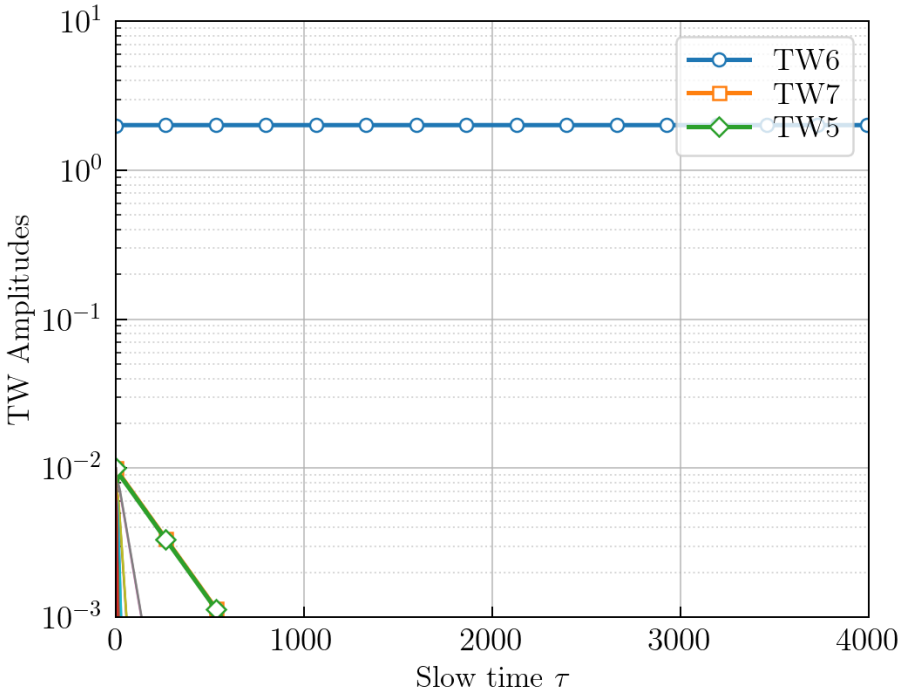

Figure 2.17: Time evolution of the TW amplitudes from the asymptotic model starting from an initial point of the bifurcation diagram in Fig. 2.15 corresponding to TW6 and a perturbation condition of $A_j = 0.01$ for the rest of TW modes. Point c ($\xi_{a_1} = 0.9$).

Additionally, the TWs are coupled in pairs, also as predicted by the linearized system of equation. Now, turning our attention to the stable state (b), from Fig. 2.16b, we see that the amplitude of TW4 remains constant in time and the other unstable TW modes directly decay exponentially from the beginning.

Figure 2.17 shows the time evolution of the TW6, which was stable. Again, the prediction of the bifurcation diagram is confirmed, since the amplitude of this TW remains constant and the rest decay exponentially. Note that the TWs with the smallest decay rate are again the two closest to the final single-TW saturated state, which are TW5 and TW7.

The same analysis is repeated for TW8 in Fig. 2.18, corresponding to points (d) and (e). The time simulation of a small perturbation around the stable point (d), exhibits the same behavior as the previous cases (Fig. 2.18b). In contrast, the perturbation around the unstable solution, shown in Fig. 2.18a, shows a nonlinear interaction between the TW modes due to the friction until TW7 is selected, resulting in a different final state than that in the case of TW4, which was TW5.

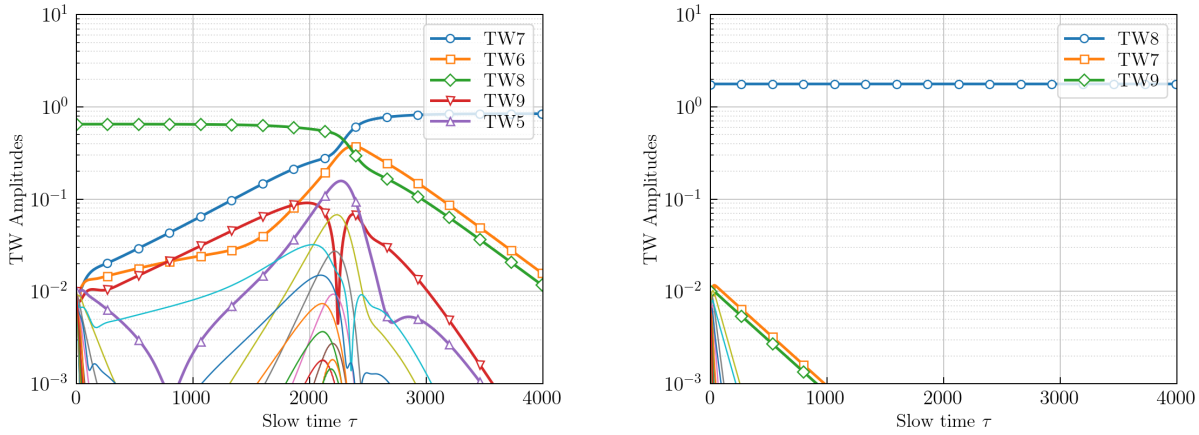

(a) Point e ($\xi_{a_1} = 0.4$). **(b)** Point d ($\xi_{a_1} = 0.8$).

Figure 2.18: Time evolution of the TW amplitudes from the asymptotic model starting from an initial point of the bifurcation diagram in Fig. 2.15 corresponding to TW8 and a perturbation condition of $A_j = 0.01$ for the rest of TW modes.

2.5 Continuation from Single-Traveling Wave Bifurcations

The bifurcation diagrams of single-TW solutions were computed analytically in the previous section, and their stability assessed with the eigenvalues of the jacobian matrix. To track the new solution branches that emerge from Hopf Bifurcation points, a numerical continuation algorithm has to be used.

Continuation methods are designed to track stationary or periodic states of systems of differential equations

$$\mathbf{w}' = \mathbf{f}(\mathbf{w}, p), \tag{2.59}$$

where p is a continuation parameter. In the case of a periodic solution, they are able to compute the Floquet multipliers at each step of the curve, which give directly the stability of the solution.

Continuation algorithms [111] have been extensively used, especially since the advent of computers. Currently, there are many excellent continuation software programs: the classical AUTO-07p [112] implemented in FORTRAN, Matlab codes such as MatCont [113] or COCO [114], or the more recent BifurcationKit.jl, implemented in the new Julia programming language [115].

In this work, the selected continuation package to study the nonlinear dynamics of the system is AUTO-07p. Before performing the continuation analysis, a modification needs to be done to the system (2.42) to make it suitable for the software. To motivate the need for this

change, we give a small comment on the system equations, which are repeated here

$$\frac{\mathrm{d}}{\mathrm{d}\tau}\begin{pmatrix} B_1 \\ \vdots \\ B_r \\ \vdots \\ B_N \end{pmatrix} = -\frac{i}{2}\mathbf{E}^H \begin{pmatrix} Q(|X_1|)-Q(R_r) & & & & \\ & \ddots & & & \\ & & Q(|X_r|)-Q(R_r) & & \\ & & & \ddots & \\ & & & & Q(|X_N|)-Q(R_r) \end{pmatrix} \mathbf{E} \begin{pmatrix} B_1 \\ \vdots \\ B_r \\ \vdots \\ B_N \end{pmatrix} + \begin{pmatrix} -(\tilde{\xi}_1-\tilde{\xi}_r)+i(\tilde{\omega}_1-\tilde{\omega}_r) & & & & \\ & \ddots & & & \\ & & 0 & & \\ & & & \ddots & \\ & & & & -(\tilde{\xi}_N-\tilde{\xi}_r)+i(\tilde{\omega}_N-\tilde{\omega}_r) \end{pmatrix} \begin{pmatrix} B_1 \\ \vdots \\ B_r \\ \vdots \\ B_N \end{pmatrix}. \tag{2.42}$$

This is a system ofcomplex differential equations invariant under the change in phase $B_j \to B_j e^{i\alpha_r}$ for all j. In other words, there is a free phase α_r. As a consequence, there is always an exact zero eigenvalue related to this symmetry of the system, which needs to be removed in order to successfully use the continuation software, since the bifurcation detection occurs precisely when the real part of an eigenvalue crosses zero.

To achieve this, the equation governing the evolution of the free phase evolution will be removed from the amplitude equations. Consider the change of variable

$$\begin{pmatrix} B_1 \\ \vdots \\ B_r \\ \vdots \\ B_N \end{pmatrix} = \begin{pmatrix} C_1 \\ \vdots \\ C_r \\ \vdots \\ C_N \end{pmatrix} e^{i\alpha_r} = \begin{pmatrix} |C_1|e^{i\hat{\alpha}_1} \\ \vdots \\ C_r \\ \vdots \\ |C_N|e^{i\hat{\alpha}_N} \end{pmatrix} e^{i\alpha_r}, \tag{2.60}$$

where C_r is a real number and the phases $\hat{\alpha}_j = \alpha_j - \alpha_r$. The phase is factored out from the TW amplitudes due to the constraints of the AUTO software, to produce a system of equations that can be implemented into its particular format. Introduction of Eq. (2.60)

into the amplitude equations gives

$$\frac{\mathrm{d}}{\mathrm{d}\tau}\begin{pmatrix} C_1 \\ \vdots \\ C_r \\ \vdots \\ C_N \end{pmatrix} + i\frac{\mathrm{d}\alpha_r}{\mathrm{d}\tau}\begin{pmatrix} C_1 \\ \vdots \\ C_r \\ \vdots \\ C_N \end{pmatrix} = -\frac{i}{2}\mathbf{E}^H \begin{pmatrix} Q(|X_1|)-Q(R_r) & & & & \\ & \ddots & & & \\ & & Q(|X_r|)-Q(R_r) & & \\ & & & \ddots & \\ & & & & Q(|X_N|)-Q(R_r) \end{pmatrix} \mathbf{E}\begin{pmatrix} C_1 \\ \vdots \\ C_r \\ \vdots \\ C_N \end{pmatrix} + \begin{pmatrix} -(\tilde{\xi}_1-\tilde{\xi}_r)+i(\tilde{\omega}_1-\tilde{\omega}_r) & & & & \\ & \ddots & & & \\ & & 0 & & \\ & & & \ddots & \\ & & & & -(\tilde{\xi}_N-\tilde{\xi}_r)+i(\tilde{\omega}_N-\tilde{\omega}_r) \end{pmatrix}\begin{pmatrix} C_1 \\ \vdots \\ C_r \\ \vdots \\ C_N \end{pmatrix}, \tag{2.61}$$

and the equation at row r takes the form

$$\frac{\mathrm{d}C_r}{\mathrm{d}\tau} + i\frac{\mathrm{d}\alpha_r}{\mathrm{d}\tau}C_r = \mathbf{t}^\top \mathbf{C}, \tag{2.62}$$

where $\mathbf{t} = -i/2[\mathbf{E}^H(Q(|\mathbf{X}|)-Q(R_r))\mathbf{E}]_{r^{th}\text{row}}$. Separating into real and imaginary parts give

$$\frac{\mathrm{d}C_r}{\mathrm{d}\tau} = \mathrm{Re}[\mathbf{t}^\top \mathbf{C}], \tag{2.63}$$

$$\frac{\mathrm{d}\alpha_r}{\mathrm{d}\tau} = \frac{1}{C_r}\mathrm{Im}[\mathbf{t}^\top \mathbf{C}]. \tag{2.64}$$

Note that, for a single-TWr solution, $\mathbf{t} = \mathbf{0}$ and we get that the phase α_r is constant, since the time evolution was factored out in the frequency m_r from Eq. (2.40). However, when exploring different solutions, this phase will in general depend on the slow time τ.

The idea is to remove Eq. (2.64) from the system, and then use the other equations for the continuation process. To do so, we first remove Eq. (2.62) from the full system, producing $N-1$ complex differential equations of the form

$$\frac{\mathrm{d}}{\mathrm{d}\tau}\begin{pmatrix} C_1 \\ \vdots \\ C_{r+1} \\ \vdots \\ C_N \end{pmatrix} = -\frac{i}{2}\mathbf{E}^H \begin{pmatrix} Q(|X_1|)-Q(R_r) & & & & \\ & \ddots & & & \\ & & Q(|X_{r+1}|)-Q(R_r) & & \\ & & & \ddots & \\ & & & & Q(|X_N|)-Q(R_r) \end{pmatrix} \mathbf{E} \begin{pmatrix} C_1 \\ \vdots \\ C_r \\ \vdots \\ C_N \end{pmatrix}$$
$$+ \begin{pmatrix} -(\tilde{\xi}_1-\tilde{\xi}_r)+i(\tilde{\omega}_1-\tilde{\omega}_r) & & & & \\ & \ddots & & & \\ & & -(\tilde{\xi}_{r+1}-\tilde{\xi}_r)+i(\tilde{\omega}_{r+1}-\tilde{\omega}_r) & & \\ & & & \ddots & \\ & & & & -(\tilde{\xi}_N-\tilde{\xi}_r)+i(\tilde{\omega}_N-\tilde{\omega}_r) \end{pmatrix} \begin{pmatrix} C_1 \\ \vdots \\ C_r \\ \vdots \\ C_N \end{pmatrix}$$
$$- \frac{1}{C_r}\mathrm{Im}[\mathbf{t}^\top \mathbf{C}] \begin{pmatrix} C_1 \\ \vdots \\ C_{r+1} \\ \vdots \\ C_N \end{pmatrix}, \tag{2.65}$$

or, more briefly,

$$\frac{\mathrm{d}}{\mathrm{d}\tau}\begin{pmatrix} C_1 \\ \vdots \\ C_{r+1} \\ \vdots \\ C_N \end{pmatrix}_{N-1\times 1} = \mathbf{T}_{N-1\times N} \begin{pmatrix} C_1 \\ \vdots \\ C_r \\ \vdots \\ C_N \end{pmatrix}_{N\times 1}, \tag{2.66}$$

where the terms have been compacted into the matrix $\mathbf{T}$ and the size of each matrix and vector has been added for clarity. Additionally, we add the real equation concerning the evolution of the amplitude C_r, which is (2.63). Thus, this forms the system of equations that needs to be solved in the continuation, where the equation for the α_r is left out.

For the continuation algorithm, the system has to be written in real and imaginary parts, in

the following way

$$\begin{pmatrix} C_1 \\ \vdots \\ C_r \\ \vdots \\ C_N \end{pmatrix} = \begin{pmatrix} u_1 \\ \vdots \\ u_r \\ \vdots \\ u_N \end{pmatrix} + i \begin{pmatrix} v_1 \\ \vdots \\ 0 \\ \vdots \\ v_N \end{pmatrix}, \tag{2.67}$$

where $v_r = 0$ since the invariant phase have been factored out. Then, the system of equations takes the form

$$\frac{\mathrm{d}}{\mathrm{d}\tau} \begin{pmatrix} u_1 \\ \vdots \\ u_{r+1} \\ \vdots \\ u_N \\ v_1 \\ \vdots \\ v_{r+2} \\ \vdots \\ v_N \end{pmatrix}_{2N-2\times 1} = \begin{pmatrix} \mathrm{Re}[\mathbf{T}] & -\mathrm{Im}[\mathbf{T}] \\ \mathrm{Im}[\mathbf{T}] & \mathrm{Re}[\mathbf{T}] \end{pmatrix}_{2N-2\times 2N} \begin{pmatrix} u_1 \\ \vdots \\ u_r \\ \vdots \\ u_N \\ v_1 \\ \vdots \\ 0 \\ \vdots \\ v_N \end{pmatrix}_{2N\times 1}, \tag{2.68}$$

along with the equation

$$\frac{\mathrm{d}u_r}{\mathrm{d}\tau} = \mathrm{Re}[\mathbf{t}^\top \mathbf{C}]. \tag{2.69}$$

Eqs. (2.68) and (2.69) are implemented in AUTO software to perform the continuation of the solutions. Additionally, the jacobian of this system is also needed to improve the quality of the continuation at the bifurcation, where a jacobian estimated by finite differences could contain significant errors. This jacobian is different from the one used in the stability of single-TW solutions in Eq. (2.58), since that jacobian was evaluated at the solution branch, but we need to also compute the jacobian without evaluating at any particular value. This derivation is left to the Appendix B.

2.5.1 Baseline Configuration

The continuation of the HB points from the bifurcation diagram in Fig. 2.15 is performed. Special attention is paid to the points where there is a stability change, since these could lead to new stable states.

For the aerodynamic damping distribution considered (Fig. 2.10), the continuation process showed the emergence of new states which were unstable for most TW modes. Therefore, these cannot be final states of the system and are omitted from the analysis.

Nevertheless, the continuation of the HB of single-TW4 showed a new stable solution, made up of contributions from all other TWs (even the stable ones) and is plotted in Fig. 2.19. This multi-TW solution emerges from the bifurcation point, and the amplitude of the TW4 decreases with respect to the single-TW solution, but the amplitude of the other TW modes increases (highlighted with different colors in the bottom of the figure). Only the 5 most significant TWs are shown, and the rest are omitted from this plot.

This branch of solutions is stable for a narrow range of the aerodynamic intensity, and then it undergoes a Torus Bifurcation (TB) after which it becomes unstable. New possible branches of solutions emerging from this point are considered out of the scope of this work.

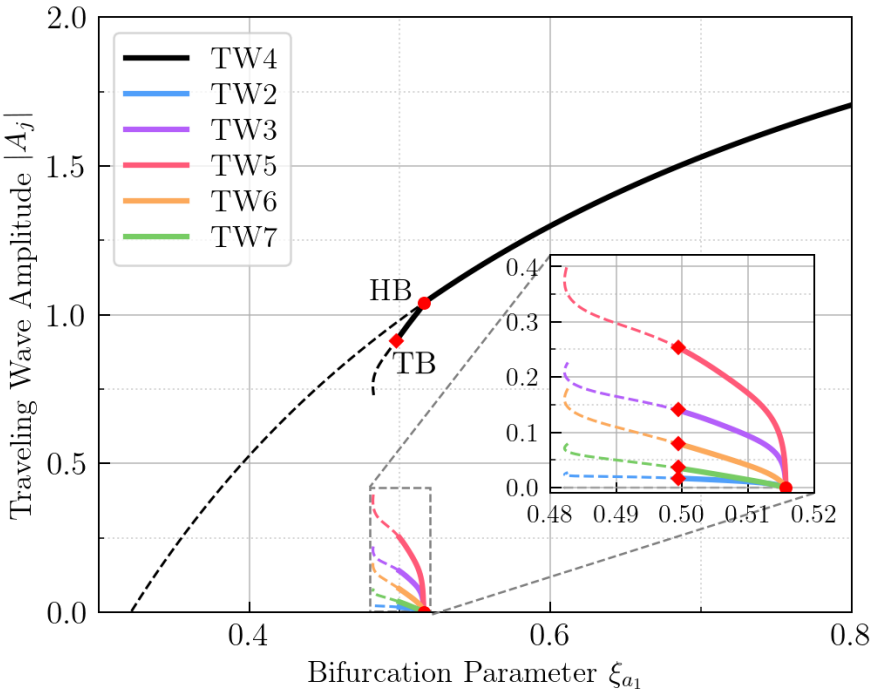

Figure 2.19: Bifurcation diagram of the TW4 solution with respect to the aerodynamic intensity parameter ξ_{a_1}. A solution branch, emerging from the single-TW state, is found with multi-TW contributions. Solid (dashed) lines represent stable (unstable) solutions.

This multi-TW branch corresponds to a solution with another frequency. The value of this new frequency with respect to the aerodynamic intensity is shown in Fig. 2.20. This frequency has to be added to m_4, which is the frequency of the single-TW flutter solution given by Eq. (2.40).

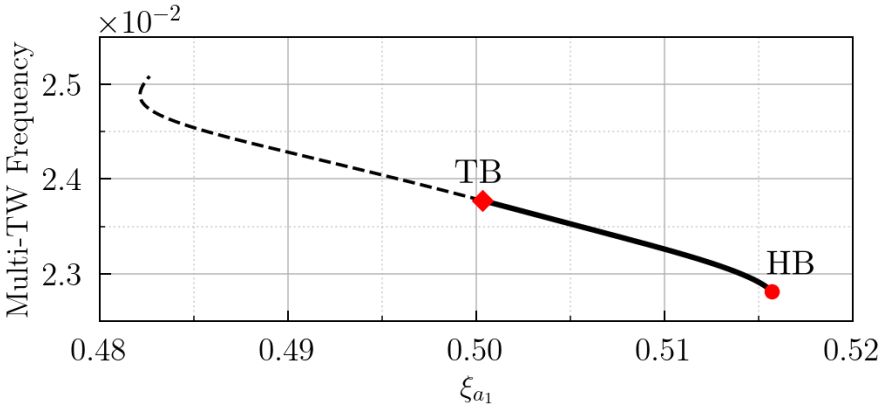

Figure 2.20: Bifurcation diagram of the TW4 solution with respect to the aerodynamic intensity parameter ξ_{a_1}. Evolution of the frequency evolution of the multi-TW solution. Solid (dashed) lines represent stable (unstable) solutions.

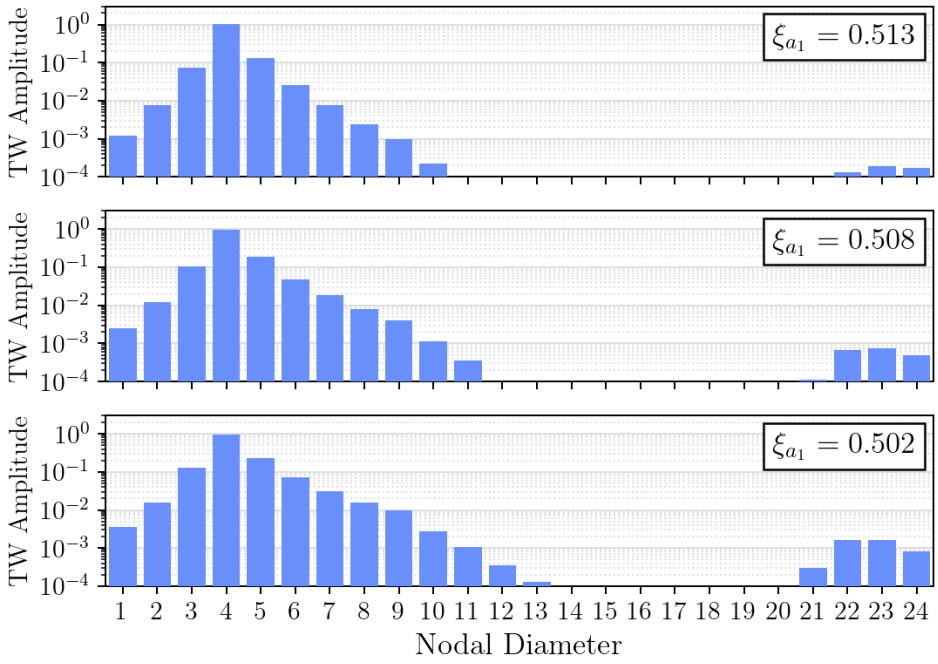

Figure 2.21: Amplitude of the different TW modes for the multi-TW states emerging from the TW4 solution.

From these figures, it can be seen that the range of existence of these solutions is $\xi_{a_1} \sim 0.5 - 0.515$. For three points distributed along the solution branch, the amplitude of the different TW modes is plotted in Fig. 2.21. As the aerodynamic intensity is decreased towards 0.5, which is closer to the TB point, the amplitude of the different TWs, except for TW4, increase, producing a solution with richer TW content.

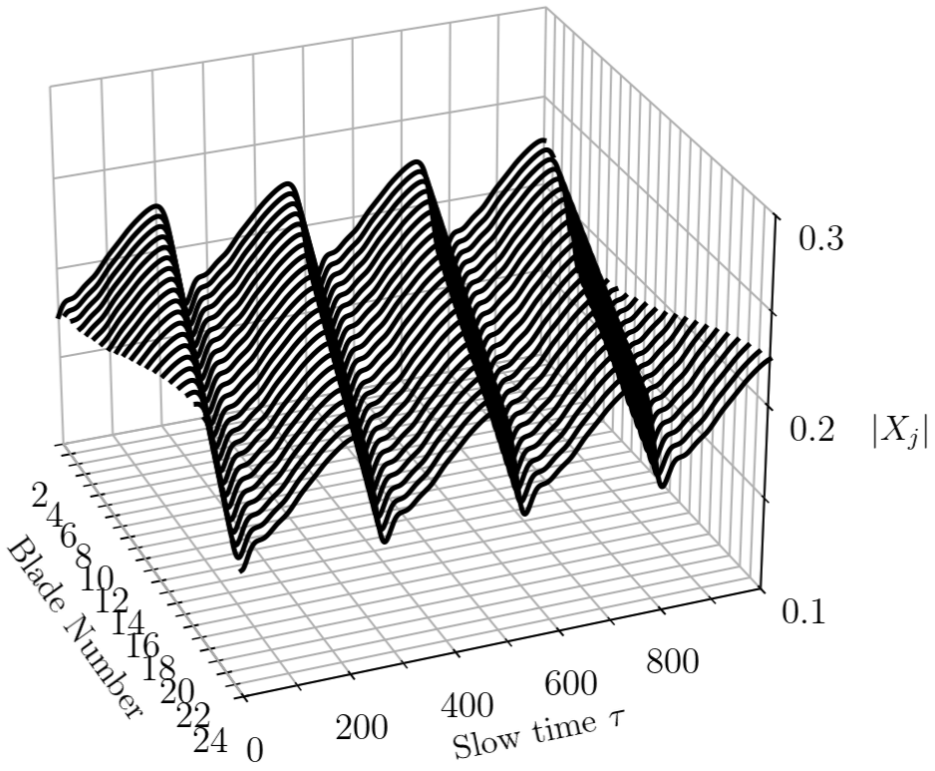

Figure 2.22: Blade displacements of the multi-TW.

In terms of blade displacements, the amplitude of the vibration of the difference blades $|X_j|$ is shown in Fig. 2.22. In this physical basis, it appears that the multi-TW solution takes the form of a traveling wave with non-uniform amplitude around the bladed disk. Actually, the solution presented in this figure is the envelope of the fast elastic oscillations, which were filtered out as a result of the asymptotic procedure. The period of this envelope, which is roughly around 300 in the slow timescale, is the one related to the new frequency found and plotted in Fig. 2.20.

Despite the complexity of these new solutions, the maximum amplitude of vibration of the blades is still smaller than that of the most unstable single-TW solution. The values are shown in Table 2.1, where there is a relative difference of 17% between the two solutions. Therefore, for a conservative estimation of the maximum amplitude of vibration of the system, it seems that the simple analysis of considering just the most unstable TW is enough.

Another interesting conclusion can be extracted by giving the system the initial value of the single-TW4 in the unstable part and, without perturbing the other TW modes, check how long does it take for a time integration to capture these multi-TW states. This procedure

Table 2.1: Maximum blade displacement comparison.

Multi-TW	TW6	Relative Difference
0.224	0.269	17%

is illustrated in Fig. 2.23, where a large time, of around $\tau = 150,000$ in the slow time, is needed until the other TWs settle and become part of the final solution. The integration time required is two orders of magnitude greater than the one needed for integration when the final state was a single-TW. Additionally, keep in mind that these are time integrations of the asymptotic model, with the oscillations of the natural frequency of the blade removed. Thus, numerical integration of the original bladed-disk system would require much more computational effort to capture these states.

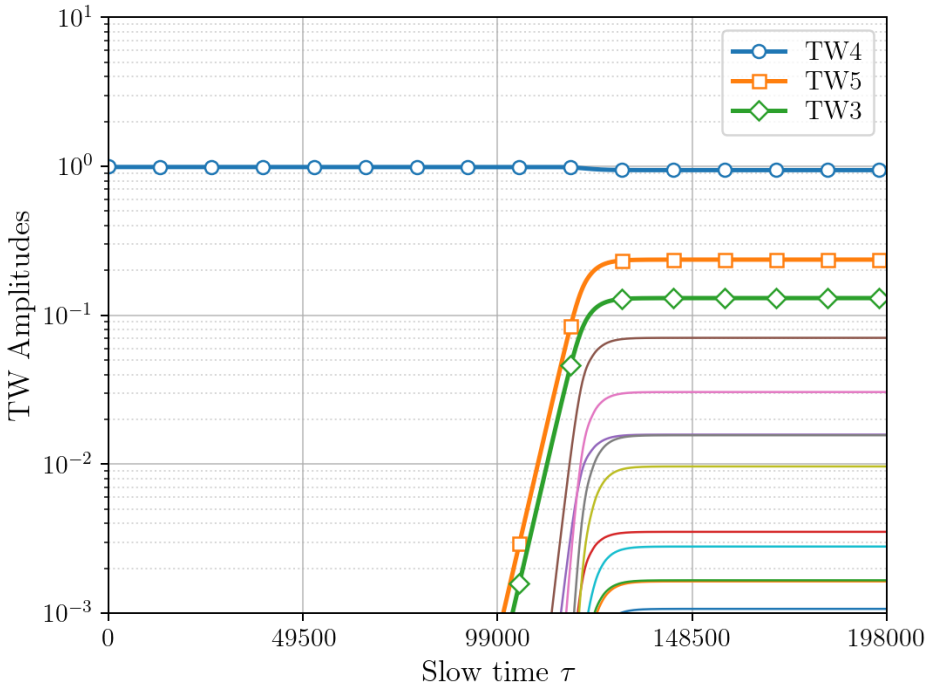

Figure 2.23: Time evolution of the TW amplitudes from the asymptotic model starting from a single-TW4 unstable solution and letting it evolve until the multi-TW states emerge.

2.5.2 Alternative Aerodynamic Configurations

Since the multi-TW states were only found for a narrow region of the aerodynamic intensity, two different distributions of aerodynamic damping were explored. These configurations are presented in Fig. 2.24, where the label "baseline" corresponds to the one analyzed in the previous part of the chapter.

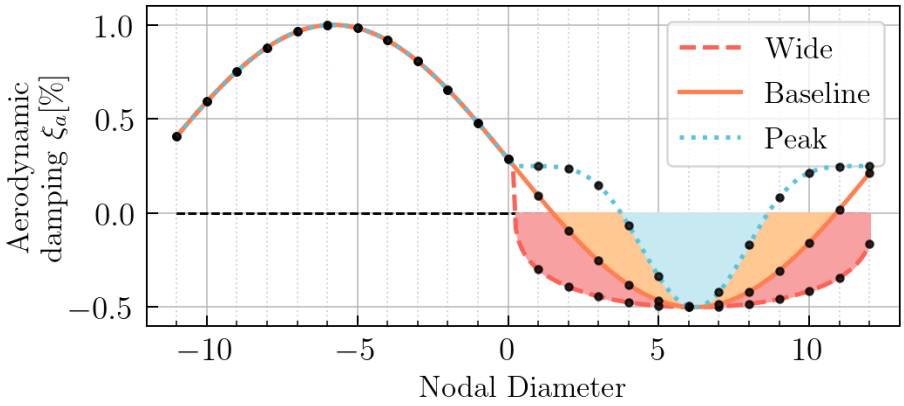

Figure 2.24: Aerodynamic damping configurations.

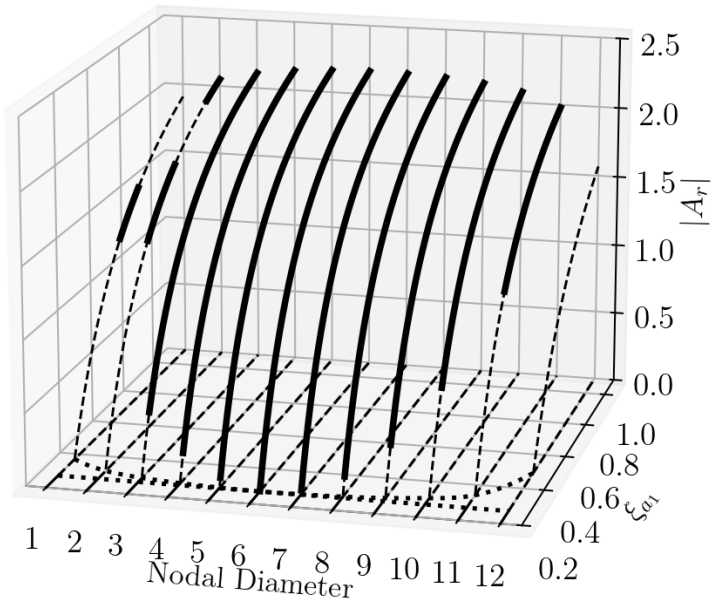

Figure 2.25: Bifurcation diagram of all the single-TW solutions with respect to the aerodynamic intensity parameter ξ_{a_1} for the wide distribution. Solid (dashed) lines represent stable (unstable) solutions.

The two alternatives are denoted as "wide", in which there are several more unstable modes with higher instability and "peak", where only a narrow band of modes is unstable.

From the two cases, only the wide distribution produced multi-TW states, which is the one analyzed here. Fig. 2.25 contains the bifurcation diagram, where now there are more single-TW states with a larger stable region. There are even some TWs that exhibit several changes

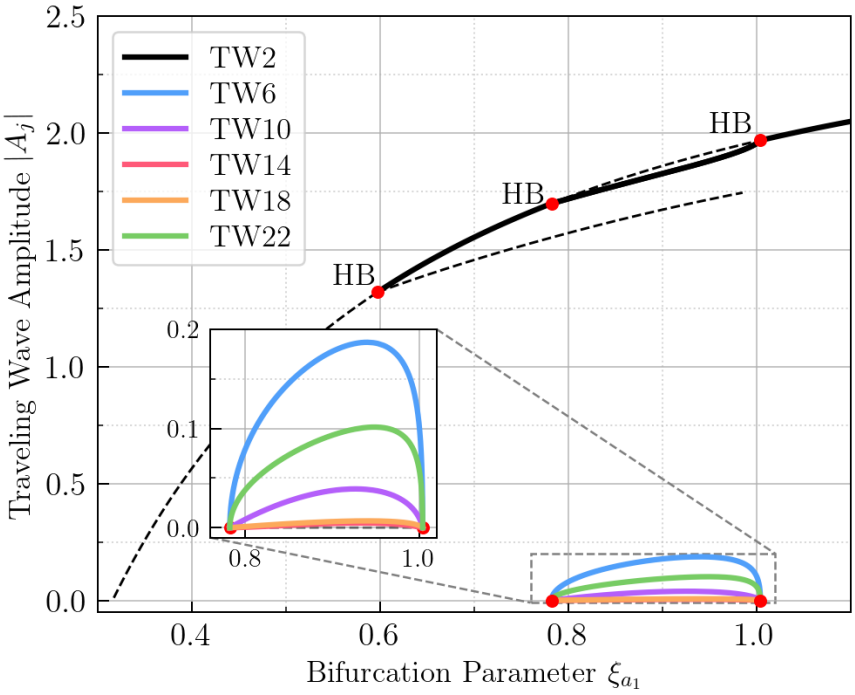

Figure 2.26: Bifurcation diagram of the TW2 solution with respect to the aerodynamic intensity parameter ξ_{a_1} for the wide distribution. A solution branch, emerging from the single-TW state, is found with multi-TW contributions. Solid (dashed) lines represent stable (unstable) solutions.

in stability, like TW1 and TW2. Overall, the bifurcation diagram looks relatively similar to the one of the baseline configuration (Fig. 2.15).

The changes in stability are also HB in this case, and the continuation is carried out with the same software as before. Multi-TW stable states were also found, bifurcating from the single-TW2 solution, as shown in Fig. 2.26. From the first HB, an unstable branch emerges, corresponding to not achievable final states for the system. Nevertheless, from the second HB, a stable branch of solutions emerges, and it connects with the third HB. This branch of solutions corresponds to a multi-TW state, in which the amplitude of TW2 is slightly less than the single-TW counterpart, but the other TW modes again grow in amplitude, as highlighted at the bottom of the plot.

In terms of physical displacements, Fig. 2.27 shows that the shape is also a non-uniform traveling wave, where the new period from this solution is related to the propagation around the bladed-disk. The maximum amplitude of the blade displacements is still smaller than that of the single-TW6 solution, but only slightly, as shown in Table 2.2, with a relative difference of 2.7%.

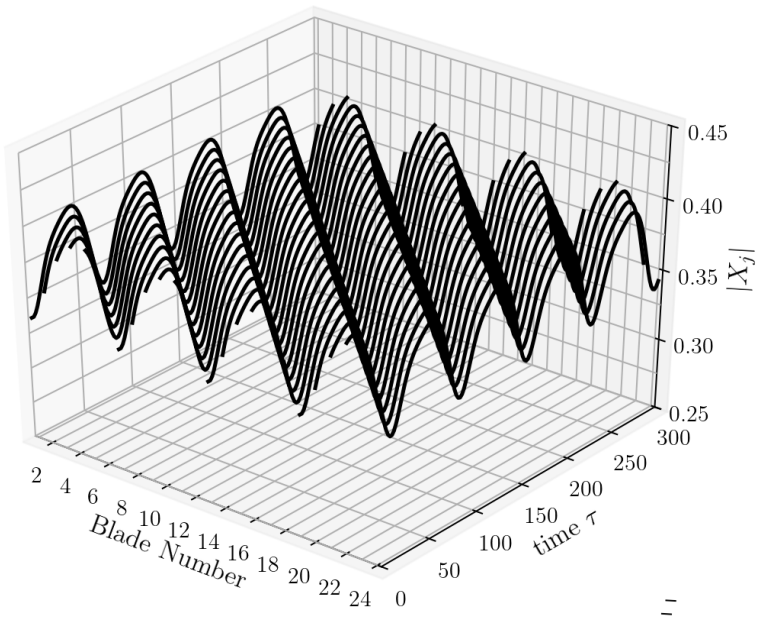

Figure 2.27: Blade displacements of the multi-TW solution emerging for the wide distribution.

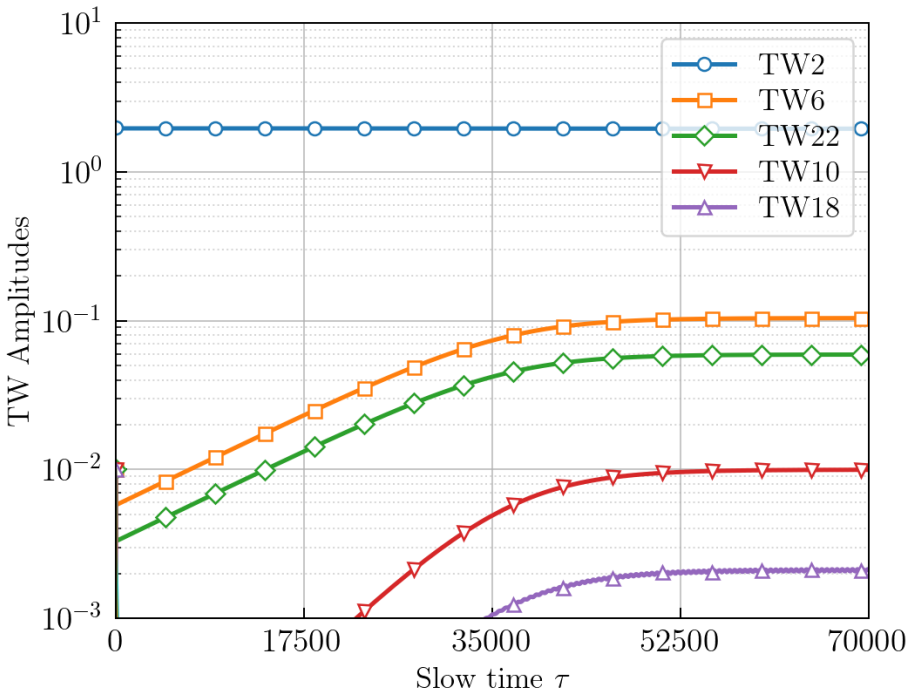

Figure 2.28: Time evolution of the TW amplitudes from the asymptotic model of the wide distribution starting from an initial condition of single-TW2 and a small perturbation for the other TW modes of $A_j = 0.01$ with $\xi_{a_1} = 0.9$.

Table 2.2: Maximum blade displacement comparison for the wide aerodynamic configuration.

Multi-TW	TW6	Relative Difference
0.4	0.411	2.7%

Finally, to verify the bifurcation diagram, time integration from a perturbation of the single-TW2 solution for $\xi_{a_1} = 0.9$ was also carried out in Fig. 2.28. Again, as obtained with the numerical continuation process, after a slow growth of the other TW modes, a stable multi-TW state is reached, that requires a very long integration time.

Chapter 3

Nonlinear Interaction of Flutter and Forced Response

During the operation of a jet engine, the rotor of a LPT is usually subjected to an external forcing. The wakes generated by the vanes of the stator are seen as a periodic forcing from the rotating frame of reference of the rotor. This forcing has the form of a TW, which could produce an amplified response when the frequency is close to a resonance crossing.

This effect can appear alongside flutter, which was analyzed in the previous chapter. Although both phenomena are of aerodynamic origin, they are completely different physical mechanisms. Flutter is a self-excited instability in which the aerodynamic forces are produced by the vibration of the blades. On the other hand, the excitation due to the wakes of the stator corresponds a forced response problem.

The simultaneous presence of both effects can be quite common in modern turbomachinery designs. A simple analysis is to compute the response due to both effects separately, and then superimpose them to obtain the total vibration. However, because of the nonlinear friction present at the fir-tree, this linear superposition often overestimates the real amplitude of the response in the system.

An initial assessment of this phenomenon was carried out in [116], where the feasibility of a blade-to-ground friction damper was analyzed with a 1 DOF model, seeking solutions synchronous with the forcing. The combination of flutter and forced response with nonlinear friction effects was also analyzed in [52] using time integration of a mass-spring system resembling the first modal family of a bladed-disk. The results for the frequency response curve showed that, sufficiently close to the resonance frequency, the system is synchronous

with the forcing. In contrast, far from the resonance, the flutter frequency also appeared in the response.

This chapter extends the asymptotic model developed in the previous chapter to account for the effects of the forced response, which translates into an additional term in the equations. The resonance curve solution is obtained analytically, and a stability analysis is performed. Then, from the points of stability change, numerical continuation is carried out to compute the bifurcation diagram of the system under different EOs of excitation.

3.1 Asymptotic equations

The mass-spring system used to model the bladed-disk is the same from Chapter 2, with the addition of an external forcing acting on each blade, as shown in Figure 3.1. The aerodynamic, friction and structural characteristics are exactly the same as in Chapter 2, with the same number of blades, $N = 24$.

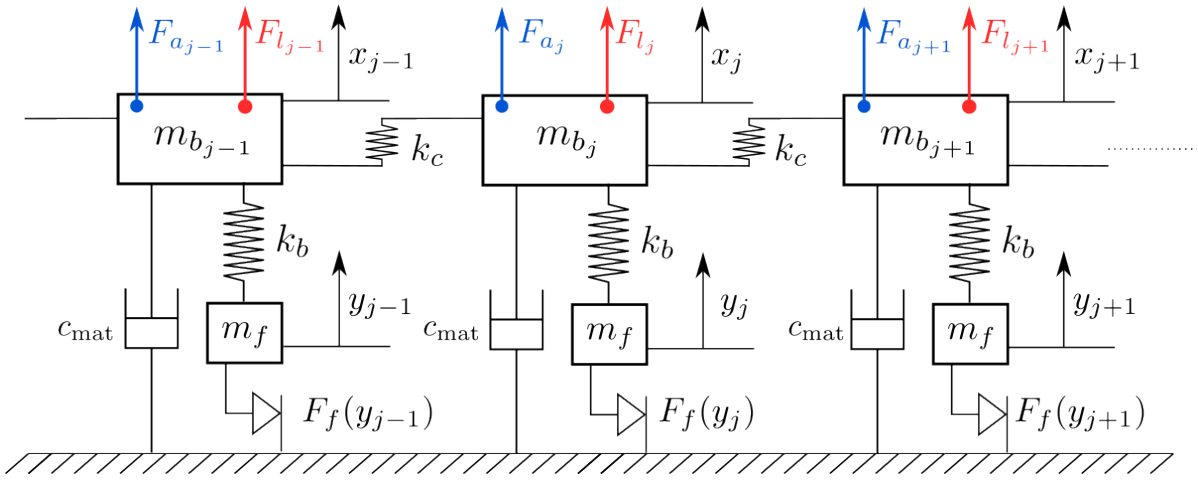

Figure 3.1: Mass-spring model representing a single family of a bladed-disk with nonlinear friction and external forcing.

The equations of motion, in dimensionless form, are completely similar to Eq. (2.3),

$$\begin{aligned} \ddot{\tilde{\mathbf{x}}} + 2\xi_{\text{mat}}\dot{\tilde{\mathbf{x}}} + (\tilde{\mathbf{x}} - \theta\tilde{\mathbf{y}}) + \tilde{\mathbf{K}}_c\tilde{\mathbf{x}} + \tilde{\mathbf{F}}_a(\tilde{\mathbf{x}}, \dot{\tilde{\mathbf{x}}}) &= \tilde{\mathbf{F}}_l, \\ \gamma\theta\ddot{\tilde{\mathbf{y}}} + (\theta\tilde{\mathbf{y}} - \tilde{\mathbf{x}}) + \tilde{\mathbf{F}}_f(\tilde{\mathbf{y}}) &= 0, \end{aligned} \tag{3.1}$$

with the inclusion of the forcing vector $\tilde{\mathbf{F}}_l$ on the right-hand side of the block of equations corresponding to blade displacements. This forcing has the form of a TW with a fixed EO,

which is expressed as

$$\tilde{\mathbf{F}}_l = \begin{pmatrix} e^{i\left(\frac{2\pi \mathrm{EO}}{N}\right)1} \\ \vdots \\ e^{i\left(\frac{2\pi \mathrm{EO}}{N}\right)N} \end{pmatrix} \tilde{F} e^{i\tilde{\omega}_f T}, \tag{3.2}$$

where $\tilde{F}$ is the amplitude of the forcing and $\tilde{\omega}_f$ the forcing frequency. Since the forced response analysis will be carried out for a frequency sweep close to the resonance frequency of the system, we expand $\tilde{\omega}_f = 1 + \Delta\tilde{\omega}_f\theta$, to rewrite the forcing as

$$\tilde{\mathbf{F}}_l = \begin{pmatrix} e^{i\left(\frac{2\pi \mathrm{EO}}{N}\right)1} \\ \vdots \\ e^{i\left(\frac{2\pi \mathrm{EO}}{N}\right)N} \end{pmatrix} \tilde{F} e^{i\Delta\omega_f \tau} e^{iT}, \tag{3.3}$$

where the slow timescale τ appears now explicitly. Following the same derivation for the asymptotic model from Chapter 2, this term would appear in Eq. (2.26). Then, since it is also proportional to e^{iT}, it has to be included in the solvability condition, and the forcing term from Eq. (3.3) appears directly in the evolution equation of the slow envelope.

In the TW basis, after factoring out the e^{iT}, the forcing takes the form

$$\mathbf{E}^H \tilde{\mathbf{F}}_l = \mathbb{1}_{\mathrm{EO}} \tilde{f} e^{i\Delta\omega_f \tau}, \tag{3.4}$$

where $\mathbb{1}_{\mathrm{EO}}$ is a vector with all elements equal to zero except for a 1 at the index equal to the EO of the excitation, and $\tilde{f}$ is the modal amplitude of the forcing. Therefore, after adding this term to the asymptotic Eq. (2.33), the system takes now the form

$$\begin{aligned} \frac{\mathrm{d}}{\mathrm{d}\tau} \begin{pmatrix} A_1 \\ \vdots \\ A_N \end{pmatrix} = &- \frac{i}{2} \mathbf{E}^H \begin{pmatrix} Q(|X_1|) & \dots & 0 \\ \vdots & \ddots & \vdots \\ 0 & \dots & Q(|X_N|) \end{pmatrix} \mathbf{E} \begin{pmatrix} A_1 \\ \vdots \\ A_N \end{pmatrix} \\ &+ \begin{pmatrix} -\tilde{\xi}_1 + i\tilde{\omega}_1 & \dots & 0 \\ \vdots & \ddots & \vdots \\ 0 & \dots & -\tilde{\xi}_N + i\tilde{\omega}_N \end{pmatrix} \begin{pmatrix} A_1 \\ \vdots \\ A_N \end{pmatrix} - \frac{i}{2} \tilde{f} e^{i\Delta\tilde{\omega}_f \tau} \mathbb{1}_{\mathrm{EO}}. \end{aligned} \tag{3.5}$$

The main difference from this set of equations to the ones with just the aerodynamic effect of flutter is that the system is no longer homogeneous. Hence, the trivial state (no blade vibration) with $A_j = 0$ for all j is no longer a solution of the system.

A relevant parameter for the analysis of this section is the EO of the excitation, since the excited TW could be unstable or stable in terms of flutter. To have a broad analysis of all

the possible cases, in this chapter we will focus on three different EOs, which are highlighted in Fig. 3.2: (A) a slightly aerodynamically unstable TW2; (B) the most unstable TW mode, TW6; and (C) one of the most aerodynamically stable modes, TW19 = TW − 5 (mod 24).

The other two parameters introduced with the forcing are the amplitude of the excitation and the forcing frequency. The amplitude, $\tilde{f}$, due to the presence of nonlinear effects, is expected to produce a maximum amplitude of the response that does not scale linearly with this parameter. The frequency of the forcing, $\Delta\tilde{\omega}_f$, will be used as the bifurcation parameter in the continuation, and the aerodynamic intensity will be fixed to $\xi_{a_1} = 0.75$, corresponding to Fig. 3.2.

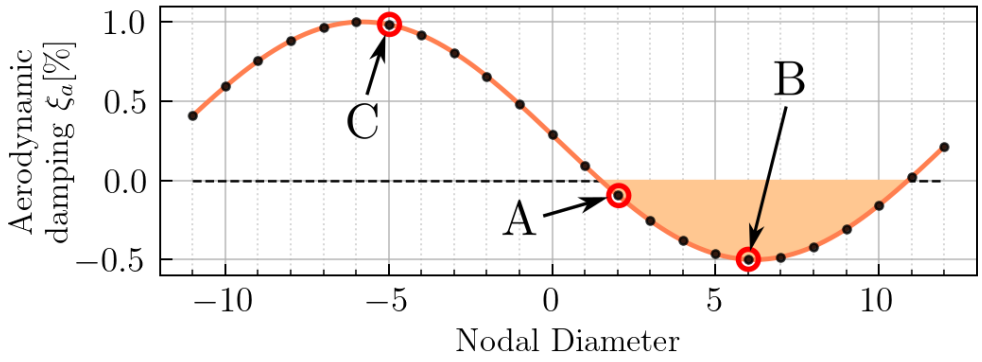

Figure 3.2: Aerodynamic damping of the system. The selected EOs of excitation for the analysis are A, B, and C, which are highlighted with a red circle.

3.2 Time Simulation Analysis

The response of the system for a fixed forcing frequency $\Delta\tilde{\omega}_f$ can be obtained by performing numerical integration of Eq. (3.5) with a time span long enough to converge to a periodic (or a more complicated) state.

To provide an initial assessment on the effect of the combination of flutter and forced response under nonlinear forces, the system will be integrated in time and compared with the resonance curve resulting from a response completely synchronous with the forcing. The analytical expression of the resonance curve is given in Section 3.3, although here will be used to compare with the final state obtained using time integration.

Additionally, since Eq. (3.5) admits just a single TW solution, where $A_{\text{EO}} \neq 0$ and $A_j = 0$ for $j \neq \text{EO}$, a simplified system with just the equation of the excited TW will be integrated. For this analysis the forcing amplitude is set to $\tilde{f} = 0.5$

3.2.1 Single Traveling Wave Analysis

The assumption of just considering the differential equation in (3.5) associated to the EO of the excitation has the consequence that flutter solutions are only possible when the excited mode is unstable (shaded region in Fig. 3.2).

(A) Aerodynamically unstable TW2

The frequency sweep is first performed when the forced mode is the aerodynamically unstable TW2, and the results are shown in Fig. 3.3. For several frequency values the system has been integrated, and the maximum blade displacements have been computed when the final state is reached. These points are highlighted with a square, and the resonance curve synchronous with the forcing is plotted with a solid blue line.

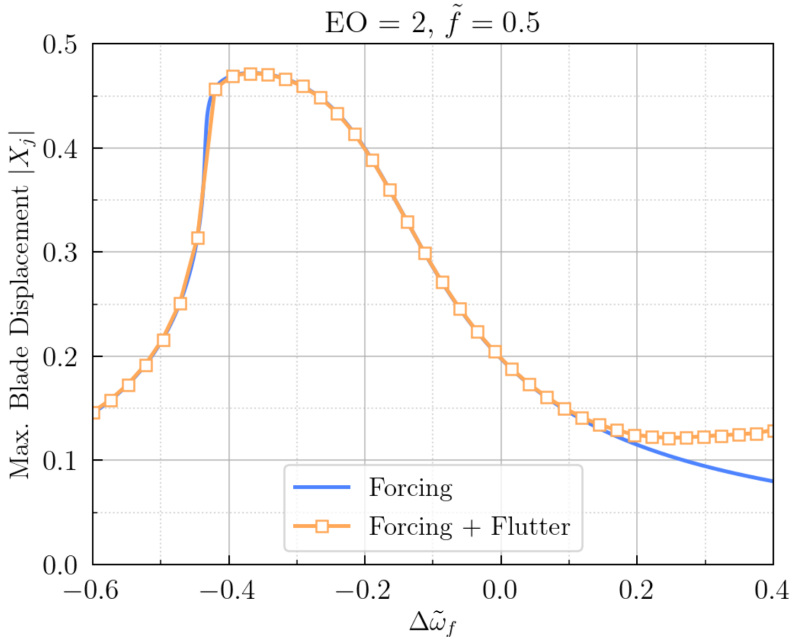

Figure 3.3: Maximum blade displacement as a function of the forcing frequency for a single TW system with a forcing of EO = 2.

For the synchronous solution, the typical resonance curve of a nonlinear oscillator is found. Time integration shows that this solution loses stability for values of the forcing frequency far from the resonance, since a solution where the flutter frequency is also present arises. Nevertheless, close to the resonance peak, the synchronous solution is stable, and the flutter frequency is completely absent from the dynamics.

(B) Aerodynamically unstable TW6

Now, we turn our attention to the most unstable aerodynamic TW, plotting the results in

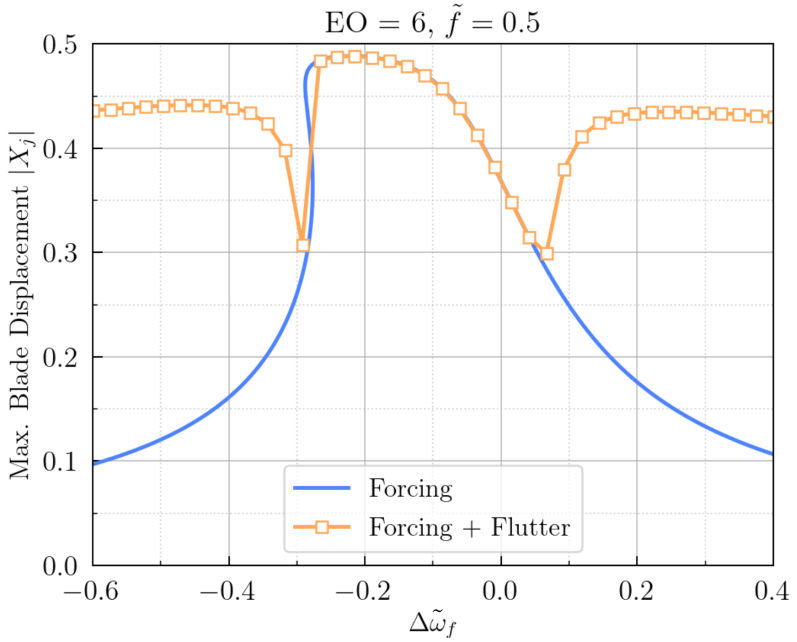

Figure 3.4: Maximum blade displacement as a function of the forcing frequency for a single TW system with a forcing of EO = 6.

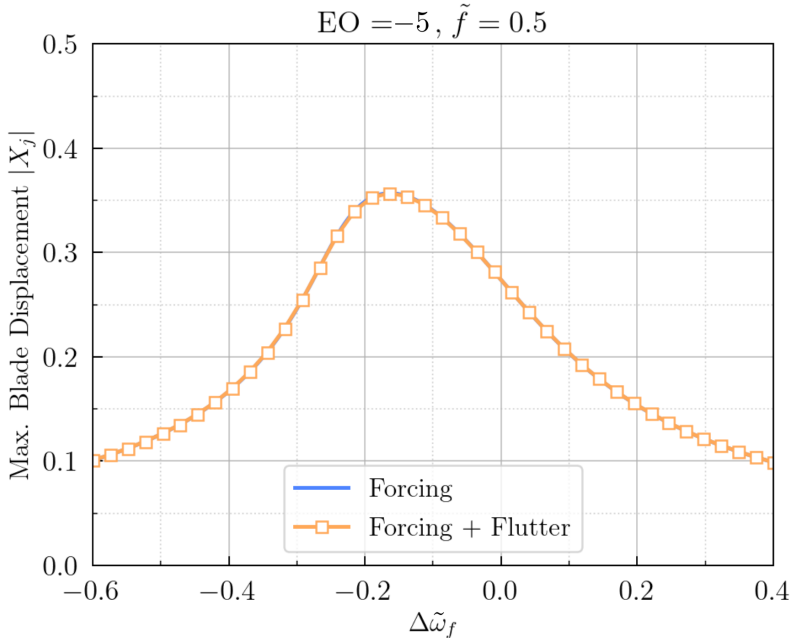

Figure 3.5: Maximum blade displacement as a function of the forcing frequency for a single TW system with a forcing of EO = −5.

Fig. 3.4. The behavior is similar to the previous case, where close to the resonance peak the synchronous solution is stable, although the amplitude of the response is now larger due to the higher instability level. As one moves away from the resonance peak, flutter saturated

solutions of TW6 emerge, with a larger amplitude than the ones from TW2, verifying the predictions from Fig. 2.15, which showed that the most unstable TW exhibited the largest amplitude of vibration.

(C) Aerodynamically stable TW−5

When the forcing is applied to an aerodynamically stable mode, such as TW−5, a flutter solution cannot be produced in the single TW system. Therefore, the stable solution to which the system evolves is just the resonance curve of the solutions locked to the forcing frequency, as shown in Fig. 3.5.

3.2.2 Full System

Time integration, for the same points presented above, is performed for the full asymptotic equations (3.5), with all TW modes included. The analysis is repeated for the same three cases, although significant differences are expected since the system could now develop solutions containing TWs different from the excited one.

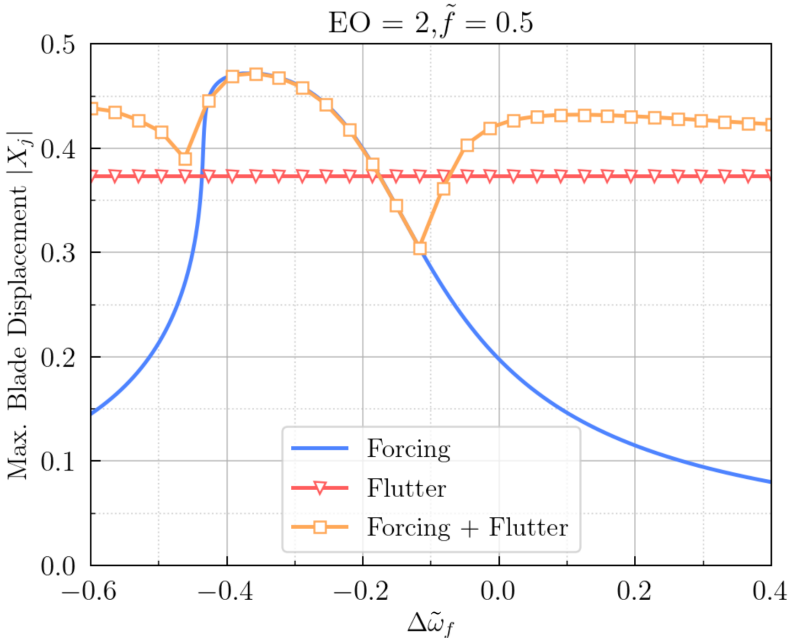

Figure 3.6: Maximum blade displacement as a function of the forcing frequency with a forcing of EO = 2.

(A) Aerodynamically unstable TW2

Figure 3.6 shows the resonance curve for EO = 2. Compared to the single TW system in Fig. 3.3, the solution periodic with the forcing loses stability earlier due to the presence of

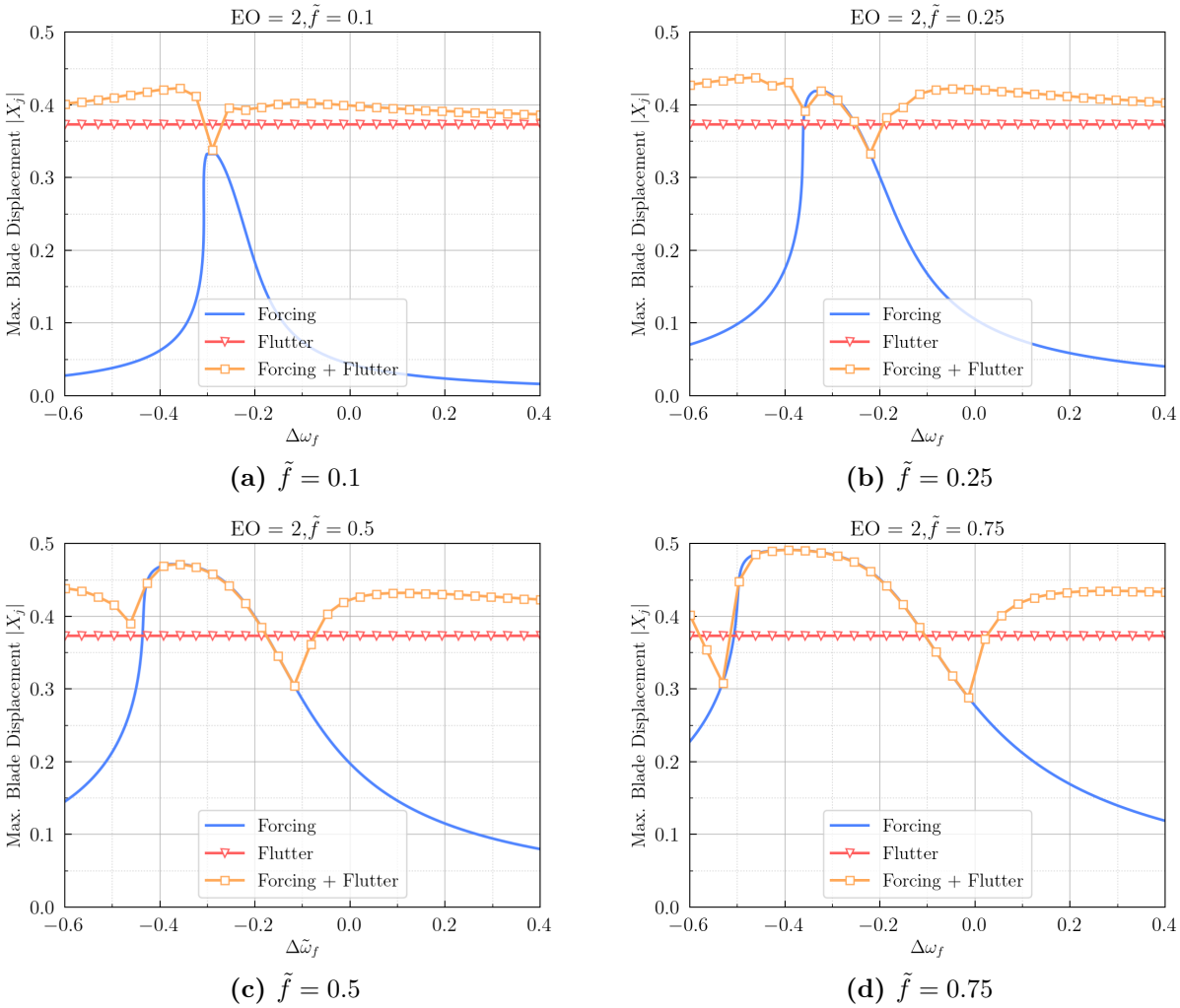

(a) $\tilde{f} = 0.1$ **(b)** $\tilde{f} = 0.25$

(c) $\tilde{f} = 0.5$ **(d)** $\tilde{f} = 0.75$

Figure 3.7: Maximum blade displacement as a function of the forcing frequency with a forcing of EO = 2. Several forcing amplitudes are included.

modes with a higher instability. Actually, the stable flutter solution that settles as a final state of the system corresponds to a more unstable TW mode (which in this case is TW6, as will also be discussed in the next section when computing the stability). To verify this fact, an additional line has been included in the plot, in red color, with the amplitude of vibration of the single-TW6 flutter saturated solution. It has been verified that, as one moves away from the resonance, the system evolves to this single-TW flutter solution, which corresponds to the ones computed from the bifurcation diagram in Fig. 2.15.

An additional exploration is performed for different values of the forcing amplitude $\tilde{f}$, to understand the effect of this parameter on the response of the system. The results are shown in Fig. 3.7. For smaller values of the forcing, $\tilde{f} = 0.1$, the stability of the synchronous solution is very narrow around the peak, and the flutter solutions are present for practically

all the frequency sweep. Then, as the value of the forcing increases, the region of stability of the synchronous solutions is enlarged, and the flutter solution emerges for frequencies further away from the resonance peak.

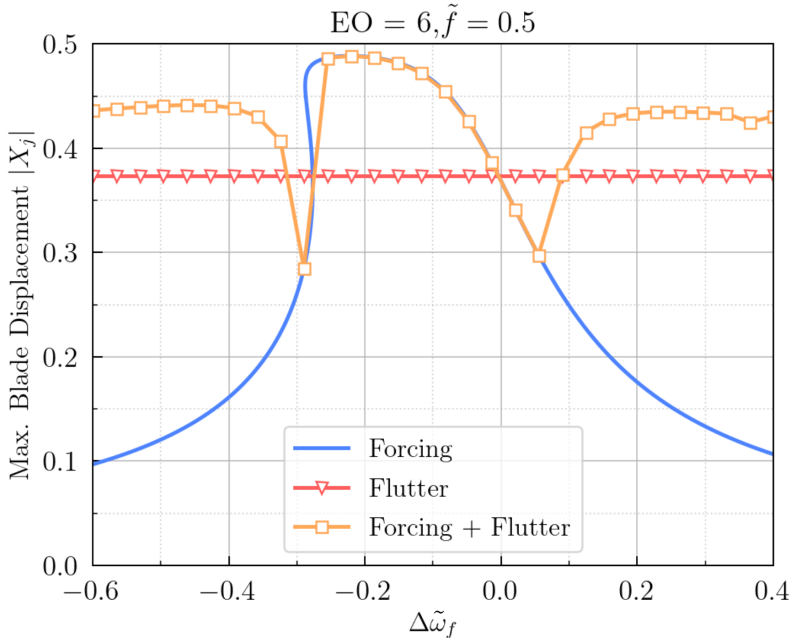

Figure 3.8: Maximum blade displacement as a function of the forcing frequency with a forcing of EO = 6.

(B) Aerodynamically unstable TW6

For the case EO = 6, we basically recover the results from the single TW system in Fig. 3.4. The resonance curve for the full system is plotted in Fig. 3.8, where the same effect of switching from a forced response solution to a flutter one away from the resonance is present. The convergence to the same flutter solution is expected because, as mentioned in the previous chapter, the most unstable single-TW appears to have the largest basin of attraction. The variation with the level of the forcing amplitude provides similar results to the ones from Fig. 3.7 and are not shown here. For the rest of the section, since the effect of the forcing amplitude is similar for all the EOs, the value of $\tilde{f} = 0.5$ will remain fixed.

(C) Aerodynamically stable TW−5

The excitation of a stable mode, such as TW−5, gives rise to new dynamics induced by the nonlinear friction, as shown in Fig. 3.9. First, due to the presence of unstable modes, this solution loses stability away from the resonance peak (this did not occur in the single TW system plotted in Fig. 3.5). In addition, a new branch of solutions emerges at the resonance, which was not present when the excited TW was aerodynamically unstable. This branch

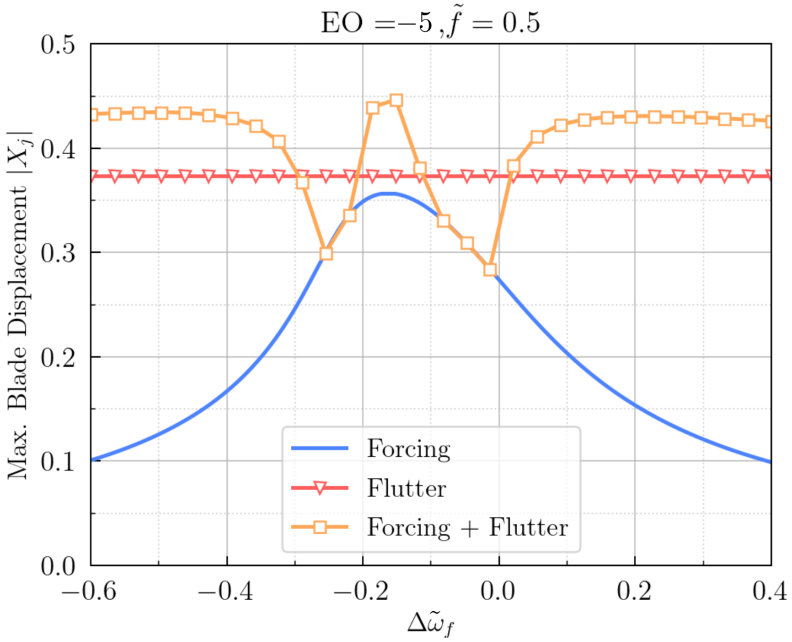

Figure 3.9: Maximum blade displacement as a function of the forcing frequency with a forcing of EO = −5.

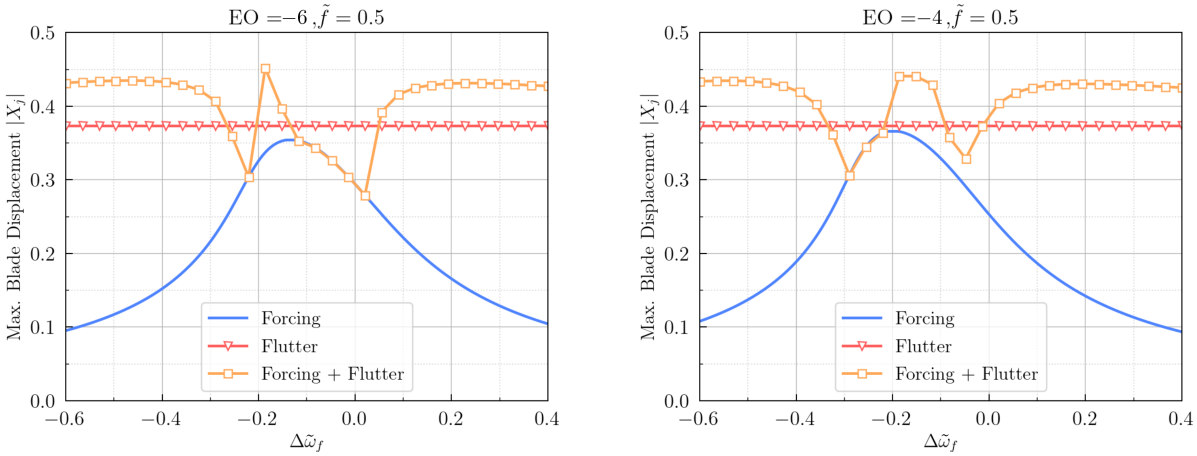

(a) EO = −6 **(b)** EO = −4

Figure 3.10: Maximum blade displacement as a function of the forcing frequency.

corresponds to a synchronous solution with the forcing, but composed with two different TWs, the one that is directly forced and an unstable mode, and it will be thoroughly analyzed in Section 3.3

To verify that this solution does not only occur for this EO of excitation, an exploration of the resonance crossing for EO = −6, −4 has been carried out. The results from Fig. 3.10 indicate that this solution branch is still present in the system, although a slight shift can be

seen around the resonance peak.

In the next section, these results are obtained again by computing the analytical expression of the periodic solution and its stability. Then, numerical continuation is performed to characterize the different states that appear at the stability changes.

3.3 Stability Analysis and Continuation

The bifurcation diagram and stability analysis of the system will be carried out starting from the synchronous to the forcing frequency. Before the formal study, similarly to the procedure used for the flutter solutions, we first introduce the change of variable

$$\begin{pmatrix} A_1 \\ \vdots \\ A_N \end{pmatrix} = \sqrt{N} \begin{pmatrix} B_1 \\ \vdots \\ B_N \end{pmatrix} e^{i\Delta\tilde{\omega}_f \tau}, \tag{3.6}$$

in Eq. (3.5) to turn the periodic solutions locked to the forcing frequency $\Delta\tilde{\omega}_f$ into steady solutions. The resulting system of equations takes the form

$$\begin{aligned} \frac{\mathrm{d}}{\mathrm{d}\tau} \begin{pmatrix} B_1 \\ \vdots \\ B_N \end{pmatrix} = &- \frac{i}{2} \mathbf{E}^H \begin{pmatrix} Q(|X_1|) & \dots & 0 \\ \vdots & \ddots & \vdots \\ 0 & \dots & Q(|X_N|) \end{pmatrix} \mathbf{E} \begin{pmatrix} B_1 \\ \vdots \\ B_N \end{pmatrix} \\ &+ \begin{pmatrix} -\tilde{\xi}_1 + i(\tilde{\omega}_1 - \Delta\tilde{\omega}_f) & \dots & 0 \\ \vdots & \ddots & \vdots \\ 0 & \dots & -\tilde{\xi}_N + i(\tilde{\omega}_N - \Delta\tilde{\omega}_f) \end{pmatrix} \begin{pmatrix} B_1 \\ \vdots \\ B_N \end{pmatrix} - \frac{i}{2\sqrt{N}} \tilde{f} \mathbb{1}_{\mathrm{EO}}. \end{aligned} \tag{3.7}$$

Following the same methodology as in the previous section, the analysis will be divided into two parts. First, the stability of the solution consisting of a single TW is studied, and then the full system is considered.

3.3.1 Single Traveling Wave Analysis

System (3.7) admits solutions with the same wavenumber EO of the forcing. These solutions have only one amplitude different from zero, $B_{\mathrm{EO}} \neq 0$ and the rest satisfy $B_j = 0$. Using this assumption, every displacement $|X_j|$ is equal, so the nonlinear part of the system of

equations is diagonal, and we just get the differential equation

$$\frac{\mathrm{d}B_{\mathrm{EO}}}{\mathrm{d}\tau} = -\frac{i}{2}Q(|X|)B_{\mathrm{EO}} + \left(-\tilde{\xi}_{\mathrm{EO}} + i(\tilde{\omega}_{\mathrm{EO}} - \Delta\tilde{\omega}_f)\right) B_{\mathrm{EO}} - \frac{i}{2\sqrt{N}}\tilde{f}, \tag{3.8}$$

for the evolution of the excited TW mode. This simplified model can be viewed as analyzing just the directly forced TW while setting the rest to zero. The solution of this differential equation could lose stability when considering the full system, since the nonlinear friction could induce a coupling between the different TW modes.

A very important remark related to Eq. (3.8) is that the equation is no longer invariant under a change in phase $B_{\mathrm{EO}} \nrightarrow B_{\mathrm{EO}}e^{i\varphi}$. This is due to the presence of the forcing term, which removes this symmetry from the system. Regarding the continuation procedure, this means that this complex equation can be used directly, since now there is not a persistent zero eigenvalue in the jacobian of the system, as it happened when analyzing the flutter solutions in Chapter 2.

For the numerical continuation of Eq. (3.8), this problem is cast into real and imaginary parts, obtaining

$$\frac{\mathrm{d}}{\mathrm{d}\tau}\begin{pmatrix} B^R_{\mathrm{EO}} \\ B^I_{\mathrm{EO}} \end{pmatrix} = \begin{pmatrix} Q^I(|X|)/2 - \tilde{\xi}_{\mathrm{EO}} & Q^R(|X|)/2 - (\tilde{\omega}_{\mathrm{EO}} - \Delta\tilde{\omega}_f) \\ -Q^R(|X|)/2 + (\tilde{\omega}_{\mathrm{EO}} - \Delta\tilde{\omega}_f) & Q^I(|X|)/2 - \tilde{\xi}_{\mathrm{EO}} \end{pmatrix} \begin{pmatrix} B^R_{\mathrm{EO}} \\ B^I_{\mathrm{EO}} \end{pmatrix} - \begin{pmatrix} 0 \\ \frac{\tilde{f}}{2\sqrt{N}} \end{pmatrix}. \tag{3.9}$$

Since the use of the jacobian is also advisable for high accuracy computation of the bifurcation points and continuing the new branches, its derivation is provided in Appendix C.1.

The forced response curve can actually be computed analytically. The resonance curve solution corresponds to a steady solution of system (3.8). This state is found by looking for solutions of the form $B_{\mathrm{EO}} = |B_{\mathrm{EO}}|e^{i\varphi} = |X|e^{i\varphi}$, where the magnitude of displacements $|X|$ is the same for each blade. Introducing this *ansatz* into Eq. (3.8), and taking $\mathrm{d}|X|/\mathrm{d}\tau = 0$, one gets

$$\frac{i}{2}Q(|X|) + \tilde{\xi}_{\mathrm{EO}} - i(\tilde{\omega}_{\mathrm{EO}} - \Delta\tilde{\omega}_f) = -\frac{i}{2|X|\sqrt{N}}\tilde{f}e^{-i\varphi}, \tag{3.10}$$

which is a complex algebraic equation. Taking the complex absolute value of both sides, and solving for the $\Delta\tilde{\omega}_f$, one gets the implicit expression of the resonance curve

$$\Delta\tilde{\omega}_f = \left(\tilde{\omega}_{\mathrm{EO}} - \frac{1}{2}Q^R(|X|)\right) \pm \sqrt{\left(\frac{\tilde{f}}{2|X|\sqrt{N}}\right)^2 - \left(\tilde{\xi}_{\mathrm{EO}} - \frac{1}{2}Q^I(|X|)\right)^2}. \tag{3.11}$$

The phase of the solution can also be obtained by equating the arguments on both sides of

the equation, giving

$$\varphi = \arctan\left(\frac{-\xi_{\mathrm{EO}} + \frac{1}{2}Q^I(|X|)}{\tilde{\omega}_{\mathrm{EO}} - \Delta\tilde{\omega}_f - \frac{1}{2}Q^R(|X|)}\right). \tag{3.12}$$

The resonance curve from Eq. (3.11) provides an analytical expression for the forced response. This is an advantage of the asymptotic formulation, enabling the fast computation of the synchronous solution.

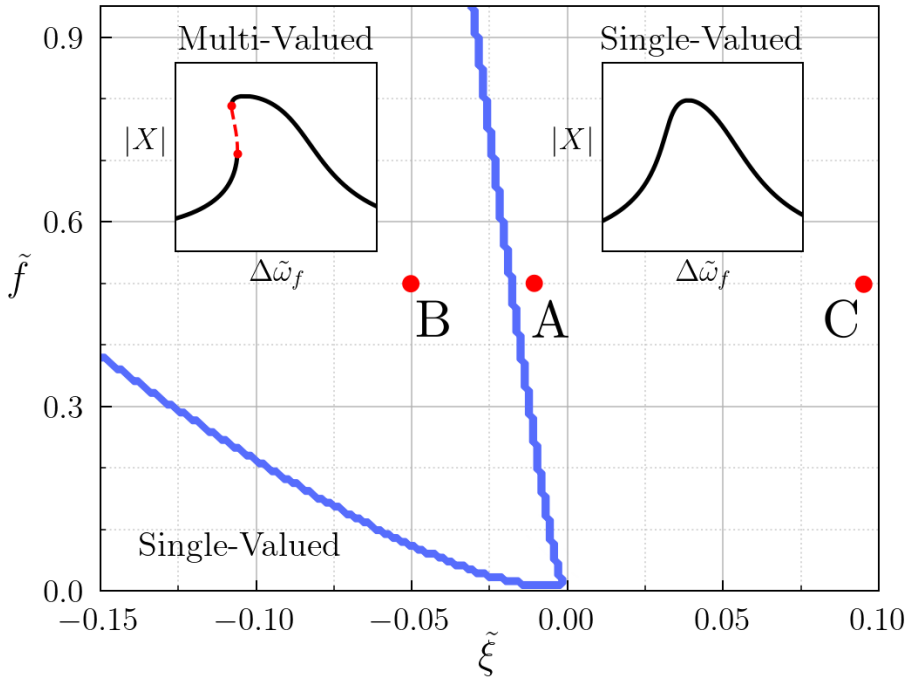

Figure 3.11: Separation between single-valued and multi-valued resonance curves in the $(\tilde{\xi}, \tilde{f})$ plane. The points A, B, C corresponds to the linear damping of the excited modes (Fig. 3.2).

Before computing the stability and follow different branches of solutions of the system, the presence of turning points in Eq. (3.11) is investigated. These points determine if there are hysteresis loops in the resonance curve, which produce sudden jumps in the amplitude of vibration of the system during a frequency sweep.

This condition is satisfied when $\mathrm{d}\Delta\tilde{\omega}_f/\mathrm{d}|X| = 0$, which yields the following nonlinear relation

$$Q^{R'} = \frac{\frac{\tilde{f}^2}{2N|X|^3} + \left(\frac{Q^I}{2} - \tilde{\xi}\right)Q^{I'}}{\sqrt{\left(\frac{\tilde{f}}{2|X|\sqrt{N}}\right)^2 - \left(\tilde{\xi} - \frac{1}{2}Q^I(|X|)\right)^2}}. \tag{3.13}$$

For several combinations of the linear damping and forcing $(\tilde{\xi}, \tilde{f})$, the boundary of the turning point region is determined, which separates single-valued from multi-valued resonance curves. The results are plotted in Fig. 3.11. From the three EO of excitation that were chosen (see Fig. 3.2), only the one corresponding to the most unstable TW6 (A) exhibits a multi-valued region where a hysteresis cycle is present. Point (B) is located very close to the boundary, but is single-valued. Finally, point (C), corresponding to one of the most stable TWs, is also single-valued.

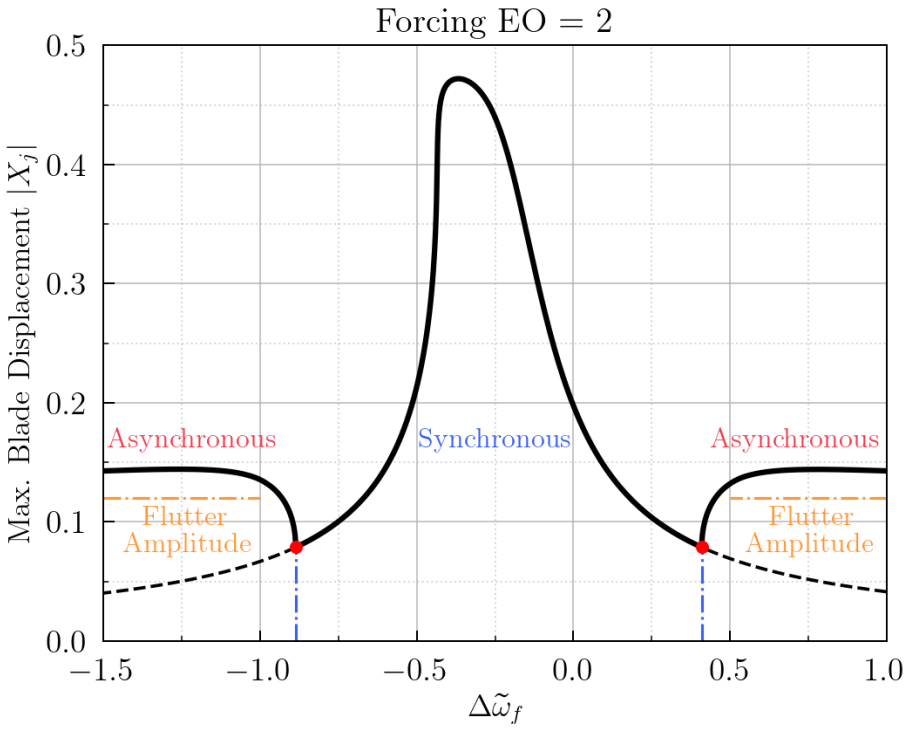

Figure 3.12: Bifurcation diagram of the single TW system with a forcing of EO = 2. Solid (dashed) lines represent stable (unstable) solutions.

Next, we compute the resonance curves with the analytical formulas and perform the continuation from the bifurcation points that appear in the solution branch.

(A) Aerodynamically unstable TW2

Figure 3.12 shows the bifurcation diagram for the slightly aerodynamically unstable TW2. The resonance curve, corresponding to a solution locked to the forcing frequency, is stable close to the resonance peak (solid line). Then, as one moves away from the resonance, a bifurcation point appears on each side (red dots). These points correspond to Hopf Bifurcations, which means that a new frequency appears in the emergent branches of the system.

The synchronous solution loses stability, which is transferred to the new branch, in which

the frequencies of forcing and flutter coexist in the dynamics of the system. As one tracks these branches far from the resonance, they tend to the single-TW2 flutter saturated solution. This is illustrated by highlighting the flutter amplitude of the single-TW solution in the plot. The results from the continuation are in total correspondence with the time domain analysis carried out in Fig. 3.3.

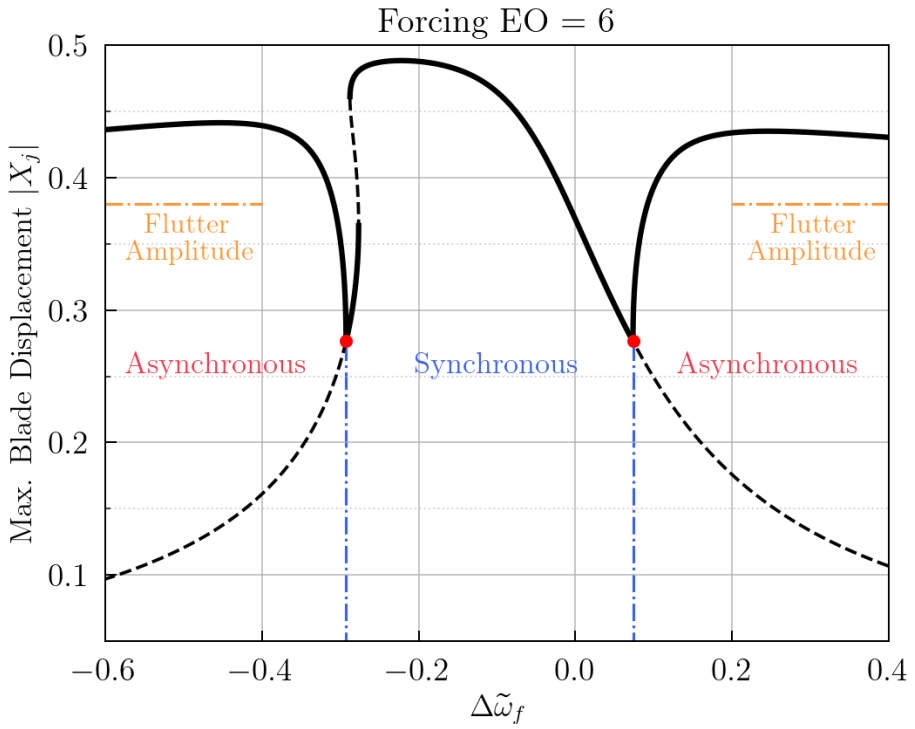

Figure 3.13: Bifurcation diagram of the single TW system with a forcing of EO = 6. Solid (dashed) lines represent stable (unstable) solutions.

(B) Aerodynamically unstable TW6

The most unstable TW6 exhibits a turning point in the resonance curve of the synchronous solution, as predicted, which is shown in Fig. 3.13. The stability of the forced response solution is more narrow than for TW2. The flutter solution that emerges has a much higher amplitude than in the previous case, since the instability level of TW6 is higher.

Then, following a similar picture to the previous case, the flutter branch of solutions evolves away from the resonance frequency until reaching the single-TW states that were determined in Fig. 2.15.

(C) Aerodynamically stable TW−5

The external excitation of a stable TW, in the single TW assumption, does not give rise to any flutter solutions, as shown in Fig. 3.14. Therefore, the solution curve corresponds

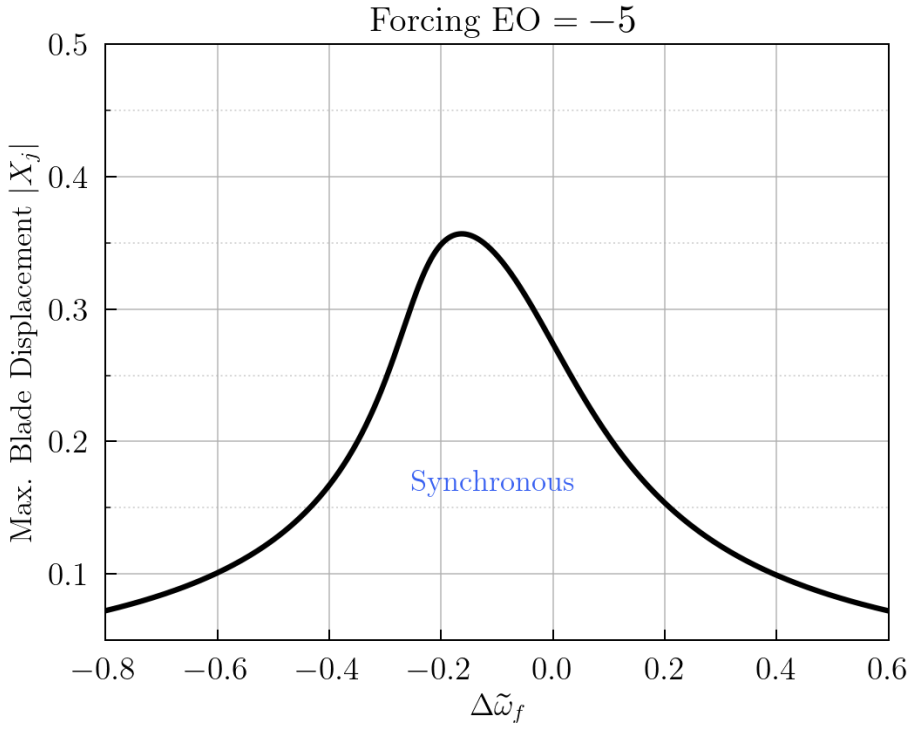

Figure 3.14: Bifurcation diagram of the single TW system with a forcing of EO = −5. Solid (dashed) lines represent stable (unstable) solutions.

to a state locked to the forcing frequency and stable in the entire frequency range that is analyzed.

3.3.2 Full System

The bifurcation diagram for the complete set of asymptotic equations (Eq. (3.7)) is presented for the same three cases from Fig. 3.2. The continuation is carried out from the system written in real variables, and the associated jacobian matrix is given in the Appendix C.2.

(A) Aerodynamically unstable TW2

TW2 is an unstable mode that can exhibit flutter, and the corresponding solution due to the instability was found when analyzing the single TW system. The resonance curve for the complete system exhibits a much narrower region of stability, as shown in Fig. 3.15. The system responds with the directly forced TW close to the resonance peak, with a solution locked to the forcing frequency. A time simulation for $\Delta\tilde{\omega}_f = -0.3$, corresponding to the peak of the resonance, has been carried out to check the stability of this solution. The results are shown in Fig. 3.16, where an initial condition of $A_j = 0.01$ was given to every TW component, and the system quickly evolves to the forced TW. Notice that the time required

to reach the final solution is much shorter than in the case with nonlinear selection of flutter saturated solutions presented in Chapter 2.

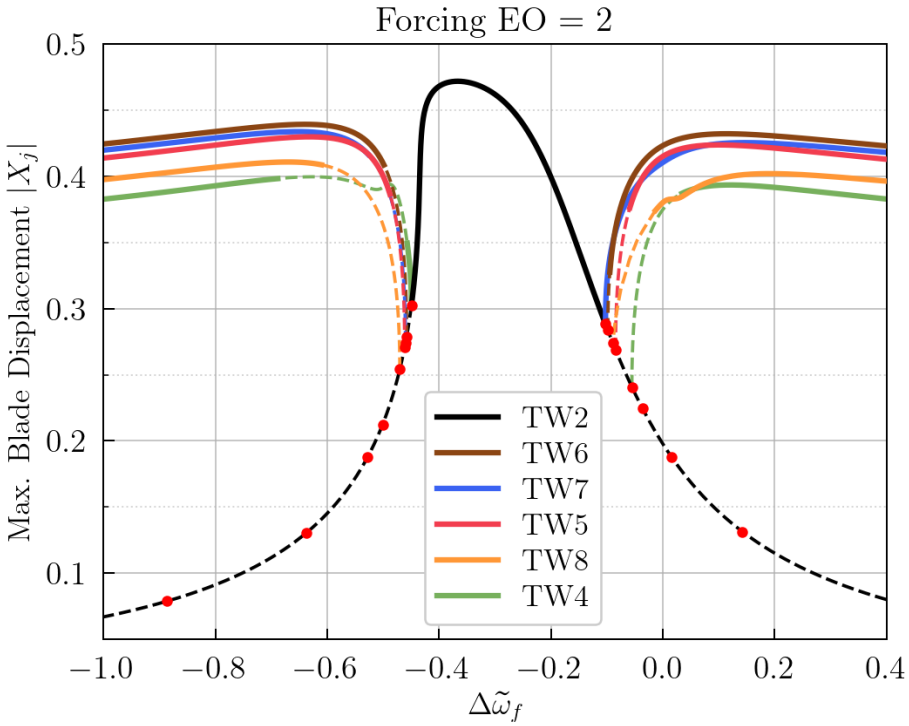

Figure 3.15: Bifurcation diagram of the full asymptotic model with a forcing of EO = 2. Solid (dashed) lines represent stable (unstable) solutions.

Coming back to the bifurcation diagram, as one moves away from the resonance several HB occur. Actually, there are as many HB as the number of aerodynamically unstable modes of the system (see Fig. 3.2).

Away from the resonance, the solution from the single TW system plotted in Fig. 3.12 is unstable in this case. Therefore, this solution is not a stable state when considering the all system modes for the current aerodynamic intensity value.

In contrast, since there were 5 stable saturated flutter solutions, from TW4 to TW8 (see Fig. 2.15), we expect to recover these solutions away from the resonance. For this reason, we show the branches of solutions emerging from the first 5 HB points closer to the resonance peak (the rest are not plotted since they are not stable). It is seen that the branch corresponding to the most unstable TW6 is stable for all the frequency range investigated. The other TWs begin with an unstable behavior until they stabilize far from the resonance. Along these branches, several Torus Bifurcations are found, but the states emerging from these points are not explored in this work.

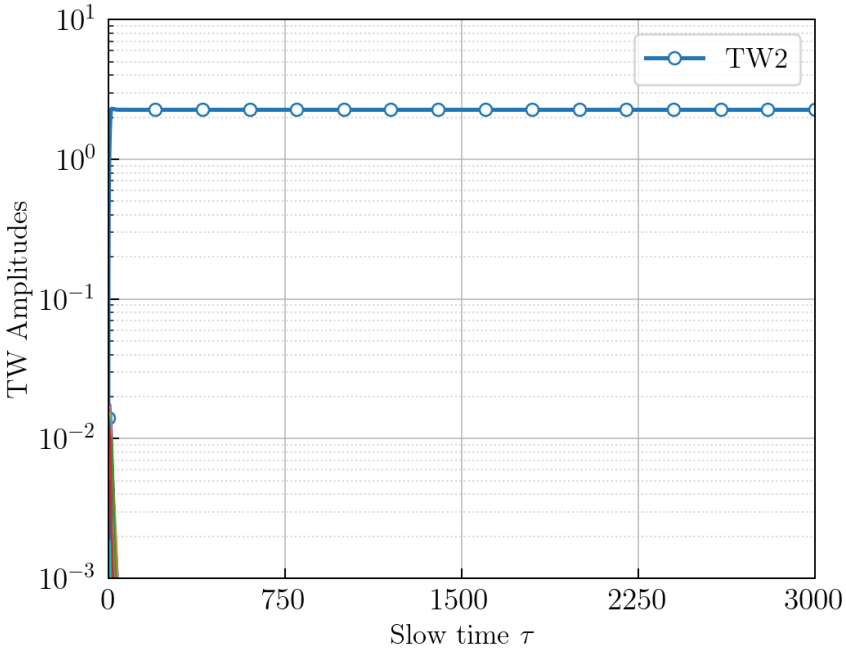

Figure 3.16: Time evolution of the TW amplitudes with an EO = 2 excitation with an initial condition of $A_j = 0.01$ and $\Delta\tilde{\omega}_f = -0.3$.

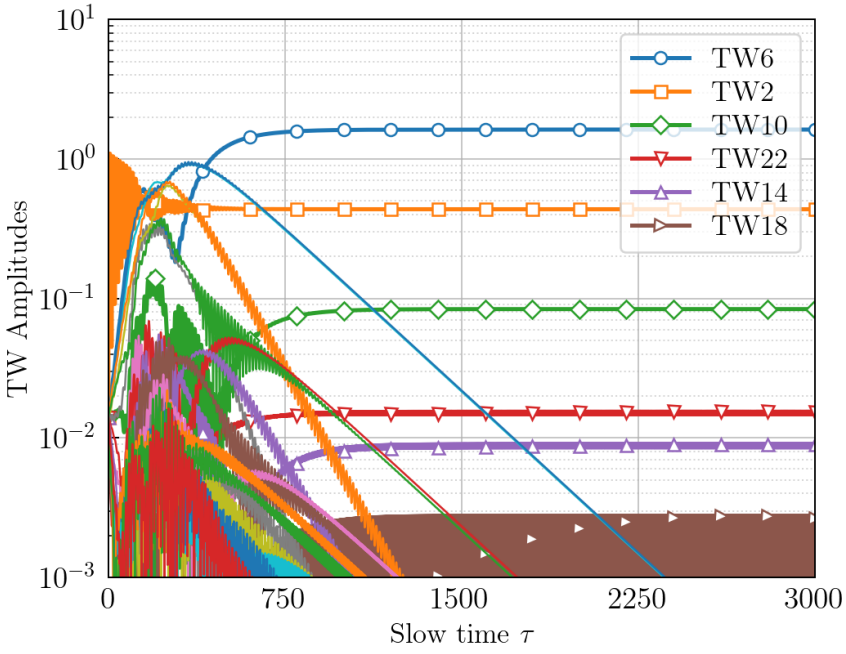

Figure 3.17: Time evolution of the TW amplitudes with an EO = 2 excitation with an initial condition of $A_j = 0.01$ and $\Delta\tilde{\omega}_f = 0.2$.

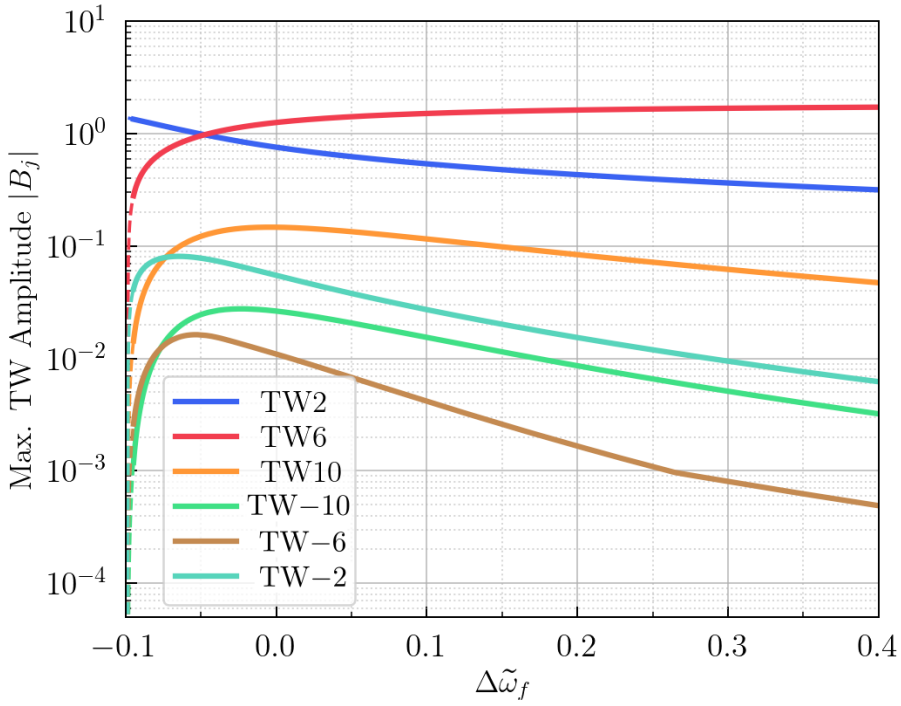

Figure 3.18: Evolution of the TW amplitudes for the flutter branch emerging from the resonance curve of the full system with EO = 2. This branch eventually corresponds to the single-TW6 flutter saturated solution.

The labels of the solution branches in Fig. 3.15 indicate the TW solution to which they will settle, eventually, after sweeping far enough from the resonance. Nevertheless, very close to the bifurcation point, these solutions are two frequency solutions and composed of many TWs, such as in the multi-TW solutions of the previous chapter. This fact can be observed directly by performing a time integration for $\Delta\tilde{\omega}_f = 0.2$, obtaining a multi-TW solution as shown in Fig. 3.17. We see that, for this forcing frequency value, which is still not too far from the bifurcation points, TW6 is dominating but the contribution of the forced TW2 and other TWs is also significant.

A more detailed look into the evolution of the TWs in the solution branch emerging from the resonance curve is given in Fig. 3.18. This is the solution that eventually corresponds to the single-TW6 flutter state. As it can be observed, close to the bifurcation (left side of the plot), only the TW2 component is present, and the others are negligible. Then, for increasing values of the forcing frequency, the other TW modes start growing until they reach a maximum, and start decaying exponentially. The only TW that remains growing and goes to a constant value is TW6, which is the single-TW solution that is reached in the end.

Therefore, the conclusion is that, due to the nonlinear effects, there is a switch between

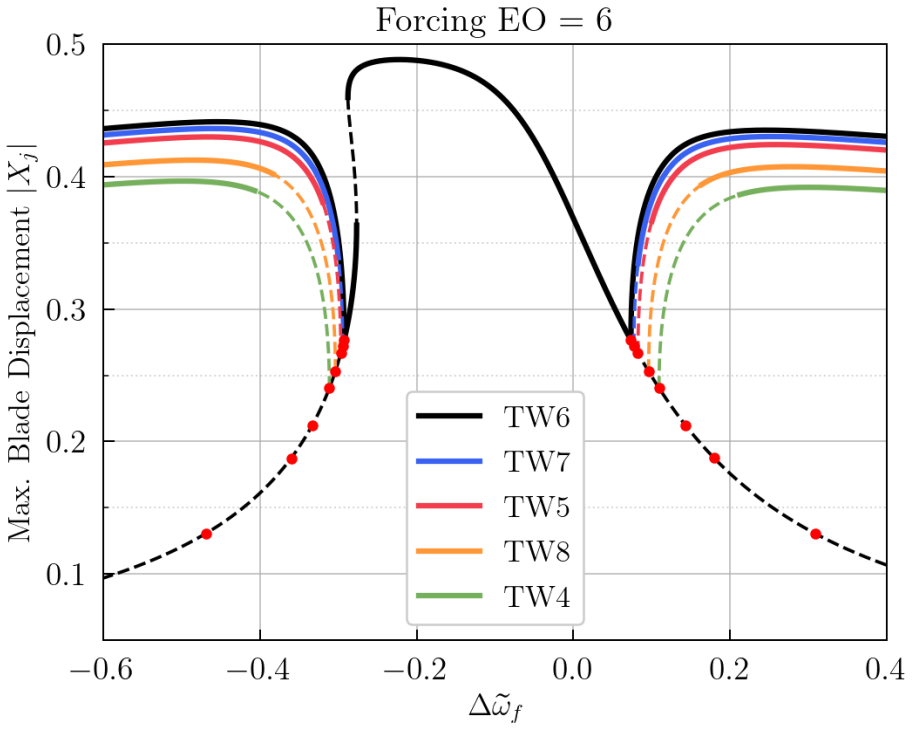

Figure 3.19: Bifurcation diagram of the full asymptotic model with a forcing of EO = 6. Solid (dashed) lines represent stable (unstable) solutions.

the state of the system where there is a vibration of the excited TW locked to the forcing frequency and the flutter solutions. Away from the resonance, in the region of the flutter dominated states, we see that every stable single-TW solution that was computed in Fig. 2.15 is recovered. Therefore, for suitable initial conditions, any of these states could be reached by the system.

(B) Aerodynamically unstable TW6

The bifurcation diagram of TW6 is very similar to TW2, as shown in Fig. 3.19. The region close to the resonance peak presents a solution with the directly excited TW locked to the forcing frequency, and then the stable single-TW flutter states emerge from the HB points. The directly forced TW6 also corresponds to the flutter solution with the highest amplitude in this case.

The branches related to other TWs have an unstable region close to the resonance, and then they gain stability as the effect of the forcing is suppressed far from the resonance peak.

(C) Aerodynamically stable TW−5

The bifurcation diagram when exciting a stable TW is very different from that of the single

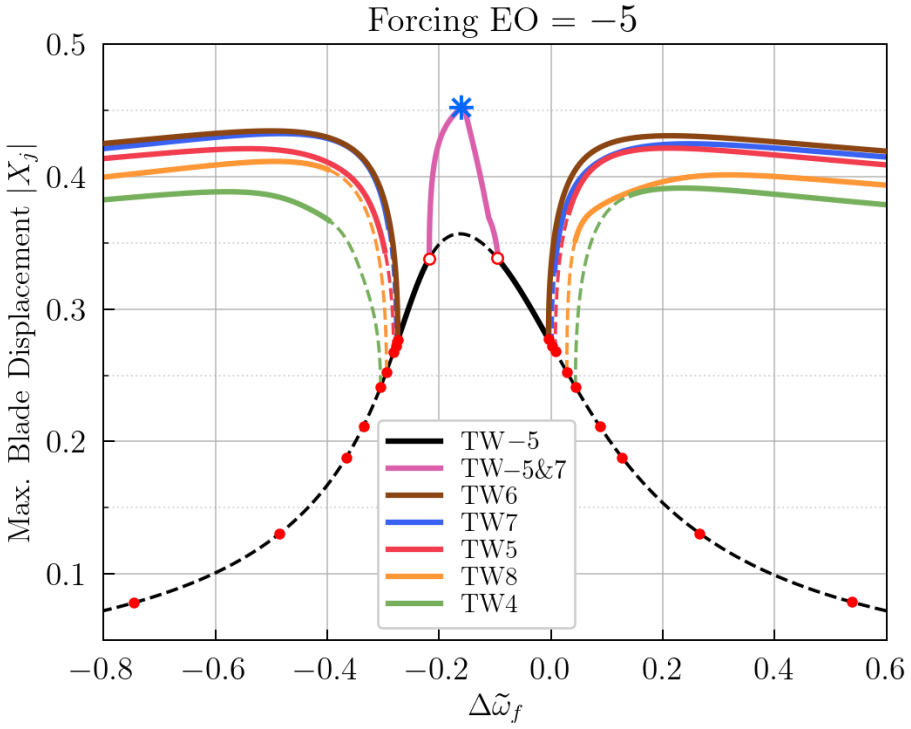

Figure 3.20: Bifurcation diagram of the full asymptotic model with a forcing of EO = −5. Solid (dashed) lines represent stable (unstable) solutions.

TW system in Fig. 3.14. The results of the continuation are shown in Fig. 3.20, where we see that the flutter solutions, away from the resonance, still exhibit the same behavior as in the previous cases.

Nevertheless, at the resonance peak, apart from a small region where the excited TW−5 is stable, a new branch of solution emerges. This solution (highlighted in pink in the plot) is actually synchronous with the forcing, but is composed of two different TWs: the excited one, TW−5, and one unstable mode, TW7.

Solutions synchronous with the forcing frequency, but composed of two different TWs, are believed to have not been reported in any previous study. This new type of solutions has a maximum amplitude of vibration at the peak (blue star in the plot) larger than any other state present in the system. The existence of this solution is caused by the nonlinear friction, which couples TW−5 with the one with a wavenumber at a distance $N/2 = 12$ from it, TW7, and their nonlinear combination does not produce any other wavenumber.

By performing a time integration at the point corresponding to the blue dot in the bifurcation diagram, the presence of this solution is verified, as shown in Fig. 3.21. The initial condition is $A_j = 0.01$ for every TW component, and the directly excited TW is the one that rises in

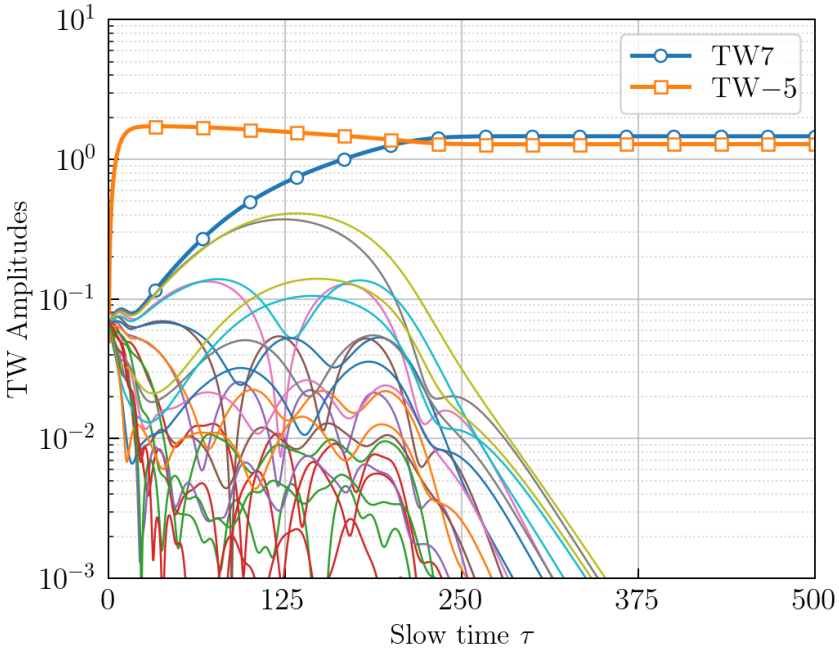

Figure 3.21: Time evolution of the TW amplitudes with an EO $= -5$ excitation with an initial condition of $A_j = 0.01$ and $\Delta\tilde{\omega}_f = -0.15$.

amplitude first. The unstable TW7 grows more slowly, and, after a nonlinear interaction with the other modes, it settles with the forced TW and the rest of the modes decay exponentially.

Physically, this solution shows the entire set of blades of the system divided into packets of two blades, where the amplitude of vibration of each blade is different. This is clearly seen when writing the solution in the displacement basis,

$$\begin{aligned} |X_j| &= |B_{\mathrm{EO}} e^{i\frac{2\pi \mathrm{EO}}{N} j + i\Delta\tilde{\omega}_f \tau} + B_{\mathrm{EO}+N/2} e^{i\frac{2\pi(\mathrm{EO}+N/2)}{N} j + i\Delta\tilde{\omega}_f \tau}| \\ &= |e^{i\frac{2\pi \mathrm{EO}}{N} j + i\Delta\tilde{\omega}_f \tau}(B_{\mathrm{EO}} + e^{i\pi j} B_{\mathrm{EO}+N/2})| \\ &= |B_{\mathrm{EO}} + (-1)^j B_{\mathrm{EO}+N/2}|. \end{aligned} \tag{3.14}$$

Thus, for two consecutive blades, the amplitudes of vibration are $|B_{\mathrm{EO}} - B_{\mathrm{EO}+N/2}|$ and $|B_{\mathrm{EO}} + B_{\mathrm{EO}+N/2}|$. The corresponding maximum amplitude of vibration, without plotting the fast oscillations with the elastic frequency, is shown in Fig. 3.22. The appearance of this solution is quite striking in a tuned bladed-disk. Normally, the response of each blade in a tuned system is the same as the others but with a time shift. Nevertheless, these solutions exhibit different vibration levels between adjacent blades.

The existence of these solutions could appear to be a particularity of the model because it

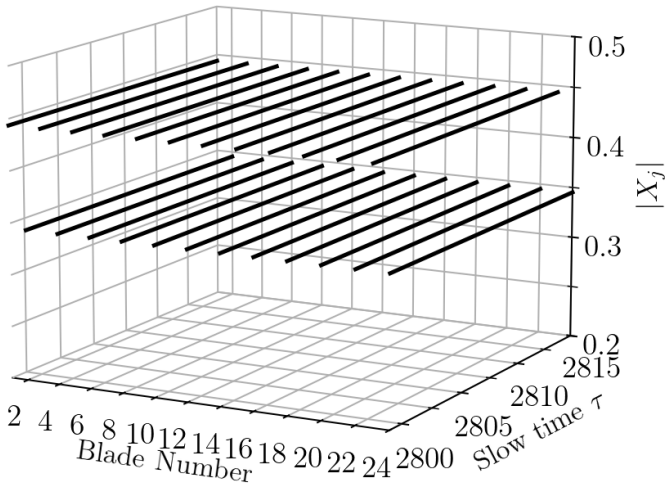

Figure 3.22: Time evolution of the amplitude of the blade displacements corresponding to a 2 TW solution synchronous with the forcing frequency.

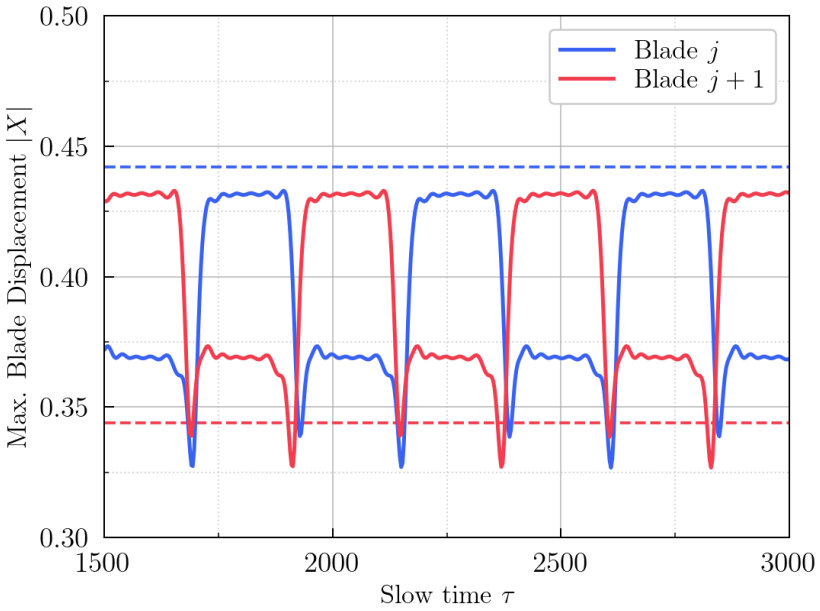

Figure 3.23: Maximum blade displacement in time for an alternating solution with two different amplitudes of vibration. This case corresponds to the excitation of a stable TW at resonance. Dashed line corresponds to the 24 blades system, and solid line to the 23 blades.

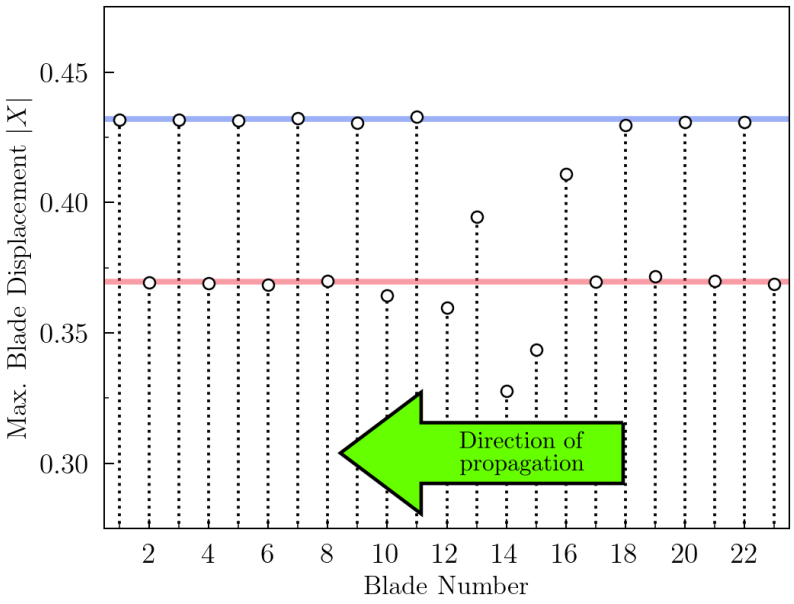

Figure 3.24: Snapshot of the maximum blade displacements of all the blades of the disk. There is a front which is propagating to the left, following the green arrow.

has an even number of blades, 24, which allows for this pattern to be formed. For this reason, an additional analysis is carried out for a bladed-disk with 23 blades, to check the robustness of these solutions. If the number of blades is odd (and in this case, additionally, it is a prime number) the nonlinear interaction does no longer respect the $N/2$ jump and can produce more TW contributions. Nevertheless, these states with alternating amplitudes are found, and Fig. 3.23 shows the time evolution of two adjacent blades. Dashed lines are used to highlight the vibration levels of two adjacent sectors from the 24 blades system, which are constant in time. In the case of 23 blades, in solid line, the presence of two different vibration levels is also observed. Since the nonlinearity now produces other TW modes, we can see that the blades are now switching between the two amplitudes of vibration after a certain amount of time, in a periodic manner. However, the structure of the solution is completely similar as the one found in a system with an even number of blades.

Taking a look at a snapshot of the amplitude of vibration of all the blades for a fixed time gives more insight into the structure of the solution. Figure 3.24 shows this alternating pattern between two vibration levels for most of the blades in the system, although there is a small region where the levels of vibration are slightly different. This corresponds to a front that is propagating in the direction highlighted by the arrow, whose effect is to switch the vibration levels of every packet of two blades. Therefore, physically, this state corresponds to a packet of two blades where each one oscillates at a different level and then, after this propagation

front reaches the packet, the blades switch vibration levels and continue oscillating with constant amplitude. Since the solution is periodic, this process is repeated in time.

3.4 Response of a Realistic Bladed-Disk

Throughout this chapter, the different states than can appear in a bladed-disk as a function of the forcing frequency have been analyzed. The bifurcation diagram from an asymptotic model was generated, exploring the cases where the excited TW is stable or unstable.

One of the main features of the solution is that, in general, close to the resonance peak the solution is composed of just the excited TW locked to the forcing frequency. Far from the resonance, this solution loses stability and the single-TW flutter saturated solution emerges. Close to the bifurcation, the flutter and forcing frequency coexist and, as one moves away from the resonance, the solution tends to the flutter only solution. In the case of the excitation of one of the most stable TWs, a new type of vibration state was found at the resonance, where the blades could have a different amplitude of oscillation even though a tuned rotor is considered.

Since the asymptotic equations were derived from a mass-spring system built to model a flat modal family of a bladed-disk, one could question if the dynamical behavior found in this model is also present when considering a realistic model of a bladed-disk, with many more degrees of freedom.

In this section, we demonstrate that the answer to this question is affirmative. Using a high-fidelity model of a bladed-disk, the nonlinear switching between flutter and forced response is explored, and the solutions with different vibration amplitude such as the ones in Fig. 3.23 are found.

3.4.1 ARIAS Low Pressure Turbine

The bladed-disk used for this analysis is the one developed in the context of the European project ARIAS [117], which is composed of $N = 144$ blades, as shown in Fig. 3.25. Each sector has about $250,000$ DOFs and the contact between the blade and the disk is modeled with eight node pairs.

The first two modal families of the ARIAS rotor are plotted in Fig. 3.26. The first one corresponds to a bending mode, where the influence of the disk is small since this family is quite flat. The second modal family, with a larger contribution of the disk for the first few NDs, corresponds to a torsion mode. The analysis carried out in this section is focused on the

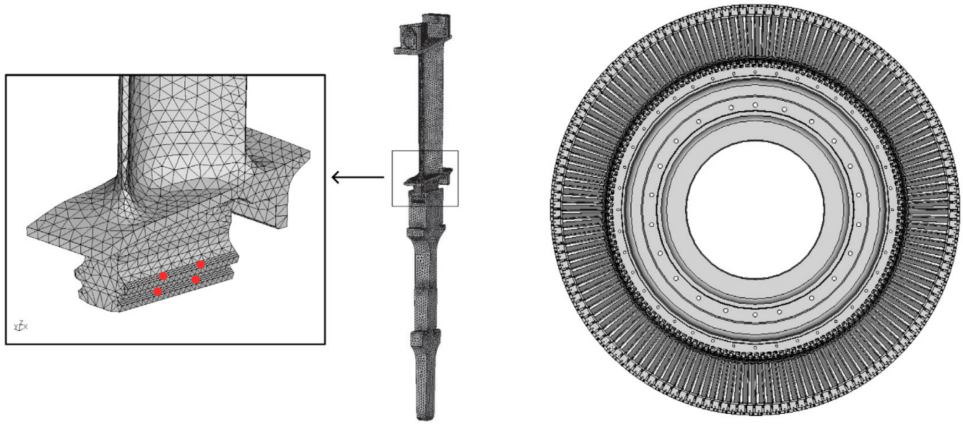

Figure 3.25: High-fidelity FEM model of the ARIAS rotor. Detail of the contacts is shown in red.

first family, where the mass-spring model is expected to capture the bladed-disk dynamics.

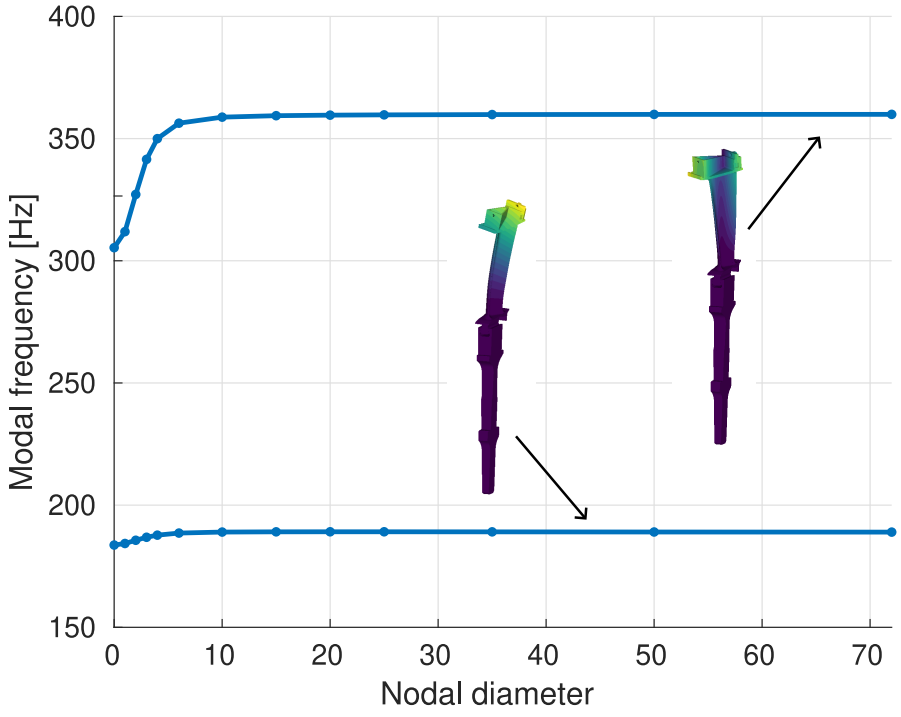

Figure 3.26: First two modal families of the ARIAS rotor.

The aerodynamic damping characteristics of the first modal family were obtained by ITP Aero using their linearized frequency domain software Must-L [118], and the resulting values are shown in Fig. 3.27 (the details of the operating point can be found in Ref. [119]).

The ARIAS rotor was designed to be unstable, and there are quite many unstable modes in the system, with the largest instability between TW20-TW28. The shape of the aerodynamic

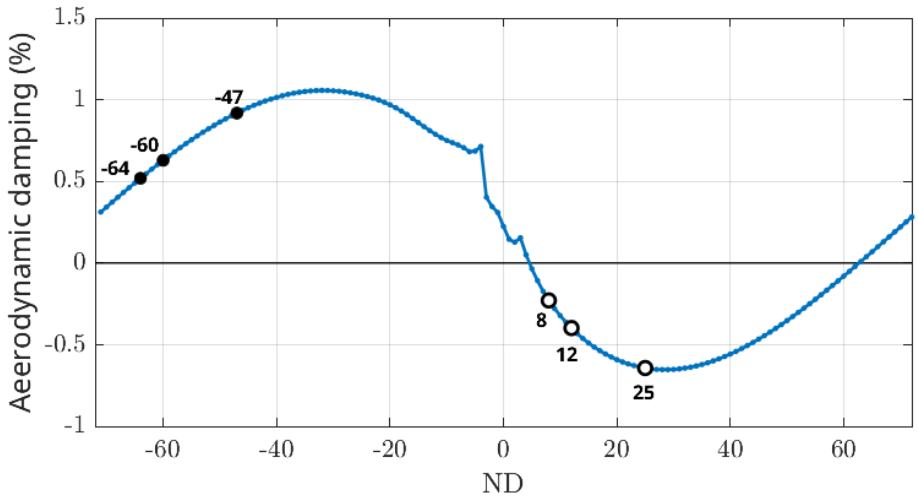

Figure 3.27: Aerodynamic damping curve of the first modal family of the ARIAS rotor. The points highlighted in black dots correspond to forced TWs and the circles colored in white are the TWs induced by the nonlinear effects.

curve is very similar to that of the asymptotic model (see Fig. 3.2). The convention here is that the positive NDs correspond to TWs rotating in opposite direction with respect to the rotor rotation, and viceversa for negative NDs.

The nonlinear friction model considered in the contacts (highlighted with red color in Fig. 3.25) is explained in [120]. The friction forces are of Coulomb type where stick, slip and gap states can be present in the system. Even though in the asymptotic model a microslip model was used, the nonlinear dissipation mechanism is expected to be quite similar.

As mentioned before, this model has $N = 144$ sectors, and each of them has a very high count of DOFs, which make direct time integration of the system extremely prohibitive, especially due to the small effect of friction which requires integration over many cycles of vibration. Therefore, some reduction technique has to be applied to the equations in order to make a time domain approach feasible.

The method used to simulate the forced response of an unstable rotor with nonlinear friction is explained in detail in [120], and only the main characteristics of the model will be highlighted. The equations of the full rotor are first expressed in TW basis, and then a Craig-Bampton (CB) reduction is applied to the linear DOFs of the structure, leaving the contacts unaltered. A convergence study for the number of CB modes showed that retaining 10 of them for each ND was enough. The resulting model is hybrid, since it has complex TW amplitudes for the retained modes and physical displacements for the contacts. It is also important to mention

that this methodology incorporates the CB modes of the entire bladed-disk, without any substructuring.

3.4.2 Switching Between Flutter and Forced Response

The first analysis consists of a frequency sweep with an excitation of EO = 4, which corresponds to an unstable mode. The sweep is carried out slow enough to avoid the presence of transient effects [49].

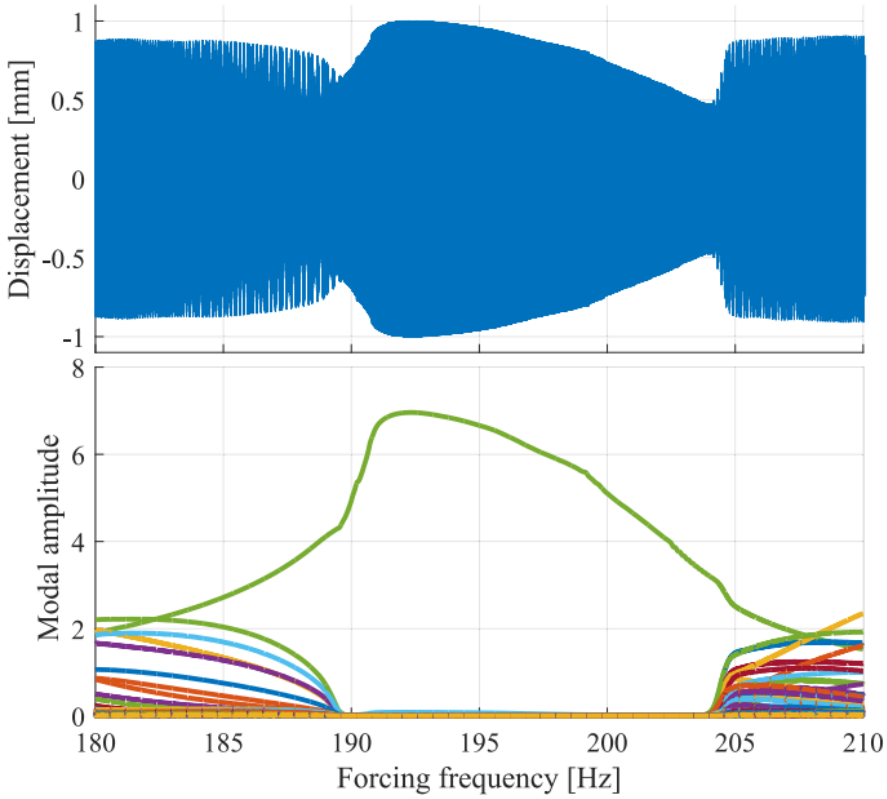

Figure 3.28: Frequency sweep of the response of the system for an excitation of TW4. The top of the plot shows the displacements of one point near the tip of one blade and the bottom corresponds to the evolution of the different TW amplitudes.

The results of the simulation are shown in Fig. 3.28. The top part of the plot shows the evolution of the displacements of a node near the tip in the direction of largest motion. Two regions can be clearly identified: one, close to the natural frequency, where the shape of the resonance curve is the typical one of a mechanical oscillator with nonlinear effects; and another one, far from the resonance, where the amplitude of vibrations grows and tends to a constant value. The bottom part of the plot gives more insight into the structure of the solution. This figure shows the evolution of the modal amplitudes of the different

TW components. As it can be seen, close to the resonance, only the contribution of one TW is present, which corresponds to the excited TW4. In contrast, as one moves far from the resonance, other TW modes start appearing, with the highest amplitude components corresponding to the most unstable ones (TW20 to TW28).

The structure of this solution is completely analogous to the one predicted by the bifurcation diagram analysis of the asymptotic model shown in Fig. 3.15. This constitutes an important validation of the capability of the asymptotic equations derived from the mass-spring model to actually capture the main aspects of the nonlinear dynamics of the bladed-disk.

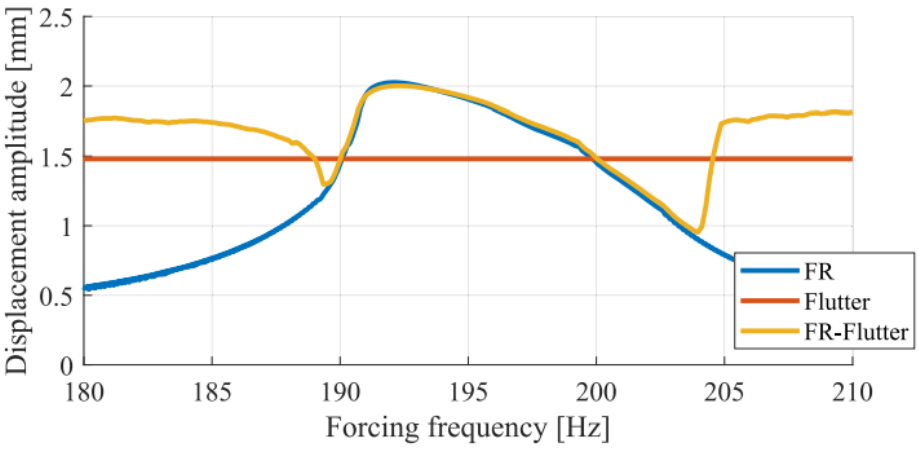

Figure 3.29: Maximum displacement for the frequency sweep of the system with a TW4 excitation of the ARIAS rotor.

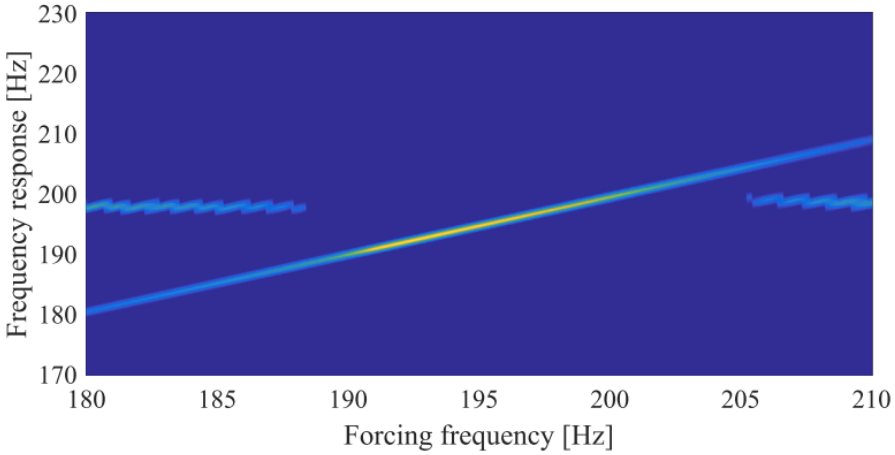

Figure 3.30: Frequency spectra of the solution corresponding to Fig. 3.28.

Moreover, we can isolate the effect of flutter and forced response and compare against their nonlinear combination (Fig. 3.29), arriving to the same conclusions as before: the linear superposition of both effects separately leads to a considerable overestimation of the solution.

The frequency spectra of the solution shown in Fig. 3.28 is plotted in Fig. 3.30. As expected, close to the resonance peak there is only the forcing frequency, and the system oscillates locked to that frequency. And, far from the resonance, flutter frequencies dominates, which agrees with the predictions from the asymptotic model.

3.4.3 States with Different Blade Vibration Amplitude

The asymptotic method predicted the existence of states where the blades exhibited different vibration amplitudes due to the nonlinear interaction (see Fig. 3.20), which corresponds to exciting the system with one of the most stable TWs. These states are now sought for in the ARIAS rotor configuration.

Before starting the analysis, we comment on the possibility of appearance of these solutions during operation. In a LPT, the stator preceding of a rotor typically has a number of vanes that satisfy $N_v \sim 2N/3$. In the ARIAS case, with $N = 144$, the number of vanes would be $N_v \sim 96$. Since the stator wakes rotate in the opposite direction to the rotational speed of the rotor, and with the sign convention of this work, this means that an excitation with $\text{EO} = 96 - 144 = -48$ is produced by the stator. For this reason, the exploration of the EOs close to -48 is carried out. It should be noted that the frequency of this excitation is quite high compared to the first family, making the existence of these solutions in a real situation less likely. Nevertheless, we highlight their appearance here to raise awareness on the turbomachinery community of the possibility of these states.

The three cases that are explored correspond to $\text{EO} = -47,\ -60,\ -64$, as highlighted in the aerodamping curve in Fig. 3.27.

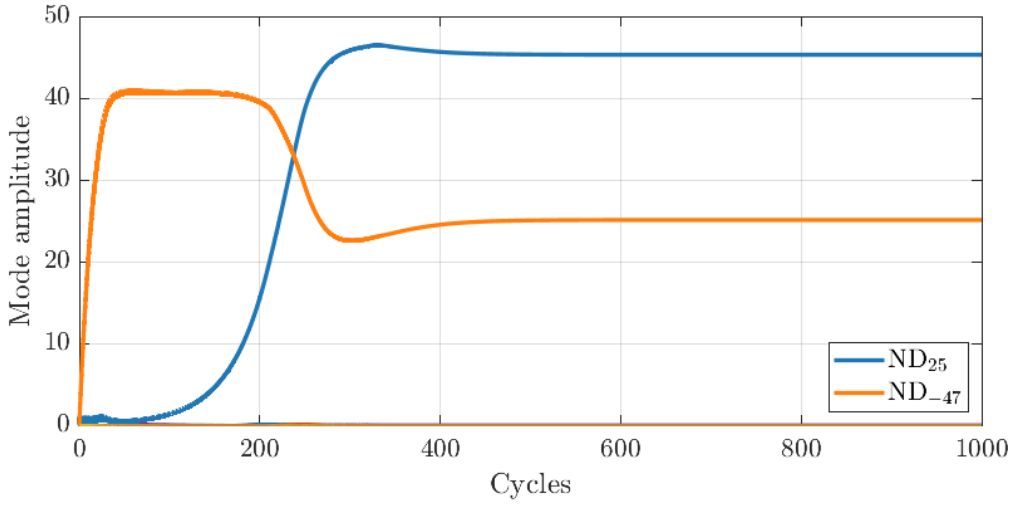

Figure 3.31: Evolution of the TW amplitudes for the ARIAS rotor with an excitation of $\text{EO} = -47$.

(A) Excitation of TW−47

From an initial condition corresponding to zero amplitude for every TW mode, the system is integrated in time for a forcing frequency equal to the blade alone resonance frequency of the TW−47. The evolution of the TW amplitudes is shown in Fig. 3.31. The directly excited TW−47 quickly grows and stabilizes at a constant amplitude at early times. Later, the amplitude of the unstable TW25 interacts with the excited TW, and the system settle to a state where both amplitudes have a significant contribution in the response of the system. TW25 is actually at a distance $N/2$ from TW−47, which is the combination of wavenumbers that the nonlinearity produces, as predicted by the asymptotic model. The growth of the unstable mode is related with the aerodynamic damping coefficient, which is small. This plot reproduces the same behavior as predicted from the asymptotic equations; see Fig. 3.21 which shows a quite similar TW evolution.

To verify that the most relevant contribution is just from the two TWs highlighted above, the TW content of the last time step is plotted in Fig. 3.32. Clearly, two peaks are dominating the response of the system, which correspond to TW−47 and TW25. The rest of the TWs have a much smaller contribution, and they correspond to higher harmonics coming from the nonlinear interaction of the two main TW modes.

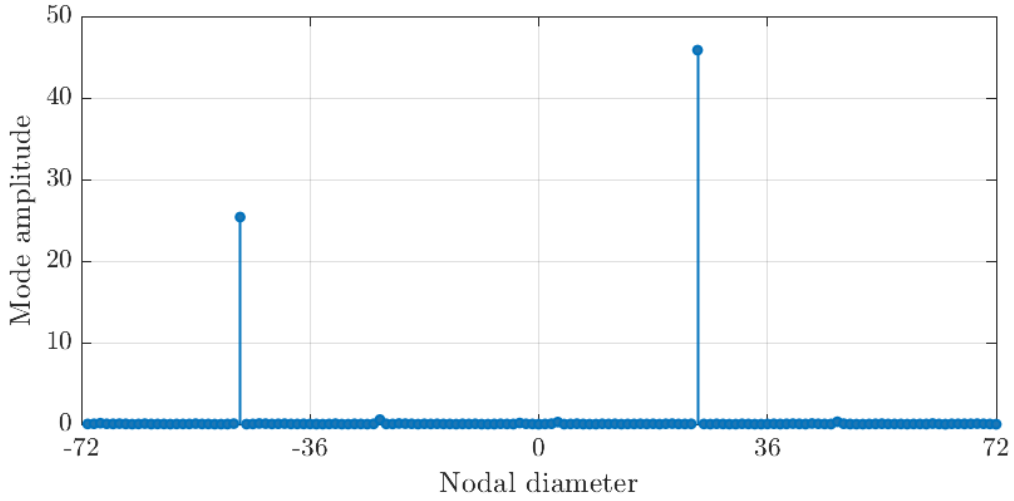

Figure 3.32: Amplitudes of the different TW modes for the ARIAS rotor with an excitation of EO = −47 at the final step of the simulation.

Since the solution is synchronous with the forcing and composed of two different TW modes, it was seen in Eq. (3.14) that this state results in a solution with two different levels of vibration. In other words, the bladed-disk could be seen as divided into packets of two blades, where each blade in the packet has a different amplitude of oscillation. Fig. 3.33 shows the evolution of the displacements in time for several consecutive blades. It can be

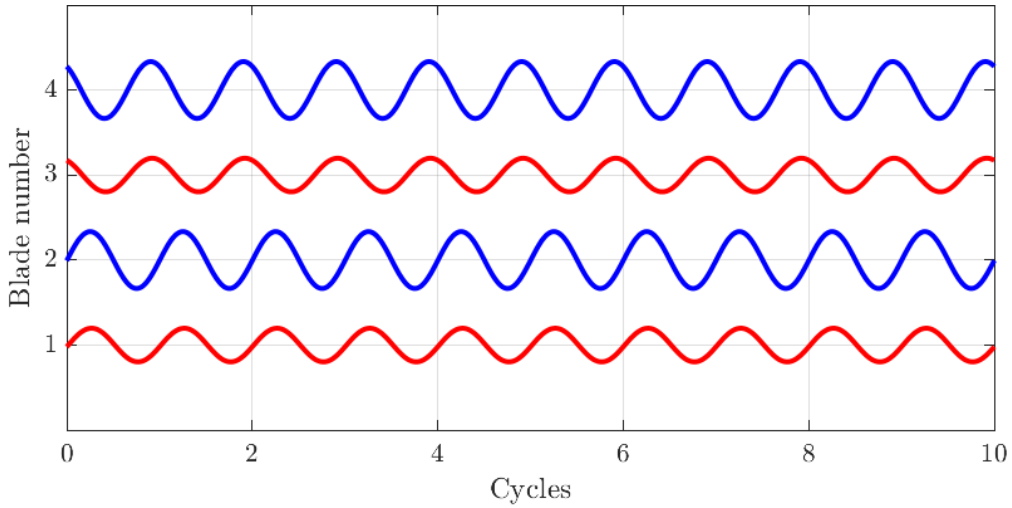

Figure 3.33: Displacement of different blades of the ARIAS rotor for the solution with EO = −47.

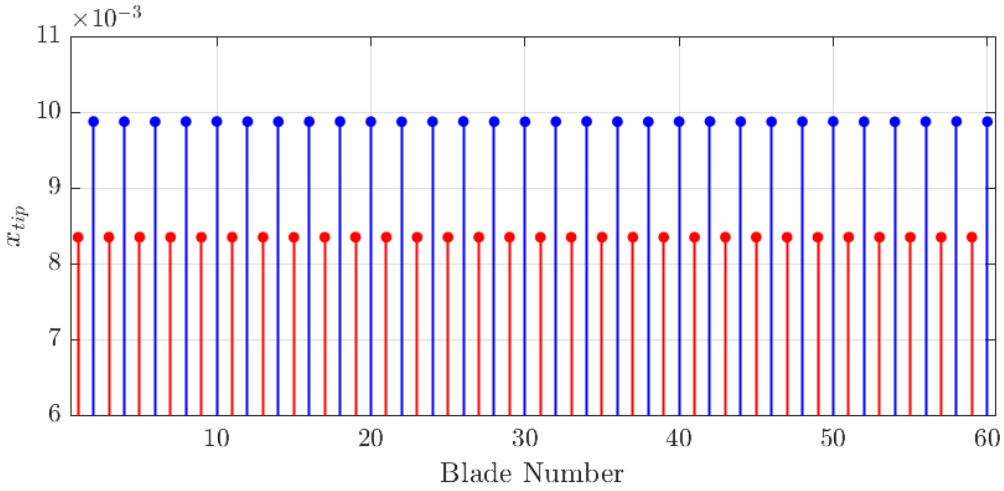

Figure 3.34: Maximum amplitude of vibration of all the blades of the ARIAS rotor for the solution with EO = −47.

seen that, for each pair of blades, one is oscillating with a larger amplitude (blue) and the other with a smaller one (red). This pattern is repeated along the entire disk, and the vibration levels are constant in time.

Further detail is shown in Fig. 3.34, where the maximum amplitude of vibration of all the blades is shown. Here, two different amplitudes of the limit cycles of oscillation are clearly observed, with approximately a 20% difference. Again, the structure of this solution was already captured in the asymptotic model, as shown in Fig. 3.22.

To verify the stability of this type of solutions, a perturbation of 5% of the amplitude of the two TW solution is added to every TW mode from the converged solution of Fig. 3.31.

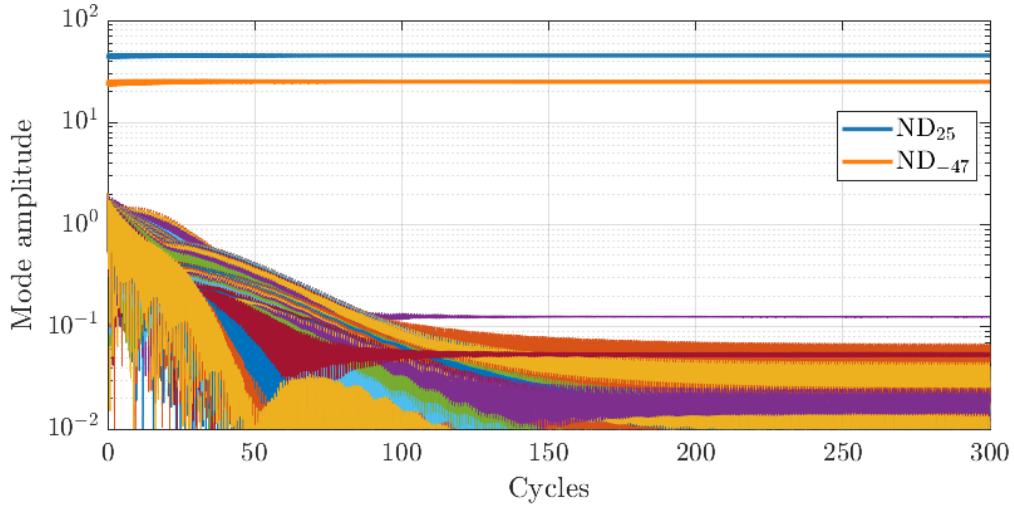

Figure 3.35: Evolution of the TW amplitudes for the ARIAS rotor with an excitation of EO = −47 from the two TW solution with a small perturbation.

The time evolution is plotted in Fig. 3.35, where it is seen that the TW modes related to the small perturbation decay until they are several order of magnitude smaller than the TW modes that dominate this solution. Therefore, it can be concluded that the presence of these states is quite robust.

(B) Excitation of TW−60

The exploration in the asymptotic model (Fig. 3.10) showed that these new type of states can also appear even if the excited TW does not exactly correspond with one of the most stable modes.

The presence of these solutions is now explored for an excitation of EO = −60, which according to the asymptotic model should couple with TW12, since −60 + 72 = 12. These TWs are highlighted in the aerodynamic damping curve in Fig. 3.27, where TW12 can be seen to have about half as much aerodynamic damping than TW25, which was the case studied previously.

Figure 3.36 shows the time evolution of the different TW amplitudes involved in the response, which displays similar dynamics. First, the forced TW−60 quickly increases in amplitude, while the unstable TW12 grows more slowly. Compared to Fig. 3.31, the unstable TW amplitude takes almost double in time to reach the same amplitude as the forced TW, which is related to the aerodynamic coefficient being almost half of the previous case. When the unstable TW reaches a comparable amplitude with respect to the directly excited TW, they interact nonlinearly until they reach a stable solution, with an amplitude constant in time. This solution is also synchronous with the forcing.

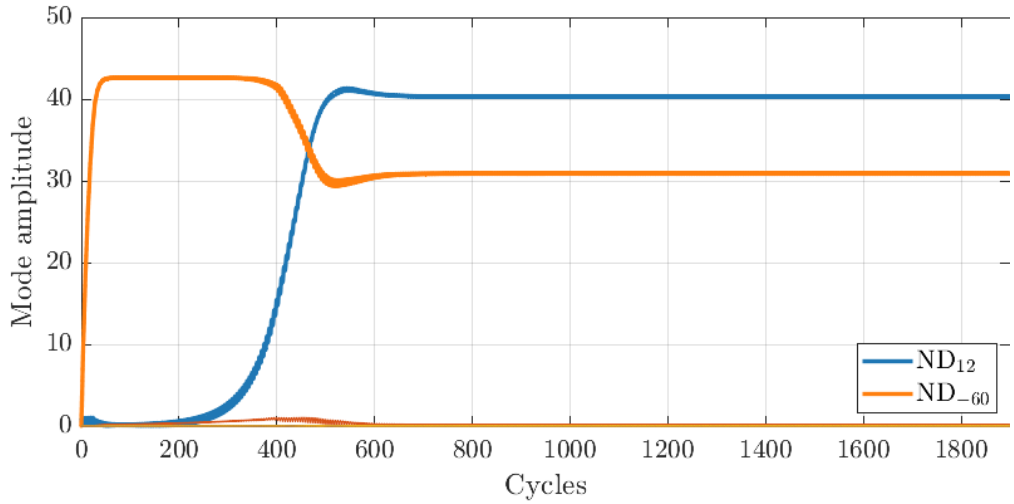

Figure 3.36: Evolution of the TW amplitudes for the ARIAS rotor with an excitation of EO = −60.

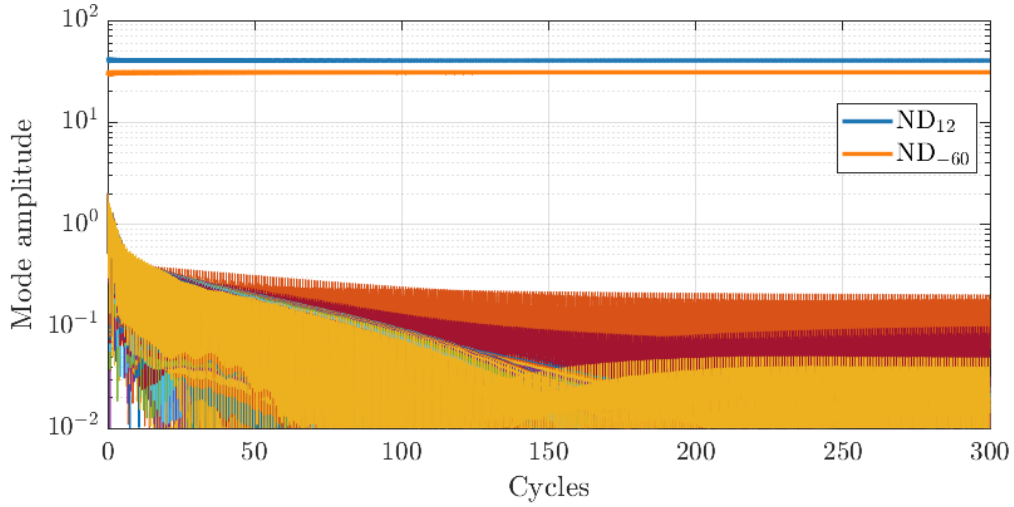

Figure 3.37: Evolution of the TW amplitudes for the ARIAS rotor with an excitation of EO = −60 from the two TW solution with a small perturbation.

The stability of the solution is again verified adding a 5% perturbation to the other TW modes, and the results are shown in Fig. 3.37. It is clearly seen that the perturbations decay in time until a solution that consists almost exclusively of TW−60 and TW12 is reached.

The results for EO = −64 are completely analogous from the ones presented here, with the directly forced TW coupled with TW8, and the plots are omitted for the sake of brevity.

Overall, it can be concluded that the main results from the asymptotic equations apply when performing the analysis of a realistic configuration. Therefore, asymptotic models seem to be a powerful tool to obtain qualitative and quantitative information about the nonlinear dynamics that sets in the system, and at an extremely reduced cost.

Chapter 4

Asymptotic Description of High-Fidelity Structures with Nonlinear Friction

The analysis of the asymptotic models developed in the previous chapters provided a clearer understanding of the nonlinear dynamics of a bladed-disk. In particular, when examining flutter and its interaction with forced response in the presence of nonlinear friction effects, the space of possible vibration states of the system was explored in detail. Then, these states were reproduced using a high-fidelity FEM model, which verified the predictions of the asymptotic equations.

Working with a high-fidelity FEM model, even after applying some dimensionality reductions, is very costly compared to an asymptotic model. Moreover, analytical investigations and bifurcation computations are much more tractable within the asymptotic framework due to their extremely reduced dimensionality. Such analyses provide highly accurate determinations of the stable solutions to the nonlinear vibration problem, and also offer deeper physical insight of the system's behavior.

Despite these advantages from the asymptotic description, a mass-spring system had to first be tuned to reproduce the dynamics of the bladed-disk in the particular regime of interest. The calibration of a lumped model is often inconvenient, since usually the available data are the mass and stiffness matrices coming from a detailed FEM model of a structure. Therefore, an asymptotic reduction directly from the FEM assembly would be highly desirable, skipping the step of the generating an intermediate lumped model.

The goal of this chapter is to apply a multiple scales technique to find a reduced asymptotic description from a high-fidelity FEM model. The derivation starts from the FEM equations

of motion, with a nonlinear force of Coulomb's type with stick, slip and gap states.

4.1 Description of the Mechanical Problem

The typical structure under analysis is a sector of a bladed-disk, where the nonlinear effects are restricted to a small region, corresponding to the interface between two components, as presented in Fig. 4.1. The contacts are highlighted in red, and are located in the attachment of the blade root to the disk.

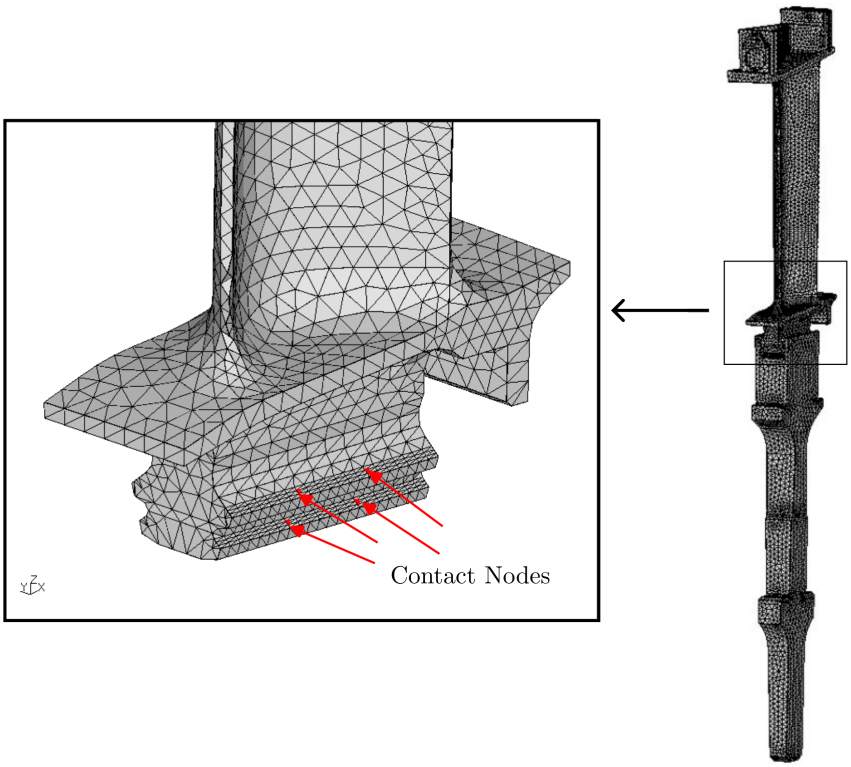

Figure 4.1: High-Fidelity FEM model of a sector of the ARIAS rotor [117]. The contact nodes at the blade root attachment are highlighted in red.

The equations of motion of the discretized structure are, in general, of the form

$$\mathbf{M}\ddot{\mathbf{X}} + \mathbf{C}\dot{\mathbf{X}} + \mathbf{K}\mathbf{X} + \mathbf{G}(\mathbf{X}, \dot{\mathbf{X}}) = \mathbf{F}(t), \tag{4.1}$$

where $\mathbf{M}$ is the mass matrix, $\mathbf{C}$ is the linear damping matrix and $\mathbf{K}$ the stiffness matrix. The vector of nonlinear forces is represented by the term $\mathbf{G}(\mathbf{X}, \dot{\mathbf{X}})$, and the external forcing is $\mathbf{F}(t)$, which is usually periodic in time.

The nonlinear forces are applied locally in the contact area, which involve a very small subset

of the total degrees of freedom of the structure. Therefore, it is convenient to introduce a distinction between the elastic DOFs, $\mathbf{x}_e$, which are related to the motion of the nodes outside the contact area; and the contact DOFs, $\mathbf{x}_c$, which are located at the interface between the blade and the disk.

The equations of motion with the DOF splitting can be expressed as

$$\begin{pmatrix} \mathbf{M}_{ee} & \mathbf{M}_{ec} \\ \mathbf{M}_{ce} & \mathbf{M}_{cc} \end{pmatrix} \begin{pmatrix} \ddot{\mathbf{x}}_e \\ \ddot{\mathbf{x}}_c \end{pmatrix} + \begin{pmatrix} \mathbf{C}_{ee} & \mathbf{C}_{ec} \\ \mathbf{C}_{ce} & \mathbf{C}_{cc} \end{pmatrix} \begin{pmatrix} \dot{\mathbf{x}}_e \\ \dot{\mathbf{x}}_c \end{pmatrix} + \begin{pmatrix} \mathbf{K}_{ee} & \mathbf{K}_{ec} \\ \mathbf{K}_{ce} & \mathbf{K}_{cc} \end{pmatrix} \begin{pmatrix} \mathbf{x}_e \\ \mathbf{x}_c \end{pmatrix} + \begin{pmatrix} 0 \\ \mathbf{g}(\mathbf{x}_c, \dot{\mathbf{x}}_c) \end{pmatrix} = \begin{pmatrix} \mathbf{f}(t) \\ 0 \end{pmatrix}, \tag{4.2}$$

where it has been made explicit that the nonlinear contact forces, $\mathbf{g}(\mathbf{x}_c, \dot{\mathbf{x}}_c)$, are only applied at the contact DOFs and depend only on the contact displacements $\mathbf{x}_c, \dot{\mathbf{x}}_c$. The external forcing, $\mathbf{f}(t)$, is applied to the elastic DOFs of the structure, as it is the usual situation for turbomachinery bladed-disks.

The case of a forcing with ND $= 0$ is considered for simplicity. Periodicity is applied at the disk side boundaries in Fig. 4.1, and all sectors have the same dynamics.

The linear damping will be modeled as proportional to the stiffness matrix, i.e., $\mathbf{C} = \beta\mathbf{K}$, where β is a constant. The value of this coefficient is chosen so that the linear damping produces just a small fraction of the dissipation coming from the friction forces at the contacts.

The contact forces are more easily described in terms of the relative displacements between the two contact nodes involved. For this reason, the contact DOFs $\mathbf{x}_c$ are assumed to represent the relative displacements between contact pairs.

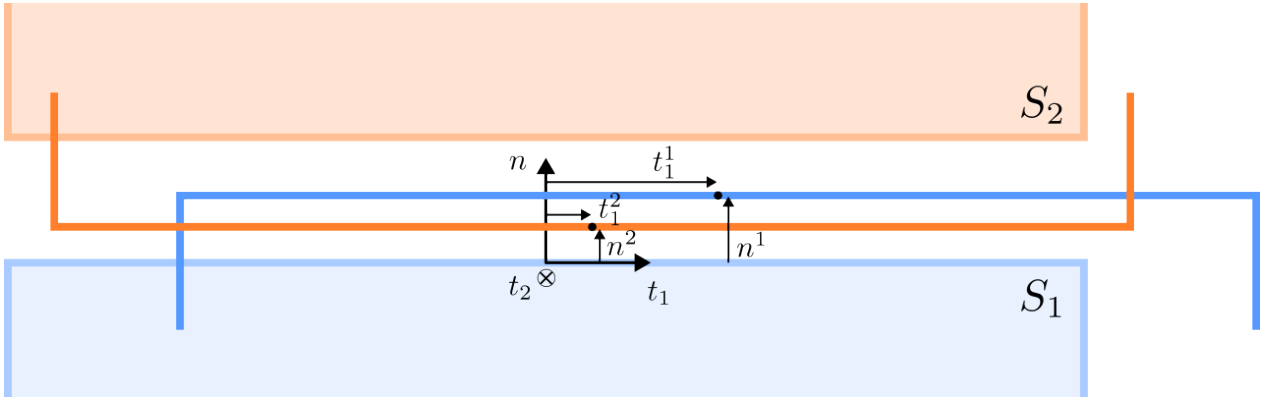

Figure 4.2: Representation of the contact DOFs as relative displacements between the two contact surfaces.

Fig. 4.2 shows a sketch of two different solids in contact, S_1 and S_2. First, a local coordinate system with the orientation of the normal, n, and two tangent directions along the surface, t_1 and t_2, is defined. This coordinate system is usually different from the one used to describe

the elastic displacements of the structure $\mathbf{x}_e$, but it is very convenient for the description of the contact forces.

The motion of the contacts during the operation is considered to be small, so the contact between the two surfaces is modeled as point to point. Then, if we focus on the displacements of one pair of contacts, we can describe the position of each node by (t_1^1, t_2^1, n^1) for solid 1 and (t_1^2, t_2^2, n^2) for solid 2. Consequently, the relative displacements between contact node pairs are defined, in the new reference, as

$$\begin{aligned} x_{t_1} &= t_1^1 - t_1^2, \\ x_{t_2} &= t_2^1 - t_2^2, \\ x_n &= n^1 - n^2. \end{aligned} \tag{4.3}$$

With this convention, note that $x_n > 0$ implies that the two solids are overlapping, whereas $x_n < 0$ means that the contact pair is separated. The vector of the contact DOFs, $\mathbf{x}_c$, is built by stacking the three components, (x_{t_1}, x_{t_2}, x_n), of each contact pair one after the other. Thus, the total size of this vector is $3N_c$, where N_c is the number of contact pairs.

4.1.1 Friction Model

The methodology described in this chapter does not require any restriction on the nonlinear law considered $\mathbf{g}(\mathbf{x}_c, \dot{\mathbf{x}}_c)$, although for the current analysis we will just focus on a friction law of Coulomb type. In particular, we consider each contact to be modeled following the so-called one dimensional Jenkins element, which is sketched in Fig. 4.3.

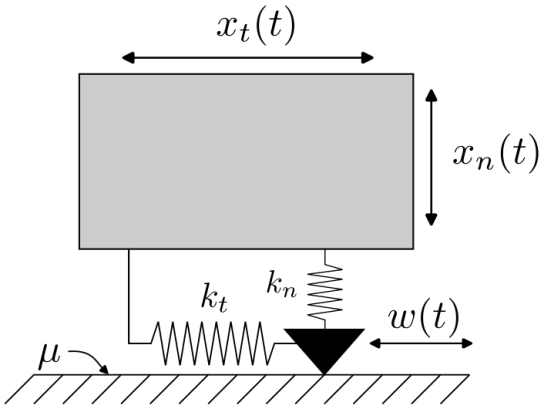

Figure 4.3: Friction Jenkins element.

The variable normal load is defined with the expression

$$N = \begin{cases} k_n x_n, & \text{if } x_n > 0 \\ 0, & \text{if } x_n \leq 0 \end{cases}, \tag{4.4}$$

where the gap states ($N = 0$) are included when the relative displacement between the contact surfaces is $x_n \leq 0$, since this means that the contact pair is separated with our convention. For the case with penetration, the normal force is modeled as a linear spring with a large stiffness constant k_n. This provides a numerically smoother representation of the transition between gap and contact states.

In the tangential direction, the friction force is defined as

$$T = \begin{cases} k_t(x_t - w) & \text{if } |k_t(x_t - w)| < \mu N \text{ and } N > 0 \text{ (stick)} \\ \pm \mu N & \text{if } |k_t(x_t - w)| \geq \mu N \text{ and } N > 0 \text{ (slip)} \\ 0 & \text{if } N = 0 \text{ (gap)} \end{cases}, \tag{4.5}$$

where x_t is the relative tangential displacement, k_t the stiffness in the tangential direction, μ the friction coefficient, and w is an additional DOF that takes into account the history of the friction forces.

With this model, three different situations are possible. First, if the absolute value of the tangential force is less than μN, the force is linear with the stiffness k_t, and this is denoted as a stick state. As the force in the contact grows, upon reaching the maximum friction force μN, the system starts to slide with a constant value of the force. This state is denoted as slip, where the w DOF is updated to have a record of the distance that the contact has slipped. This DOF is introduced because, if the force on the contact is reduced, it would enter again the stick regime, and w represents the new position from which the force is linear again. The last possible state is contact separation, where the normal and tangential forces are zero, and this is denoted as a gap state.

To visualize the shape of the friction cycles, the tangential force, T, is plotted as a function of the relative tangential displacement, x_t, in Fig. 4.4 for a typical periodic forcing. First, the friction is explored for a constant normal force, shown in Fig. 4.4a. Starting from the origin, the force grows linearly with slope given by k_t, in the stick regime, until the maximum friction force μN is reached, and then the contact starts sliding in a slip state. The value of x_t increases until the force is reduced, and the system enters back in a stick state on the right part of the figure. This new stick state is shifted from the previous one by w, which,

as commented before, accounts for the history of the system. Then, the system follows a periodic motion with transitions between stick and slip states, where the friction DOF w keeps track of the contact slip distance.

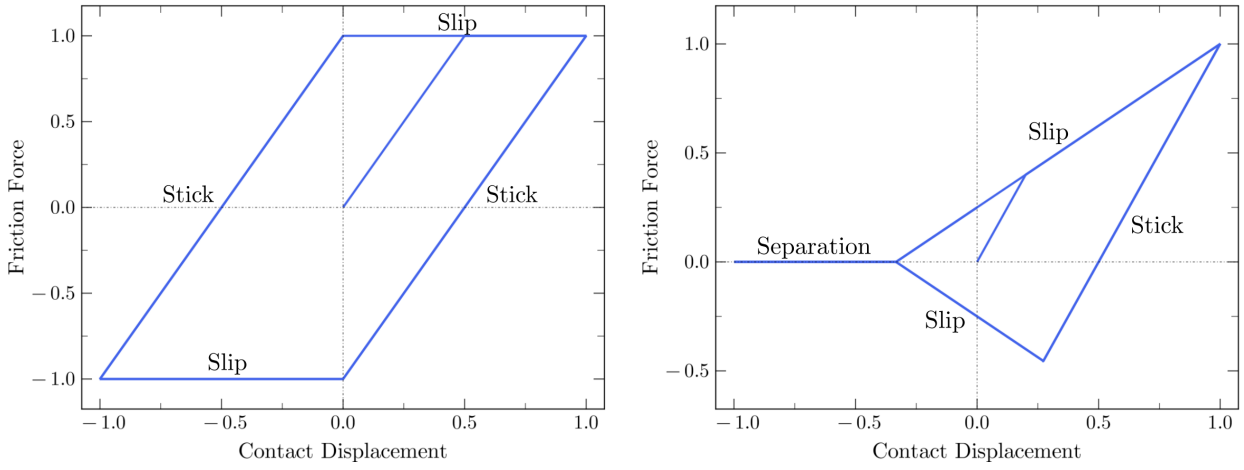

(a) Constant normal force

(b) Variable normal force

Figure 4.4: Friction cycles for the Coulomb's stick/slip model.

A more realistic situation can be found when the normal force is not constant and changes in time. Fig. 4.4b shows the friction cycle for this situation, where now the slip states are not represented by a line with zero slope, since the normal load is changing throughout the cycle. Apart from the usual stick states, a new region appears on the left side of the plot, where the force in the tangential direction is exactly zero because the contact has separated, producing a gap state. In this case, the overall area of the friction cycle is reduced, which can be relevant because the energy dissipated is proportional to this quantity.

This friction model can represent highly nonlinear situations, since a structure can have a subset of the contacts separated and others in stick/slip states at the same time. Each node has two DOFs in the tangent direction, x_{t_1} and x_{t_2}, and the friction will be considered as having two one-dimensional Jenkins elements, one acting in each direction. This choice is made since the comparison with a 2D friction element produced very similar effects, see [27].

4.1.2 Craig-Bampton Projection

A Craig-Bampton [30] projection of the system is introduced. The purpose of this procedure is not to reduce the equations of motion; it is introduced to simplify the derivation of the asymptotic model. Since there is no reduction involved, the CB process will be treated just as a change of basis of the original equations.

To perform this change of basis, two different types modes have to be computed. The linear

part of the system, related to $\mathbf{x}_e$, is partially expressed in a modal basis by assuming that the contact surfaces are bonded together (full-stuck), which implies that $\mathbf{x}_c = \mathbf{0}$. Then, neglecting the linear damping, since it will be considered small, we can compute the full-stuck elastic modes from the eigenvalue problem

$$(-\omega_n^2 \mathbf{M}_{ee} + \mathbf{K}_{ee})\phi_n = 0, \tag{4.6}$$

which are stored in the matrix Φ, with the modes as columns. These modes are normalized with respect to the mass matrix, i.e., $\Phi^\top \mathbf{M}_{ee} \Phi = \mathbf{I}$.

The effect of the contact DOFs on the elastic part of the system is accounted for by the static equilibrium equation

$$\mathbf{K}_{ee}\mathbf{x}_e + \mathbf{K}_{ec}\mathbf{x}_c = \mathbf{0}, \tag{4.7}$$

and the elastic displacements are expressed in terms of the contacts as

$$\mathbf{x}_e = -\mathbf{K}_{ee}^{-1}\mathbf{K}_{ec}\mathbf{x}_c = \Psi \mathbf{x}_c, \tag{4.8}$$

where Ψ is the matrix containing the so-called constrained modes. Basically, this matrix contains the effect of a unit displacement in each contact DOF on the elastic displacements.

Now, any elastic displacement vector can be written as a linear combination of the full-stuck modes, Φ, and the constrained modes, Ψ, since they span the entire vector space. The CB transformation matrix is then defined as

$$\begin{pmatrix} \mathbf{x}_e \\ \mathbf{x}_c \end{pmatrix} = \begin{pmatrix} \Phi & \Psi \\ \mathbf{0} & \mathbf{I} \end{pmatrix} \begin{pmatrix} \mathbf{a} \\ \mathbf{x}_c \end{pmatrix} = \mathbf{T}_{\mathrm{CB}} \begin{pmatrix} \mathbf{a} \\ \mathbf{x}_c \end{pmatrix}, \tag{4.9}$$

where the vector $\mathbf{a}$ contains the amplitudes of the full-stuck modes.

If all the full-stuck modes are kept, the matrix $\mathbf{T}_{\mathrm{CB}}$ just defines a mere change of basis without any loss of accuracy. Usually, when performing a Craig-Bampton reduction, one normally just keeps a few modes in the matrix Φ. However, as commented before, the projection performed here (with all modes kept) is just made in order to simplify the derivation of the asymptotic model in the next section.

Introducing the change of variables (4.9) into the equations of motion (4.2) and premultiplying

by $\mathbf{T}_{\mathrm{CB}}^{\top}$ gives the transformed equations

$$\begin{pmatrix} \mathbf{I} & \mathbf{M}_{ax} \\ \mathbf{M}_{xa} & \mathbf{M}_{xx} \end{pmatrix} \begin{pmatrix} \ddot{\mathbf{a}} \\ \ddot{\mathbf{x}}_c \end{pmatrix} + \beta \begin{pmatrix} \mathbf{\Omega}_a^2 & \mathbf{0} \\ \mathbf{0} & \mathbf{K}_{xx} \end{pmatrix} \begin{pmatrix} \dot{\mathbf{a}} \\ \dot{\mathbf{x}}_c \end{pmatrix} + \begin{pmatrix} \mathbf{\Omega}_a^2 & \mathbf{0} \\ \mathbf{0} & \mathbf{K}_{xx} \end{pmatrix} \begin{pmatrix} \mathbf{a} \\ \mathbf{x}_c \end{pmatrix} + \begin{pmatrix} 0 \\ \mathbf{g}(\mathbf{x}_c, \dot{\mathbf{x}}_c) \end{pmatrix} = \begin{pmatrix} \mathbf{f}_a(t) \\ \mathbf{f}_x(t) \end{pmatrix}, \tag{4.10}$$

where the different terms are defined as

$$\begin{aligned} \mathbf{M}_{ax} &= \mathbf{M}_{xa}^{\top} = \Phi^{\top}\mathbf{M}_{ee}\Psi + \Phi^{\top}\mathbf{M}_{ec}, \\ \mathbf{M}_{xx} &= \Psi^{\top}\mathbf{M}_{ee}\Psi + \Psi^{\top}\mathbf{M}_{ec} + \mathbf{M}_{ce}\Psi + \mathbf{M}_{cc}, \\ \mathbf{K}_{xx} &= \mathbf{K}_{cc} - \Psi^{\top}\mathbf{K}_{ee}\Psi, \\ \mathbf{\Omega}_a^2 &= \mathbf{diag}(\omega_j^2), \\ \mathbf{f}_a &= \Phi^{\top}\mathbf{f}, \quad \mathbf{f}_x = \Psi^{\top}\mathbf{f}. \end{aligned} \tag{4.11}$$

The frequencies ω_j are the ones from the full-stuck modes, and the rest of the terms are obtained by performing the corresponding projections. The advantage of this basis is that there is no coupling between the modal amplitudes $\mathbf{a}$ and the contact DOFs $\mathbf{x}_c$ in the stiffness matrix. This will allow applying, in the next section, an asymptotic procedure completely similar to the one developed in Chapter 2.

The rest of the chapter is devoted to the derivation of the asymptotic equations and its application to mechanical structures with nonlinear friction effects. As an introduction to the method, the computation of the natural frequencies with linear contact forces is first carried out using a perturbative approach in the next section. This intermediate step before the dynamic analysis is done to highlight the importance that the constrained modes have to accurately estimate the effect of the contact forces, since a straightforward approximation can underestimate them by a large amount. Then, following a similar procedure, the methodology is extended to the nonlinear case.

4.2 Linear Modes Calculation

Consider the eigenpair (ω_n^2, ϕ_n) computed from the full-stuck problem in Eq. (4.6). From this initial approximation, a systematic perturbative procedure is developed in this section to compute the successive corrections to the natural frequencies and mode shapes of the system when the contact forces are included.

The computation of mode shapes requires the considered system of equations to be linear and, therefore, the contact forces $\mathbf{g}(\mathbf{x}_c, \dot{\mathbf{x}}_c)$ will be modeled as $\mathbf{K}_f\mathbf{x}_c$, where the contacts are considered to be acting in the linear regime from the expressions given in Eqs. (4.4) and

(4.5), and without gap states.

4.2.1 Failure of the Straightforward Approximation

With the assumption that the contact forces are linear, the complete eigenvalue problem takes the form

$$\left[-\omega^2 \begin{pmatrix} \mathbf{M}_{ee} & \mathbf{M}_{ec} \\ \mathbf{M}_{ce} & \mathbf{M}_{cc} \end{pmatrix} + \begin{pmatrix} \mathbf{K}_{ee} & \mathbf{K}_{ec} \\ \mathbf{K}_{ce} & \mathbf{K}_{cc} + \mathbf{K}_f \end{pmatrix}\right] \begin{pmatrix} \mathbf{x}_e \\ \mathbf{x}_c \end{pmatrix} = \begin{pmatrix} \mathbf{0} \\ \mathbf{0} \end{pmatrix}. \tag{4.12}$$

We will start by making the following asymptotic expansions

$$\begin{aligned} \omega^2 &= \omega^{(0)2} + \omega^{(1)2} + \omega^{(2)2} + \cdots, \\ \mathbf{x}_e &= \mathbf{x}_e^{(0)} + \mathbf{x}_e^{(1)} + \mathbf{x}_e^{(2)} + \cdots, \\ \mathbf{x}_c &= \mathbf{x}_c^{(0)} + \mathbf{x}_c^{(1)} + \mathbf{x}_c^{(2)} + \cdots, \end{aligned} \tag{4.13}$$

where each subsequent order is assumed to be much smaller than the previous one. These expansions are inserted into the eigenvalue problem (4.12) and a sequence of problems is generated for each approximation order.

We make the assumption that the motion of the contact displacements is much smaller than the elastic ones, i.e., $\mathbf{x}_c^{(0)} \ll \mathbf{x}_e^{(0)}$. With this full-stuck assumption, we take, at leading order

$$\mathbf{x}_c^{(0)} = \mathbf{0}, \tag{4.14}$$

and solve for the elastic displacements from the first block of Eq. (4.12), getting

$$(-\omega^{(0)2}\mathbf{M}_{ee} + \mathbf{K}_{ee})\mathbf{x}_e^{(0)} = 0, \tag{4.15}$$

which is precisely the equation for the full-stuck modes. From here, we choose to analyze the mode n, described by the eigenpair (ω_n^2, ϕ_n). Therefore, the leading order approximation of the frequency is $\omega^{(0)2} = \omega_n^2$ and the elastic displacements are given by $\mathbf{x}_e^{(0)} = \phi_n$.

To compute the next order correction of the contact displacements, we use now the second block of Eq. (4.12), which gives

$$\mathbf{K}_{ce}\mathbf{x}_e^{(0)} + (\mathbf{K}_{cc} + \mathbf{K}_f)\mathbf{x}_c^{(1)} = 0, \tag{4.16}$$

where the inertia terms are discarded since they are much smaller than the stiffness. Physically, this means that the frequency of the motion of the contact DOFs is much higher than

the modal frequency. This point is explained in more detail in the next subsection, where the correct form of the asymptotic model is given.

The first correction of the contact displacements is obtained by solving the linear system (4.16), which gives

$$\mathbf{x}_c^{(1)} = -(\mathbf{K}_{cc} + \mathbf{K}_f)^{-1}\mathbf{K}_{ce}\phi_n. \tag{4.17}$$

As it will be apparent below, this step is the responsible for the failure of the approximation, since this correction of the contacts does not include the motion induced in the elastic displacements by the constrained modes, which turns out to be of the same order of magnitude as the corrections to the full-stuck modes.

If we continue with this straightforward approximation process, to compute the first correction to the natural frequency, we come back to the first block of the eigenvalue problem to get

$$(-\omega^{(0)2}\mathbf{M}_{ee} + \mathbf{K}_{ee})\mathbf{x}_e^{(1)} = \omega^{(1)2}\mathbf{M}_{ee}\mathbf{x}_e^{(0)} - \mathbf{K}_{ec}\mathbf{x}_c^{(1)}, \tag{4.18}$$

where again the inertia term of the contacts has been discarded due to being much smaller than the rest. To obtain the first correction, we have to apply a solvability condition, since the linear operator on the left-hand side is singular. This condition is obtained by taking the inner product of the equation with the full-stuck mode ϕ_n (the matrix is symmetric), which gives the frequency correction

$$\omega^{(1)2} = \phi_n^\top \mathbf{K}_{ec}\mathbf{x}_c^{(1)}. \tag{4.19}$$

This approximation is tested in a model presented in Fig. 4.5. This toy model represents a simplified blade. The lateral structures have the DOFs on the bottom part fixed, and they interact with the blade through a surface which contains six contact pairs in each side (highlighted in red in the figure). As commented before, the contact forces are just linear springs in this simple case.

We focus on the analysis of the first frequency, whose exact value is $\omega_{\text{exact}} = 203.34$ Hz. The full-stuck frequency, ω_1, is

$$\omega_1 = 204.30 \text{ Hz}. \tag{4.20}$$

From the perturbative expansion, we expect to approximate the exact value with

$$\omega_{\text{exact}} \approx \omega_1 + \omega_1^{(1)}. \tag{4.21}$$

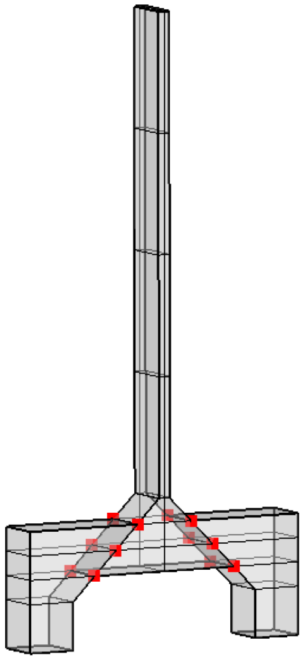

Figure 4.5: Simplified structure with a central beam connected by two attachments to the ground. The contact nodes are highlighted in red.

Using the formula for the first correction, we obtain

$$\omega_1 + \omega_1^{(1)} = 204.28 \text{ Hz}, \tag{4.22}$$

so the first correction is very small, and the corrected value is practically the same as the full-stuck frequency. In other words, the procedure derived in this section underestimates the effect of the contact forces by a large amount. This fact bares resemblance to the results in the recent works [76]–[78], where it was found that using just a set of stick modes in the elastic part to characterize the friction forces consistently underestimated the nonlinear dissipation (standard energy method).

The process outlined here is equivalent to the energy method: (i) first the full-stuck mode is computed, (ii) then it is used to obtain the displacements of the contacts, and (iii) the work produced by the forces induced at the contact by the full-stuck mode is evaluated using expression (4.19). In this simple case, since the problem is conservative (contact forces are just linear springs), there is no dissipation obtained from the energy method, only a correction in frequency. Nevertheless, when retaining friction effects, the nonlinear dissipation, although small, is essential to accurately compute the response of the system.

In the next subsection, we start from the Craig-Bampton formulation, and highlight the key

difference that allows to obtain the accurate approximation of the natural frequencies of the system.

4.2.2 Correct Asymptotic Approximation

The eigenvalue problem using the Craig-Bampton transformation is given by

$$\left[-\omega^2 \begin{pmatrix} \mathbf{I} & \mathbf{M}_{ax} \\ \mathbf{M}_{xa} & \mathbf{M}_{xx} \end{pmatrix} + \begin{pmatrix} \mathbf{\Omega}_a^2 & \mathbf{0} \\ \mathbf{0} & \mathbf{K}_{xx} + \mathbf{K}_f \end{pmatrix}\right] \begin{pmatrix} \mathbf{a} \\ \mathbf{x}_c \end{pmatrix} = \begin{pmatrix} \mathbf{0} \\ \mathbf{0} \end{pmatrix}. \tag{4.23}$$

Again, we start by making the following asymptotic expansions

$$\begin{aligned} \omega^2 &= \omega_n^2 + \omega_n^{(1)2} + \omega_n^{(2)2} + \cdots, \\ \mathbf{a} &= \mathbf{a}^{(0)} + \mathbf{a}^{(1)} + \mathbf{a}^{(2)} + \cdots, \\ \mathbf{x}_c &= \mathbf{x}_c^{(0)} + \mathbf{x}_c^{(1)} + \mathbf{x}_c^{(2)} + \cdots, \end{aligned} \tag{4.24}$$

where, as before, the leading order term of the frequency is the full-stuck frequency ω_n^2.

Zeroth order: Following a similar approach to the previous asymptotic models, at leading order we make the assumption that the displacements of the contacts are much smaller than the modal amplitudes, i.e., $\mathbf{x}_c^{(0)} \ll \mathbf{a}^{(0)}$. With this full-stuck assumption, we take

$$\mathbf{x}_c^{(0)} = \mathbf{0}, \tag{4.25}$$

and solve for the modal amplitudes from the first block of Eq. (4.23), getting

$$(\omega_k^2 - \omega_n^2) a_k^{(0)} = 0, \tag{4.26}$$

whose solution is $a_k^{(0)} = 0$ for $k \neq n$. If $k = n$, we may take $a_n^{(0)} = 1$ since the full-stuck modes were already normalized to be orthogonal with respect to the $\mathbf{M}_{ee}$ matrix. This leading order term from the modal amplitude is expected, since we are just recovering the results from the full-stuck assumption, i.e. that the first approximation of the mode is ϕ_n.

First order: At this order, after introducing Eq. (4.24) into Eq. (4.23), from the equations corresponding to the contact DOFs we get

$$-\omega_n^2 \mathbf{M}_{xa} \mathbf{a}^{(0)} - \omega_n^2 \mathbf{M}_{xx} \mathbf{x}_c^{(1)} + (\mathbf{K}_{xx} + \mathbf{K}_f) \mathbf{x}_c^{(1)} = 0. \tag{4.27}$$

The first correction of the contact displacements can be directly obtained by solving the

linear system

$$(\mathbf{K}_{xx} + \mathbf{K}_f - \omega_n^2 \mathbf{M}_{xx})\mathbf{x}_c^{(1)} = \omega_n^2 \mathbf{M}_{xa}\mathbf{a}^{(0)}. \tag{4.28}$$

An important remark is that the term $\omega_n^2 \mathbf{M}_{xx}$ is again much smaller than the contact stiffness, and it could be safely neglected. This has been verified empirically, and is a consequence of ω_n being related to the modal frequency and not to the contact motion. In order for the inertial term to be of the same size as the stiffness terms, one would have to use the frequency of vibration computed from the contact stiffness matrix $\mathbf{K}_{xx}$. This frequency is expected to be much higher than ω_n, since the modal stiffness is usually much smaller than the physical stiffness between the contact nodes.

A key difference with respect to the previous derivation in Eq. (4.16) is that $\mathbf{K}_{xx}$ contains now an additional term apart from $\mathbf{K}_{cc}$. Recalling its definition

$$\mathbf{K}_{xx} = \mathbf{K}_{cc} - \Psi^\top \mathbf{K}_{ee} \Psi, \tag{4.29}$$

we see that the term $\Psi^\top \mathbf{K}_{ee}\Psi$ is now present, where Ψ are the so-called constrained modes in the Craig-Bampton process. These modes take into account the effect of the motion of the contact DOFs on the elastic displacements. The motion of the contacts induces displacements that are similar to a rigid body motion of the elastic DOFs of the structure, and this contribution is crucial to obtain an accurate estimation of the linear modes, since the correction of the amplitude of the full-stuck mode is of the same order as the contribution from the constrained modes. It is very important to highlight that this effect is not nonlinear, since we are studying a completely linear problem.

To write it more explicitly, the valid correction of the contact displacements is

$$\mathbf{x}_c^{(1)} = -(\mathbf{K}_{cc} - \Psi^\top \mathbf{K}_{ee}\Psi + \mathbf{K}_f)^{-1}\mathbf{K}_{ce}\phi_n, \tag{4.30}$$

whereas in the previous section we obtained

$$\mathbf{x}_c^{(1)} = -(\mathbf{K}_{cc} + \mathbf{K}_f)^{-1}\mathbf{K}_{ce}\phi_n. \tag{4.17}$$

After computing the contact correction, one could go back to the equation of the modal amplitudes, which at this order is

$$(\omega_k^2 - \omega_n^2)a_k^{(1)} = \omega_n^2(\mathbf{M}_{ax}\mathbf{x}_c^{(1)})_k + \omega_n^{(1)2} a_k^{(0)}. \tag{4.31}$$

The notation $(\mathbf{M}_{ax}\mathbf{x}_c^{(1)})_k$ is used to represent the kth component of the vector. If we take $k =$

n on this equation, which corresponds to the solvability condition, the frequency correction is directly computed as

$$\omega_n^{(1)2} = -\omega_n^2(\mathbf{M}_{ax}\mathbf{x}_c^{(1)})_n. \tag{4.32}$$

The term $\omega_n^2(\mathbf{M}_{ax}\mathbf{x}_c^{(1)})_n$ can be written in terms of the original FEM matrices in a very simple way

$$-\omega_n^2(\mathbf{M}_{ax}\mathbf{x}_c^{(1)})_n = -\omega_n^2(\phi_n^\top \mathbf{M}_{ee}\Psi + \phi_n^\top \mathbf{M}_{ec})\mathbf{x}_c^{(1)} = \phi_n^\top \mathbf{K}_{ec}\mathbf{x}_c^{(1)} - \omega_n^2\phi_n^\top \mathbf{M}_{ec}\mathbf{x}_c^{(1)}, \tag{4.33}$$

where the third equality follows from the definition of the full-stuck eigenvector $\omega_n^2\mathbf{M}_{ee}\phi_n = \mathbf{K}_{ee}\phi_n$, and is further simplified using the expression of the constrained modes $\Psi = -\mathbf{K}_{ee}^{-1}\mathbf{K}_{ec}$. By the same argument as before, the inertia terms related to the contact are expected to be much smaller than the stiffness term, so that

$$-\omega_n^2(\mathbf{M}_{ax}\mathbf{x}_c^{(1)})_n \approx \phi_n^\top \mathbf{K}_{ec}\mathbf{x}_c^{(1)}. \tag{4.34}$$

Therefore, the frequency correction can be now expressed as

$$\omega_n^{(1)2} = \phi_n^\top \mathbf{K}_{ec}\mathbf{x}_c^{(1)}, \tag{4.35}$$

which is just a simple projection along corresponding full-stuck mode after solving a linear system of the size of the contacts to compute $\mathbf{x}_c^{(1)}$. This is the same result as the one from the previous subsection, but now the first approximation of the contacts is computed taking into account the constrained modes.

The first order modal amplitude can be computed by taking $k \neq n$ in Eq. (4.31), which gives

$$a_k^{(1)} = -\frac{\phi_k^\top \mathbf{K}_{ec}\mathbf{x}_c^{(1)}}{\omega_k^2 - \omega_n^2}. \tag{4.36}$$

The amplitude of the nth mode remains free, and in this case it is chosen so that $a_n^{(1)} = 0$, i.e., the first correction is orthogonal to the full-stuck nth mode. This is a convenient choice in perturbation theory, and does not affect the computation of the correction (see [121] for more details) since this vector is contained in the nullspace of the operator $(\omega_k^2 - \omega_n^2)$. This choice implies that the eigenvector computed from the asymptotic expansion is no longer normalized with respect to the mass matrix, but this is not required to proceed obtaining subsequent approximations.

In terms of physical displacements, using the CB transformation from Eq. (4.9), we may

write

$$\begin{aligned} \mathbf{x}_e &= \phi_n + \Psi \mathbf{x}_c^{(1)} + \Phi \mathbf{a}^{(1)} + \cdots , \\ \mathbf{x}_c &= \mathbf{0} + \mathbf{x}_c^{(1)} + \cdots , \end{aligned} \tag{4.37}$$

where the elastic displacements are corrected with some contribution of the full-stuck modes contained in $\mathbf{a}^{(1)}$ and another from the contact correction $\mathbf{x}_c^{(1)}$ through the constrained modes Ψ.

These expressions are again applied to the simplified structure shown in Fig. 4.5. Recall that the value of the first exact frequency is $\omega_{\text{exact}} = 203.34$ Hz. Using the corrected perturbative expansion developed in this section, we obtain

$$\omega_1 + \omega_1^{(1)} = 203.32 \text{ Hz}, \tag{4.38}$$

which is now exact up to 0.5%, with an error 50 times smaller than in the previous case.

4.3 Asymptotic Model

The asymptotic model for the nonlinear vibrations of a mechanical system is now derived. As a reference, we repeat the equations of motion of the system

$$\begin{pmatrix} \mathbf{M}_{ee} & \mathbf{M}_{ec} \\ \mathbf{M}_{ce} & \mathbf{M}_{cc} \end{pmatrix} \begin{pmatrix} \ddot{\mathbf{x}}_e \\ \ddot{\mathbf{x}}_c \end{pmatrix} + \beta \begin{pmatrix} \mathbf{K}_{ee} & \mathbf{K}_{ec} \\ \mathbf{K}_{ce} & \mathbf{K}_{cc} \end{pmatrix} \begin{pmatrix} \dot{\mathbf{x}}_e \\ \dot{\mathbf{x}}_c \end{pmatrix} + \begin{pmatrix} \mathbf{K}_{ee} & \mathbf{K}_{ec} \\ \mathbf{K}_{ce} & \mathbf{K}_{cc} \end{pmatrix} \begin{pmatrix} \mathbf{x}_e \\ \mathbf{x}_c \end{pmatrix} + \begin{pmatrix} 0 \\ \mathbf{g}(\mathbf{x}_c, \dot{\mathbf{x}}_c) \end{pmatrix} = \begin{pmatrix} \mathbf{f}(t) \\ 0 \end{pmatrix}. \tag{4.2}$$

As mentioned before, the derivation will be carried out from the equations expressed in the CB basis, which are given by

$$\begin{pmatrix} \mathbf{I} & \mathbf{M}_{ax} \\ \mathbf{M}_{xa} & \mathbf{M}_{xx} \end{pmatrix} \begin{pmatrix} \ddot{\mathbf{a}} \\ \ddot{\mathbf{x}}_c \end{pmatrix} + \beta \begin{pmatrix} \mathbf{\Omega}_a^2 & \mathbf{0} \\ \mathbf{0} & \mathbf{K}_{xx} \end{pmatrix} \begin{pmatrix} \dot{\mathbf{a}} \\ \dot{\mathbf{x}}_c \end{pmatrix} + \begin{pmatrix} \mathbf{\Omega}_a^2 & \mathbf{0} \\ \mathbf{0} & \mathbf{K}_{xx} \end{pmatrix} \begin{pmatrix} \mathbf{a} \\ \mathbf{x}_c \end{pmatrix} + \begin{pmatrix} 0 \\ \mathbf{g}(\mathbf{x}_c, \dot{\mathbf{x}}_c) \end{pmatrix} = \begin{pmatrix} \mathbf{f}_a(t) \\ \mathbf{f}_x(t) \end{pmatrix}. \tag{4.10}$$

The reason of using the CB formulation, as illustrated in the previous section with the linear mode analysis, is that it naturally incorporates the constrained modes, which are key to correctly estimate the effect of the contact forces. Throughout the derivation of the model, the results will be related to the original FEM matrices for numerical implementation, since the projection into the CB basis is only convenient for the theoretical derivation.

The asymptotic model is developed to study the forced response close to a resonance crossing, and therefore the frequency of the forcing term is assumed to be close to one of the natural frequencies of the structure. The main assumption of the model is that the motion of the

system will be close to the corresponding full-stuck mode, since the motion of the contacts is expected to be small. The nonlinear forces, acting on the contacts, provide a relevant mechanism of dissipation. The evolution of the amplitude of vibration along the corresponding full-stuck mode will vary slowly in a timescale governed by the small effect of friction.

Following the same procedure as in Chapter 2, we separate the two timescales present in the problem. We use t to denote the fast timescale, associated to the elastic oscillations of the structure. The slower timescale, τ, is related to the evolution of the slow envelope of the amplitude of vibration, in a similar way as was depicted in Fig. 2.6. Starting from the system projected in the CB basis, we expand the modal amplitudes and contact displacements in an asymptotic expansion as functions of these two times, obtaining

$$\begin{aligned} \mathbf{a}(t,\tau) &= \mathbf{a}^{(0)}(t,\tau) + \mathbf{a}^{(1)}(t,\tau) + \cdots, \\ \mathbf{x}_c(t,\tau) &= \mathbf{x}_c^{(0)}(t,\tau) + \mathbf{x}_c^{(1)}(t,\tau) + \cdots, \end{aligned} \tag{4.39}$$

where each subsequent order in the expansion is much smaller than the previous one. The time derivatives have to be also expressed in terms of the two variables,

$$\begin{aligned} \frac{\mathrm{d}}{\mathrm{d}t} &= \frac{\partial}{\partial t} + \frac{\partial}{\partial \tau}, \\ \frac{\mathrm{d}^2}{\mathrm{d}t^2} &= \frac{\partial^2}{\partial t^2} + 2\frac{\partial^2}{\partial t \partial \tau} + \frac{\partial^2}{\partial \tau^2}, \end{aligned} \tag{4.40}$$

where the terms involving the derivative with respect to τ will be considered smaller than the ones with the fast timescale t since $\tau \gg t$.

Zeroth order: At leading order, the contacts are assumed to be fully stuck (with no relative motion between the solids in contact), which can be expressed as $\mathbf{x}_c^{(0)} = \mathbf{0}$. Introducing this condition and the expansions in Eqs. (4.39), (4.40) into Eq. (4.10), we obtain the following simple oscillator equation for each modal amplitude

$$(\partial_{tt} + \omega_k^2) a_k^{(0)} = 0. \tag{4.41}$$

Assuming that the full-stuck modes are well separated in frequency, and that we perform the analysis close to one of these frequencies, denoted by ω_A, we can study just the mode of interest, which is mathematically stated as

$$a_k^{(0)} = 0, \tag{4.42}$$

for $k \neq A$, and

$$a_A^{(0)}(t,\tau) = A(\tau)e^{i\omega_A t} + \text{c.c.}, \tag{4.43}$$

which is the solution of a harmonic oscillator with a slowly varying amplitude $A(\tau)$. Therefore, at zeroth order, we have that the motion of our system is close to the full-stuck mode of interest ϕ_A, but modulated with an amplitude that is changing with the slow timescale and needs to be resolved at subsequent orders in the perturbation expansion.

In terms of physical displacements, the motion of the DOFs of the structure is given by

$$\begin{aligned} \mathbf{x}_e^{(0)}(t,\tau) &= A(\tau)e^{i\omega_A t}\boldsymbol{\phi}_A + \text{c.c.}, \\ \mathbf{x}_c^{(0)}(t,\tau) &= \mathbf{0}. \end{aligned} \tag{4.44}$$

First order: The nonlinear forces, linear damping and external forcing are considered as first order corrections, in order to produce a distinguished limit that captures all small effects present in the system. From the contact equations, we get

$$\mathbf{M}_{xa}\mathbf{a}_{tt}^{(0)} + \mathbf{M}_{xx}\mathbf{x}_{c_{tt}}^{(1)} + \mathbf{K}_{xx}\mathbf{x}_c^{(1)} + \mathbf{g}(\mathbf{x}_c^{(1)}, \dot{\mathbf{x}}_c^{(1)}) = 0, \tag{4.45}$$

and, moving to the left-hand side the unknown correction of the contacts, we get

$$\mathbf{M}_{xx}\mathbf{x}_{c_{tt}}^{(1)} + \mathbf{K}_{xx}\mathbf{x}_c^{(1)} + \mathbf{g}(\mathbf{x}_c^{(1)}, \dot{\mathbf{x}}_c^{(1)}) = -\mathbf{M}_{xa}\mathbf{a}_{tt}^{(0)}. \tag{4.46}$$

From this equation, on the left-hand side, the inertia terms can be neglected compared to the stiffness and nonlinear forces, $\mathbf{M}_{xx}\mathbf{x}_{c_{tt}}^{(1)} \ll \mathbf{K}_{xx}\mathbf{x}_c^{(1)}, \mathbf{g}(\mathbf{x}_c^{(1)}, \dot{\mathbf{x}}_c^{(1)})$. This has been validated empirically in the analysis, and the physical reason, as in the linear mode computation, is that the contact stiffness is much larger than the modal stiffness. Therefore, the frequency associated with the contact motion will much higher than the modal frequency. In other words, the timescale for the contact motion is smaller than the modal displacements, and therefore it could be assumed that the contacts adjust instantaneously to the changes of the forcing coming from the right-hand side, similarly to a quasi-steady approximation.

Additionally, the term $\mathbf{M}_{xa}\mathbf{a}_{tt}^{(0)}$ can be simplified, because there is only one component of the modal amplitude vector that is different from zero. Therefore, we have

$$\begin{aligned} \mathbf{M}_{xa}\mathbf{a}_{tt}^{(0)} &= -\omega_A^2(\Psi^\top \mathbf{M}_{ee}\boldsymbol{\phi}_A + \mathbf{M}_{ce}\boldsymbol{\phi}_A)(A(\tau)e^{i\omega_A t} + \text{c.c. }) \\ &= (\mathbf{K}_{ce}\boldsymbol{\phi}_A - \omega_A^2\mathbf{M}_{ce}\boldsymbol{\phi}_A)(2|A|\cos(\omega_A t + \varphi_A)) \\ &\approx 2|A|\cos(\omega_A t + \varphi_A)\mathbf{K}_{ce}\boldsymbol{\phi}_A, \end{aligned} \tag{4.47}$$

where the inertial term related to the contacts $-\omega_A^2 \mathbf{M}_{ce}\phi_A$ has also been neglected. The first term on the right-hand side was simplified using $-\omega_A^2 \mathbf{M}_{ee}\phi_A = -\mathbf{K}_{ee}\phi_A$ which follows from the definition of the full-stuck modes, and the definition of the constrained modes (Eq. 4.8) has been also used to further simplify the expression. The term φ_A is the phase of the complex amplitude $A(\tau)$. After putting all together, in order to compute the first correction of the contact displacements, we need to solve

$$\mathbf{K}_{xx}\mathbf{x}_c^{(1)} + \mathbf{g}(\mathbf{x}_c^{(1)}, \dot{\mathbf{x}}_c^{(1)}) = -2|A|\cos(\omega_A t + \varphi_A)\mathbf{K}_{ce}\phi_A. \tag{4.48}$$

This is a quasi-static equation of the size of the contacts in which the fast timescale t acts as a parameter on the right-hand side. The phase φ_A could be ignored since a change in the initial time could be used to absorb it, without loss of generality. The process to compute $\mathbf{x}_c^{(1)}$ is to solve, for a fixed value of the amplitude $|A|$, Eq. (4.48) for several periods of the frequency ω_A. Using the friction laws from Eqs. (4.4) and (4.5), the system usually takes at least two cycles to relax to a periodic state, due to the memory effects of the friction. Keep in mind that the term $\mathbf{K}_{xx} = \mathbf{K}_{cc} - \Psi^\top \mathbf{K}_{ee}\Psi$ contains the effect of the constrained modes which, as remarked before, are crucial to estimate the effect of the nonlinear forces. In fact, neglecting this term would lead to a significant underestimation of the nonlinear dissipation, as it will be explained in the results.

In this work, this system (4.48) is solved as a nonlinear set of equations for each value of t on the right-hand side. Another possibility could be to use a HBM method to obtain directly the Fourier coefficients of $\mathbf{x}_c^{(1)}$, using the modal amplitude $|A|$ as the continuation variable (since the frequency in this process is fixed to the full-stuck one).

Solving Eq. (4.48) is the more computationally expensive part of the asymptotic procedure, where a nonlinear system of the size of the contacts has to be solved several times. This is a considerable reduction since the number of DOFs of the complete system is much larger. An important remark of the asymptotic process, as it will be made explicit in the final equation, is that this process is done just once, and is used to characterize the nonlinear forces in the asymptotic equation.

After solving the Eq. (4.48), the evolution of the contact displacements is a periodic function of the fast time that can be expressed in terms of a Fourier series

$$\mathbf{x}_c^{(1)}(t,\tau) = \sum_{k=-\infty}^{\infty} \mathbf{P}_k(|A|)e^{ik\omega_A t}e^{ik\varphi_A}, \tag{4.49}$$

where $\mathbf{P}_k(|A|)$ is the Fourier amplitude vector. Going back to the amplitude equations, which

are diagonal in the terms involving the modal amplitudes, we have

$$(\partial_{tt} + \omega_k^2) a_k^{(1)} = -2a_{k_{t\tau}}^{(0)} - (\mathbf{M}_{ax}\mathbf{x}_{c_{tt}}^{(1)})_k - \beta\omega_k^2 a_{k_t}^{(0)} + (f_k e^{i\omega_A t} e^{i\Delta\omega_f \tau} + \text{c.c.}), \tag{4.50}$$

for $k = 1, \ldots, N_a$, where N_a is the total number of full-stuck modes. The term $(\mathbf{M}_{ax}\mathbf{x}_{c_{tt}}^{(1)})_k$ represents the kth row of this vector. In this expression, we have assumed that the forcing is harmonic, and that the frequency of the forcing is close to ω_A, to inspect the vicinity of the resonance crossing. The value f_k is the projection of the forcing amplitude vector onto the full-stuck mode ϕ_k.

To obtain the evolution of the slow envelope A, we consider the previous equation when $k = A$, which corresponds to the only component of the modal amplitude of zeroth order which is different from zero. Then, since the right-hand side terms contain solutions from the nullspace of the left-hand side operator, we need to apply the solvability condition by removing all the terms proportional to $e^{i\omega_A t}$. This is exactly the same process that was carried out in Chapter 2, in Eq. (2.27). By doing so, one gets

$$2i\omega_A \frac{\mathrm{d}A}{\mathrm{d}\tau} = \omega_A^2 (\mathbf{M}_{ax}\mathbf{P}_1)_A e^{i\varphi_A} - i\beta\omega_A^3 A + f_A e^{i\Delta\omega_f \tau}. \tag{4.51}$$

Similar to Eq. (4.33), the nonlinear term can be simplified in the following way

$$\begin{aligned} \omega_A^2 (\mathbf{M}_{ax}\mathbf{P}_1)_A &= \omega_A^2 (\phi_A^\top \mathbf{M}_{ee}\Psi + \phi_A^\top \mathbf{M}_{ec})\mathbf{P}_1, \\ &= -\phi_A^\top \mathbf{K}_{ec}\mathbf{P}_1 - \omega_A^2 \phi_A^\top \mathbf{M}_{ec}\mathbf{P}_1, \\ &\approx -\phi_A^\top \mathbf{K}_{ec}\mathbf{P}_1. \end{aligned} \tag{4.52}$$

The complex friction coefficient is defined as

$$Q(|A|) = -\frac{\phi_A^\top \mathbf{K}_{ec}\mathbf{P}_1}{|A|}, \tag{4.53}$$

since then $\omega_A^2 (\mathbf{M}_{ax}\mathbf{P}_1)_A e^{i\varphi_A} = Q(|A|)A$. Putting all together, we find the differential equation for the slow envelope

$$\frac{\mathrm{d}A}{\mathrm{d}\tau} = -\frac{i}{2\omega_A} Q(|A|)A - \xi_A A - \frac{i}{2\omega_A} f_A e^{i\Delta\omega_f \tau}. \tag{4.54}$$

where $\xi_A = \beta\omega_A^2/2$. This one-dimensional nonlinear oscillator gives a description of the slow time dynamics of the system close to a resonance crossing. Notice that this equation is exactly the same as the one obtained for a mass-spring system in Eq. (3.8). Even though there has

been no discussion about the aerodynamic forces, they could be included just by modifying the linear damping term ξ_A, since in a bladed-disk the aerodynamics effects are usually considered linear. This would enable to perform similar studies to the ones presented in Fig. (3.12) where switching between forced response solutions and flutter could be considered. After obtaining the amplitude A one can go back to the physical displacements using (4.44).

The following analysis will focus exclusively on this equation. Nonetheless, a brief consideration of its extension to a cyclic system will be provided. In the case of a flat family, where each individual ND has a very similar mode shape, the nonlinear friction function remains identical to $Q(|A|)$, as computed here. Consequently, the system can be extended to a cyclic configuration with exactly the same structure as Eq. (3.5), where the same friction function appears in all contact force terms, and the aerodynamic coefficients for the different NDs are included as linear terms for each TW. Nevertheless, if the family is not flat, meaning that mode shapes within the same family can differ significantly for different NDs, a modification would be required. In that scenario, each distinct mode shape must be taken into account during the projection step of the derivation the asymptotic equation, and a more complicated set of envelope equations is produced.

Now, we restrict ourselves to the analysis of the asymptotic equation (4.54), in particular focusing on just the forced response problem, since we will consider that $\xi_A > 0$ (and hence no solutions due to a linear instability could arise). The resonance curve is found by making the assumption of a periodic solution with the same frequency as the forcing, taking the form $A = |A|e^{i\Delta\omega_f \tau}e^{i\varphi_A}$. Plugging this expression into Eq. (4.54), and making $\mathrm{d}|A|/\mathrm{d}\tau = 0$, one obtains the complex equation

$$\frac{i}{2\omega_A}Q(|A|) + \xi_A + i\Delta\omega_f = -\frac{i}{2|A|\omega_A}fe^{-i\varphi}, \tag{4.55}$$

which can be solved similarly to Eq. (3.10). The resonance curve and the phase of the response are given by

$$\Delta\omega_f = -\frac{Q^R(|A|)}{2\omega_A} \pm \sqrt{\left(\frac{f_A}{2|A|\omega_A}\right)^2 - \left(\frac{Q^I(|A|)}{2\omega_A} - \xi_A\right)^2}, \tag{4.56}$$

$$\tan\varphi_A = \frac{\xi_A - Q^I(|A|)}{2\omega_A\Delta\omega_f + Q^R(|A|)}, \tag{4.57}$$

where we recall that the symbols Q^R, Q^I denote the real and imaginary parts of the complex friction coefficient, respectively. Eq. (4.56) gives the expression of the resonance curve, relating the forcing frequency, $\Delta\omega_f$, and the amplitude of vibration, $|A|$. This expression allows

for quick parametric studies in terms of the forcing amplitude f_A and the linear damping ξ_A, with the cost of just evaluating this simple analytical formula. As commented before, the part that is computationally expensive from the asymptotic model is the determination of the complex friction coefficient $Q(|A|)$, which involve solving a problem of the size of the contacts (Eq. 4.48). Once this is done, the analysis can be carried out directly in this simple one-dimensional nonlinear oscillator, which contains the relevant aspects of the dynamics of the structure. An important remark is that the periodic state with the forcing is just one of the solutions of the problem, since there are no assumptions made on the slow temporal evolution of the displacements. This provides an alternative to HBM methods, which typically require a priori knowledge of the frequencies present in the system, which can be challenging when more than one frequency appears in the solution, as in the case of the interaction of flutter and forcing explored in Chapter 3.

4.4 Application to Mechanical Structures

The asymptotic model derived in Eq. (4.54) is now validated using two FEM models, computing the resonance curves and validating the results against direct time integration.

4.4.1 Simplified Structure

We consider the same toy model presented in Fig. 4.5. The total number of DOFs in the structure is around 3000, making it feasible to perform a time integration of the complete structure, although typically many cycles are needed until convergence due to the small effect of nonlinear friction.

We investigate the first modal frequency of this system, which is close to 200 Hz for this model and corresponds to a bending mode of the blade (flap). The contact forces are given by the laws presented in Eqs. (4.4) and (4.5). The external forcing is applied on the tip of the blade, in the bending direction.

First, several time simulations have been conducted close to the resonance peak, and the forcing amplitude has been adjusted so that the nonlinear effects of the contacts are relevant. The behavior as a function of time of one of the contacts in each row from the blade-support interface (top, middle and bottom), highlighted with red dots in Fig. 4.5, is discussed now. Due to the symmetry of the excitation, only the motion of one side of the contact surface is discussed.

Figure 4.6 shows the contact information for the top row in the contact surface. The simula-

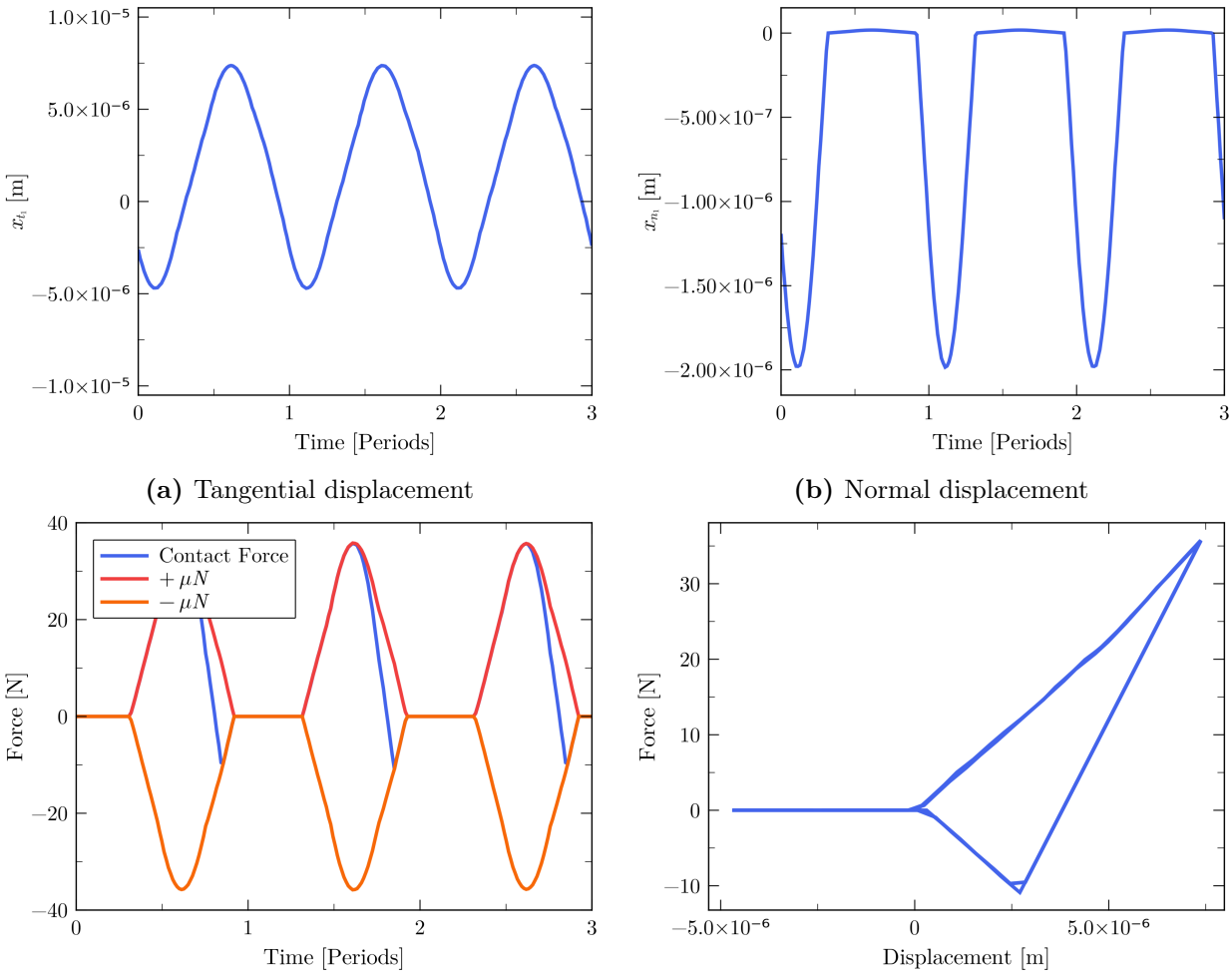

(a) Tangential displacement

(b) Normal displacement

(c) Friction forces

(d) Friction cycle

Figure 4.6: Contact information over three periods of the forcing frequency corresponding to the top row in Fig. 4.5.

tions contain three consecutive periods after the solution has converged to a periodic state. First, in Fig. 4.6a, the oscillations of the dominant tangential displacement x_{t_1} are plotted. The time evolution is sinusoidal but with small contributions of higher harmonics, as it was expected due to the presence of nonlinear terms. The evolution of the normal displacements is given in Fig. 4.6b. Recall that this DOF represents the relative displacement between the contact node pairs, so a negative value corresponds to separation. As it can be seen, when the normal displacement becomes positive, the values are much smaller than the negative ones, because in that regime the strong spring that was put in the normal direction is acting. The friction forces, in Fig. 4.6c, are drawn along with the friction limit, $\pm\mu N$. The normal load is clearly changing, and there are parts during one period of oscillation where the contact is in gap state, since the friction force is identically zero. During contact, there is a slip part when

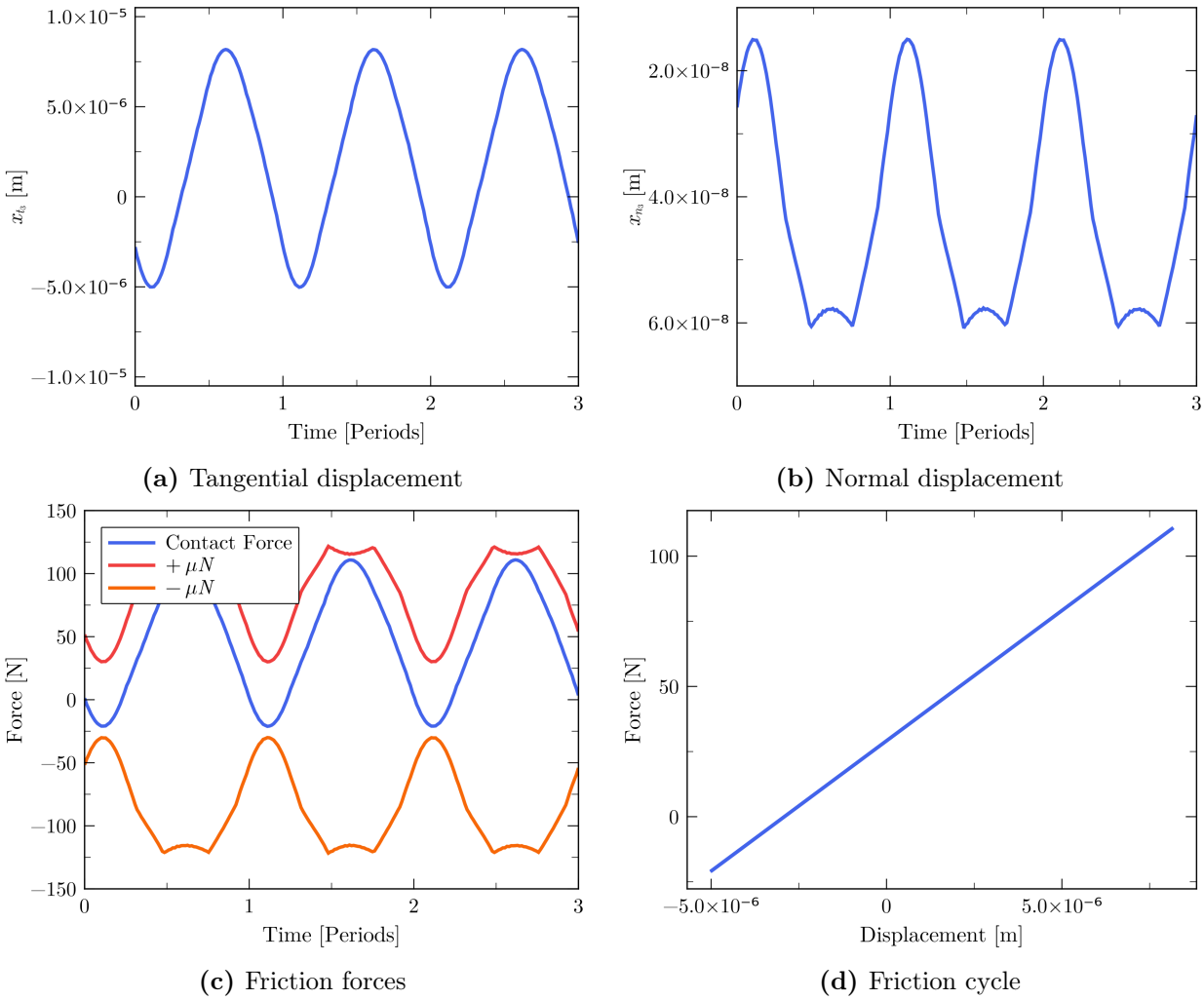

(a) Tangential displacement

(b) Normal displacement

(c) Friction forces

(d) Friction cycle

Figure 4.7: Contact information over three periods of the forcing frequency corresponding to the middle row in Fig. 4.5.

the tangential force is exactly $\pm\mu N$, and there is also a region with stick state, corresponding to the case where the blue line of the friction force can be seen between the two limits. In terms of the cycle, the shape matches the expected one from the friction model, as shown in Fig. 4.6d. The area of the cycle is directly related to the nonlinear dissipation, and we clearly see the alternation of stick, slip and gap states.

Next, we investigate the motion of the middle row of contacts from Fig. 4.5. The results are shown in Fig. 4.7, where major differences with respect to the previous row can be observed. The evolution of the tangential displacements (Fig. 4.7a) is quite similar, but the normal relative displacements are now always positive (Fig. 4.7b). This implies that the pair of nodes is always in contact, with no gap states. The friction forces, plotted in Fig. 4.7c, now show the system completely in stick regime, and there is no dissipation since the slip limit is

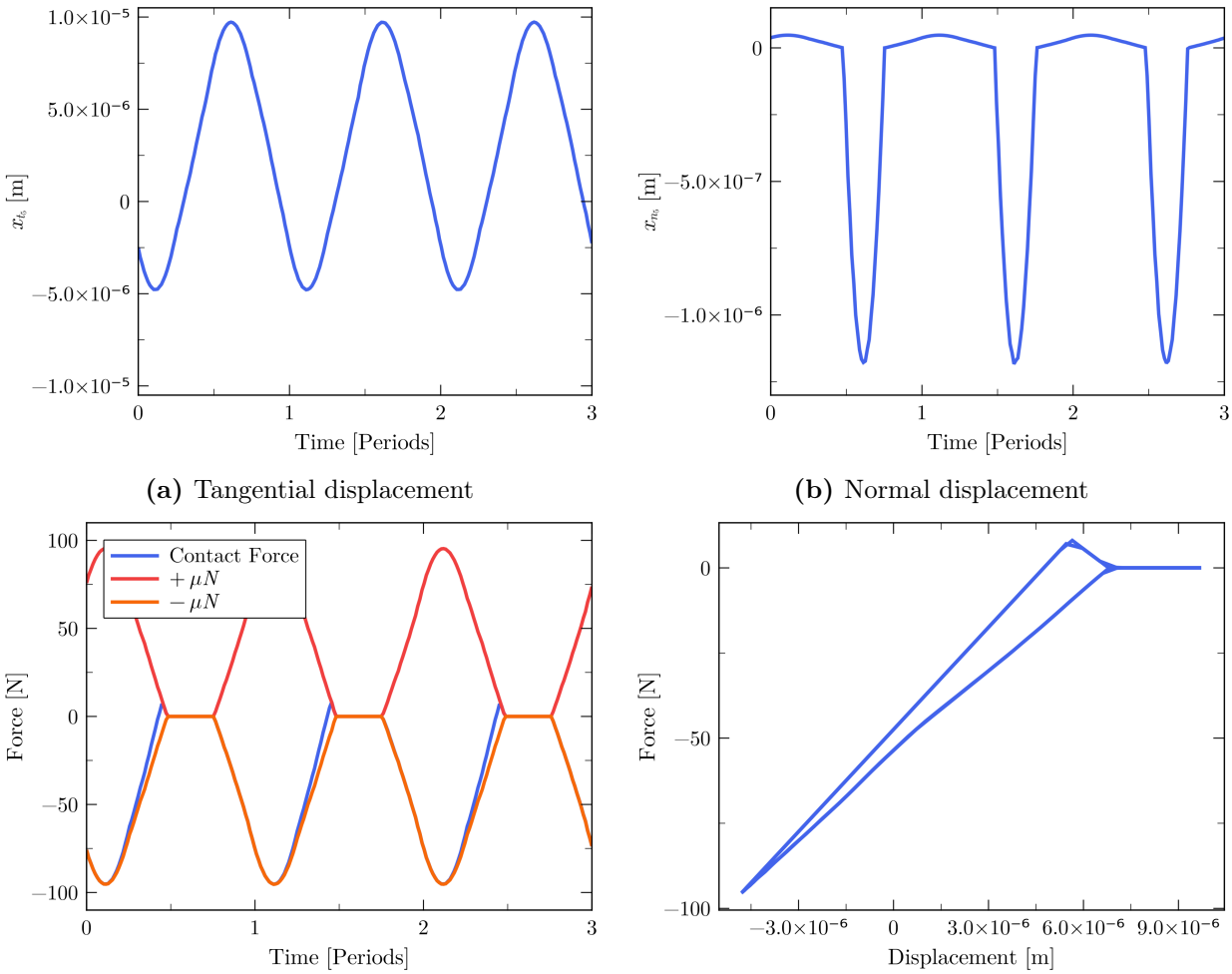

(a) Tangential displacement

(b) Normal displacement

(c) Friction forces

(d) Friction cycle

Figure 4.8: Contact information over three periods of the forcing frequency corresponding to the bottom row in Fig. 4.5.

not reached, despite the change in normal load. This can be clearly seen in the friction cycle (Fig. 4.7d), which has the form of a straight line.

Finally, the information of the bottom row of contacts is shown in Fig. 4.8. These contacts show a very similar behavior to the top row, where again there is a transition between stick, slip and gap states.

After this initial analysis, the goal of the asymptotic model is to capture the information of this complex transitions, where each contact could be in a different state, and encode them in a single complex function $Q(|A|)$, which is the only nonlinear term of the one-dimensional oscillator equation in Eq. (4.54).

The complex friction function is constructed using the expression (4.53) in terms of the modal

amplitude $|A|$. The resulting real and imaginary parts are shown in Figs. 4.9 and 4.10, respectively. The real part is associated with the nonlinear frequency shift of the resonance peak, which is nonzero even for $|A| = 0$. This behavior is due to the fact that, when the amplitude of vibration is small, the contacts act linearly in the stick regime, reducing the global stiffness of the structure with respect to the full-stuck case.

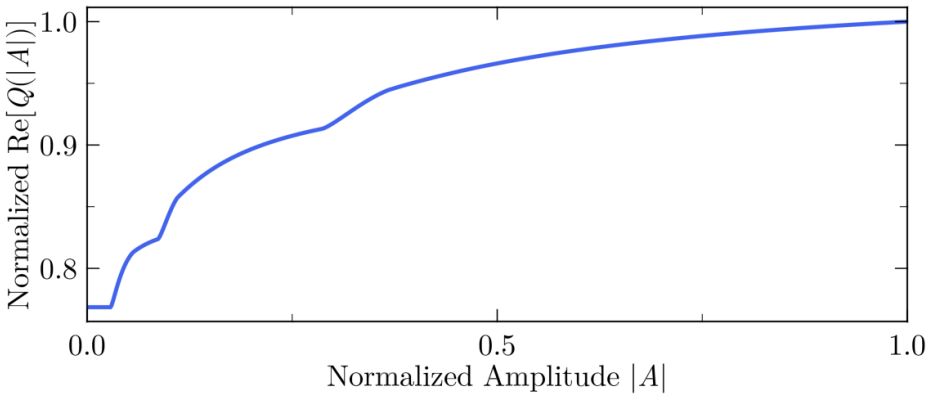

Figure 4.9: Real part of the complex friction coefficient.

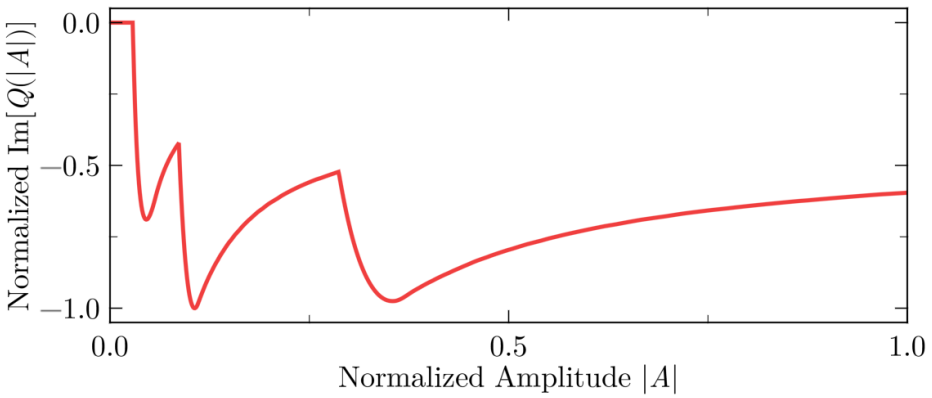

Figure 4.10: Resonance crossing of the first modal frequency of the simplified structure.

The imaginary part, related to the nonlinear dissipation of the contact forces, has much more interesting physical content. For smaller amplitudes, the dissipation is zero, since none of the contacts is slipping, which is necessary to dissipate energy. Then, as the amplitude of vibration grows, the nonlinear damping shows several peaks, and the dissipation does not increase monotonically with the amplitude of vibration (higher dissipation means more negative damping). This is because the maxima and minima shown in this plot are actually related to contact transitions, where one of the contact could switch from fully stick cycles to a motion with a transition between stick and slip. In addition, other contacts could exhibit a gap state, in which there is no dissipation and hence the nonlinear damping decreases. This

is the reason why the shape of this curve is far from monotone, encoding the information of the complex contact transitions. This is a major difference from the simple model considered in Chapter 2, where the nonlinear damping increased monotonically with the amplitude of vibration.

Notice that this type of nonlinearity is quite different from a geometrical one, which are usually included by doing a Taylor expansion and retaining the first resonant nonlinear terms in the expansion, and that typically takes the simple form $A|A|^2$. In this case, the friction function $Q(|A|)$ is much more complicated.

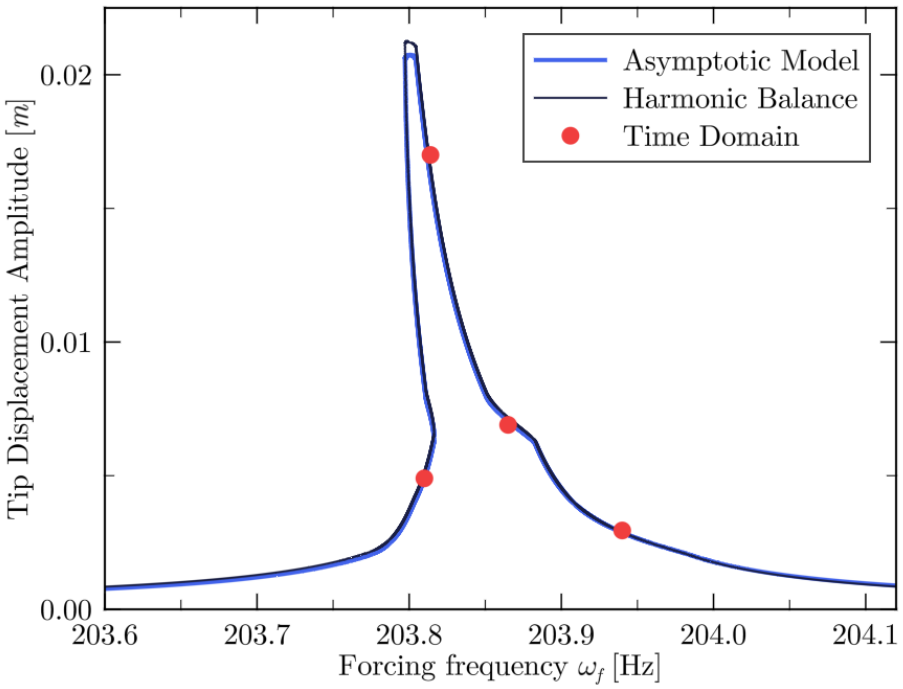

Figure 4.11: Resonance crossing of the first modal frequency of the simplified structure.

With the characterization of the nonlinear effects, the resonance curve of the system can be obtained directly from Eq. (4.56). Fig. 4.11 shows the results after evaluating the analytical expression. The response is clearly nonlinear, where, for large enough amplitude, the curve bends to the left, which is the typical behavior when there are gap and slip states. Additionally, on the left part of the resonance crossing, there is a coexistence of multiple states, so depending on the initial conditions different final solutions could be reached.

For several points in the curve, highlighted as red dots, time integration of full FEM system has been carried out. These points usually took over 2000 cycles to reach convergence, due to the local and small effect of friction. As it can be seen from the plot, there is a very good agreement between the asymptotic model and the time domain simulations. Additionally,

using a HBM method, the resonance curve has been computed, and the results are also in good agreement with the asymptotic model.

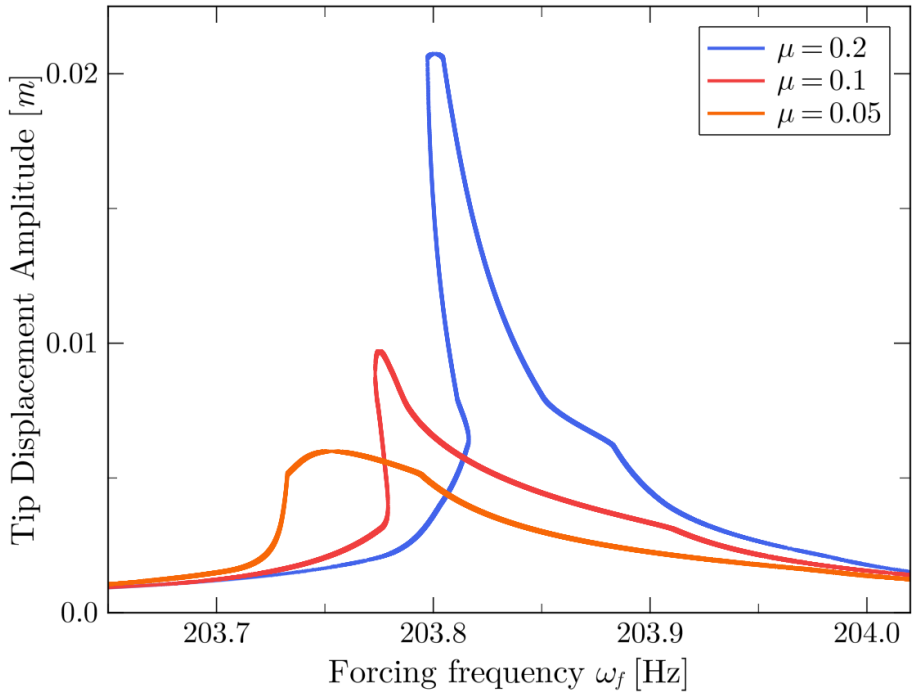

Figure 4.12: Parametric analysis in terms of the friction coefficient μ of the resonance curve of the simplified structure.

As commented before, one of the advantages of the asymptotic model, apart from reducing the analysis of the complete structure to a single equation, is the ability to perform quick parametric studies. Just to show a brief example, in Fig. 4.12, several resonance curves have been computed for different friction coefficient values. In this case, the amplitude of the response is reduced for lower friction coefficients. The reason is that the slip limit is reached more quickly by the contacts, and hence they start dissipating at lower amplitudes of vibration.

4.4.2 Approximation Without the Constrained Modes

As a complementary analysis, the asymptotic model is derived without taking into account the constrained modes in the solution of the contact displacement correction. This is done by setting $\mathbf{K}_{xx} = \mathbf{K}_{cc}$ in Eq. (4.48).

In Section 4.2, it was established that neglecting the constrained modes implied large errors in the estimation of the contact effect, even though the problem was linear.

For the dynamic analysis, we see this effect through the nonlinear coefficient Q that accounts

for the friction dissipation. Figs. 4.13 and 4.14 show the real and imaginary parts of the complex friction coefficient, respectively. The solid line indicates the solution when the asymptotic model is derived correctly, and the dashed line shows the values for the case where the constrained modes are neglected.

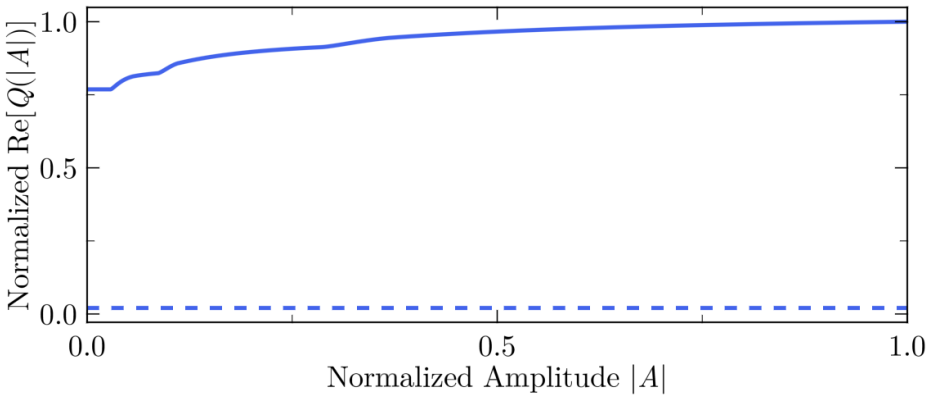

Figure 4.13: Real part of the complex friction coefficient. Solid line: approximation with constrained modes. Dashed line: approximation without constrained modes.

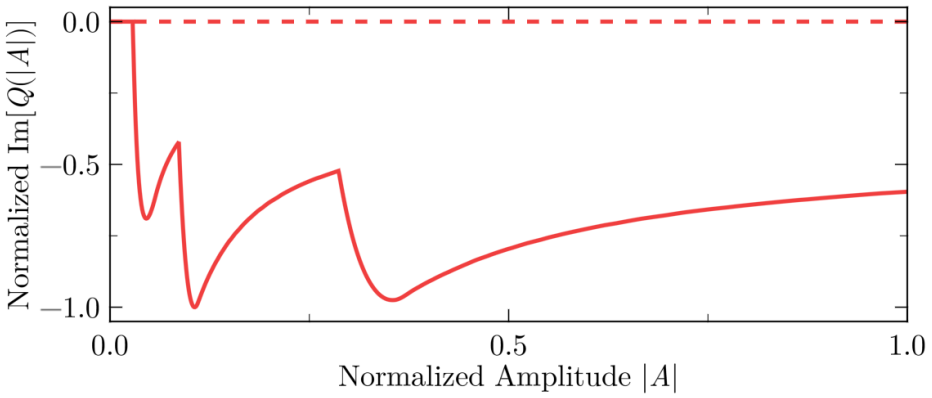

Figure 4.14: Resonance crossing of the first modal frequency of the simplified structure. Solid line approximation with constrained modes. Dashed line: approximation without constrained modes.

From the analysis of the real part, in Fig. 4.13, we see that the frequency correction without the constrained modes is nonzero, but takes a much smaller value. As it happened in Section 4.2, the correction of the frequency is underestimated by an order of magnitude, approximately.

More importantly, the imaginary part of the friction coefficient, shown in Fig. 4.14, which is related to the nonlinear damping, is much smaller than the correct values, providing almost no dissipation.

This underestimation of the nonlinear friction effects is similar to what was found in [76]–[78], where a fully coupled approach had to be used to accurately capture the dissipation induced by nonlinear forces present in the contact interfaces. From the analysis of this chapter, this effect seems to be related to the contribution of constrained modes, and not with the nonlinearity of the contact laws, since this problem was also present in the linear case studied in Section 4.2.

4.4.3 Realistic Structure

The asymptotic model is now applied to the ARIAS sector from Fig. 4.1, targeting the first mode which shows a nonlinear response quite similar to that of the simplified model analyzed before.

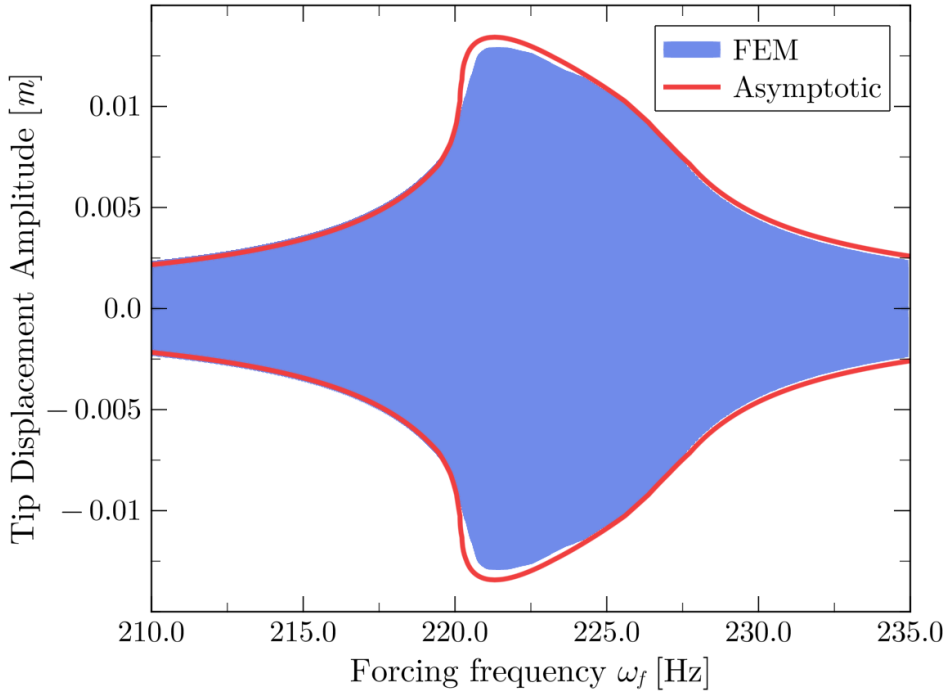

Figure 4.15: Resonance curve of the first modal frequency of the ARIAS blade.

As commented before, this analysis is restricted to an excitation with ND0. The comparison against time domain, due to the large number of DOFs of this structure, is carried out with the reduction technique explained in [120], which was also used in Chapter 3 to validate the findings of the asymptotic model in the flutter and forced response problem.

The results of the asymptotic model and the time integration are shown in Fig. 4.15. As it can be seen, the agreement is quite good, validating the asymptotic tool even in the case of a high-fidelity FEM model. An additional comment is that, due to the expensive

calculations of the time domain analysis, the forced response computed directly from the FEM was carried out by doing a slow frequency sweep. Therefore, transient effects could appear as a consequence of this process [49]. On the other hand, in the asymptotic model one goes directly to the resonance curve, without any transient effects.

Chapter 5

Interaction of Modes From Different Families

This chapter is devoted to extending the asymptotic formulation to the study of the interaction of two modes under nonlinear friction. This problem is of clear engineering interest, and can appear when two modes from different families of a bladed-disk are excited simultaneously.

There have been several efforts in the past for the computation of quasi-periodic solutions by using HBM [81]–[83]. In these works, for several nonlinearities (although not dry friction) the HBM methodology was extended to include harmonics of two frequencies, requiring an a priori knowledge of their values in the system.

The extension to dry friction forces was carried out very recently in [85], for the case of two forcing terms with different frequencies of excitation. The case of interest is when each forcing frequency is close to a natural frequency of the structure, and hence two modes of the structure with different contact cycles will be excited. This interaction can be highly nonlinear, and the linear superposition can greatly overestimate the final amplitude of the oscillations.

We derive an asymptotic model for the amplitude of the modes involved, that contains the relevant dynamics of the system. The analysis is focused on the forced response of the system, where each forcing term is conducting a frequency sweep close to a natural frequency of the system. The resulting amplitude equations are verified using time domain integration on a conceptual mass-spring model.

5.1 Asymptotic Model

The equations describing the motion of the structure are exactly the same as in Chapter 4, and are given by

$$\begin{pmatrix} \mathbf{M}_{ee} & \mathbf{M}_{ec} \\ \mathbf{M}_{ce} & \mathbf{M}_{cc} \end{pmatrix} \begin{pmatrix} \ddot{\mathbf{x}}_e \\ \ddot{\mathbf{x}}_c \end{pmatrix} + \begin{pmatrix} \mathbf{C}_{ee} & \mathbf{C}_{ec} \\ \mathbf{C}_{ce} & \mathbf{C}_{cc} \end{pmatrix} \begin{pmatrix} \dot{\mathbf{x}}_e \\ \dot{\mathbf{x}}_c \end{pmatrix} + \begin{pmatrix} \mathbf{K}_{ee} & \mathbf{K}_{ec} \\ \mathbf{K}_{ce} & \mathbf{K}_{cc} \end{pmatrix} \begin{pmatrix} \mathbf{x}_e \\ \mathbf{x}_c \end{pmatrix} + \begin{pmatrix} 0 \\ \mathbf{g}(\mathbf{x}_c, \dot{\mathbf{x}}_c) \end{pmatrix} = \begin{pmatrix} \mathbf{f}(t) \\ 0 \end{pmatrix}, \tag{5.1}$$

where the description of the different terms was given after Eq. (4.2). To study the mode interaction, we assume that the forcing takes the form

$$\mathbf{f}(t) = \mathbf{f}^A \sin(\omega_{f_A} t) + \mathbf{f}^B \sin(\omega_{f_B} t), \tag{5.2}$$

where $\mathbf{f}^A$, $\mathbf{f}^B$ are the forcing vectors, and ω_{f_A}, ω_{f_B} are the forcing frequencies. The regime of interest is when the forcing frequencies are close to two distinct natural frequencies of the system, with different mode shapes and different friction cycles at the contacts.

The derivation of the asymptotic model will follow closely the process described in Section 4.3, working directly from the system expressed in the CB basis. For this reason, many steps of the derivation are omitted here, since they will be exactly the same as in the previous chapter, and only the main differences are highlighted.

Again, the main idea of the model is to split the response into two timescales, and obtain a simplified description in the timescale where the friction effects are relevant. Using an asymptotic expansion for the modal amplitudes and contact displacements, we have

$$\begin{aligned} \mathbf{a}(t,\tau) &= \mathbf{a}^{(0)}(t,\tau) + \mathbf{a}^{(1)}(t,\tau) + \cdots, \\ \mathbf{x}_c(t,\tau) &= \mathbf{x}_c^{(0)}(t,\tau) + \mathbf{x}_c^{(1)}(t,\tau) + \cdots, \end{aligned} \tag{5.3}$$

which are introduced in the equations of motion and solved order by order.

Zeroth order: Assuming again that the motion of the contacts is small, we set $\mathbf{x}_c^{(0)} = \mathbf{0}$, and obtain the resulting equation for the full-stuck modal amplitudes

$$(\partial_{tt} + \omega_k^2) a_k^{(0)} = 0. \tag{5.4}$$

In this case we have two different active modes, $k = A, B$, and the solution will be given by

$$a_k^{(0)} = 0, \tag{5.5}$$

for $k \neq A, B$ and

$$a_A^{(0)}(t,\tau) = A(\tau)e^{i\omega_A t} + \text{c.c.}, \tag{5.6}$$

$$a_B^{(0)}(t,\tau) = B(\tau)e^{i\omega_B t} + \text{c.c.}, \tag{5.7}$$

where $A(\tau)$ and $B(\tau)$ are the slowly varying amplitudes of the excited modes, and ω_A, ω_B the associated full-stuck frequencies. In terms of elastic displacements, this results in

$$\mathbf{x}_e^{(0)}(t,\tau) = A(\tau)e^{i\omega_A t}\phi_A + B(\tau)e^{i\omega_B t}\phi_B + \text{c.c.}, \tag{5.8}$$

where ϕ_A and ϕ_B are the mode shapes associated with the frequencies ω_A and ω_B, respectively.

First order: Following the same procedure from Eqs. (4.45) to (4.48), we obtain the equation to compute the first order correction of the contact displacements

$$\mathbf{K}_{xx}\mathbf{x}_c^{(1)} + \mathbf{g}(\mathbf{x}_c^{(1)}, \dot{\mathbf{x}}_c^{(1)}) = -2|A|\cos(\omega_A t + \varphi_A)\mathbf{K}_{ce}\phi_A - 2|B|\cos(\omega_B t + \varphi_B)\mathbf{K}_{ce}\phi_B, \tag{5.9}$$

which is again a quasi-static equation where the fast timescale t acts as a parameter. However, there is an additional difficulty with respect to the previous analysis: a shift in the initial time cannot remove the phases φ_A and φ_B, since at least their difference would remain as an additional parameter.

For this reason, to solve this equation for the contact displacements, is more convenient to introduce two different time variables,

$$t_A = \omega_A t + \varphi_A, \quad t_B = \omega_B t + \varphi_B, \tag{5.10}$$

such that the problem can be written as

$$\mathbf{K}_{xx}\mathbf{x}_c^{(1)} + \mathbf{g}(\mathbf{x}_c^{(1)}, \dot{\mathbf{x}}_c^{(1)}) = -2|A|\cos(t_A)\mathbf{K}_{ce}\phi_A - 2|B|\cos(t_B)\mathbf{K}_{ce}\phi_B. \tag{5.11}$$

The goal is to compute the surface $\mathbf{x}_c^{(1)}$ as a function of the two short times t_A and t_B, which in analogy to the asymptotic models of the previous chapters, will allow us to characterize completely the nonlinear friction effects in the reduced asymptotic equation.

This step resembles the one introduced in [85], although there are some differences. In that work, an HBM approach was utilized, which assumes a certain set of Fourier harmonics for the contacts displacements and then computes them with a Newton iteration, where the nonlinear friction forces are evaluated with AFT (Alternated Fourier Time) techniques [59].

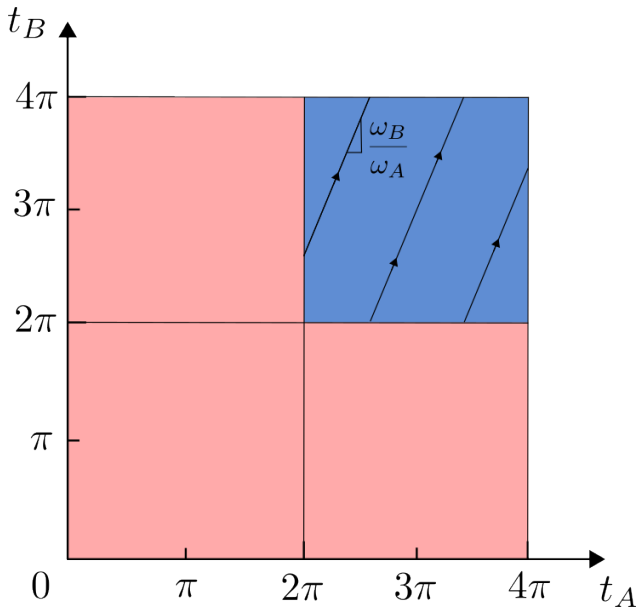

Figure 5.1: Strategy to solve Eq. (5.13) in the two timescales.

In contrast, in our analysis, the contact displacements from Eq. (5.11) are solved directly in time domain by considering t_A and t_B acting as parameters. For a friction model that depends on the velocity of the contacts, $\dot{\mathbf{x}}_c^{(1)}$, we need to transform the time derivatives to account for the two timescales, which is done by

$$\frac{\partial}{\partial t} \rightarrow \omega_A \frac{\partial}{\partial t_A} + \omega_B \frac{\partial}{\partial t_B}, \tag{5.12}$$

and hence, the problem to compute the static displacements is transformed to

$$\mathbf{K}_{xx}\mathbf{x}_c^{(1)} + \mathbf{g}\left(\mathbf{x}_c^{(1)}, \omega_A \frac{\partial \mathbf{x}_c^{(1)}}{\partial t_A} + \omega_B \frac{\partial \mathbf{x}_c^{(1)}}{\partial t_B}\right) = -2|A|\cos(t_A)\mathbf{K}_{ce}\phi_A - 2|B|\cos(t_B)\mathbf{K}_{ce}\phi_B. \tag{5.13}$$

This is an implicit partial differential equation in t_A and t_B, and we look for a solution $\mathbf{x}_c^{(1)}$ periodic on both variables. In order to solve it we use a uniform two-dimensional grid in the t_A and t_B directions. The problem has to be solved at least for two periods in each direction, as it is usually necessary for the friction cycles to settle to a periodic state in each direction. In Fig. 5.1 the converged two-dimensional surface is represented in blue, and the real trajectories of the system are shown in a black continuous line, with a slope of ω_B/ω_A since both timescales are related to the physical time t. If the ratio of the frequencies is irrational, the trajectory will fill the whole surface during the motion, corresponding to a quasi-periodic response.

After solving the problem, the contact displacements can be expressed as a two-dimensional Fourier series as

$$\mathbf{x}_c^{(1)}(t_A, t_B, \tau) = \sum_{n=-\infty}^{\infty} \sum_{m=-\infty}^{\infty} \mathbf{P}_{nm}(|A|, |B|) e^{int_A} e^{imt_B}, \tag{5.14}$$

where the Fourier coefficients $\mathbf{P}_{nm}(|A|, |B|)$ now depend on the two modal amplitudes. The relevant Fourier coefficients to characterize the nonlinear effects are the first harmonic in each direction, i.e. $\mathbf{P}_{10}$ and $\mathbf{P}_{01}$, in analogy to the process described in previous chapters.

In terms of the original timescale, the contact displacements are given by

$$\mathbf{x}_c^{(1)}(t, \tau) = \sum_{n=-\infty}^{\infty} \sum_{m=-\infty}^{\infty} \mathbf{P}_{nm}(|A|, |B|) e^{in(\omega_A t + \varphi_A)} e^{im(\omega_B t + \varphi_B)}. \tag{5.15}$$

With this expression, one can go back to the modal amplitude equations which, at first order, take the form

$$(\partial_{tt} + \omega_k^2) a_k^{(1)} = -2a_{kt\tau}^{(0)} - (\mathbf{M}_{ax} \mathbf{x}_{ctt}^{(1)})_k - \beta \omega_k^2 a_{kt}^{(0)} + (f_k^A e^{i\omega_A t} e^{i\Delta\omega_A \tau} + f_k^B e^{i\omega_B t} e^{i\Delta\omega_B \tau} + \text{c.c.}), \tag{5.16}$$

where the forcing frequencies are expressed as a small deviation of the full-stuck frequencies, to study the resonance crossings. We denote with $\Delta\omega_A$ and $\Delta\omega_B$ the deviations of the forcing frequency from each respective resonance frequency. Recall that the term $(\mathbf{M}_{ax} \mathbf{x}_{ctt}^{(1)})_k$ denotes the component k of that vector. For each k, we have a differential equation which is very similar to the one from the previous chapter (see Eq. (4.50)). In contrast to that case, there are now two solvability conditions to be applied, since the terms containing both the first harmonic of the frequencies ω_A and ω_B present in the right-hand side belong to the nullspace of the linear operator of the left-hand side.

Therefore, for $k = A$, we set to zero all the terms that are proportional to $e^{i\omega_A t}$, and we obtain a differential equation for the modal amplitude $A(\tau)$

$$2i\omega_A \frac{\mathrm{d}A}{\mathrm{d}\tau} = \omega_A^2 (\mathbf{M}_{ax} \mathbf{P}_{10})_A e^{i\varphi_A} - i\beta\omega_A^3 A + f_A e^{i\Delta\omega_A \tau}, \tag{5.17}$$

where $f_A^A \equiv f_A$ for the sake of simplicity. And, then, for $k = B$, the solvability condition corresponding to removing the terms proportional to $e^{i\omega_B t}$ gives

$$2i\omega_B \frac{\mathrm{d}B}{\mathrm{d}\tau} = \omega_B^2 (\mathbf{M}_{ax} \mathbf{P}_{01})_B e^{i\varphi_B} - i\beta\omega_B^3 B + f_B e^{i\Delta\omega_B \tau}. \tag{5.18}$$

Recall from Eq. (4.52) that the terms $\omega_A^2(\mathbf{M}_{ax}\mathbf{P}_{10})_A$, $\omega_B^2(\mathbf{M}_{ax}\mathbf{P}_{01})_B$ could be simplified to

$$\begin{aligned}\omega_A^2(\mathbf{M}_{ax}\mathbf{P}_{10})_A &\approx -\phi_A^\top \mathbf{K}_{ec}\mathbf{P}_{10},\\ \omega_B^2(\mathbf{M}_{ax}\mathbf{P}_{01})_B &\approx -\phi_B^\top \mathbf{K}_{ec}\mathbf{P}_{01},\end{aligned} \tag{5.19}$$

and, since we now have two relevant Fourier coefficients to describe the nonlinear dissipation, we may introduce two different complex friction functions

$$\begin{aligned}Q_A(|A|,|B|) &= -\frac{\phi_A^\top \mathbf{K}_{ec}\mathbf{P}_{10}(|A|,|B|)}{|A|},\\ Q_B(|A|,|B|) &= -\frac{\phi_B^\top \mathbf{K}_{ec}\mathbf{P}_{01}(|A|,|B|)}{|B|},\end{aligned} \tag{5.20}$$

where each one depends on the amplitude of both modes. With this definition, we may rewrite the nonlinear terms as

$$\omega_A^2(\mathbf{M}_{ax}\mathbf{P}_{10})_A e^{i\varphi_A} = Q_A(|A|,|B|)A, \quad \omega_B^2(\mathbf{M}_{ax}\mathbf{P}_{01})_B e^{i\varphi_B} = Q_B(|A|,|B|)B, \tag{5.21}$$

and arrive to the final asymptotic system

$$\frac{\mathrm{d}A}{\mathrm{d}\tau} = -\frac{i}{2\omega_A}Q_A(|A|,|B|)A - \xi_A A - \frac{i}{2\omega_A}f_A e^{i\Delta\omega_A\tau}, \tag{5.22}$$

$$\frac{\mathrm{d}B}{\mathrm{d}\tau} = -\frac{i}{2\omega_B}Q_B(|A|,|B|)B - \xi_B B - \frac{i}{2\omega_B}f_B e^{i\Delta\omega_B\tau}, \tag{5.23}$$

where the linear damping coefficients are defined as $\xi_A = \beta\omega_A^2/2$ and $\xi_B = \beta\omega_B^2/2$. For the modal interaction problem, our asymptotic description now consists of two nonlinear differential equations for each of the modal amplitudes, which evolve in the slowly varying time τ. The coupling between the modes only occurs due to the nonlinear friction terms Q_A and Q_B, and hence it is expected that the response of the system will differ from the simple linear superposition of the two modes.

The nonlinear terms Q_A and Q_B, which are two-dimensional functions, are expected to have a complicated shape, with a non-monotone behavior, since these friction induced nonlinearities are more complex than the standard cubic term that comes from just retaining the first resonant term of the Taylor expansion in the case of geometric nonlinearities.

As commented in the previous chapter, linear aerodynamic instabilities could be added by modifying the linear damping terms ξ_A and ξ_B, which may introduce more complicated dynamics in the system, but this study is considered out of the scope of this work.

The periodic solutions from Eqs. (5.22), (5.23), can be obtained by assuming a solution of the form of $A = |A|e^{i\Delta\omega_A\tau}e^{i\varphi_A}$ and $B = |B|e^{i\Delta\omega_B\tau}e^{i\varphi_B}$, and introducing it into the equations. Then, by making $\mathrm{d}|A|/\mathrm{d}\tau = \mathrm{d}|B|/\mathrm{d}\tau = 0$, we compute directly the final amplitude of vibration after the transient, obtaining

$$\Delta\omega_A = -\frac{Q_A^R(|A|,|B|)}{2\omega_A} \pm \sqrt{\left(\frac{f_A}{2|A|\omega_A}\right)^2 - \left(\frac{Q_A^I(|A|,|B|)}{2\omega_A} - \xi_A\right)^2}, \tag{5.24}$$

$$\Delta\omega_B = -\frac{Q_B^R(|A|,|B|)}{2\omega_B} \pm \sqrt{\left(\frac{f_B}{2|B|\omega_B}\right)^2 - \left(\frac{Q_B^I(|A|,|B|)}{2\omega_B} - \xi_B\right)^2}, \tag{5.25}$$

which are two analytical expressions for the frequency sweep across ω_A and ω_B, respectively. These expressions, after the characterization of the nonlinear friction through the Q_A, Q_B functions, allow for very fast parametric studies.

The phase of each modal amplitude can also be directly obtained

$$\tan\varphi_A = \frac{\xi_A - Q_A^I(|A|,|B|)}{2\omega_A\Delta\omega_A + Q_A^R(|A|,|B|)}, \tag{5.26}$$

$$\tan\varphi_B = \frac{\xi_B - Q_B^I(|A|,|B|)}{2\omega_B\Delta\omega_B + Q_B^R(|A|,|B|)}, \tag{5.27}$$

and easily evaluated for each point of the resonance curves. These asymptotic expressions are validated in the next section using a conceptual mass-spring model.

5.2 Application to Lumped Model

An application of the theory developed in the previous section is presented here. The goal is to analyze the forced response of a simplified system with nonlinear friction, when two modes with different friction cycles are simultaneously excited. In particular, attention will be paid to the description of the nonlinear friction in the asymptotic setup, since it gives some physical insight into the modal interaction

5.2.1 Model Description

The system is a mass-spring model, shown in Fig. 5.2. There are two masses, m_1 and m_2, which are used to represent the modal masses of the first and second mode, whose displacements are x_{e_1} and x_{e_2}, respectively. There is an additional mass, m_c, representing the contact, which can move in two directions, x_{c_1} and x_{c_2}, and produces a nonlinear force

$\mathbf{g}(\mathbf{x}_c, \dot{\mathbf{x}}_c)$.

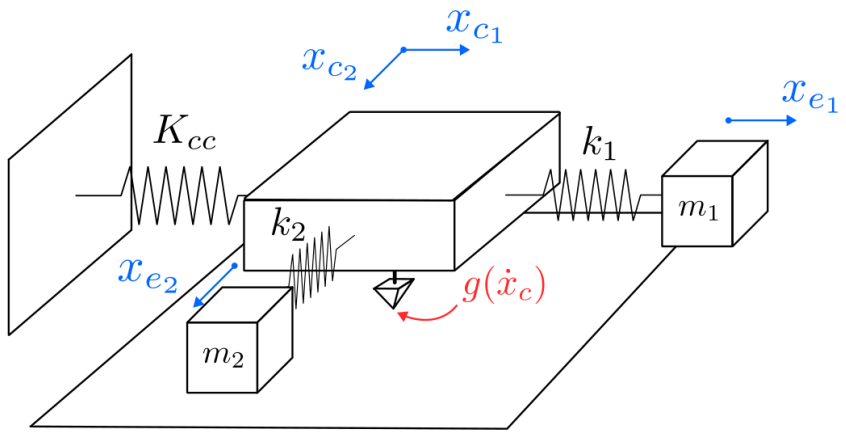

Figure 5.2: Sketch of the lumped model to study mode interaction.

For simplicity, the friction law used here is a smoothed version of Coulomb's law. A constant normal load is assumed, and, in the tangential direction of the contact surface, the force is given by

$$g(\dot{x}_t) = \mu N \tanh\left(\frac{\dot{x}_t}{\alpha}\right), \tag{5.28}$$

where μ is the friction coefficient, N the normal load, $\dot{x}_t$ the relative velocity of the contact point, and α a regularization parameter. For small values of α, the friction force gets close to $\sim \mu N \text{sgn}(\dot{x})$, which is the Coulomb limit ($\text{sgn}(\cdot)$ denotes the sign function). In the contact surface, two different directions can be considered, so the friction is modeled as two 1D friction elements.

The system matrices, corresponding to the formulation of Eq. (5.1), are given by

$$\begin{aligned}
\mathbf{M}_{ee} &= \begin{pmatrix} m_1 & 0 \\ 0 & m_2 \end{pmatrix}, \quad \mathbf{M}_{ec} = \begin{pmatrix} 0 & 0 \\ 0 & 0 \end{pmatrix}, \quad \mathbf{M}_{cc} = \begin{pmatrix} m_c & 0 \\ 0 & m_c \end{pmatrix}, \\
\mathbf{K}_{ee} &= \begin{pmatrix} k_1 & 0 \\ 0 & k_2 \end{pmatrix}, \quad \mathbf{K}_{ec} = \begin{pmatrix} -k_1 & 0 \\ 0 & -k_2 \end{pmatrix}, \quad \mathbf{K}_{cc} = \begin{pmatrix} k_1 + k_{c_1} & k_p \\ k_p & k_2 + k_{c_2} \end{pmatrix},
\end{aligned} \tag{5.29}$$

and the forcing vector takes the form

$$\mathbf{f}(t) = \begin{pmatrix} f_A \sin(\omega_A t) \\ f_B \sin(\omega_B t) \end{pmatrix}, \tag{5.30}$$

where each element excites one of the masses, m_1 or m_2. The values of the different parameters are given in Table 5.1, which have been selected to produce significant modal interaction.

Table 5.1: Parameters of the mass-spring model.

m_1	m_2	m_c	k_1	k_2	k_{c_1}	k_{c_2}	k_p	μN	f_A	f_B
1.0	1.0	0.01	1.0	1.7^2	20	40	15	2.0	0.15	0.25

The stiffness values k_1 and k_2, which represent the modal stiffness, are selected to be much smaller than the contact stiffness, as it is usually the case in more realistic systems. Note that, in this case, we have that $\omega_A = 1$, $\omega_B = 1.7$ and the associated full-stuck mode shapes are $\phi_A = (1, 0)^\top$ and $\phi_B = (0, 1)^\top$. These modes are chosen to be orthogonal to represent a situation with interacting modes with very different friction cycles.

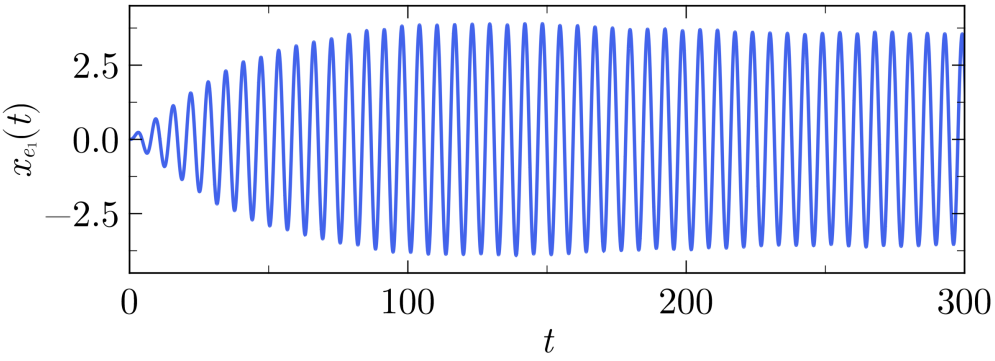

Figure 5.3: Evolution of the displacements of mass m_1 using time integration.

Before applying the asymptotic procedure, in order to understand the nonlinear character of the system, several time integrations have been carried out. The forcing frequencies are selected to be close to each respective resonance. The results of the displacements of the first modal mass m_1 are shown in Fig. 5.3. After an initial transient, the solution settles to a state with two frequencies.

The contact behavior is more interesting due to the presence of the nonlinearity, and it is shown in Fig. 5.4, starting from a converged solution without the transient. A comparison with a forcing exciting only a single mode is included to highlight the differences when both modes are active at the same time. First, Fig. 5.4a shows the response in the direction x_{c_1}, where it can be clearly observed that the oscillations are nonlinear. For the case with just one excitation forcing on that mode, the solution is periodic (blue line). If the two modes are excited at the same time (red), the oscillations of the contact in this direction correspond to a two-frequency solution. In the other contact direction, x_{c_2}, the behavior is similar, as shown in Fig. 5.4b.

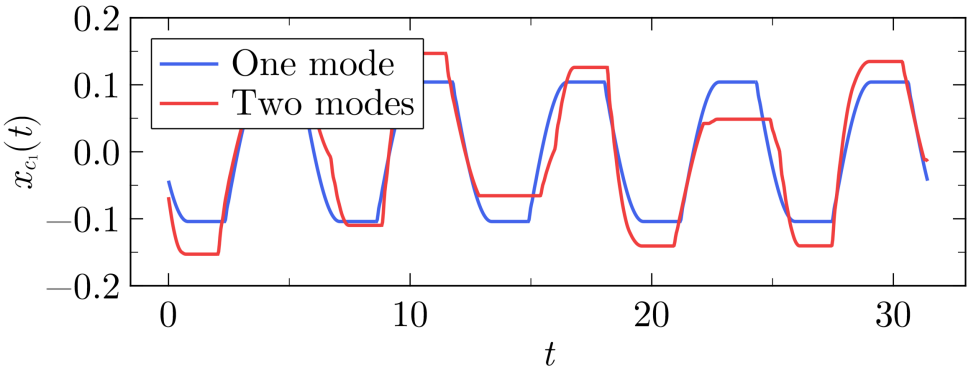

(a) Direction x_{c_1}

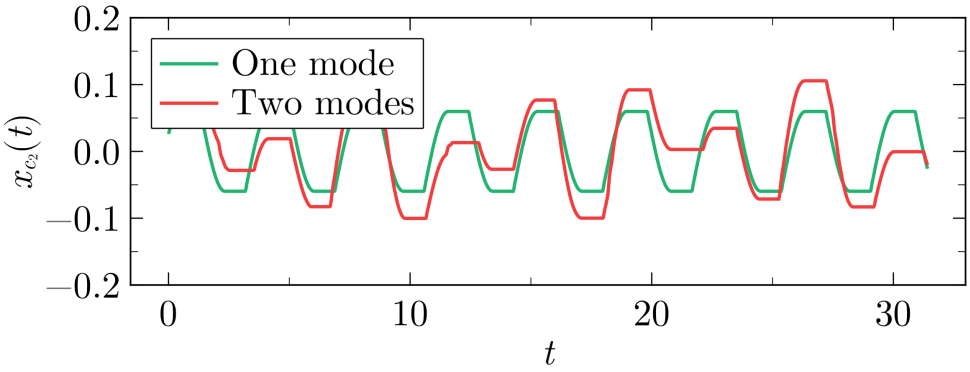

(b) Direction x_{c_2}

Figure 5.4: Evolution of the contact displacements using time integration. Comparison between one and two excited modes is shown.

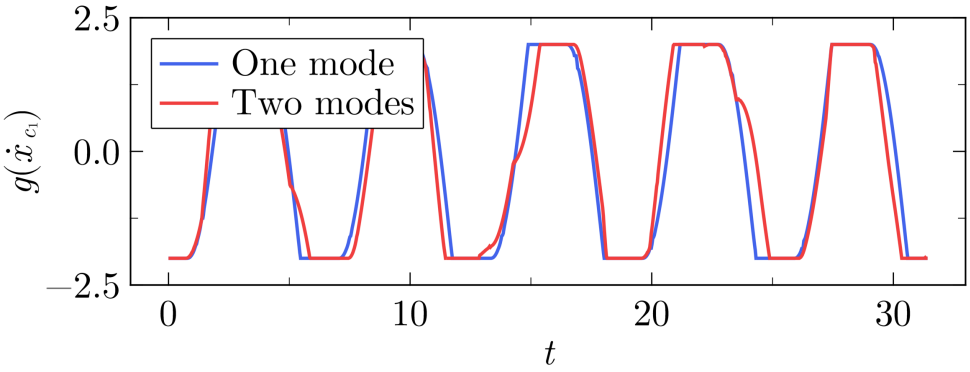

Figure 5.5: Evolution of the friction force using time integration. Comparison between one and two excited modes is shown.

The evolution of the nonlinear friction force is presented in Fig. 5.5, where the same comparison of one and two forcings is made. This represents the evolution of the force in the x_{c_1} direction, which alternates between states of $\pm\mu N$, given by the changes of the sign in the velocity. In the case of just one mode, the solution is perfectly periodic, as expected. When two modes are considered, the two frequency behavior is evident from the plot.

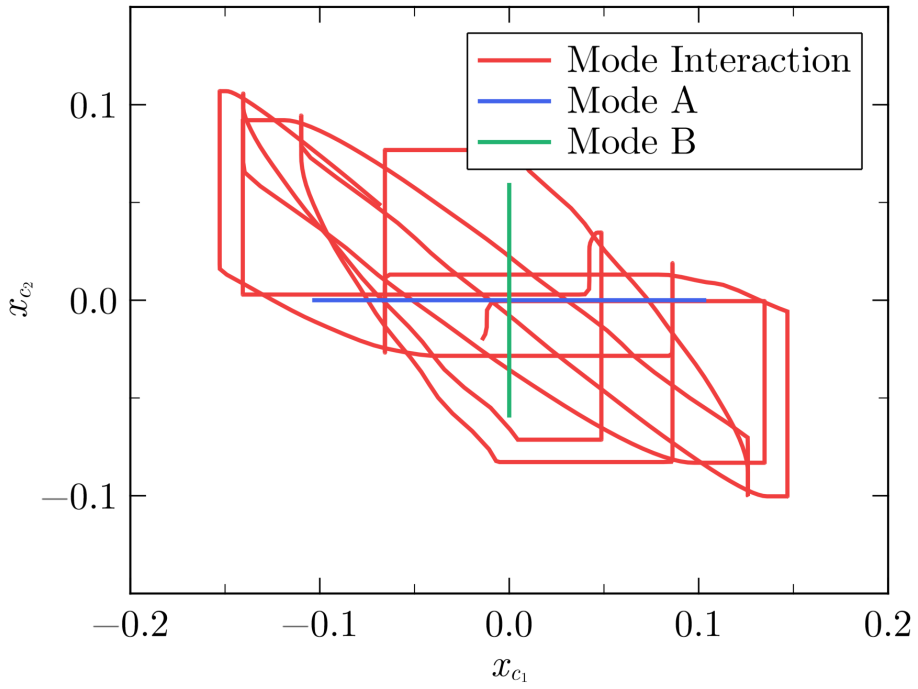

Figure 5.6: Trajectories of the contact displacement for excitation of each mode alone and the combination of both.

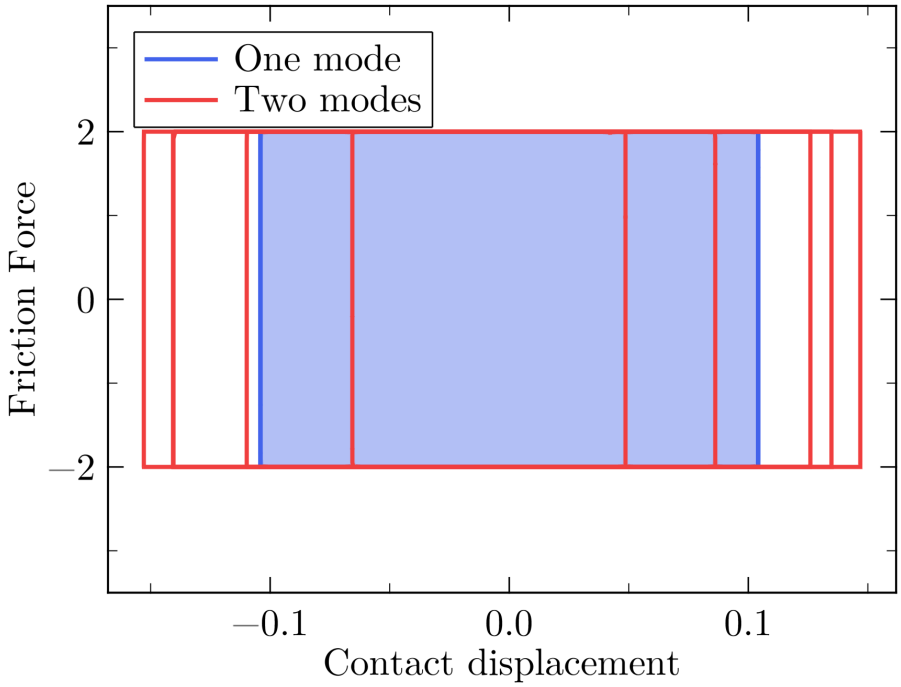

Figure 5.7: Friction cycles for the x_{c_1} direction. Comparison between one and two excited modes.

Inspecting the evolution of the position of the contact in the (x_{c_1}, x_{c_2}) plane, the modal

interaction due to the friction element becomes apparent. This is shown in Fig. 5.6, where the trajectories when either mode A or B is excited consists of a straight line. However, the trajectory deviates greatly from a simple linear superposition when both modes are active, see the red line in Fig. 5.6.

As a final comment of this preliminary time integration analysis, the nonlinear dissipation of the contact is evaluated. Computing the friction cycles in the x_{c_1} direction, we obtain the results shown in Fig. 5.7. Considering a single mode, the solution is periodic, and the area of the cycle remains constant throughout the motion (blue rectangle in Fig. 5.7). On the other hand, when both modes are active, if we plot 5 consecutive periods of the cycle, we see that the area of the cycle is changing during each period, due to the mode interaction (red line in Fig. 5.7).

5.2.2 Asymptotic Model

The characterization of the nonlinear friction in the asymptotic model is carried out now to obtain the functions Q_A and Q_B. As described in the previous section, one needs to solve the contact equation (5.13) to obtain the first correction of the contact displacements. The solution of this equation is a function that is periodic on each of the time variables t_A and t_B, for every fixed value of $|A|$ and $|B|$.

For this example, and taking $|A| = 1.3$ and $|B| = 0.75$, the surface of the contact displacement correction $x_{c_1}^{(1)}$ is shown in Fig. 5.8. As mentioned before, two cycles had to be solved in each direction in order to converge to this solution, which as one can see is periodic in t_A and t_B

A usual representation in the context of nonlinear dynamics of a two-frequency solution is a torus, shown in Fig. 5.9. The two angles that parametrize the torus are associated with the two different frequencies of the system, and the true trajectories of the system are highlighted in the plot with a solid line. The slope of this line on the surface of the torus is given by ω_B/ω_A, and this is the two-frequency solution that arises due to the mode interaction. This is because the relation between the two times is

$$t_B = \frac{\omega_B}{\omega_A}(t_A - \varphi_A) + \varphi_B, \tag{5.31}$$

which is a straight line in the (t_A, t_B) plane.

Several validations have been carried out to verify the accuracy of the asymptotic methodology. First, the relative value of the different terms on Eq. (5.13), have been compared with the results obtained by time integration. Fig. 5.10 shows the evolution of the elastic and

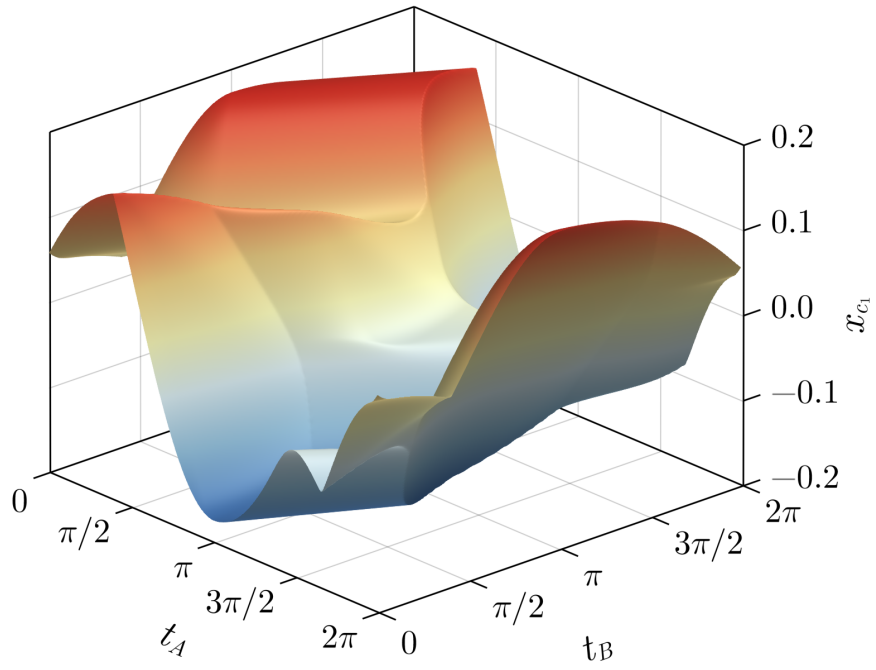

Figure 5.8: Contact displacement correction $x_{c_1}^{(1)}$ as a function of the two timescales t_A and t_B.

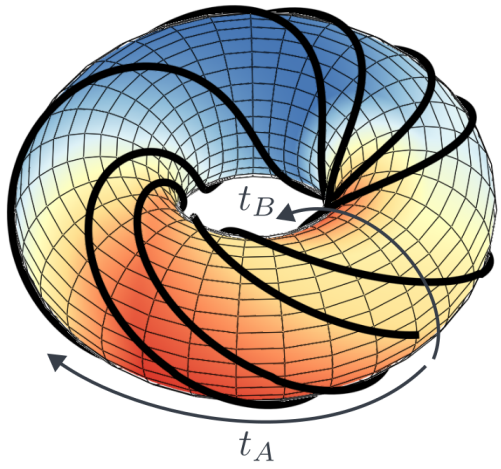

Figure 5.9: Contact displacement correction $x_{c_1}^{(1)}$ as a function of the two timescales t_A and t_B (torus representation). The true trajectories of the system are highlighted with a solid line.

friction forces in Eq. (5.13) with respect to time, whose sum is close to a sinusoidal curve, as expected given the form of the right-hand side of Eq. (5.13). Then, in dashed line, the expression evaluated from the full-time integration results is included, obtaining a very good

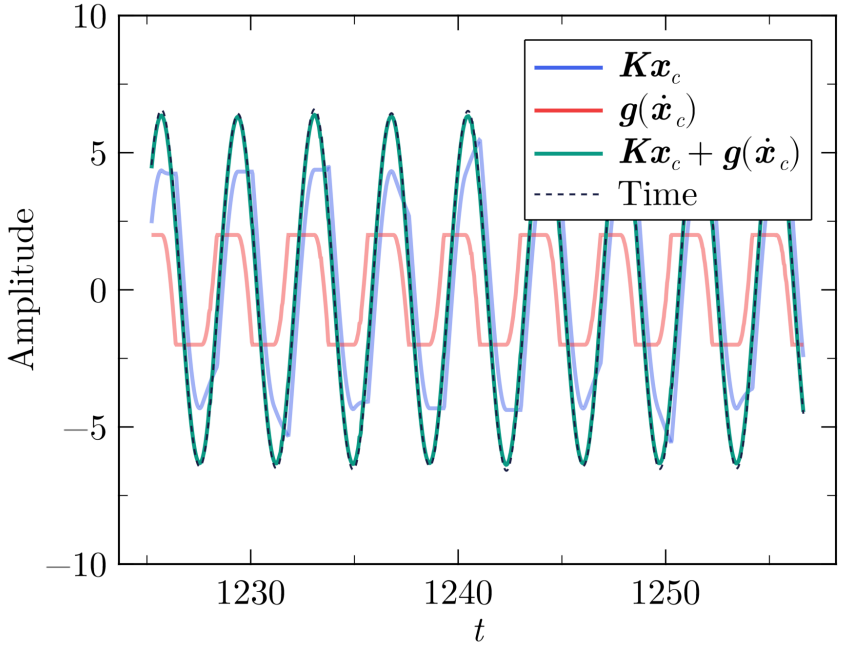

Figure 5.10: Comparison against time integration of the results obtained by the correction of the asymptotic model.

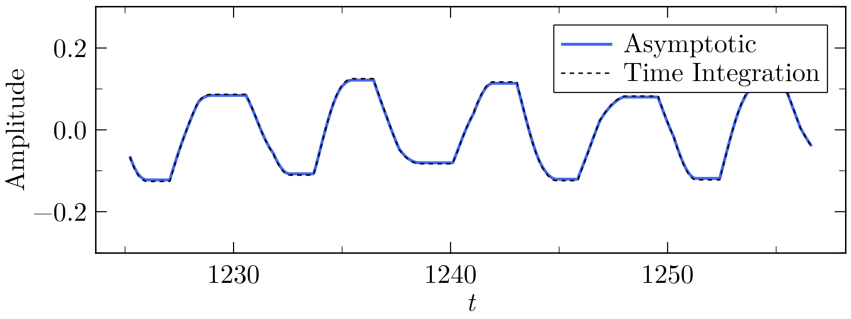

(a) Direction x_{c_1}

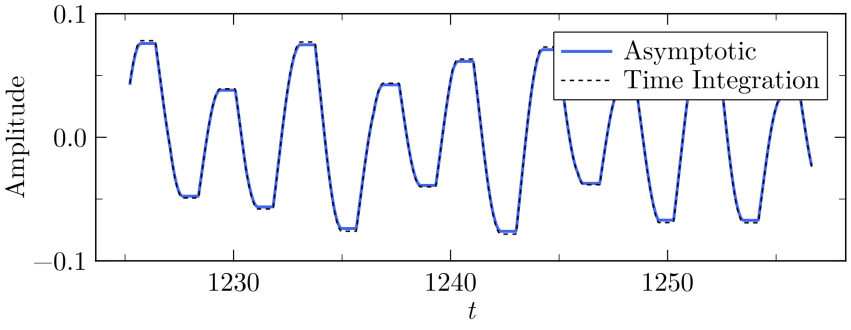

(b) Direction x_{c_2}

Figure 5.11: Validation of the quasi-periodic solutions obtained by tracking the correction computed from the asymptotic model.

matching, where just slight differences can be appreciated close to the peaks.

Additionally, the displacements of the contacts have been compared. In the asymptotic model, these displacements are obtained by traversing the surface in Fig. 5.8 in the straight line given by the slope from Eq. (5.31). The validation is shown in Fig. 5.11, where both contact directions are plotted in Figs (a) and (b). As one can see, the evolution shows two frequencies, and the agreement with the time evolution approach is quite good.

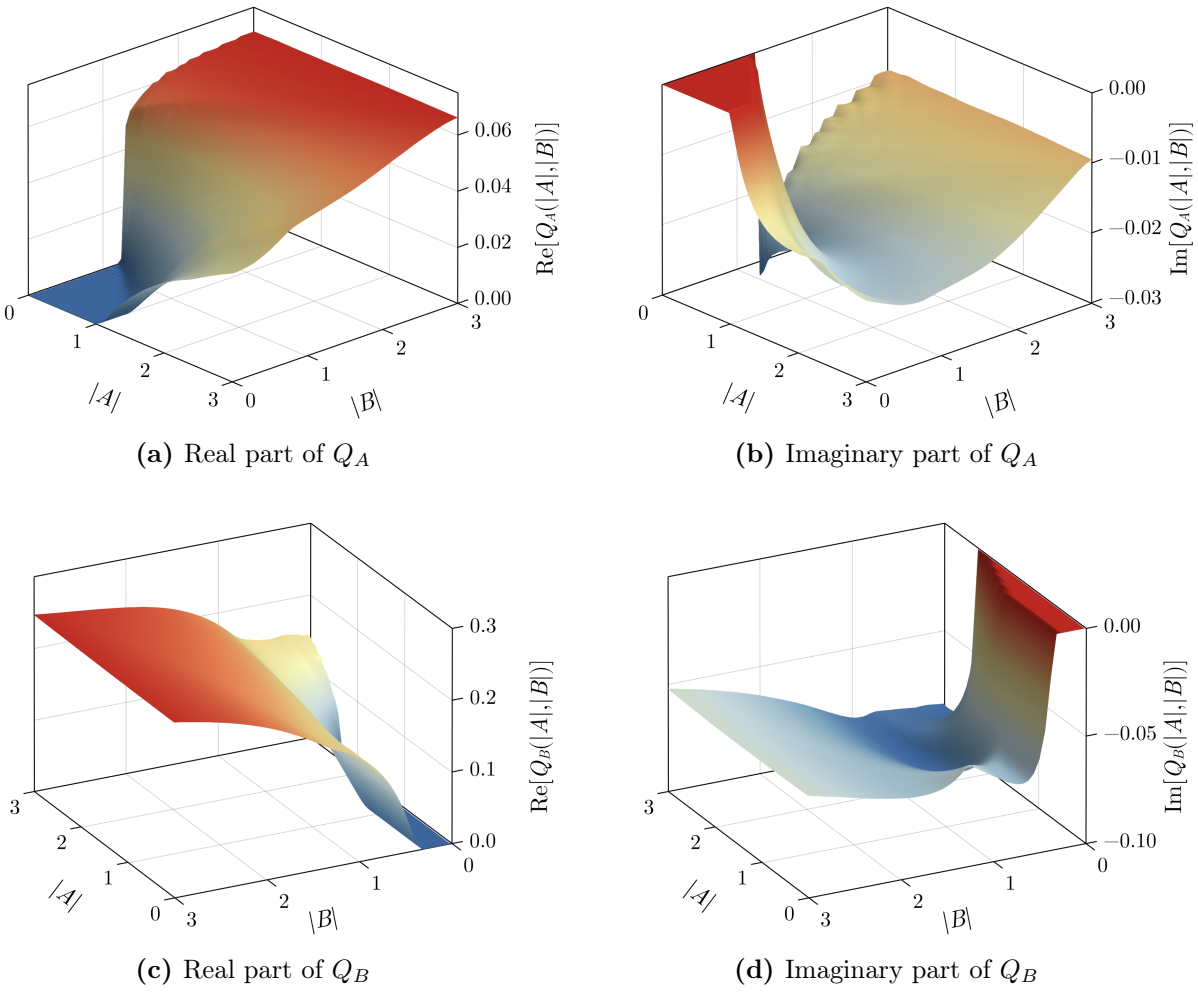

(a) Real part of Q_A

(b) Imaginary part of Q_A

(c) Real part of Q_B

(d) Imaginary part of Q_B

Figure 5.12: Complex friction coefficients Q_A and Q_B as a function of the modal amplitudes.

Taking the two relevant Fourier harmonics from the contact displacement solution, one can directly compute the friction coefficients using Eq. (5.20). Then, since each coefficient is a complex function of two variables, their real and imaginary parts can be plotted as a surface.

The results are presented in Fig. 5.12. First, focusing in the real part of Q_A, one can see that the nonlinear frequency shift related to the first mode clearly depends on the amplitude

of B. For low values of this mode B, the frequency correction increases for larger values of the amplitude $|A|$. Nevertheless, for large values of $|B|$, the correction appears to be almost constant. Regarding the imaginary part of Q_A, it can be observed that the amount of dissipation is highly coupled with mode $|B|$. The maximum dissipation, related to more negative values of the friction coefficient, is achieved for a nonzero value of $|B|$. The surfaces of the friction coefficient Q_B exhibit a similar behavior.

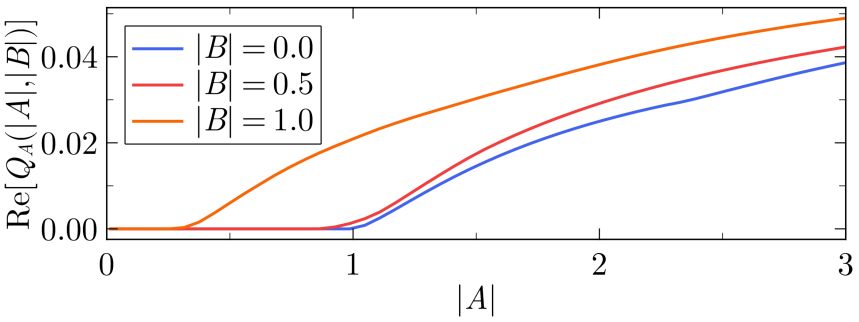

(a) Real part of Q_A

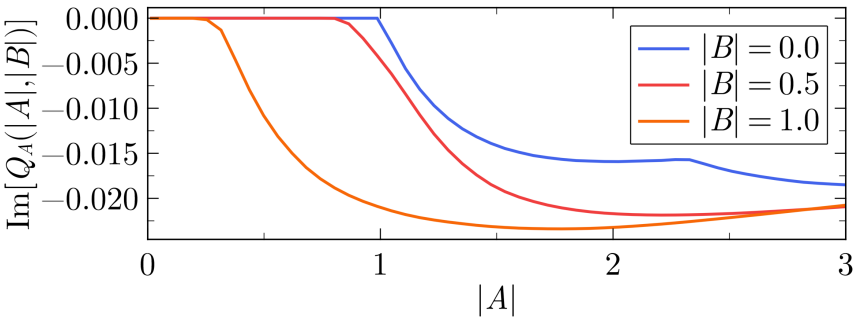

(b) Imaginary part of Q_A

Figure 5.13: Friction coefficient Q_A as a function of the amplitude $|A|$ for several values of $|B|$.

A more clear analysis of the dissipation is obtained by analyzing the friction coefficient Q_A as a function of $|A|$ for several values of $|B| = 0.0, 0.5, 1.0$. These results are shown in Fig. 5.13. Regarding the real part, as a consequence of the friction law used in this section which just depends on the velocity of the contact, the frequency shift for low amplitudes of mode $|A|$ is zero. Then, as the amplitude of mode $|B|$ is increased, the frequency shift becomes larger and departs from zero at a lower value of $|A|$. Regarding the nonlinear dissipation, we can see that increasing the modal amplitude $|A|$ does not necessarily always increase the damping. This is because the dissipation is dictated by the area of the friction cycle, which is not necessarily larger for higher amplitudes. For larger values of $|B|$, the point of maximum damping is shifted to lower values of $|A|$. An important remark from this analysis is that when both modes are active, the dissipation coming from the nonlinear force is larger than when just only one mode is excited.

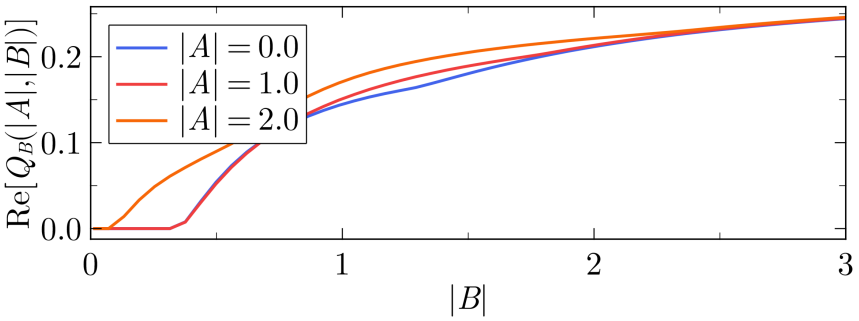

(a) Real part of Q_B

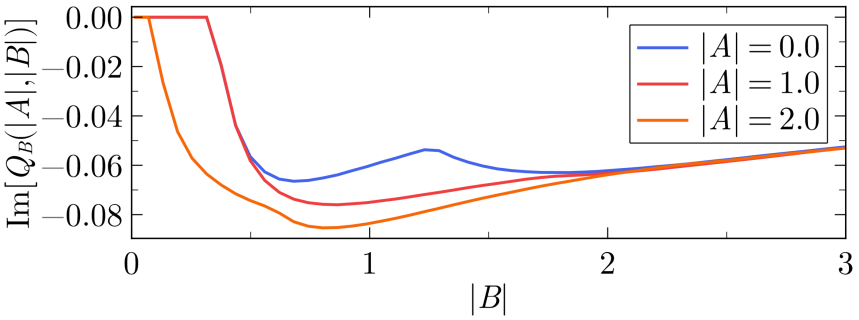

(b) Imaginary part of Q_B

Figure 5.14: Friction coefficient Q_B as a function of the amplitude $|B|$ for several values of $|A|$.

We repeat the same analysis for the nonlinear term of the other amplitude equation Q_B. The results are shown in Fig. 5.14. Similarly as before, the real part of the coefficient starts from zero, and it departs from this value before if the amplitude of mode $|A|$ is larger. Then, the value of this shift increases with $|B|$, and for values of $|B| \sim 3$ the different curves collapse into one. Regarding the imaginary part, the nonlinear dissipation is maximum at intermediate values of $|B|$, depending on the details of the motion of the contact (when it starts to enter in sliding and the interaction with the other mode). As the amplitude of mode $|A|$ is increased, the nonlinear damping is increased, although for larger values of $|B|$ they converge to the same value.

The forced response can be obtained by evaluating the analytical expressions (5.24) and (5.25). A sweep in $\Delta\omega_A$ and $\Delta\omega_B$ is carried out, and the maximum amplitude of the response, given by $\sqrt{|A|^2 + |B|^2}$, is plotted in Fig. 5.15, showing the resonance curve for the interaction of the two modes.

In blue, we have highlighted the frequency sweep of mode A when $\Delta\omega_B = -0.2$, which is the case when the response is made basically only from mode A. Similarly, for $\Delta\omega_A = 0.2$, a frequency sweep of mode B is highlighted in green.

However, closer to the region of both resonance frequencies, we see clearly the interaction

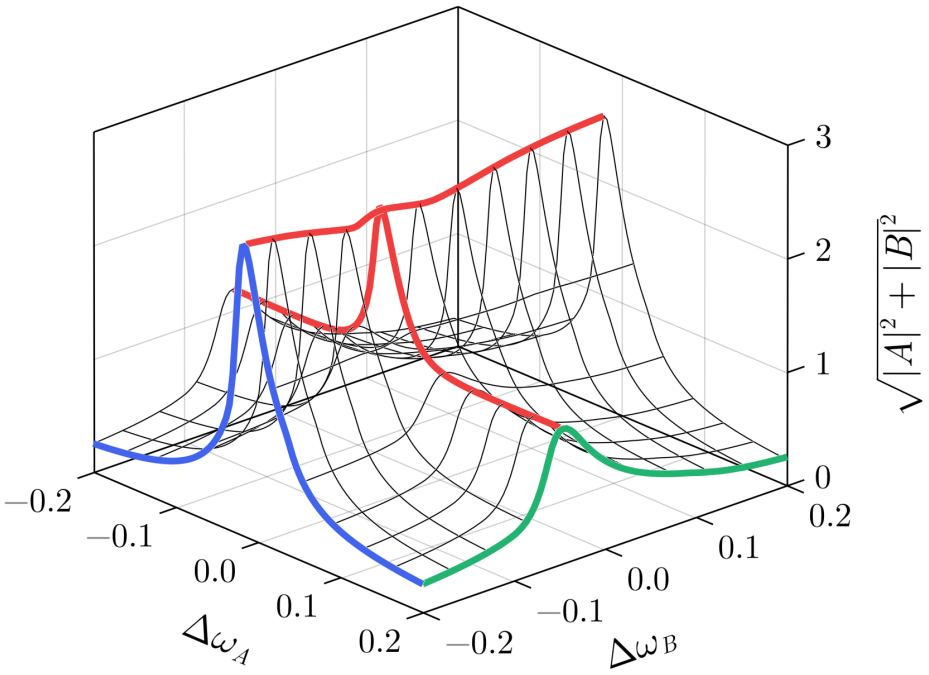

Figure 5.15: Resonance curve for the interaction of modes.

between both modes, which are highlighted in red. Doing a frequency sweep in $\Delta\omega_A$ for a fixed value of $\Delta\omega_B$ close to the resonance frequency, we see that the maximum amplitude of the response is actually smaller than when just a single mode is excited. The explanation is that, even though both modes are simultaneously excited, the nonlinear damping is larger, and hence there is more dissipation. In addition, far from the resonance we recover a constant value which corresponds to the amplitude of mode B when mode A is absent from the solution.

In the other direction, for a sweep in $\Delta\omega_B$ when mode A is excited close to the resonance, we see a similar effect. At the resonance, the amplitude of vibration decreases due to an amplified effect of the nonlinear friction. Far from the resonance, the system tends to the case with only mode A.

Finally, these solutions at resonance are compared against the linear superposition of the modes in Fig. 5.16. On the top part, we have the frequency sweep corresponding to mode A. For the value of $\Delta\omega_B = -0.2$, in which the effect of mode B is negligible, the resulting resonance curve is plotted. Close to the resonance, which is about $\Delta\omega_B = -0.046$, the solution containing the modal interaction is plotted using a red line. As mentioned before, the maximum amplitude of this response is actually smaller than that when just one mode is excited. The linear superposition is highlighted with a black line, which clearly overestimates

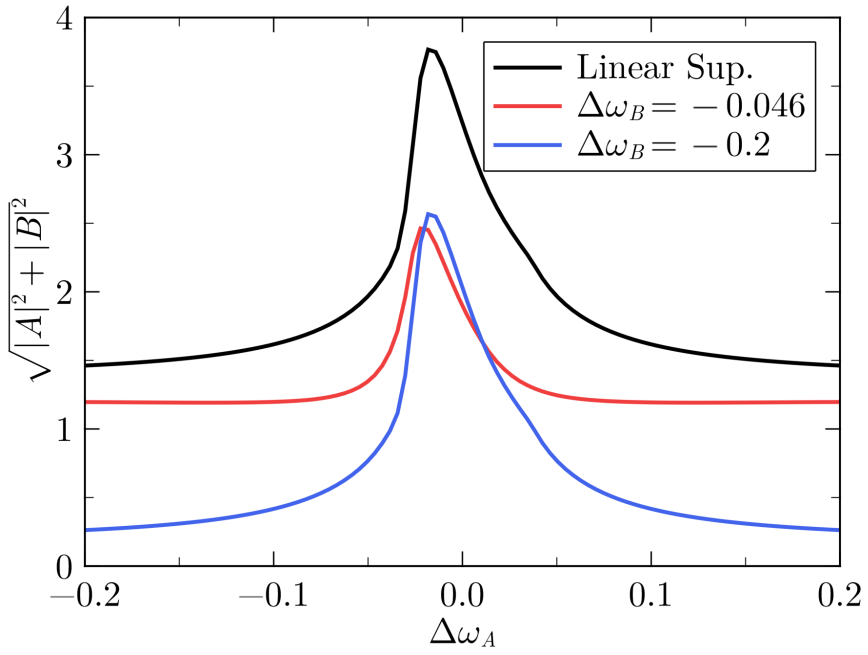

(a) Frequency sweep of $\Delta\omega_A$

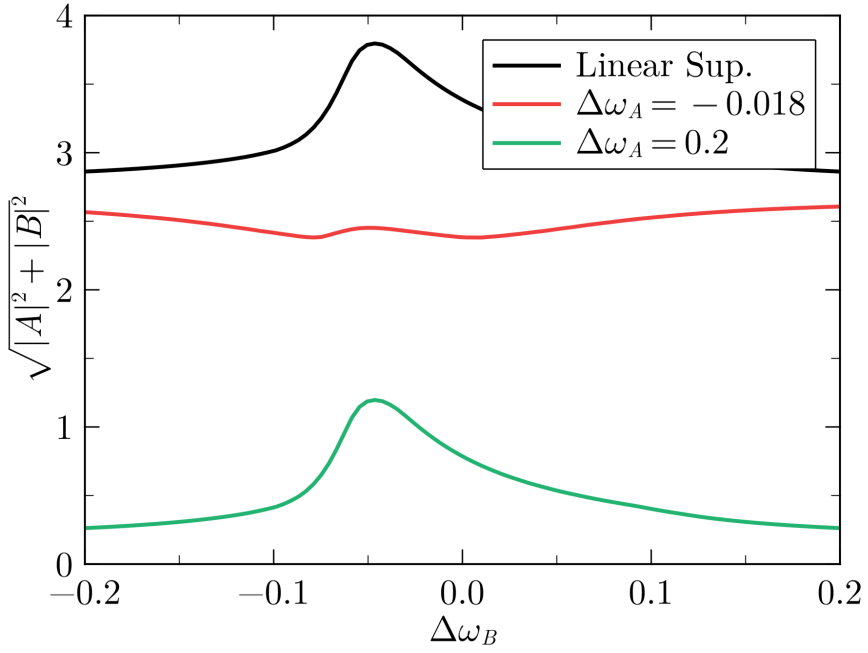

(b) Frequency sweep of $\Delta\omega_B$

Figure 5.16: Frequency sweep around each resonance frequency for the interaction of modes including a comparison with the linear superposition of modes.

the real response by a large amount, since the maximum peak is almost 4, compared to 2.5 when nonlinear mode interaction effects are retained. On the bottom of this plot, we perform the same analysis but considering a frequency sweep of mode B. Again, it is seen

that the linear superposition significantly overestimates the response of the system, making the modeling of nonlinear friction effects essential to accurately capture the dynamics of the system.

Chapter 6

Discussion

The goal of this chapter is to provide a joint discussion of the main topics addressed throughout this dissertation. This section is included as a separate chapter following the university's recommendation. For detailed descriptions and in-depth discussion of the different problems, refer to the corresponding chapters.

In this thesis, asymptotic methods have been applied successfully to both simplified and high-fidelity models. This work demonstrates their utility in understanding the complex dynamics of the system and providing an extremely reduced yet accurate description.

6.1 Asymptotic Methods in Simplified Models

In the study of simplified models, a multiple scales asymptotic technique was introduced to investigate flutter-saturated solutions due to nonlinear friction. As a function of the aerodynamic intensity parameter, single-traveling wave (TW) saturated solutions and their stability were computed. For instance, for TW2, the bifurcation diagram is shown in Fig. 6.1. In the figure, the single-TW solution is plotted in black, with solid lines representing stable solutions and dashed lines representing unstable solutions. The system undergoes several Hopf bifurcations, resulting in a solution with an additional frequency and multi-TW components.

Moreover, the interaction of flutter and forced response under nonlinear friction was analyzed. A nonlinear analysis was conducted to explore the solution space as a function of the forcing frequency, producing bifurcation diagrams such as the one presented in Fig. 6.2 for a forcing with EO = 6. The results show that the system's behavior depends significantly on the forcing frequency due to the nonlinearity. When the forcing is close to the resonance frequency, the

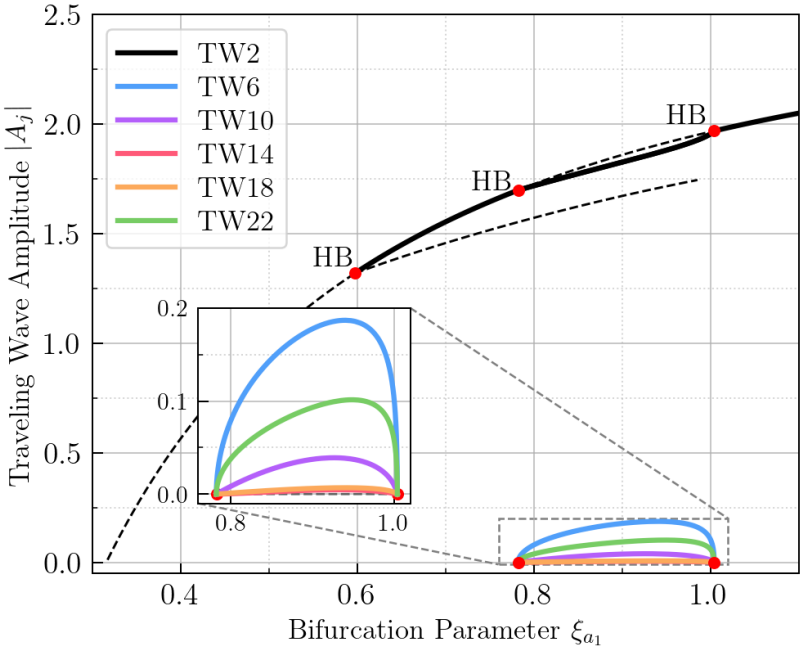

Figure 6.1: Bifurcation diagram of the TW2 solution with respect to the aerodynamic intensity parameter ξ_{a_1} for the wide distribution. A solution branch, emerging from the single-TW state, is found with multi-TW contributions. Solid (dashed) lines represent stable (unstable) solutions.

system responds synchronously. However, far from resonance, flutter-saturated solutions are recovered.

If the excitation corresponds to a stable TW, such as EO $= -5$, a new type of solution was found at the resonance peak, as illustrated in Fig. 6.3. This solution is synchronous with the forcing but composed of two different TWs: the excited one and an unstable mode. As a result, the blades of the system oscillate at different amplitudes despite the rotor being perfectly tuned.

The different solutions found in the asymptotic models were validated against numerical time simulations of a high-fidelity structure. Specifically, a rotor from the European ARIAS project, comprised of 144 blades, was analyzed. The results show that the dynamics captured by the asymptotic model are also present in the realistic structure.

6.2 Asymptotic Methods in High-Fidelity FEM Models

The asymptotic equations were directly extended to the analysis of high-fidelity FEM structures. This formulation allows obtaining a very reduced description directly from the FEM

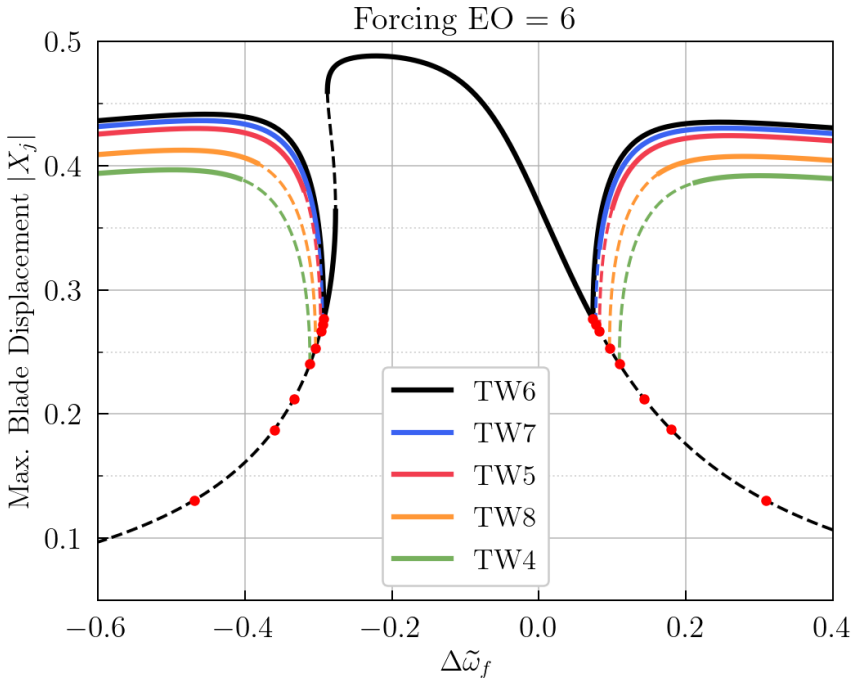

Figure 6.2: Bifurcation diagram of the full asymptotic model with a forcing of EO = 6. Solid (dashed) lines represent stable (unstable) solutions.

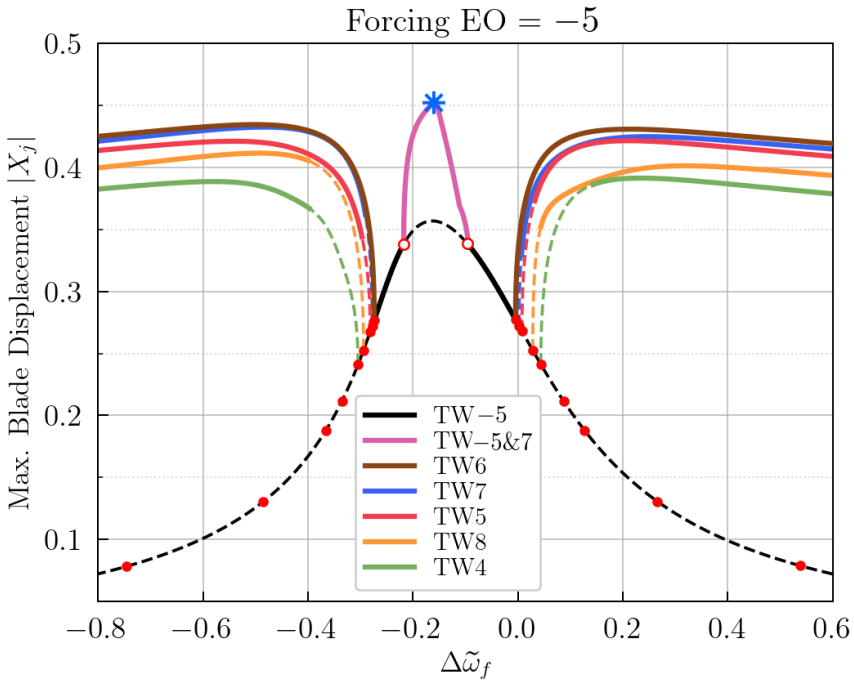

Figure 6.3: Bifurcation diagram of the full asymptotic model with a forcing of EO = −5. Solid (dashed) lines represent stable (unstable) solutions.

assembly matrices, facilitating the application of these techniques to real structures.

In practice, it is necessary to characterize the nonlinear friction forces by solving a system of the size of the contacts. The information on the different contact transitions and states due to dry friction is encoded into a single complex friction function. This nonlinearity is then introduced into a single nonlinear oscillator differential equation, allowing the forced response to be obtained through the evaluation of a simple analytical formula.

The results from the asymptotic model were compared against direct time integration of the ARIAS rotor. A comparison is shown in Fig. 6.4, presenting a frequency sweep across the first resonance frequency of the system. The results indicate that the agreement between the asymptotic model and the time integration of the FEM is good.

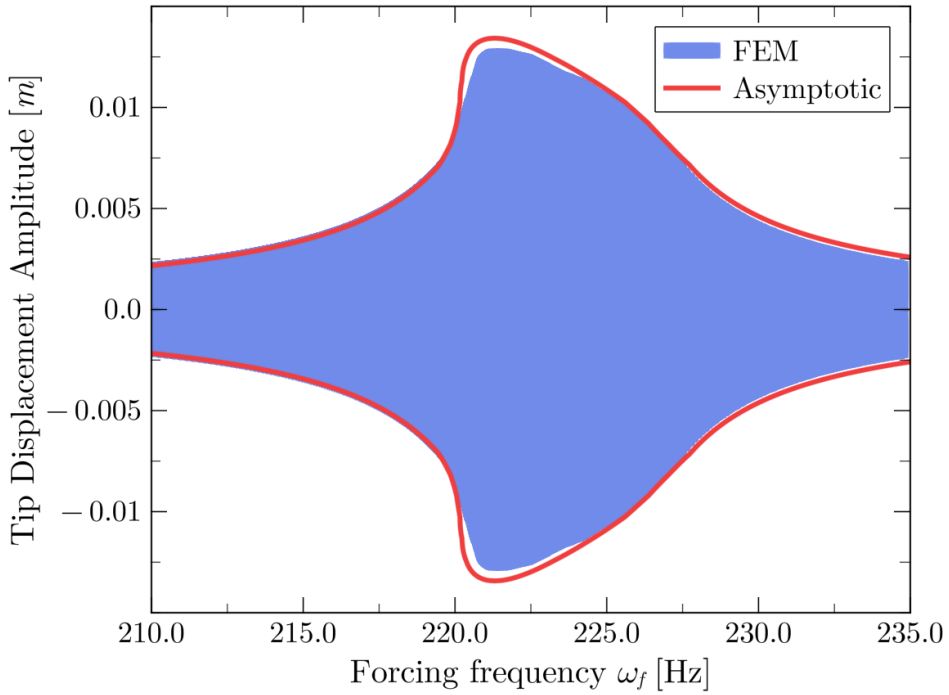

Figure 6.4: Resonance curve of the first modal frequency of the ARIAS blade.

Chapter 7

Conclusions and Future Work

7.1 Summary of the Main Findings

This dissertation analyzes nonlinear vibrations in turbomachinery due to friction effects for different configurations. The main contributions of the different topics that have been studied are summarized below.

First, in Chapter 2, an asymptotic model, based on a simplified mass-spring system representing the first modal family of a tuned low-pressure turbine bladed disk, was used to understand the different flutter saturated states. The reduced model was derived using the method of multiple scales, obtaining a description in the slow timescale where friction effects become relevant. The different saturated flutter states and their stability were analyzed. More complex solutions were identified using numerical continuation techniques, tracking new solution branches emerging at stability changes. The conclusions from this study are:

- Several single-TW saturated flutter solutions coexist for a given level of aerodynamic intensity. These states are usually related to the most aerodynamically unstable modes, and their saturated amplitude is reached when the nonlinear friction compensates the aerodynamic instability. This confirms the findings of previous works where numerical time integration usually showed the most aerodynamically unstable mode as the final state in the system, after very long integration times. Several single-TWs are possible as final states, where the most unstable one in terms of flutter seemed to have the largest basin of attraction.
- The advantage of the analysis of the asymptotic equations is that no time integration was required, since a bifurcation analysis of the stationary/periodic states is feasible.

This removes the uncertainty of time integration, in which convergence is never completely ensured because another state could develop on a much longer timescale.

- The linearized system around a single-TW solution showed that TW modes are coupled in pairs with wavenumbers $k \pm r$, where r is the TW index of the solution of interest. This explains why the decay of the TW modes during time integration usually occurs in pairs. The decay rate is determined by the difference in aerodynamic damping between the modes, which can be very small, resulting in very long convergence times.
- From the branches corresponding to the TW solutions, several bifurcation points were found, leading to multi-TW solutions. These states consist of multiple TW modes coupled through nonlinear friction and physically represent a nonlinear TW propagating continuously through the bladed-disk.
- Multi-TW solutions are set in the system over significantly longer timescales than single-TW saturated solutions, which makes the analysis using time domain simulations more difficult.
- Despite the complexity of the multi-TW solutions, the maximum blade vibration amplitude for a fixed aerodynamic intensity remained lower than that of the most aerodynamically unstable TW. From a fatigue perspective, this suggests that considering only the most unstable single-TW solution may be a conservative and safe assumption.

The analysis was then extended in Chapter 3 to include the interaction between an external forcing in the form of a TW (forced response) and flutter, both coupled through the nonlinear friction at the blade attachment. The results show that a linear superposition of both effects is not valid, as nonlinear interactions produce a switching between forced response and flutter during a frequency sweep. The analysis was conducted using the asymptotic model, where different solution branches were tracked and the space of possible states was characterized. The main findings of this chapter can be summarized as follows:

- Using the asymptotic model, periodic solutions locked to the forcing frequency can be readily found; a simple analytical expression is derived to compute the resonance curve. This provides a significant advantage over other methods, as it enables efficient parametric studies. This solution serves as the starting point for subsequent bifurcation analysis, since the aerodynamic instability of certain TW modes leads to the emergence of new solutions from this basic family of periodic states.
- This type of nonlinear single-TW analysis is common in the literature when the Harmonic Balance Method (HBM) is used to describe the forced response of realistic sys-

tems.

- A preliminary analysis was performed on a restricted system assuming the presence of only one TW, with the forcing having the same form as that TW. When the excitation engine order (EO) corresponded to a stable TW, the only solution found was periodic and locked to the forcing. When the excited TW was aerodynamically unstable, the system responded with the forcing frequency near the resonance peak. However, far from resonance, the solution transitioned to a flutter state, and the amplitude approached that of the single-TW flutter solution, as the effect of the forcing is reduced.
- In the case of the complete system (without the single-TW restriction), the bifurcation diagram of possible solutions revealed richer dynamics. When an unstable TW was forced, the stable solution near the resonance peak remained locked to the forcing frequency. However, due to the presence of additional unstable modes, new bifurcation points emerged away from resonance, each corresponding to a different single-TW flutter solution. These new solution branches involved two frequencies: the forcing frequency and an additional one. Close to the bifurcation point, the solutions contained multiple TW modes, but as the distance from resonance increased, only one TW amplitude remained. Far from the peak, these solutions asymptotically approached the single-TW flutter states identified in the previous chapter.
- When a stable TW mode was excited, the bifurcation diagram was similar, except near the resonance peak, where a new type of solution appeared. These states consisted of two TWs: the directly forced one and an unstable TW mode. In physical terms, for a bladed-disk with an even number of blades, these solutions represented a pattern in which the disk was divided into packets of two blades, each exhibiting a different maximum vibration amplitude. Thus, even in a tuned system, individual blades could respond differently. The same pattern was observed in rotors with an odd number of blades, although in that case, other TW modes contributed, and the pattern included a slowly propagating front that switched the amplitude state of the blades.
- The results from the asymptotic model were verified using a realistic bladed-disk from the European project ARIAS. Nonlinear switching between flutter and forced response was observed when the excitation targeted an unstable TW mode. Additionally, the states with different blade vibration amplitudes, corresponding to forcing a stable TW, were also identified. These results confirm that the asymptotic model accurately captures the effect of the friction nonlinearity, which is responsible for the emergence of these solutions.

An application of the asymptotic method to high-fidelity FEM models was carried out in Chapter 4. The main objective was to eliminate the need for calibrating a mass-spring model to study the system vibrations in a specific regime of interest, and instead use information directly from the original FEM. The analysis was restricted to a single sector of a bladed-disk with periodic boundary conditions, which can be interpreted as an ND0 excitation of the system. Under this assumption, the procedure is general and can be applied to other mechanical systems without specific restrictions on the nonlinear force, provided that the relative displacements between contact node pairs remain much smaller than those of the involved mode. The main conclusions obtained are listed below:

- A drastic reduction is possible for mechanical structures, as nonlinear forces are typically localized in the contact regions between components. These contact areas involve a very small subset of DOFs compared to the total number in the structure.
- Exploiting the fact that motion at the contact interfaces is much smaller than the modal displacements, a systematic asymptotic methodology was developed. The nonlinear friction in the asymptotic model is characterized by a complex friction coefficient, which is computed by solving a nonlinear system of the size of the contact DOFs.
- To accurately capture the nonlinear dissipation, the correction using the linear modes must be complemented by the inclusion of the constrained modes of the system: they capture the forces in the contacts resulting from their motion through coupling with the elastic DOFs. If this contribution is excluded, the resulting dissipation is significantly underestimated. Notably, this effect is not due to the nonlinearity of the problem, as it is observed in a purely linear configuration. This point can be regarded as a modification of the standard energy method to compute dissipation in the system.
- Once the nonlinear forces are characterized, the system dynamics reduce to a single complex differential equation. The forced response can then be analyzed by solving this equation, which yields a simple analytical expression for the resonance curve. Additional effects, such as linear instabilities, can be incorporated and studied within this reduced framework, which is significantly simpler than the full FEM model.
- The approach was validated using a simplified FEM model, showing very good agreement between the asymptotic model predictions and full time-integration results. The analysis included a nonlinear friction law with stick, slip, and gap states to represent realistic contact dynamics.
- The asymptotic equation was also applied to approximate the forced response of the first mode of a realistic bladed-disk from the European project ARIAS. The comparison

with time integration results again showed very good agreement.

Finally, in Chapter 5, the asymptotic methodology was extended to study a new case of nonlinear mode interaction. Specifically, the focus was on the forced response when two modes with different mode shapes and friction cycles are excited simultaneously. Since this technique is introduced here for the first time, a conceptual study based on a lumped model was conducted to validate the methodology. The main findings are the following:

- The simultaneous excitation of two different modes required solving a system defined on the contact DOFs over two independent timescales to obtain the asymptotic approximation of the nonlinear friction. The solution is a function periodic in both timescales.
- The effect of the nonlinear friction is encoded into two distinct complex friction coefficients, each associated with one of the vibration modes. These functions depend on the vibration amplitudes of both modes, and the interaction between them appears only through these terms. As expected, the mode interaction occurs solely via nonlinear effects.
- The asymptotic model in this case consists of two equations, one governing the slow-time evolution of each interacting mode. Periodic solutions can be directly computed, and analytical expressions for the resonance crossings were obtained.
- Using a lumped model calibrated to represent the interaction of two distinct modes under nonlinear friction, the asymptotic methodology was applied and validated against direct time integration results.
- When both modes are active, the nonlinear dissipation generally increases. As a result, the maximum displacement of the system with both modes excited is typically smaller than when only one mode is excited. Therefore, linear superposition significantly overestimates the total vibration amplitude.

7.2 Future Work

Throughout this thesis, asymptotic techniques were used to understand the vibration states of a bladed disk with nonlinear friction. In addition, a methodology has been developed to simplify the dynamics of high-fidelity FEM systems, enabling the use of asymptotic methods in industrial configurations. It has been proven that asymptotic models are a powerful tool to analyze the nonlinear vibrations of these structures, along with time domain integration and harmonic balance.

A list of future lines of investigation is included below:

- Inclusion of mistuning in the asymptotic equations to study the effect of these small terms in the problem of flutter interaction with forced response and nonlinear friction forces.
- Extend the asymptotic methodology to cyclic structures and high-fidelity FEM descriptions. In the case of a flat family, the extension of the asymptotic model is expected to be straightforward. On the other hand, for a family with a higher disk influence, a more careful study has to be carried out.
- Check the dependence of the asymptotic dissipation function Q on the discretization of the contact area. How relevant is it? Is the friction a global effect, somehow insensitive to the details of the contact area?
- Application of the asymptotic techniques to other configurations, such as interlock blades, where free cantilever modes do not adequately describe the system motion. The approach of using full-stuck modes as the initial approximation, as done in this work, is expected to be effective in these cases as well.
- Explore the possibility of including nonlinear structural effects in the asymptotic equations.

Appendix A

Method of Multiple Scales

A brief introduction to the method of multiple scales is given by analyzing the classical Duffing oscillator, described by the following differential equation

$$\ddot{x} + \tilde{\xi}\dot{x} + x + \epsilon x^3 = 2F_0 \cos(\omega_f t), \tag{A.1}$$

which models a damped oscillator with a nonlinear spring. This spring has a stiffening effect as the amplitude of vibration increases, since $\epsilon > 0$. The linear damping coefficient is retained through the term $\tilde{\xi}$ and the forcing term on the right-hand side has a constant amplitude $2F_0$ and a frequency ω_f.

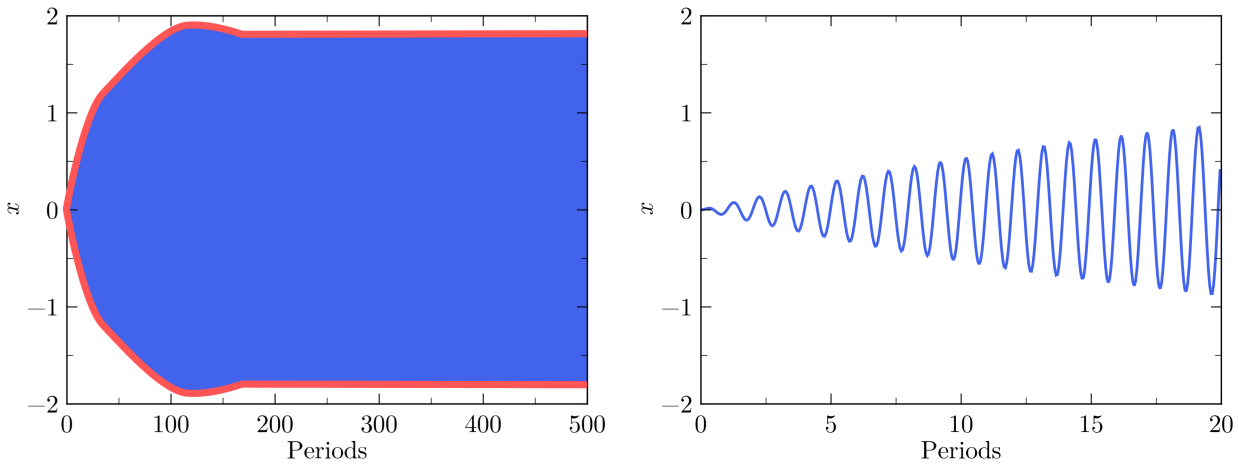

(a) 500 forcing cycles

(b) 20 forcing cycles

Figure A.1: Time evolution of the amplitude of the Duffing Oscillator for $\omega_f = 1.01$.

The goal is to study the resonance crossing of the nonlinear system in the limit where the nonlinearity is weak, i.e., $\epsilon \ll 1$. Since the forcing amplitude and linear damping are also

usually small, we will explicitly write them as $\tilde{\xi} = \epsilon\xi$ and $F_0 = \epsilon f_0$, which will be convenient when applying the systematic procedure of multiple scales. For the analysis, the values of $\epsilon = 0.01,\ \xi = 1,\ f_0 = 1$ are selected.

First, to gain insight on why the application of a multiple scales technique can be useful, a time domain simulation is performed for $\omega_f = 1.01$, which is expected to be close to the resonance peak. The results are shown in Fig. A.1. To the left, in Fig. A.1a, the response corresponding to the first 500 elastic cycles is presented, where the individual oscillations cannot be distinguished. To see these oscillations, the detail of the first 20 periods is also shown in Fig. A.1b.

Nevertheless, looking at the global response, it appears that another timescale is present in the system, much longer compared to the elastic one in blue, which has been highlighted in red in Fig. A.1a. This timescale describes the evolution of the slow envelope of the oscillations, which is the one related to the nonlinear effects of the system (and also affected by the linear damping). Thus, the goal of the method of multiple scales is to compute the differential equation that governs the slow dynamics of the system, eliminating the fast oscillations which are usually not of practical interest.

In order to perform the systematic derivation of the asymptotic model, we rewrite the differential equation with the explicit dependence on the small parameter ϵ, obtaining

$$\ddot{x} + x + \epsilon(\xi\dot{x} + x^3 - f_0 e^{i\omega_f t} + \text{ c.c.}) = 0, \tag{A.2}$$

where the forcing term has been cast in complex form for convenience. The idea of the method of multiple scales is to assume that the solution does not depend on a single timescale, but on two timescales: t, the fast timescale related the elastic oscillations with the natural frequency of the system, and $\tau = \epsilon t$, the slow timescale related to the evolution of the envelope. Thus, the solution of the system is now written as a function of two variables $x(t, \tau)$, which is expanded in a perturbation series in terms of ϵ as

$$x(t,\tau) = x^{(0)}(t,\tau) + \epsilon x^{(1)}(t,\tau) + \epsilon^2 x^{(2)}(t,\tau) + \cdots . \tag{A.3}$$

The first and second time derivative operators are also written in terms of the two timescales as

$$\begin{aligned} \dot{x} &= x_t + \epsilon x_\tau, \\ \ddot{x} &= x_{tt} + 2\epsilon x_{t\tau} + \epsilon^2 x_{\tau\tau}, \end{aligned} \tag{A.4}$$

where the subscripts denote partial derivatives with respect to the corresponding variable.

Substituting Eqs. (A.3), and (A.4) into Eq. (A.2) and collecting terms of the same order in ϵ gives

$$(x_{tt}^{(0)} + x^{(0)}) + \epsilon(x_{tt}^{(1)} + x^{(1)} + 2x_{t\tau}^{(0)} + \xi x_t^{(0)} + x^{(0)3} - f_0 e^{i\omega_f t} + \text{ c.c.}) + \mathcal{O}(\epsilon^2) = 0. \tag{A.5}$$

Now, we solve Eq. (A.5) by equating the terms of the same order in ϵ to zero. The zeroth-order equation $\mathcal{O}(\epsilon^0)$ is

$$x_{tt}^{(0)} + x^{(0)} = 0, \tag{A.6}$$

which is a linear undamped oscillator whose solution is

$$x^{(0)}(t,\tau) = A(\tau)e^{it} + \text{ c.c.}. \tag{A.7}$$

The fast elastic oscillations are contained in the term e^{it} and the amplitude $A(\tau)$ depends on the slow timescale, to be resolved in the subsequent order. The first-order equation $\mathcal{O}(\epsilon)$ is

$$x_{tt}^{(1)} + x^{(1)} = -2x_{t\tau}^{(0)} - \xi x_t^{(0)} - x^{(0)3} + f_0 e^{i\omega_f t} + \text{ c.c.}, \tag{A.8}$$

where the same linear operator appears on the left-hand side, but now applied to the first order correction of the solution. The right-hand side only depends on terms from the previous correction, which is a common feature in perturbation methods. Explicitly, these terms can be computed as

$$\begin{aligned} x_{t\tau}^{(0)} &= iA_\tau e^{it} + \text{ c.c.}, \\ x_t^{(0)} &= iAe^{it} + \text{ c.c.}, \\ x^{(0)3} &= A^3 e^{3it} + 3|A|^2 A e^{it} + \text{ c.c.}. \end{aligned} \tag{A.9}$$

Additionally, since the frequency sweep of interest is performed close to the resonance frequency, we can write the forcing frequency as $\omega_f = 1 + \epsilon\Delta\omega_f$. By doing so, and also plugging Eq. (A.9) into Eq. (A.8), we get

$$x_{tt}^{(1)} + x^{(1)} = (-2iA_\tau - i\xi A - 3|A|^2 A + f_0 e^{i\Delta\omega_f \tau})e^{it} - A^3 e^{3it} + \text{ c.c.}. \tag{A.10}$$

The function e^{it} is a solution of the homogeneous problem in Eq. (A.10). As a consequence, to produce bounded periodic solutions in this problem, we need to apply the so-called solvability conditions to the right-hand side of the system. This condition means that we have to eliminate the resonant terms, which are the ones proportional to the solution of the homogeneous problem (otherwise terms of the form te^{it} would appear). In this problem, this

translates in enforcing the term in parentheses multiplying e^{it} to be zero, which gives a complex differential equation for the amplitude

$$\frac{\mathrm{d}A}{\mathrm{d}\tau} + \frac{\xi}{2}A = \frac{3}{2}i|A|^2A - i\frac{f_0}{2}e^{i\Delta\omega_f\tau}. \tag{A.11}$$

This differential equation is nonlinear due to the first term after the equal sign. Since we are interested in the study of periodic solutions synchronous with the forcing frequency, we could search for them directly in this equation, by assuming the *ansatz* $A(\tau) = |A|e^{i\Delta\omega_f\tau}e^{i\varphi}$, giving

$$\left(\frac{\mathrm{d}|A|}{\mathrm{d}\tau} - i\Delta\omega_f|A|\right)e^{i\varphi} + \frac{\xi}{2}|A|e^{i\varphi} = \frac{3}{2}i|A|^3e^{i\varphi} - i\frac{f_0}{2}. \tag{A.12}$$

The resonance curve corresponds to the case where the amplitude is constant, $\mathrm{d}|A|/\mathrm{d}\tau = 0$, resulting in the algebraic complex equation

$$i\left(\Delta\omega_f - \frac{3}{2}|A|^2\right) + \frac{\xi}{2} = -i\frac{f_0}{2|A|}e^{-i\varphi}. \tag{A.13}$$

Taking the absolute value of this equation gives a relation between modulus of the amplitude $|A|$ and the forcing frequency $\Delta\omega_f$, which is the resonance curve of the system given by the asymptotic model. The phase φ could also be obtained relating the phases of this equation, although the result is omitted here.

The expression of the resonance curve is

$$\Delta\omega_f = \frac{3}{2}|A|^2 \pm \sqrt{\left(\frac{f_0}{2|A|}\right)^2 - \left(\frac{\xi}{2}\right)^2}, \tag{A.14}$$

which is plotted in Fig. A.2 for the set of parameters considered at the beginning of this section. The asymptotic resonance curve is compared against direct time integration of the system and also a harmonic balance approach, which retains 10 harmonics. As can be seen from the figure, in this range of values where the asymptotic description is valid, the agreement between the asymptotic equation and the other two methods is excellent.

The asymptotic model from Eq. (A.14) has the additional advantage, with respect to the other methods, that it just requires the evaluation of a simple analytical expression. In contrast, one would have to solve a differential equation (time domain) or a system of non-linear equations (Harmonic Balance). This huge reduction is particularly useful for larger systems, possibly related to industrial applications, where parametric studies over a wide range become feasible. Additionally, the asymptotic expansion gives an analytical expression

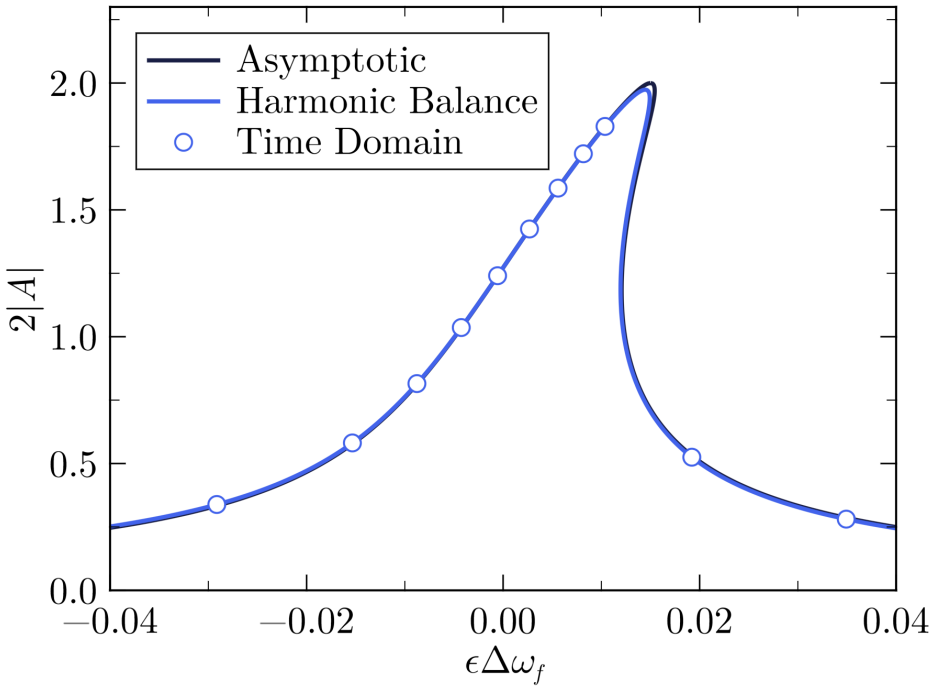

Figure A.2: Resonance crossing of the Duffing Oscillator system.

that allows a more deep understanding between the relation of the different quantities that appear in the system.

Appendix B

Single Traveling Wave Jacobian

Starting from the system in TW basis

$$\frac{\mathrm{d}}{\mathrm{d}\tau}\begin{pmatrix} B_1 \\ \vdots \\ B_r \\ \vdots \\ B_N \end{pmatrix} = -\frac{i}{2}\mathbf{E}^H \begin{pmatrix} Q(|X_1|)-Q(R_r) & & & & \\ & \ddots & & & \\ & & Q(|X_r|)-Q(R_r) & & \\ & & & \ddots & \\ & & & & Q(|X_N|)-Q(R_r) \end{pmatrix} \mathbf{E} \begin{pmatrix} B_1 \\ \vdots \\ B_r \\ \vdots \\ B_N \end{pmatrix} + \begin{pmatrix} -(\tilde{\xi}_1-\tilde{\xi}_r)+i(\tilde{\omega}_1-\tilde{\omega}_r) & & & & \\ & \ddots & & & \\ & & 0 & & \\ & & & \ddots & \\ & & & & -(\tilde{\xi}_N-\tilde{\xi}_r)+i(\tilde{\omega}_N-\tilde{\omega}_r) \end{pmatrix} \begin{pmatrix} B_1 \\ \vdots \\ B_r \\ \vdots \\ B_N \end{pmatrix}, \tag{B.1}$$

the transformation $\mathbf{X} = \mathbf{EB}$ is applied to write it in the displacement basis, since the nonlinear friction terms are diagonal here. After applying the transformation, one gets

$$\frac{\mathrm{d}}{\mathrm{d}\tau}\begin{pmatrix} X_1 \\ \vdots \\ X_r \\ \vdots \\ X_N \end{pmatrix} = -\frac{i}{2} \begin{pmatrix} Q(|X_1|)-Q(R_r) & & & & \\ & \ddots & & & \\ & & Q(|X_r|)-Q(R_r) & & \\ & & & \ddots & \\ & & & & Q(|X_N|)-Q(R_r) \end{pmatrix} \begin{pmatrix} X_1 \\ \vdots \\ X_r \\ \vdots \\ X_N \end{pmatrix} + \mathbf{E}\mathbf{D}_a\mathbf{E}^H\mathbf{X}, \tag{B.2}$$

where the aerodynamic and structural damping and frequency corrections have been renamed to $\mathbf{D}_a$ for simplicity. The linearization around a state $\mathbf{Z}$ can be expressed as

$$X_j = Z_j + z_j, \tag{B.3}$$

where $j = 1, \ldots, N$ and $|z_j| \ll |Z_j|$. Since the nonlinear friction depends on the modulus of $|X_j|$, we write the first order approximation, which is

$$|X_j| \approx |Z_j| + \frac{1}{2}\left(\frac{Z_j}{|Z_j|}\bar{z}_j + \frac{\bar{Z}_j}{|Z_j|}z_j\right). \tag{B.4}$$

Therefore, the linearization of the friction coefficient can be expressed as

$$\begin{aligned} Q(|X_j|) &\approx Q(|Z_j|) + Q'(|Z_j|)(|X_j| - |Z_j|) \\ &\approx Q(|Z_j|) + \frac{Q'(|Z_j|)}{2|Z_j|}(\bar{Z}_j z_j + Z_j \bar{z}_j). \end{aligned} \tag{B.5}$$

Substituting Eq. (B.5) into Eq. (B.2), and retaining only up to linear terms give

$$\begin{aligned} \frac{\mathrm{d}}{\mathrm{d}\tau}\begin{pmatrix} z_1 \\ \\ z_r \\ \vdots \\ z_N \end{pmatrix} = &-\frac{i}{2}\begin{pmatrix} Q(|Z_1|) - Q(R_r) & & & & \\ & \ddots & & & \\ & & Q(|Z_r|) - Q(R_r) & & \\ & & & \ddots & \\ & & & & Q(|Z_N|) - Q(R_r) \end{pmatrix}\begin{pmatrix} z_1 \\ \vdots \\ z_r \\ \vdots \\ z_N \end{pmatrix} \\ &-\frac{i}{2}\begin{pmatrix} \frac{Q'(|Z_1|)}{2|Z_1|}(\bar{Z}_1 z_1 + Z_1 \bar{z}_1) & & & & \\ & \ddots & & & \\ & & \frac{Q'(|Z_r|)}{2|Z_r|}(\bar{Z}_r z_r + Z_r \bar{z}_r) & & \\ & & & \ddots & \\ & & & & \frac{Q'(|Z_N|)}{2|Z_N|}(\bar{Z}_N z_N + Z_N \bar{z}_N) \end{pmatrix}\begin{pmatrix} Z_1 \\ \vdots \\ Z_r \\ \vdots \\ Z_N \end{pmatrix} \\ &+ \mathbf{E}\mathbf{D}_a\mathbf{E}^H\mathbf{z}. \end{aligned} \tag{B.6}$$

Rearranging the system in a more compact form results in

$$\begin{aligned} \frac{\mathrm{d}\mathbf{z}}{\mathrm{d}\tau} = &-\frac{i}{2}\mathbf{diag}\left(\frac{Q'(|Z_j|)Z_j}{2|Z_j|}Z_j\right)\bar{\mathbf{z}} \\ &-\frac{i}{2}\mathbf{diag}\left(Q(|Z_j|) - Q(R_r) + \frac{Q'(|Z_j|)Z_j}{2|Z_j|}\bar{Z}_j\right)\mathbf{z} \\ &+\mathbf{E}\mathbf{D}_a\mathbf{E}^H\mathbf{z}, \end{aligned} \tag{B.7}$$

or, in TW basis

$$\frac{\mathrm{d}\mathbf{a}}{\mathrm{d}\tau} = \mathbf{Q}_2\bar{\mathbf{a}} + \mathbf{Q}_1\mathbf{a} + \mathbf{D}_a\mathbf{a}, \tag{B.8}$$

where the matrices $\mathbf{Q}_1$ and $\mathbf{Q}_2$ are defined as

$$\begin{aligned}\mathbf{Q}_1 &= -\frac{i}{2}\mathbf{E}^H\mathbf{diag}\left(Q(|Z_j|) - Q(R_r) + \frac{Q'(|Z_j|)Z_j}{2|Z_j|}\bar{Z}_j\right)\mathbf{E},\\ \mathbf{Q}_2 &= -\frac{i}{2}\mathbf{E}^H\mathbf{diag}\left(\frac{Q'(|Z_j|)Z_j}{2|Z_j|}Z_j\right)\bar{\mathbf{E}}.\end{aligned} \tag{B.9}$$

Since the continuation software requires the system to be in real variables, we can write $\mathbf{a} = \mathbf{u} + i\mathbf{v}$ and get

$$\frac{\mathrm{d}}{\mathrm{d}\tau}\begin{pmatrix}\mathbf{u}\\ \mathbf{v}\end{pmatrix} = \begin{pmatrix}\mathbf{Q}_1^R + \mathbf{Q}_2^R + \mathbf{D}_a^R & -\mathbf{Q}_1^I + \mathbf{Q}_2^I - \mathbf{D}_a^I\\ \mathbf{Q}_1^I + \mathbf{Q}_2^I + \mathbf{D}_a^I & \mathbf{Q}_1^R - \mathbf{Q}_2^R + \mathbf{D}_a^R\end{pmatrix}\begin{pmatrix}\mathbf{u}\\ \mathbf{v}\end{pmatrix} \equiv \mathbf{J}\begin{pmatrix}\mathbf{u}\\ \mathbf{v}\end{pmatrix}, \tag{B.10}$$

where $\mathbf{J}$ is the desired jacobian matrix.

For the pseudo-arclength continuation, the derivative with respect to the bifurcation parameter ξ_{a_1} is also required. Denoting the original system of differential equations (B.1) as

$$\frac{\mathrm{d}\mathbf{B}}{\mathrm{d}\tau} = \mathbf{F}(\mathbf{B}, \xi_{a_1}), \tag{B.11}$$

we have that the terms that depend on the parameter from $\mathbf{F}(\mathbf{B}, \xi_{a_1})$ are just

$$\frac{i}{2}Q(R_r)\begin{pmatrix}B_1\\ \vdots\\ B_r\\ \vdots\\ B_N\end{pmatrix} + \begin{pmatrix}-(\tilde{\xi}_1 - \tilde{\xi}_r) & & & & \\ & \ddots & & & \\ & & 0 & & \\ & & & \ddots & \\ & & & & -(\tilde{\xi}_N - \tilde{\xi}_r)\end{pmatrix}\begin{pmatrix}B_1\\ \vdots\\ B_r\\ \vdots\\ B_N\end{pmatrix}. \tag{B.12}$$

Recall that the aerodynamic damping coefficient was expressed as

$$\xi_a^j = \xi_{a_0} - \xi_{a_1}\sin\left(\frac{2\pi j}{N} + \xi_{a_2}\right) \quad (\%), \tag{2.9}$$

so that

$$\frac{\mathrm{d}\tilde{\xi}_j}{\mathrm{d}\xi_{a_1}} = \frac{\mathrm{d}\xi_a^j}{\mathrm{d}\xi_{a_1}} = -\sin\left(\frac{2\pi j}{N} + \xi_{a_2}\right). \tag{B.13}$$

The complex friction function $Q(R_r)$ depends on the bifurcation parameter, since

$$Q^I(R_r) = 2\tilde{\xi}_r. \tag{2.39}$$

Therefore, the derivative

$$\frac{\mathrm{d}Q}{\mathrm{d}\xi_{a_1}} = \frac{\mathrm{d}Q}{\mathrm{d}R_r}\frac{\mathrm{d}R_r}{\mathrm{d}\xi_{a_1}} = (Q^{R'}(R_r) + iQ^{I'}(R_r))\frac{\mathrm{d}R_r}{\mathrm{d}\xi_{a_1}}, \tag{B.14}$$

where the derivative of R_r with respect to ξ_{a_1} can is

$$\frac{\mathrm{d}R_r}{\mathrm{d}\xi_{a_1}} = \frac{2}{Q^{I'}(R_r)}\frac{\mathrm{d}\tilde{\xi}_r}{\mathrm{d}\xi_{a_1}}, \tag{B.15}$$

which is found by implicitly differentiating Eq. (2.39). Thus,

$$\frac{\mathrm{d}Q}{\mathrm{d}\xi_{a_1}} = 2\left(\frac{Q^{R'}(R_r)}{Q^{I'}(R_r)} + i\right)\frac{\mathrm{d}\tilde{\xi}_r}{\mathrm{d}\xi_{a_1}}. \tag{B.16}$$

Finally, for the derivative with respect to the bifurcation parameter one has

$$\frac{\mathrm{d}\mathbf{F}}{\mathrm{d}\xi_{a_1}} = \begin{pmatrix} \ddots & & \\ & \sin\left(\frac{2\pi j}{N} + \xi_{a_2}\right) - i\frac{Q^{R'}(R_r)}{Q^{I'}(R_r)}\sin\left(\frac{2\pi r}{N} + \xi_{a_2}\right) & \\ & & \ddots \end{pmatrix} \begin{pmatrix} \vdots \\ B_j \\ \vdots \end{pmatrix}. \tag{B.17}$$

Appendix C

Flutter and Forced Response Jacobian

In this appendix the jacobian matrix for the problem of the interaction of flutter and forced response under nonlinear friction is derived.

As explained in Chapter 3, two problems are considered: the simplified description of a one TW system and the complete asymptotic equations. The bifurcation parameter in this problem is the frequency of the forcing $\Delta\tilde{\omega}_f$.

C.1 One Traveling Wave System

The jacobian is obtained by linearizing the system of equations

$$\frac{\mathrm{d}}{\mathrm{d}\tau}\begin{pmatrix} B^R_{\mathrm{EO}} \\ B^I_{\mathrm{EO}} \end{pmatrix} = \begin{pmatrix} Q^I(|X|)/2 - \tilde{\xi}_{\mathrm{EO}} & Q^R(|X|)/2 - (\tilde{\omega}_{\mathrm{EO}} - \Delta\tilde{\omega}_f) \\ -Q^R(|X|)/2 + (\tilde{\omega}_{\mathrm{EO}} - \Delta\tilde{\omega}_f) & Q^I(|X|)/2 - \tilde{\xi}_{\mathrm{EO}} \end{pmatrix} \begin{pmatrix} B^R_{\mathrm{EO}} \\ B^I_{\mathrm{EO}} \end{pmatrix} - \begin{pmatrix} 0 \\ \frac{\tilde{f}}{2\sqrt{N}} \end{pmatrix}, \tag{3.9}$$

which are denoted as

$$\frac{\mathrm{d}}{\mathrm{d}\tau}\begin{pmatrix} B^R_{\mathrm{EO}} \\ B^I_{\mathrm{EO}} \end{pmatrix} = \begin{pmatrix} F_1(B^R_{\mathrm{EO}}, B^I_{\mathrm{EO}}, \Delta\tilde{\omega}_f) \\ F_2(B^R_{\mathrm{EO}}, B^I_{\mathrm{EO}}, \Delta\tilde{\omega}_f) \end{pmatrix}, \tag{C.1}$$

for brevity. Recall that, for this one TW system, $|X| = |B_{\mathrm{EO}}|$, so the derivatives of the nonlinear terms are

$$\begin{aligned} \frac{\mathrm{d}Q^I}{\mathrm{d}B^R_{\mathrm{EO}}} &= Q^{I\prime}\frac{\mathrm{d}|B_{\mathrm{EO}}|}{\mathrm{d}B^R_{\mathrm{EO}}} = \frac{B^R_{\mathrm{EO}}}{|B_{\mathrm{EO}}|}Q^{I\prime}, \quad \frac{\mathrm{d}Q^I}{\mathrm{d}B^I_{\mathrm{EO}}} = Q^{I\prime}\frac{\mathrm{d}|B_{\mathrm{EO}}|}{\mathrm{d}B^I_{\mathrm{EO}}} = \frac{B^I_{\mathrm{EO}}}{|B_{\mathrm{EO}}|}Q^{I\prime}, \\ \frac{\mathrm{d}Q^R}{\mathrm{d}B^R_{\mathrm{EO}}} &= Q^{R\prime}\frac{\mathrm{d}|B_{\mathrm{EO}}|}{\mathrm{d}B^R_{\mathrm{EO}}} = \frac{B^R_{\mathrm{EO}}}{|B_{\mathrm{EO}}|}Q^{R\prime}, \quad \frac{\mathrm{d}Q^R}{\mathrm{d}B^I_{\mathrm{EO}}} = Q^{R\prime}\frac{\mathrm{d}|B_{\mathrm{EO}}|}{\mathrm{d}B^I_{\mathrm{EO}}} = \frac{B^I_{\mathrm{EO}}}{|B_{\mathrm{EO}}|}Q^{R\prime}, \end{aligned} \tag{C.2}$$

because $|B_{\mathrm{EO}}| = \sqrt{(B_{\mathrm{EO}}^R)^2 + (B_{\mathrm{EO}}^I)^2}$. Thus, the jacobian matrix is

$$\mathbf{J} = \begin{pmatrix} \mathbf{J}_{11} & \mathbf{J}_{12} \\ \mathbf{J}_{21} & \mathbf{J}_{22} \end{pmatrix}, \tag{C.3}$$

where

$$\begin{aligned}
\mathbf{J}_{11} &= \frac{Q^I(|X|)}{2} - \tilde{\xi}_{\mathrm{EO}} + \frac{Q^{I'}(|X|)}{2}\frac{(B_{\mathrm{EO}}^R)^2}{|B_{\mathrm{EO}}|} + \frac{Q^{R'}(|X|)}{2}\frac{B_{\mathrm{EO}}^R B_{\mathrm{EO}}^I}{|B_{\mathrm{EO}}|}, \\
\mathbf{J}_{12} &= \frac{Q^R(|X|)}{2} - (\tilde{\omega}_{\mathrm{EO}} - \Delta\tilde{\omega}_f) + \frac{Q^{R'}(|X|)}{2}\frac{(B_{\mathrm{EO}}^I)^2}{|B_{\mathrm{EO}}|} + \frac{Q^{I'}(|X|)}{2}\frac{B_{\mathrm{EO}}^R B_{\mathrm{EO}}^I}{|B_{\mathrm{EO}}|}, \\
\mathbf{J}_{21} &= -\frac{Q^R(|X|)}{2} + (\tilde{\omega}_{\mathrm{EO}} - \Delta\tilde{\omega}_f) - \frac{Q^{R'}(|X|)}{2}\frac{(B_{\mathrm{EO}}^R)^2}{|B_{\mathrm{EO}}|} + \frac{Q^{I'}(|X|)}{2}\frac{B_{\mathrm{EO}}^R B_{\mathrm{EO}}^I}{|B_{\mathrm{EO}}|}, \\
\mathbf{J}_{22} &= \frac{Q^I(|X|)}{2} - \tilde{\xi}_{\mathrm{EO}} + \frac{Q^{I'}(|X|)}{2}\frac{(B_{\mathrm{EO}}^I)^2}{|B_{\mathrm{EO}}|} - \frac{Q^{R'}(|X|)}{2}\frac{B_{\mathrm{EO}}^R B_{\mathrm{EO}}^I}{|B_{\mathrm{EO}}|}.
\end{aligned} \tag{C.4}$$

The derivatives with respect to the forcing frequency, which are also needed for the pseudo-arclength continuation, are

$$\begin{aligned}
\frac{\partial F_1}{\partial \Delta\tilde{\omega}_f} &= B_{\mathrm{EO}}^I, \\
\frac{\partial F_2}{\partial \Delta\tilde{\omega}_f} &= -B_{\mathrm{EO}}^R.
\end{aligned} \tag{C.5}$$

C.2 Full System

The asymptotic description of the flutter and forced response problem is

$$\frac{\mathrm{d}}{\mathrm{d}\tau}\begin{pmatrix} B_1 \\ \vdots \\ B_N \end{pmatrix} = -\frac{i}{2}\mathbf{E}^H \begin{pmatrix} Q(|X_1|) & \dots & 0 \\ \vdots & \ddots & \vdots \\ 0 & \dots & Q(|X_N|) \end{pmatrix} \mathbf{E} \begin{pmatrix} B_1 \\ \vdots \\ B_N \end{pmatrix} + \begin{pmatrix} -\tilde{\xi}_1 + i(\tilde{\omega}_1 - \Delta\tilde{\omega}_f) & \dots & 0 \\ \vdots & \ddots & \vdots \\ 0 & \dots & -\tilde{\xi}_N + i(\tilde{\omega}_N - \Delta\tilde{\omega}_f) \end{pmatrix} \begin{pmatrix} B_1 \\ \vdots \\ B_N \end{pmatrix} - \frac{i}{2\sqrt{N}}\tilde{f}\mathbb{1}_{\mathrm{EO}}, \tag{3.7}$$

where every TW mode of the family is considered. The complete system is also denoted as

$$\frac{\mathrm{d}\mathbf{B}}{\mathrm{d}\tau} = \mathbf{F}(\mathbf{B}, \Delta\tilde{\omega}_f), \tag{C.6}$$

for brevity. We introduce the matrices

$$\begin{aligned} \mathbf{Q}_1 &= -\frac{i}{2}\mathbf{E}^H \mathbf{diag}\left(Q(|X_j|) + \frac{Q'(|X_j|)X_j}{2|X_j|}\bar{X}_j\right)\mathbf{E}, \\ \mathbf{Q}_2 &= -\frac{i}{2}\mathbf{E}^H \mathbf{diag}\left(\frac{Q'(X_j|)X_j}{2|X_j|}X_j\right)\bar{\mathbf{E}}, \end{aligned} \tag{C.7}$$

which come from the linearization of the nonlinear friction term, following a completely analogous derivation to Appendix B (but with the term $Q(R_r)$ missing here). Additionally, we denote

$$\zeta = \mathbf{diag}(-\tilde{\xi}_j + i(\tilde{\omega}_j - \Delta\tilde{\omega}_f)), \tag{C.8}$$

Then, after splitting the system into real and imaginary parts, the jacobian takes the form

$$\mathbf{J} = \begin{pmatrix} \mathbf{Q}_1^R + \mathbf{Q}_2^R + \zeta^R & -\mathbf{Q}_1^I + \mathbf{Q}_2^I - \zeta^I \\ \mathbf{Q}_1^I + \mathbf{Q}_2^I + \zeta^I & \mathbf{Q}_1^R - \mathbf{Q}_2^R + \zeta^R \end{pmatrix}. \tag{C.9}$$

The derivative with respect to the forcing frequency is just

$$\begin{aligned} \frac{\partial \mathbf{F}^R}{\partial \Delta\tilde{\omega}_f} &= \mathbf{B}^I, \\ \frac{\partial \mathbf{F}^I}{\partial \Delta\tilde{\omega}_f} &= -\mathbf{B}^R. \end{aligned} \tag{C.10}$$

References

[1] A. Collar, "The expanding domain of aeroelasticity", *The Aeronautical Journal*, vol. 50, no. 428, pp. 613–636, 1946. DOI: 10.1017/S0368393100120358.

[2] E. H. Dowell, *A modern course in aeroelasticity*. Springer Nature, 2021, vol. 264. DOI: 10.1007/978-3-030-74236-2.

[3] O. Bendiksen, R. E. Kielb, and K. C. Hall, "Turbomachinery aeroelasticity", *Encyclopedia of Aerospace Engineering*, 2010. DOI: 10.1002/9780470686652.eae156.

[4] Z. S. Spakovszky, "Instabilities everywhere! hard problems in aero-engines", *Journal of Turbomachinery*, vol. 145, no. 2, p. 021 011, Oct. 2022. DOI: 10.1115/1.4055424.

[5] R. Kielb, J. Barter, O. Chernycheva, and T. Fransson, "Flutter of low pressure turbine blades with cyclic symmetric modes: A preliminary design method", *Journal of Turbomachinery*, vol. 126, no. 2, pp. 306–309, Jun. 2004. DOI: 10.1115/1.1650380.

[6] B. Cowles, "High cycle fatigue in aircraft gas turbines—an industry perspective", *International Journal of Fracture*, vol. 80, pp. 147–163, 1996. DOI: 10.1007/BF00012667.

[7] Y. El-Aini, R. deLaneuville, A. Stoner, *et al.*, "High cycle fatigue of turbomachinery components-industry perspective", in *33rd joint propulsion conference and exhibit*, 1997, p. 3365. DOI: 10.2514/6.1997-3365.

[8] T. Nicholas, "Critical issues in high cycle fatigue", *International Journal of Fatigue*, vol. 21, S221–S231, 1999. DOI: 10.1016/S0142-1123(99)00074-2.

[9] D. E. Thomson and J. T. Griffin, "The national turbine engine high cycle fatigue program", *Global Gas Turbine News*, vol. 39, no. 1, pp. 14–17, 1999.

[10] G. Strang, *Introduction to linear algebra*. SIAM, 2022.

[11] H. Georgi, *The physics of waves*. Prentice Hall Englewood Cliffs, NJ, 1993.

[12] S. Rodríguez Blanco, "Reduced models for the study of aeroelastic vibrations in turbomachinery", 2023. DOI: 10.20868/UPM.thesis.80795.

[13] D. Ewins, "Control of vibration and resonance in aero engines and rotating machinery – an overview", *International Journal of Pressure Vessels and Piping*, vol. 87, no. 9, pp. 504–510, 2010, Dynamic Loading of Components and Structures. DOI: 10.1016/j.ijpvp.2010.07.001.

[14] A. V. Srinivasan, "Flutter and resonant vibration characteristics of engine blades: An igti scholar paper", ser. Turbo Expo, vol. Volume 4: Manufacturing Materials and Metallurgy; Ceramics; Structures and Dynamics; Controls, Diagnostics and Instrumentation; Education; IGTI Scholar Award, Jun. 1997, V004T17A001. DOI: 10.1115/97-GT-533.

[15] A. Vega and R. Corral, "Physics of vibrating airfoils at low reduced frequency", ser. Turbo Expo, vol. Volume 7B: Structures and Dynamics, Jun. 2013, V07BT33A008. DOI: 10.1115/GT2013-94906.

[16] M. Krack, L. Salles, and F. Thouverez, "Vibration prediction of bladed disks coupled by friction joints", *Archives of Computational Methods in Engineering*, vol. 24, pp. 589–636, 2017. DOI: 10.1007/s11831-016-9183-2.

[17] E. Petrov and D. Ewins, "State-of-the-art dynamic analysis for non-linear gas turbine structures", *Proceedings of the Institution of Mechanical Engineers, Part G: Journal of Aerospace Engineering*, vol. 218, no. 3, pp. 199–211, 2004. DOI: 10.1243/0954410041872906.

[18] B. Yang, M. Chu, and C. Menq, "Stick-slip-separation analysis and non-linear stiffness and damping characterization of friction contacts having variable normal load", *Journal of Sound and Vibration*, vol. 210, no. 4, pp. 461–481, 1998. DOI: 10.1006/jsvi.1997.1305.

[19] U. Olofsson, "Cyclic micro-slip under unlubricated conditions", *Tribology International*, vol. 28, no. 4, pp. 207–217, 1995. DOI: 10.1016/0301-679X(94)00001-7.

[20] E. P. Petrov and D. J. Ewins, "Method for analysis of nonlinear multiharmonic vibrations of mistuned bladed disks with scatter of contact interface characteristics",

Journal of Turbomachinery, vol. 127, no. 1, pp. 128–136, Feb. 2005. DOI: 10.1115/1.1812781.

[21] D. Jiang, C. Pierre, and S. Shaw, "Nonlinear normal modes for vibratory systems under harmonic excitation", *Journal of Sound and Vibration*, vol. 288, no. 4, pp. 791–812, 2005. DOI: 10.1016/j.jsv.2005.01.009.

[22] E. P. Petrov and D. J. Ewins, "Generic friction models for time-domain vibration analysis of bladed disks", *Journal of Turbomachinery*, vol. 126, no. 1, pp. 184–192, Mar. 2004. DOI: 10.1115/1.1644557.

[23] E. P. Petrov, "A high-accuracy model reduction for analysis of nonlinear vibrations in structures with contact interfaces", *Journal of Engineering for Gas Turbines and Power*, vol. 133, no. 10, p. 102 503, May 2011. DOI: 10.1115/1.4002810.

[24] A. Rizvi, C. W. Smith, R. Rajasekaran, and K. E. Evans, "Dynamics of dry friction damping in gas turbines: Literature survey", *Journal of Vibration and Control*, vol. 22, no. 1, pp. 296–305, 2016. DOI: 10.1177/1077546313513051.

[25] S. Nacivet, C. Pierre, F. Thouverez, and L. Jezequel, "A dynamic lagrangian frequency–time method for the vibration of dry-friction-damped systems", *Journal of Sound and Vibration*, vol. 265, no. 1, pp. 201–219, 2003. DOI: 10.1016/S0022-460X(02)01447-5.

[26] C. M. Firrone, S. Zucca, *et al.*, "Modelling friction contacts in structural dynamics and its application to turbine bladed disks", *Numerical Analysis-Theory and Application*, vol. 14, pp. 301–334, 2011. DOI: 10.5772/25128.

[27] S. Zucca, C. M. Firrone, and M. M. Gola, "Numerical assessment of friction damping at turbine blade root joints by simultaneous calculation of the static and dynamic contact loads", *Nonlinear Dynamics*, vol. 67, pp. 1943–1955, 2012. DOI: 10.1007/s11071-011-0119-y.

[28] G. Zara, T. M. Berruti, and S. Zucca, "The impact of different equilibrium hypothesis on the non-linear response of bladed disks", ser. Turbo Expo, vol. Volume 10B: Structures and Dynamics — Fatigue, Fracture, and Life Prediction; Probabilistic Methods; Rotordynamics; Structural Mechanics and Vibration, Jun. 2024, V10BT27A007. DOI: 10.1115/GT2024-123245.

[29] E. Dowell, "Reduced-order modeling: A personal journey", *Nonlinear Dynamics*, vol. 111, no. 11, pp. 9699–9720, 2023. DOI: 10.1007/s11071-023-08398-7.

[30] R. R. Craig Jr and M. C. Bampton, "Coupling of substructures for dynamic analyses.", *AIAA journal*, vol. 6, no. 7, pp. 1313–1319, 1968. DOI: 10.2514/3.4741.

[31] R. R. Craig Jr and C.-J. Chang, "A review of substructure coupling methods for dynamic analysis", *NASA. Langley Res. Center Advan. in Eng. Sci., Vol. 2*, 1976.

[32] R. R. Craig Jr and C.-J. Chang, "Free-interface methods of substructure coupling for dynamic analysis", *AIAA Journal*, vol. 14, no. 11, pp. 1633–1635, 1976. DOI: 10.2514/3.7264.

[33] M.-T. Yang and J. H. Griffin, "A reduced-order model of mistuning using a subset of nominal system modes", *Journal of Engineering for Gas Turbines and Power*, vol. 123, no. 4, pp. 893–900, Mar. 1999. DOI: 10.1115/1.1385197.

[34] M.-T. Yang and J. H. Griffin, "A normalized modal eigenvalue approach for resolving modal interaction", *Journal of Engineering for Gas Turbines and Power*, vol. 119, no. 3, pp. 647–650, Jul. 1997. DOI: 10.1115/1.2817033.

[35] D. M. Feiner and J. H. Griffin, "A fundamental model of mistuning for a single family of modes", *Journal of Turbomachinery*, vol. 124, no. 4, pp. 597–605, Nov. 2002. DOI: 10.1115/1.1508384.

[36] M. P. Castanier, G. Óttarsson, and C. Pierre, "A reduced order modeling technique for mistuned bladed disks", *Journal of Vibration and Acoustics*, vol. 119, no. 3, pp. 439–447, Jul. 1997. DOI: 10.1115/1.2889743.

[37] R. Bladh, M. P. Castanier, and C. Pierre, "Reduced order modeling and vibration analysis of mistuned bladed disk assemblies with shrouds", *Journal of Engineering for Gas Turbines and Power*, vol. 121, no. 3, pp. 515–522, Jul. 1999. DOI: 10.1115/1.2818503.

[38] R. Bladh, M. P. Castanier, and C. Pierre, "Component-mode-based reduced order modeling techniques for mistuned bladed disks—part i: Theoretical models", *Journal of Engineering for Gas Turbines and Power*, vol. 123, no. 1, pp. 89–99, Apr. 2000. DOI: 10.1115/1.1338947.

[39] Y. Bhartiya and A. Sinha, "Reduced order model of a multistage bladed rotor with geometric mistuning via modal analyses of finite element sectors", *Journal of Turbomachinery*, vol. 134, no. 4, p. 041 001, Jul. 2011. DOI: 10.1115/1.4003224.

[40] Y. Bhartiya and A. Sinha, "Reduced order modeling of a bladed rotor with geometric mistuning via estimated deviations in mass and stiffness matrices", *Journal of Engineering for Gas Turbines and Power*, vol. 135, no. 5, p. 052 501, Apr. 2013. DOI: 10.1115/1.4007783.

[41] M. P. Castanier and C. Pierre, "Using intentional mistuning in the design of turbomachinery rotors", *AIAA journal*, vol. 40, no. 10, pp. 2077–2086, 2002. DOI: 10.2514/2.1542.

[42] Y.-J. Chan and D. J. Ewins, "Prediction of vibration response levels of mistuned integral bladed disks (blisks): Robustness studies", *Journal of Turbomachinery*, vol. 134, no. 4, p. 044 501, Jul. 2011. DOI: 10.1115/1.4003646.

[43] Y. Duan, C. Zang, and E. P. Petrov, "Forced response analysis of high-mode vibrations for mistuned bladed disks with effective reduced-order models", *Journal of Engineering for Gas Turbines and Power*, vol. 138, no. 11, p. 112 502, Jun. 2016. DOI: 10.1115/1.4033513.

[44] C. Joannin, B. Chouvion, F. Thouverez, J.-P. Ousty, and M. Mbaye, "A nonlinear component mode synthesis method for the computation of steady-state vibrations in non-conservative systems", *Mechanical Systems and Signal Processing*, vol. 83, pp. 75–92, 2017. DOI: 10.1016/j.ymssp.2016.05.044.

[45] S. M. Pourkiaee, S. Zucca, and R. G. Parker, "Relative cyclic component mode synthesis: A reduced order modeling approach for mistuned bladed disks with friction interfaces", *Mechanical Systems and Signal Processing*, vol. 163, p. 108 197, 2022. DOI: 10.1016/j.ymssp.2021.108197.

[46] M. Mitra and B. I. Epureanu, "Dynamic modeling and projection-based reduction methods for bladed disks with nonlinear frictional and intermittent contact interfaces", *Applied Mechanics Reviews*, vol. 71, no. 5, p. 050 803, Sep. 2019. DOI: 10.1115/1.4043083.

[47] A. Koscso and E. P. Petrov, "Blade root joint modelling and analysis of effects of their geometry variability on the nonlinear forced response of tuned and mistuned

bladed disks", ser. Turbo Expo, vol. Volume 11: Structures and Dynamics: Structural Mechanics, Vibration, and Damping; Supercritical CO2, Sep. 2020, V011T30A024. DOI: 10.1115/GT2020-15225.

[48] W. Tang, S. Baek, and B. I. Epureanu, "Reduced-order models for blisks with small and large mistuning and friction dampers", *Journal of Engineering for Gas Turbines and Power*, vol. 139, no. 1, p. 012 507, Sep. 2016. DOI: 10.1115/1.4034212.

[49] H.-P. Hackenberg and A. Hartung, "An approach for estimating the effect of transient sweep through a resonance", *Journal of Engineering for Gas Turbines and Power*, vol. 138, no. 8, p. 082 502, Mar. 2016. DOI: 10.1115/1.4032664.

[50] J. Tong, C. Zang, and E. P. Petrov, "Accurate interpolation of the dependency of modal properties on the rotation speed for the transient response analysis of bladed disks", *Journal of Engineering for Gas Turbines and Power*, vol. 144, no. 2, p. 021 022, Dec. 2021. DOI: 10.1115/1.4052501.

[51] R. Corral and J. M. Gallardo, "Non-linear dynamics of multi-mode unstable bladed-disks: Part i—description of a canonical model and phenomenological results", ser. Turbo Expo, vol. Volume 6: Structures and Dynamics, Parts A and B, Jun. 2011, pp. 1331–1341. DOI: 10.1115/GT2011-45983.

[52] R. Corral, J. M. Gallardo, and R. Ivaturi, "Conceptual analysis of the non-linear forced response of aerodynamically unstable bladed-discs", ser. Turbo Expo, vol. Volume 7A: Structures and Dynamics, Jun. 2013, V07AT32A001. DOI: 10.1115/GT2013-94851.

[53] R. Corral and J. M. Gallardo, "Nonlinear dynamics of bladed disks with multiple unstable modes", *AIAA journal*, vol. 52, no. 6, pp. 1124–1132, 2014. DOI: 10.2514/1.J051812.

[54] J. Gross and M. Krack, "Multi-wave vibration caused by flutter instability and nonlinear tip-shroud friction", 2, vol. 142, Jan. 2020, p. 021 013. DOI: 10.1115/1.4044884.

[55] M. Krack, L. Panning-von Scheidt, and J. Wallaschek, "On the interaction of multiple traveling wave modes in the flutter vibrations of friction-damped tuned bladed disks", *Journal of Engineering for Gas Turbines and Power*, vol. 139, no. 4, p. 042 501, Oct. 2016. DOI: 10.1115/1.4034650.

[56] S. Tatzko and M. Jahn, "On the use of complex numbers in equations of nonlinear structural dynamics", *Mechanical Systems and Signal Processing*, vol. 126, pp. 626–635, 2019. DOI: 10.1016/j.ymssp.2019.02.041.

[57] E. P. Petrov, "A method for use of cyclic symmetry properties in analysis of nonlinear multiharmonic vibrations of bladed disks", *Journal of Turbomachinery*, vol. 126, no. 1, pp. 175–183, Mar. 2004. DOI: 10.1115/1.1644558.

[58] M. Krack and J. Gross, *Harmonic balance for nonlinear vibration problems*. Springer, 2019, vol. 1. DOI: 10.1007/978-3-030-14023-6.

[59] T. M. Cameron and J. H. Griffin, "An alternating frequency/time domain method for calculating the steady-state response of nonlinear dynamic systems", *Journal of Applied Mechanics*, vol. 56, no. 1, pp. 149–154, Mar. 1989. DOI: 10.1115/1.3176036.

[60] G. Ashcroft, C. Frey, and H.-P. Kersken, "On the development of a harmonic balance method for aeroelastic analysis", in *Proceedings of the 6th. European Conference on Computational Fluid Dynamics-ECFD VI*, 2014, pp. 5885–5896.

[61] C. M. Firrone, S. Zucca, and M. M. Gola, "The effect of underplatform dampers on the forced response of bladed disks by a coupled static/dynamic harmonic balance method", *International Journal of Non-Linear Mechanics*, vol. 46, no. 2, pp. 363–375, 2011. DOI: 10.1016/j.ijnonlinmec.2010.10.001.

[62] C. Schwingshackl, E. Petrov, and D. Ewins, "Measured and estimated friction interface parameters in a nonlinear dynamic analysis", *Mechanical Systems and Signal Processing*, vol. 28, pp. 574–584, 2012, Interdisciplinary and Integration Aspects in Structural Health Monitoring. DOI: 10.1016/j.ymssp.2011.10.005.

[63] K. Y. Sanliturk, M. Imregun, and D. J. Ewins, "Harmonic balance vibration analysis of turbine blades with friction dampers", *Journal of Vibration and Acoustics*, vol. 119, no. 1, pp. 96–103, Jan. 1997. DOI: 10.1115/1.2889693.

[64] E. P. Petrov, "Analysis of bifurcations in multiharmonic analysis of nonlinear forced vibrations of gas turbine engine structures with friction and gaps", *Journal of Engineering for Gas Turbines and Power*, vol. 138, no. 10, p. 102 502, Apr. 2016. DOI: 10.1115/1.4032906.

[65] E. P. Petrov and D. J. Ewins, "Analytical formulation of friction interface elements for analysis of nonlinear multi-harmonic vibrations of bladed disks", *Journal of Turbomachinery*, vol. 125, no. 2, pp. 364–371, Apr. 2003. DOI: 10.1115/1.1539868.

[66] S. Quaegebeur, B. Chouvion, and F. Thouverez, "Nonlinear cyclic reduction for the analysis of mistuned cyclic systems", *Journal of Sound and Vibration*, vol. 499, p. 116 002, 2021. DOI: 10.1016/j.jsv.2021.116002.

[67] C. Berthold, J. Gross, C. Frey, and M. Krack, "Fully coupled analysis of flutter induced limit cycles: Frequency versus time domain methods", 7, vol. 145, May 2023, p. 071 009. DOI: 10.1115/1.4062408.

[68] C. Berthold, J. Gross, C. Frey, and M. Krack, "Analysis of friction-saturated flutter vibrations with a fully coupled frequency domain method", *Journal of Engineering for Gas Turbines and Power*, vol. 142, no. 11, p. 111 007, Oct. 2020. DOI: 10.1115/1.4048650.

[69] A. Förster and M. Krack, "An efficient method for approximating resonance curves of weakly-damped nonlinear mechanical systems", *Computers & Structures*, vol. 169, pp. 81–90, 2016. DOI: 10.1016/j.compstruc.2016.03.003.

[70] S. Zucca, J. Borrajo, and M. M. Gola, "Forced response of bladed disks in cyclic symmetry with underplatform dampers", ser. Turbo Expo, vol. Volume 5: Marine; Microturbines and Small Turbomachinery; Oil and Gas Applications; Structures and Dynamics, Parts A and B, May 2006, pp. 921–929. DOI: 10.1115/GT2006-90785.

[71] A. Y. T. Leung and T. Ge, "Toeplitz jacobian matrix for nonlinear periodic vibration", *Journal of Applied Mechanics*, vol. 62, no. 3, pp. 709–717, Sep. 1995. DOI: 10.1115/1.2897004.

[72] S. Tatzko and M. Jahn, "On the use of complex numbers in equations of nonlinear structural dynamics", *Mechanical Systems and Signal Processing*, vol. 126, pp. 626–635, 2019. DOI: 10.1016/j.ymssp.2019.02.041.

[73] R. M. Rosenberg, "The normal modes of nonlinear n-degree-of-freedom systems", *Journal of Applied Mechanics*, vol. 29, no. 1, pp. 7–14, Mar. 1962. DOI: 10.1115/1.3636501.

[74] D. Laxalde and F. Thouverez, "Complex non-linear modal analysis for mechanical systems: Application to turbomachinery bladings with friction interfaces", *Journal of Sound and Vibration*, vol. 322, no. 4, pp. 1009–1025, 2009. DOI: 10.1016/j.jsv.2008.11.044.

[75] M. Krack, "Nonlinear modal analysis of nonconservative systems: Extension of the periodic motion concept", *Computers & Structures*, vol. 154, pp. 59–71, 2015. DOI: 10.1016/j.compstruc.2015.03.008.

[76] C. Berthold, J. Gross, C. Frey, and M. Krack, "Development of a fully-coupled harmonic balance method and a refined energy method for the computation of flutter-induced limit cycle oscillations of bladed disks with nonlinear friction contacts", *Journal of Fluids and Structures*, vol. 102, p. 103 233, 2021. DOI: 10.1016/j.jfluidstructs.2021.103233.

[77] C. Berthold, J. Gross, C. Frey, and M. Krack, "Fully coupled forced response analysis of nonlinear turbine blade vibrations in the frequency domain", *Journal of Fluids and Structures*, vol. 127, p. 104 112, 2024. DOI: 10.1016/j.jfluidstructs.2024.104112.

[78] C. Berthold, J. Gross, C. Frey, and M. Krack, "Fully coupled analysis of flutter induced limit cycles: Frequency versus time domain methods", *Journal of Engineering for Gas Turbines and Power*, vol. 145, no. 7, p. 071 009, May 2023. DOI: 10.1115/1.4062408.

[79] A. Grolet and F. Thouverez, "On a new harmonic selection technique for harmonic balance method", *Mechanical Systems and Signal Processing*, vol. 30, pp. 43–60, 2012. DOI: 10.1016/j.ymssp.2012.01.024.

[80] M. Guskov and F. Thouverez, "Harmonic balance-based approach for quasi-periodic motions and stability analysis", *Journal of Vibration and Acoustics*, vol. 134, no. 3, p. 031 003, Apr. 2012. DOI: 10.1115/1.4005823.

[81] E. Sarrouy and J.-J. Sinou, "Non-linear periodic and quasi-periodic vibrations in mechanical systems-on the use of the harmonic balance methods", *Advances in vibration analysis research*, vol. 21, p. 419, 2011. DOI: 10.5772/15638.

[82] F. Fontanela, A. Grolet, L. Salles, and N. Hoffmann, "Computation of quasi-periodic localised vibrations in nonlinear cyclic and symmetric structures using harmonic balance methods", *Journal of Sound and Vibration*, vol. 438, pp. 54–65, 2019. DOI: 10.1016/j.jsv.2018.09.002.

[83] L. Guillot, P. Vigué, C. Vergez, and B. Cochelin, "Continuation of quasi-periodic solutions with two-frequency harmonic balance method", *Journal of Sound and Vibration*, vol. 394, pp. 434–450, 2017. DOI: 10.1016/j.jsv.2016.12.013.

[84] B. Zhou, F. Thouverez, and D. Lenoir, "A variable-coefficient harmonic balance method for the prediction of quasi-periodic response in nonlinear systems", *Mechanical Systems and Signal Processing*, vol. 64-65, pp. 233–244, 2015. DOI: 10.1016/j.ymssp.2015.04.022.

[85] N. N. Balaji, J. Gross, and M. Krack, "Harmonic balance for quasi-periodic vibrations under nonlinear hysteresis", *Journal of Sound and Vibration*, vol. 590, p. 118 570, 2024. DOI: 10.1016/j.jsv.2024.118570.

[86] H. Poincaré, *Les méthodes nouvelles de la mécanique céleste*. Gauthier-Villars et fils, imprimeurs-libraires, 1893, vol. 2.

[87] H. Poincaré, *New methods of celestial mechanics*. National Aeronautics and Space Administration, 1967.

[88] C. Martel and R. Corral, "Asymptotic description of maximum mistuning amplification of bladed disk forced response", *Journal of Engineering for Gas Turbines and Power*, vol. 131, no. 2, p. 022 506, Dec. 2008. DOI: 10.1115/1.2968868.

[89] D. M. Feiner and J. H. Griffin, "Mistuning identification of bladed disks using a fundamental mistuning model—part i: Theory", *Journal of Turbomachinery*, vol. 126, no. 1, pp. 150–158, Mar. 2004. DOI: 10.1115/1.1643913.

[90] D. M. Feiner and J. H. Griffin, "Mistuning identification of bladed disks using a fundamental mistuning model—part ii: Application", *Journal of Turbomachinery*, vol. 126, no. 1, pp. 159–165, Mar. 2004. DOI: 10.1115/1.1643914.

[91] O. Khemiri, C. Martel, and R. Corral, "Asymptotic description of damping mistuning effects on the forced response of turbomachinery bladed disks", *Journal of Sound and Vibration*, vol. 332, no. 20, pp. 4998–5013, 2013. DOI: 10.1016/j.jsv.2013.04.030.

[92] D. Whitehead, "Effect of mistuning on the vibration of turbo-machine blades induced by wakes", *Journal of mechanical engineering science*, vol. 8, no. 1, pp. 15–21, 1966. DOI: 10.1243/JMES_JOUR_1966_008_004_02.

[93] J. J. Sánchez-Álvarez and C. Martel, "Key action mechanisms of intentional mistuning", *Applied Sciences*, vol. 11, no. 12, p. 5650, 2021. DOI: 10.3390/app11125650.

[94] C. Martel and J. J. Sánchez-Álvarez, "Intentional mistuning effect in the forced response of rotors with aerodynamic damping", *Journal of Sound and Vibration*, vol. 433, pp. 212–229, 2018. DOI: 10.1016/j.jsv.2018.07.020.

[95] C. Martel, R. Corral, and J. M. Llorens, "Stability increase of aerodynamically unstable rotors using intentional mistuning", *Journal of Turbomachinery*, vol. 130, no. 1, p. 011 006, Dec. 2007. DOI: 10.1115/1.2720503.

[96] R. Corral, O. Khemiri, and C. Martel, "Design of mistuning patterns to control the vibration amplitude of unstable rotor blades", *Aerospace Science and Technology*, vol. 80, pp. 20–28, 2018. DOI: 10.1016/j.ast.2018.06.034.

[97] L. Carassale, V. Denoël, C. Martel, and L. Panning-von Scheidt, "Key features of the transient amplification of mistuned systems", *Journal of Engineering for Gas Turbines and Power*, vol. 143, no. 3, p. 031 016, Feb. 2021. DOI: 10.1115/1.4049501.

[98] C. Martel and R. Corral, "Flutter amplitude saturation by nonlinear friction forces: An asymptotic approach", ser. Turbo Expo, vol. Volume 7B: Structures and Dynamics, Jun. 2013, V07BT33A001. DOI: 10.1115/GT2013-94068.

[99] C. Martel, R. Corral, and R. Ivaturi, "Flutter amplitude saturation by nonlinear friction forces: Reduced model verification", *Journal of Turbomachinery*, vol. 137, no. 4, p. 041 004, Oct. 2014. DOI: 10.1115/1.4028443.

[100] C. Martel and J. A. Martín, "Asymptotic description of forced response vibration saturation by friction forces", *Journal of Engineering for Gas Turbines and Power*, vol. 142, no. 1, p. 011 022, Dec. 2019. DOI: 10.1115/1.4044934.

[101] J. A. Martin and C. Martel, "Simplification of the forced response of mistuned bladed disks using multiple scales techniques", *Nonlinear Dynamics*, vol. 104, pp. 2037–2049, 2021. DOI: 10.1007/s11071-021-06397-0.

[102] The European Commission, *FP7 project 213414, FUTURE: Flutter-free turbomachinery blades (*`http://www.future-project.eu/`*)*. 2008-2013.

[103] M. H. Holmes, *Introduction to perturbation methods*. Springer Science & Business Media, 2012, vol. 20. DOI: 10.1007/978-1-4614-5477-9.

[104] J. K. Kevorkian and J. D. Cole, *Multiple scale and singular perturbation methods*. Springer Science & Business Media, 2012, vol. 114. DOI: 10.1007/978-1-4612-3968-0.

[105] C. M. Bender and S. A. Orszag, *Advanced mathematical methods for scientists and engineers I: Asymptotic methods and perturbation theory*. Springer Science & Business Media, 2013. DOI: 10.1007/978-1-4757-3069-2.

[106] A. Sinha and J. H. Griffin, "Effects of friction dampers on aerodynamically unstable rotor stages", *AIAA Journal*, vol. 23, no. 2, pp. 262–270, 1985. DOI: 10.2514/3.8904.

[107] A. Sinha and J. Griffin, "Stability of limit cycles in frictionally damped and aerodynamically unstable rotor stages", *Journal of Sound and Vibration*, vol. 103, no. 3, pp. 341–356, 1985. DOI: 10.1016/0022-460X(85)90427-4.

[108] S. Wiggins *et al.*, "Introduction to applied nonlinear dynamical systems and chaos", DOI: 10.1007/b97481.

[109] S. H. Strogatz, *Nonlinear dynamics and chaos: with applications to physics, biology, chemistry, and engineering*. CRC press, 2018.

[110] J. Guckenheimer and P. Holmes, *Nonlinear oscillations, dynamical systems, and bifurcations of vector fields*. Springer Science & Business Media, 2013, vol. 42. DOI: 10.1007/978-1-4612-1140-2.

[111] E. L. Allgower and K. Georg, *Numerical continuation methods: an introduction*. Springer Science & Business Media, 2012, vol. 13. DOI: 10.1007/978-3-642-61257-2.

[112] E. J. Doedel and B. Oldeman, "Auto-07p: Continuation and bifurcation software", *Montreal, QC: Concordia University Canada*, 1998.

[113] A. Dhooge, W. Govaerts, Y. A. Kuznetsov, W. Mestrom, A. Riet, and B. Sautois, "Matcont and cl matcont: Continuation toolboxes in matlab", *Universiteit Gent, Belgium and Utrecht University, The Netherlands*, 2006.

[114] Z. Ahsan, H. Dankowicz, M. Li, and J. Sieber, "Methods of continuation and their implementation in the coco software platform with application to delay differential equations", *Nonlinear Dynamics*, vol. 107, no. 4, pp. 3181–3243, 2022. DOI: 10.1007/s11071-021-06841-1.

[115] R. Veltz, "Bifurcationkit.jl", Jul. 2020.

[116] A. Sinha and J. H. Griffin, "Friction damping of flutter in gas turbine engine airfoils", *Journal of Aircraft*, vol. 20, no. 4, pp. 372–376, 1983. DOI: 10.2514/3.44878.

[117] The European Commission, "H2020 project 769346, ARIAS: Advanced Research Into Aeromechanical Solutions", 2018-2023, Available online: http://www.arias-project.eu (Accessed on 17 November 2022).

[118] R. Corral, A. Escribano, F. Gisbert, A. Serrano, and C. Vasco, "Linear and non-validation of a linear multigrid accelerated unstructured navier-stokes solver for the computation of turbine blades on hybrid grids", in *9th AIAA/CEAS Aeroacoustics Conference and Exhibit*. DOI: 10.2514/6.2003-3326.

[119] J. M. Gallardo, O. Bermejo, J. Hernández, *et al.*, "Experimental research into aeroelastic phenomena in turbine rotor blades inside arias eu project", *Journal of Turbomachinery*, vol. 146, no. 7, p. 071 009, Jun. 2024. DOI: 10.1115/1.4065621.

[120] S. Rodríguez-Blanco, J. González-Monge, and C. Martel, "Interaction of flutter and forced response in a low pressure turbine rotor with friction damping and mistuning effects", *Journal of Sound and Vibration*, vol. 572, p. 118 181, 2024. DOI: 10.1016/j.jsv.2023.118181.

[121] B. Zwiebach, *Mastering quantum mechanics: essentials, theory, and applications*. MIT Press, 2022.